UNIVERSITY OF SOUTHERN QUEENSLAND

COUPLED/COMBINED COMPACT IRBF SCHEMES FOR FLUID FLOW AND FSI PROBLEMS

A thesis submitted by

CAM MINH TRI TIEN

B. Eng. (Hon.), Ho Chi Minh City University of Technology, Vietnam, 2008

M. Eng. (Hon.), Konkuk University, South Korea, 2010

For the award of the degree of

Doctor of Philosophy

2016

Dedication

To my parents

Cam Minh Tien and Bich Lien Pham

and

my wife

Thi To Uyen Nguyen

Abstract

Fluid structure interaction (FSI), in which static, moving, deforming structural components interact with a fluid, is one of the most important representatives of multi-physics problems. It includes a vast variety of applications, ranging from large-scale problems such as dynamic instabilities of a bridge subject to a strong wind in construction industry, to small-scale problems such as the blood stream through heart valves in bio-mechanics. Apart from experiments, extensive effort has been expended on the development of numerical methods for FSI problems. However, despite the high attention there still is a lack of established methods which are able to offer highly accurate solution, robustness, as well as efficiency to a general FSI problem.

The present work is concerned with further developments of high-order approximation methods based on coupled/combined compact integrated radial basis function (IRBF) stencils and their applications in fluid flow and FSI problems. In our numerical examples, results show that the present schemes generally produce more accurate solutions and better convergence rates than standard methods (e.g. finite difference method (FDM) and high-order compact (HOC) finite difference method) reported in the literature. The main contributions of this study are summarised: (i) developing a fully coupled approach for fluid flow problems; (ii) developing coupled and combined compact forms of the novel IRBF approximation method; (iii) incorporating the high-order coupled compact IRBF into domain decomposition (DD) algorithms for large-scale problems; (iv) proposing a simple but effective preconditioning technique which is employed in the process of converting the radial basis function (RBF) coefficient space into the physical space. The preconditioning technique allows the compact IRBF schemes to be

employed with large values of the shape parameters where the most accurate solutions may be found; and, (v) incorporating the coupled and combined compact IRBF approximation schemes into the fluid flow and FSI solvers for highly accurate solutions. These contributions are detailed as follows.

The direct fully coupled velocity-pressure approach in the Cartesian-grid point-collocation structure is implemented in combination with the high-order compact IRBF for fluid flow problems. Numerical examples indicate that the results of the present scheme are superior to those of the FDM and HOC schemes in terms of the solution accuracy and convergence rates with the grid refinement.

A new coupled compact scheme based on IRBF approximations is presented, where first- and second-order derivatives are constructed over a three-point stencil in each direction. The starting points of the coupled compact scheme are second-order derivatives, producing two integration constants. Nodal values of the first- and second-order derivatives (extra information) at the side nodes of the stencil are sequentially included, via the two integration constants, in the approximation of each derivative at the middle node. Then, the extra information of the nodal first- and second-order derivative values are connected together by means of their identity equations. Owing to its coupling of the extra information, the coupled compact IRBF scheme becomes more accurate, stable and efficient than the normal compact IRBF scheme in which nodal values of first-order derivatives are included for the approximation of the first-order derivative while nodal values of second-order derivatives are included for the approximation of the second-order derivative.

Highly accurate serial and parallel algorithms, using the coupled compact IRBF, are developed for large-scale heat and fluid flow problems which the IRBF-Single domain approach may not be able to deal with, due to the physical memory limitation or the ill-condition problem. The proposed serial and parallel schemes with less computing cost are able to produce almost the same level of accuracy as that of the single domain scheme.

An advanced version of the coupled compact scheme, namely the combined compact IRBF, is presented. The combined compact scheme is also based on the

three-point stencil in each direction. However, the combined compact scheme has different characters: its starting points are fourth-order derivatives, producing four integration constants so that nodal values of first- and second-order derivatives (four extra information) at the side nodes are allowed to be included at once for the approximation of the first- and second-order derivatives at the middle node. No identity equations for connection are required. As a result, the combined compact produces better solution accuracy in a more straight-forward manner than the coupled compact.

The increasing flat region of RBF is of particular interest since it often corresponds to the most accurate RBF approximations. Therefore, the preconditioning technique is introduced to provide stable calculations of IRBF approximations at large values of the shape parameter, where the ill-condition problem becomes severe.

The present high-order accurate approximation schemes are incorporated into the fluid flow solver (the fully coupled velocity-pressure method) and FSI solver (the immersed boundary method), to produce very accurate solutions for viscous flow and FSI problems.

A range of fluid flow and FSI problems are conducted to verify the proposed schemes and to demonstrate their attractiveness. Numerical results in terms of solution accuracy, stability and efficiency are reported in detail and they are compared and in good agreement with corresponding analytical solutions or in favours with results obtained by some other schemes, which are reported the literature, where possible.

Certification of Thesis

I certify that the idea, experimental work, results and analyses, software and conclusions reported in this thesis are entirely my own effort, except where otherwise acknowledged. I also certify that the work is original and has not been previously submitted for any other award.

_____   _____

Cam Minh Tri Tien   Date

ENDORSEMENT

_____   _____

Prof. Thanh Tran-Cong, Principal supervisor   Date

_____   _____

Prof. Nam Mai-Duy, Co-supervisor   Date

_____   _____

Dr. Canh-Dung Tran, Co-supervisor   Date

Acknowledgements

wife, my best friend and great companion, who encouraged, supported, entertained and helped me get through this challenging period in the most positive way.

Papers Resulting from the Research

Journal papers

1. **C. M. T. Tien**, N. Thai-Quang, N. Mai-Duy, C.-D. Tran and T. Tran-Cong (2014). A fully coupled scheme for viscous flows in regular and irregular domains using compact integrated RBF approximation, *Applied Mechanics & Materials*, 553: 138–143. DOI: 10.4028/www.scientific.net/AMM.553.138.

2. **C. M. T. Tien**, N. Thai-Quang, N. Mai-Duy, C.-D. Tran and T. Tran-Cong (2015). High-order fully coupled scheme based on compact integrated RBF approximation for viscous flows in regular and irregular domains, *Computer Modeling in Engineering & Sciences*, 105 (4): 301–340. DOI: 10.3970/cmes.2015.105.301.

3. **C. M. T. Tien**, N. Thai-Quang, N. Mai-Duy, C.-D. Tran and T. Tran-Cong (2015). A three-point coupled compact integrated RBF scheme for second-order differential problems, *Computer Modeling in Engineering & Sciences*, 104 (6): 425–469. DOI: 10.3970/cmes.2015.104.425.

4. **C. M. T. Tien**, N. Pham-Sy, N. Mai-Duy, C.-D. Tran and T. Tran-Cong (2015). A high-order coupled compact integrated RBF approximation based domain decomposition algorithm for second-order differential problems, *Computer Modeling in Engineering & Sciences*, 104 (4): 251–304. DOI: 10.3970/cmes.2015.104.251.

5. **C. M. T. Tien**, N. Mai-Duy, C.-D. Tran and T. Tran-Cong (2016). A numerical study of compact approximations based on flat integrated radial basis functions for second-order differential equations, *Computers &*

Mathematics with Applications (under review).

6. **C. M. T. Tien**, D. Ngo-Cong, N. Mai-Duy, C.-D. Tran and T. Tran-Cong (2016). High-order fluid solver based on a combined compact integrated RBF approximation and its fluid-structure interaction applications, *Computers & Fluids*, 131: 151–168. DOI: 10.1016/j.compfluid.2016.03.021.

7. N. Mai-Duy, T. T. V. Le, **C. M. T. Tien**, D. Ngo-Cong and T. Tran-Cong (2016). Compact approximation stencils based on integrated flat radial basis functions, *Engineering Analysis with Boundary Elements (submitted)*.

8. D. Ngo-Cong, **C. M. T. Tien**, T. Nguyen-Ky, D.-A. An-Vo, N. Mai-Duy, D. V. Strunin and T. Tran-Cong (2016). A compact radial basis function scheme for flow in heterogeneous soils, *International Journal for Numerical Methods in Fluids (under review)*.

Conference papers

1. **C. M. T. Tien**, N. Thai-Quang, N. Mai-Duy, C.-D. Tran and T. Tran-Cong (2013). A fully coupled scheme for viscous flows in regular and irregular domains using compact integrated RBF approximation, *Proceedings: the 1st Australian Conference Computational Mechanics*, University of Sydney, Sydney, Australia.

2. **C. M. T. Tien**, D. Ngo-Cong, N. Mai-Duy, C.-D. Tran and T. Tran-Cong (2015). Stable integrated RBF calculation using preconditioning and high-order compact approximation for second-order PDEs, *Eleventh International Conference on CFD in the Minerals & Process Industries*, CSIRO, Melbourne, Australia.

Table of Contents

Acronyms & Abbreviations

1D-IRBF . . . . . One Directional-Integrated Radial Basis Function

ADI . . . . Alternating Direction Implicit

BEM . . . . Boundary Element Method

CFD . . . . Computational Fluid Dynamics

CN . . . . Crank-Nicholson

DD . . . . Domain Decomposition

DEM . . . . Diffusive Element Method

DRBF . . . . Direct/Differential Radial Basis Function

EFG . . . . Element-Free Galerkin

EHOC . . . . Exponential High-Order Compact

FDM . . . . Finite Difference Method

FE/BE . . . . Forward Euler/Backward Euler

FEM . . . . Finite Element Method

FPM . . . . Finite Point Method

FSI . . . . Fluid Structure Interaction

FVM . . . . Finite Volume Method

GFDM . . . . General Finite Different Method

GMRES . . . . . . Generalised Minimal RESidual

HOC .... High(er)-Order Compact

HOC-BEM .. High-Order Compact Boundary Element Method

HOC-FDM .. High-Order Compact Finite Difference Method

HPD .... Hybrid PaDé

IBM .... Immersed Boundary Method

IRBF .... Indirect/Integrated Radial Basis Function

MLPG .... Meshless Local Petrov-Galerkin

MLS .... Moving Least Squares

MP .... MidPoint

MQ .... MultiQuadric

N-S .... Navier-Stokes

ODE .... Ordinary Differential Equation

PDE .... Partial Differential Equation

PDE .... PaDÉ

PIM .... Point Interpolation Method

PISO .... Pressure-Implicit with Splitting of Operator

PU .... Partition of Unity

PUFEM ...... Partition of Unity Finite Element Method

RBF .... Radial Basis Function

RHS .... Right Hand Side

RK .... Runge-Kutta

RKPM .... Reproducing Kernel Particle Method

SCGS .... Symmetrical Coupled Gauss-Seidel

SIMPLE ..... Semi-Implicit Method for Pressure Linked Equations

List of Figures

List of Tables

Chapter 1

Introduction

The chapter starts with Section 1.1 stating the motivation of the present research. Section 1.2 reviews numerical methods for fluid structure interaction. Following this, Section 1.3 briefly introduces the idea behind the immersed boundary method (IBM) and derives the IBM equations. Then, Section 1.4 reviews high-order approximation methods. Next, Section 1.5 briefly reviews element-free approximation methods, followed by a brief overview of direct and indirect radial basis function methods for approximation of function and its derivatives, which is given in Section 1.6. The objectives of the thesis is presented in Section 1.7. Finally, the outline of the thesis is described in Section 1.8.

1.1 Motivation

Fluid structure interaction (FSI) in which one or more structures interact with an internal or surrounding fluid flow is of great importance for numerous applications. The driving applications can be found in a variety of fields such as aerospace, energy production, automotive, micro-fluidic and biomedical, civil and construction engineering. FSI is part of various problems of air, sea and land vehicle motion and flow physics, energy conversion and power generation, chemical reactors and transport processes, energy preservation and environmental sustainability, biomedicine, noise and acoustics amongst others.

The numerical solution of FSI has been in the past few decades an object of keen

interest from researchers. However, thorough study of such problems remains a challenge due to their strong nonlinearity and multidisciplinary requirements (Chakrabarti, 2005). In practice, it is impossible to derive analytical solutions to most of FSI problems, while laboratory experiments are not always available. Therefore, to investigate the fundamental physics of the complicated interaction between fluids and solids, numerical methods are usually considered (Hou et al., 2012a). Fortunately, the numerical solution of FSI has become more popular during recent years, owing in part to the ability to address more computationally expensive problems with recent advances of computer technology (Avi et al., 2011).

Over the past decades, high-order approximation schemes for solving partial differential equations (PDEs), governing many problems in engineering and sciences including FSI applications, have gained a lot of effort from researchers. The traditional first-order upwind and second-order central finite difference methods generally require sufficiently fine meshes (Kun et al., 2012) to achieve acceptable accuracy. The computational cost of those methods is therefore relatively high. High-order methods, by which comparable accuracy can be obtained using much coarser discretisation, have been developed to alleviate those difficulties.

Despite the high attention there still is a lack of established methods which are capable of dealing with a general FSI problem, offering high accuracy, robustness, as well as efficiency. Particularly, most of numerical methods for FSI problems are based on the finite difference, finite element, and finite volume methods which possess low rate of convergence. This thesis will develop high-order approximation methods and implement them to solve fluid flow and FSI problems with the focus on improving the solution accuracy and computational efficiency.

1.2 Review of numerical methods for FSI

Numerical procedures for solving the FSI problems may be generally classified into two approaches: the monolithic and the partitioned. Figure 1.1 illustrates the solution procedure of the monolithic and partitioned approaches. In the

monolithic approach (Hubner et al., 2004; Ryzhakov et al., 2010), the equations governing the fluid flow and displacement of the structure are solved simultaneously with a single solver. The interfacial conditions are implicit in the solution procedure. This approach can potentially achieve better accuracy for a multidisciplinary problem, but it may require substantially more resources and expertise to develop and maintain such special codes. In contrast, the partitioned approach (Badia et al., 2008; Vierendeels et al., 2008; Wood et al., 2010) separately solves the governing equations in the flow domain with a flow solver and in the structure domain with a structure solver. The interfacial conditions are used explicitly to communicate information between the fluid and the structure solutions. The advantage of the latter approach is the ability to integrate existing disciplinary (i.e., fluidic and structural) algorithms and reduce the code development time by utilising available codes or numerical algorithms that have been validated and used for solving many complex fluid or structural problems (Hou et al., 2012a).
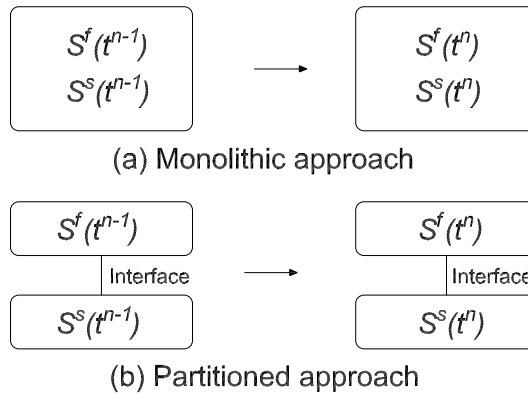
Figure 1.1 Schematic of (a) monolithic approach and (b) partitioned approach for fluid structure interaction problems, where S^f and S^s denote the fluid and structure solutions, respectively.

Another general classification of the FSI solution procedures is based on the treatment of meshes: the conforming mesh methods and the non-conforming mesh methods. The distinction between these two types of meshes can be observed in Fig 1.2, where a tubular solid (tube) is moving in a fluid domain. The conforming mesh methods consider the interface conditions as physical boundary conditions, which treat the interface location as part of the solution, and require meshes that conform to the moving interface and boundary surface. Owing to the movement and/or deformation of the solid structure, mesh updating

is required as the solution is advanced. The conforming mesh methods, e.g. arbitrary Lagrangian-Eulerian and generalised Gauss-Seidel approaches, have some limitations which include time consuming process of mesh regeneration and low accuracy when solving large deformation problems due to mesh distortions. On the other hand, the non-conforming mesh methods, e.g. immersed boundary and immersed interface approaches, treat the boundary location and the related interface conditions as constraints imposed on the model equations. As a result, fluid and solid equations can be solved independently from each other in their respective coordinate systems, and mesh updating is not necessary.

(a) Conforming mesh   (b) Non-conforming mesh
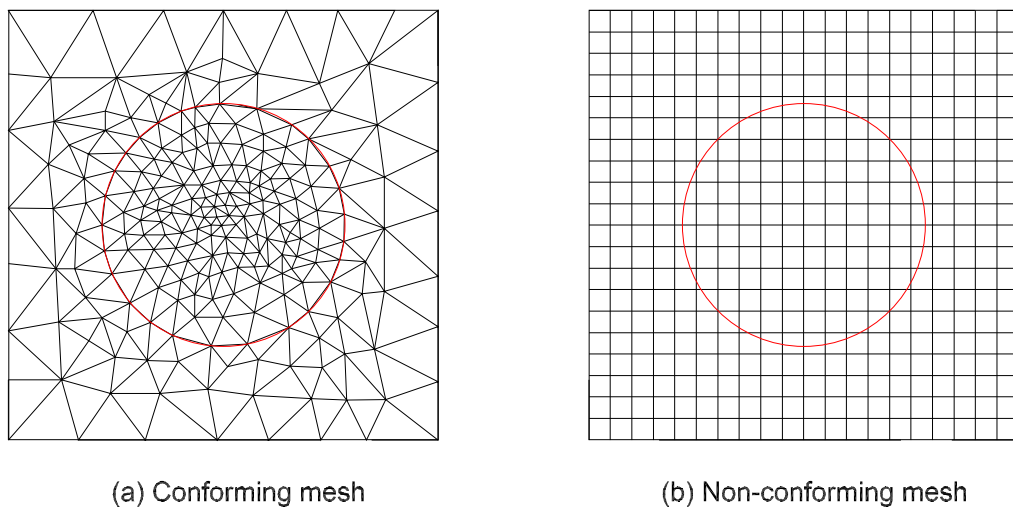
Figure 1.2 Example of (a) conforming mesh and (b) non-conforming mesh, where the red circle represents the structure.

Most of the non-conforming mesh methods are based on the framework of the immersed methods in which force-equivalent terms are added to fluid equations to represent the FSI and to avoid mesh updating in the numerical procedure. The immersed structure can be either a boundary, for example a curve (2D) and a surface (3D), or a body with finite area (2D) and volume (3D), either rigid or flexible. One of the most popular procedures for the immersed methods is the immersed boundary method (IBM), originally proposed by Peskin (1977). The IBM solves the fluid equations with an additional term, the FSI force, which represents the effects of the immersed boundary acting on the fluid motion. The FSI force is computed explicitly from the structure configuration, which is then used to compute the fluid velocity in the fluid equations. The non-slip condition is imposed so that the immersed boundary must move at the local fluid velocity.

The location of the boundary is updated by an evolution equation. The need for mesh updating is completely eliminated.

There have been several books and reviews related to the numerical study of the FSI problems. Morand and Ohayon (1995) presented a number of numerical methods dealing with interaction problems between structures and internal fluids, with applications focused on sloshing, hydro-elasticity, and structural acoustics. Dowell and Hall (2001) provided a discussion of developments and challenges of numerical methods for FSI problems, with the emphasis on the enhanced physical understanding and dramatic reductions in computational cost made possible by reduced-order models, time linearisation, and methodologies drawn from dynamic system theory. Mittal and Iaccarino (2005) extensively reviewed FSI techniques based on the IBM for viscous flows with immersed (or embedded) boundaries. Sotiropoulos and Yang (2014) summarised different immersed boundary methods for imposing boundary conditions, efficient iterative algorithms for solving Navier-Stokes equations. Results from a wide range of the application of such methods were also presented. The largest number of applications of these methods are currently found in biological and multiphase flows. In addition to these, IBM has also been developed for applications in complex turbulent flows, and multi-material and multi-physics simulations.

1.3 Fundamentals of immersed boundary method

The immersed boundary method (IBM) is a mathematical framework for studying FSI problems, which was originally devised by Peskin (1977) to simulate the heart valve flow. The main idea of the IBM is to use Eulerian variables for the fluid mechanics together with Lagrangian variables for structural mechanics; and, the Eulerian variables are defined on a fixed Cartesian grid whereas the Lagrangian variables are defined on a curvilinear grid that moves freely through the fixed Cartesian grid. The interaction between fluid and structure can be modelled by a well chosen discretised approximation to the Dirac delta function. The IBM method has now evolved into a general useful method and has been widely used in numerous applications.

For simplicity, we consider a viscous incompressible fluid in a two-dimensional domain $\Omega = [0,1]^2$ using the Eulerian coordinates $\mathbf{x} = (x, y)$, containing a single closed immersed fibre $\Gamma \subset \Omega$, using the Lagrangian coordinates $s \in [0,1]$. The immersed boundary curve, Γ, is described by the function $\mathbf{X}(s, t)$. An example setup of two dimensional fluid domain with a single immersed boundary curve is shown in Figure 1.3.
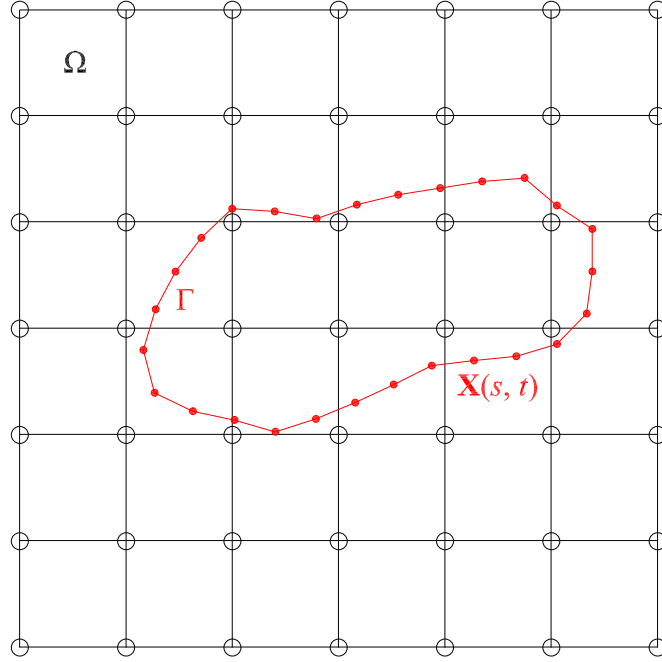
Figure 1.3 Example discrete immersed boundary curve and underlying discretised Eulerian grid.

The motion of the fluid-membrane is governed by the incompressible Navier-Stokes equations

$$\rho \left(\frac{\partial \mathbf{u}}{\partial t} + \mathbf{u} \cdot \nabla \mathbf{u} \right) = -\nabla p + \mu \nabla^2 \mathbf{u} + \mathbf{f}, \tag{1.1}$$

$$\nabla \cdot \mathbf{u} = 0, \tag{1.2}$$

where $\mathbf{u}(\mathbf{x}, t) = (u(\mathbf{x}, t), v(\mathbf{x}, t))$ and $p(\mathbf{x}, t)$ are the fluid velocity and pressure at location $\mathbf{x}$ and time t, respectively; ρ and μ are the constant fluid density and dynamic viscosity, respectively; and, $\mathbf{f}(\mathbf{x}, t) = (f_x(\mathbf{x}, t), f_y(\mathbf{x}, t))$ is the external body force through which the immersed boundary is coupled to the fluid

$$\mathbf{f}(\mathbf{x}, t) = \int_\Gamma \mathbf{F}(s, t) \delta(\mathbf{x} - \mathbf{X}(s, t)) ds, \tag{1.3}$$

where $\mathbf{X}(s,t) = (X(s,t), Y(s,t))$ is a parametric curve representing the immersed boundary configuration; the delta function $\delta(\mathbf{x}) = d_h(x)d_h(y)$ is a Cartesian product of one-dimensional Dirac delta functions and is to transmit the Lagrangian immersed boundary force from Γ onto adjacent Eulerian fluid nodes; and, $\mathbf{F}(s,t)$ is the elastic force density which is a function of the current immersed boundary configuration

$$\mathbf{F}(s,t) = \boldsymbol{\mathcal{F}}\left(\mathbf{X}(s,t)\right) = \sigma \frac{\partial}{\partial s}\left(\frac{\partial \mathbf{X}(s,t)}{\partial s}\left(1 - \frac{\varepsilon}{|\frac{\partial \mathbf{X}(s,t)}{\partial s}|}\right)\right), \qquad (1.4)$$

where σ and ε are the spring constant and elastic strain of the structure, respectively.

The final equation needed to close the system is an evolution equation for the immersed boundary, which comes from the simple requirement that Γ must travel at the local fluid velocity (the non-slip condition)

$$\frac{\partial \mathbf{X}(s,t)}{\partial t} = \mathbf{U}(\mathbf{X}(s,t),t) = \int_{\Omega} \mathbf{u}(\mathbf{x},t)\delta(\mathbf{x} - \mathbf{X}(s,t))d\mathbf{x}, \qquad (1.5)$$

where $\mathbf{U}$ is the boundary speed. The delta function δ here imposes the Eulerian flow velocity on the adjacent Lagrangian boundary nodes.

In the IBM, like other numerical approaches, the variable approximation plays an important role in the solution accuracy, stability and efficiency of the method. Next section will outline high-order numerical approximation methods based on radial basis functions (RBFs) which can be incorporated into the IBM to enhance its performance.

1.4 Review of high-order approximation methods

Recently, there has been a great interest in the development and application of high-order approximation algorithms for the numerical solution of the second-order differential equations which govern fluid flow and FSI problems. Higher-order compact (HOC) finite difference methods (Hirsh, 1975; Rubin and Khosla, 1977; Adam, 1977; Noye and Tan, 1989), which usually require fewer grid points

to achieve a certain level of accuracy, have been widely used in numerical calculations for various problems involving incompressible and compressible flows. These approaches possess the robustness of the FDM and the exponential convergence rate of spectral-like methods. In the HOC-FDMs, the derivative values at a particular node are implicitly approximated not only from the function values in the stencil but also from the values of the derivatives at its neighboring nodes. Numerical results produced by HOC approaches have a higher order of accuracy for the same number of grid points in comparison with those of the FDM. Overall, the HOC-FDM schemes are found to be robust, efficient and accurate for most computational fluid dynamics applications. Extensive study and discussion of the resolution characteristics of HOC-FDM families on a uniform grid was reported in (Lele, 1992). Since then, the compact schemes have attained wide popularity in solving various problems including fluid flow and FSI. A thorough review of the issues involving the instability of the high-order boundary closures on uniform grids and a deep discussion of the underlying concepts of the HOC-FDMs was given in (Colonius, 2004).

Another class of highly accurate numerical schemes for PDEs is the radial basis function method. The RBF methods have significantly attracted attention from researchers because of its simplicity, meshless nature and exponential convergence characteristic. Kansa (1990a,b) first proposed the use of RBFs as approximants (here referred to as direct/differential RBF or DRBF methods). In the DRBF method, a closed form RBF approximating function is first obtained from a set of training points and the derivative functions are then calculated directly from the closed form RBF. Mai-Duy and Tran-Cong (2001a, 2003) then introduced the idea of using indirect/integrated radial basis functions (IRBFs) for solving PDE problems. In the IRBF approach, the highest-order derivatives under interest are decomposed into a set of RBFs; and, expressions for the lower derivatives and its function are then obtained through integration processes. Various numerical studies in (Mai-Duy and Tran-Cong, 2001a, 2003, 2005; Sarra, 2006; Shu and Wu, 2007) have shown that the integral approach is more accurate than the differential approach. It is believed that the integration process is averagely less sensitive to noise. In the IRBF methods, the integration process gives rise to integration

constants through which extra equations can be employed. A one-dimensional IRBF scheme was developed in (Mai-Duy and Tanner, 2007). It was reported to be more effective and accurate than the original two-dimensional one because its conversion matrices are smaller and possess better condition numbers. These global RBF schemes have several advantages such as fast convergence, meshless nature, and simple implementation. However, their RBF matrices are still fully populated and thus become much more ill-conditioned as the number of the RBF is increased. To resolve these drawbacks, Mai-Duy and Tran-Cong (2011) proposed a five-point compact IRBF scheme that is capable of solving second-order elliptic PDEs. The compact local scheme has much smaller conversion matrices and can avoid the information loss. As a result, it is more effective and produces more accurate solutions than its global counterparts. Mai-Duy and Tran-Cong (2013) further proposed a three-point compact IRBF scheme where only nodal values of second-order derivatives (i.e. extra information) are incorporated into the approximations. While, Thai-Quang et al. (2012b) proposed another three-point compact IRBF scheme in which the extra information includes nodal values of both the first- and second-order derivatives for the computation of the derivatives. Several other approaches using RBFs for solving engineering and scientific problems have been recently reported, see for example (An-Vo et al., 2010; Kosec et al., 2011; Ngo-Cong et al., 2012; Sellountos et al., 2012; Thai-Quang et al., 2013; Mramor et al., 2013; Elgohary et al., 2014a,b; Hon et al., 2015) and the references therein.

Some other HOC methods include the PaDÉ (PDE) method proposed in (You, 2006), the exponential high-order compact scheme (EHOC) of Tian and Ge (2007), the high-order compact boundary value method (HOC-BVM) of Dehghan and Mohebbi (2008), the high-order hybrid Padé (HPD) method introduced in (Ma et al., 2012) and references therein.

1.5 Review of element-free approximation methods

Traditional element-based methods such as the finite element method (FEM) and finite volume method (FVM) were originally defined on elements of data points in

which each point has a fixed number of predefined neighbours. The connectivity between neighbours can be used to define mathematical operators such as the derivative.

However, in simulations where the material being simulated can move around (as in computational fluid dynamics) or where large deformations of the material can happen (as in simulations of plastic materials), the connectivity of the element can be difficult to maintain and computational errors eventually develop during the simulation. If the element becomes tangled or degenerate, the operators defined on it may no longer produce correct results. The element may be regenerated, however this can be time-consuming and introduce error, since all existing data points must be mapped onto continuously updated data points. Element-free approximation methods were introduced with the objective of eliminating those drawbacks.

In element-free methods, the approximation is built from nodes. These set of nodes do not form elements, which means that no connectivity between the nodes is required, at least for the field variable interpolation (Liu, 2003). Generally, there are two approaches to handle the governing differential equation, namely the weak and strong forms. In the weak form methods, the governing differential equations are first transformed into their corresponding weak form, and then solved by numerical integration techniques. The governing equations and boundary conditions are satisfied averagely over a domain instead of at individual nodes. While, in the strong form methods, the derivative terms from the governing differential equations are discretised directly, and the system of equations is obtained in terms of the values of the approximate function at the field nodes. The governing equation is satisfied at all the nodes in the internal domain and the boundary condition is satisfied at every boundary node. In general, the element-free methods based on the weak form are considered numerically more stable than those based on the strong form. However, the strong form methods can be more accurate, easy to use, and economical to compute (Li and Mulay, 2013).

One of the first element-free methods is the smooth particle hydrodynamics (SPH) method proposed by Lucy (1977) and Gingold and Monaghan (1977). It was orig-

inally developed for solving problems in astrophysics and later in fluid dynamics (Nguyen et al., 2008). Since the original SPH suffered from spurious instabilities and inconsistencies, many improvements based on both the strong and weak forms were incorporated into SPH (Belytschko et al., 1996; Dilts, 1999; Bonet and Kulasegaram, 2000; Rabczuk et al., 2004).

Some of the methods based on the weak form approach include the diffusive element methods (DEMs) developed by Nayroles et al. (1992), the element-free Galerkin (EFG) method devised in (Belytschko et al., 1994), the reproducing kernel particle method (RKPM) proposed in (Liu et al., 1995), h-p cloud method (Duarte and Oden, 1996) and partition of unity finite element method (PUFEM) (Babuska and Melenk, 1997), the meshless local Petrov-Galerkin (MLPG) approach (Atluri and Zhu, 1998), the point interpolation method (PIM) based on RBFs (Wang and Liu, 2002b), and the local Kriging method (Li et al., 2004). Some of the developed methods based on the strong form approach include the general finite different method (GFDM) devised in (Girault, 1974; Liszka and Orkisz, 1980), the DRBF collocation method (Kansa, 1990a,b), the finite point method (FPM) developed by Onate et al. (1996), the IRBF collocation method (Mai-Duy and Tran-Cong, 2001a), the Hermit cloud method (Li et al., 2003a). Among these, the element-free methods utilising RBFs, such as the IRBF methods, were reported to be simple to implement and highly accurate. Also, the RBF based methods have been widely employed in different areas of applications including fluid dynamics for the last three decades because of their element-free nature and exponential convergence rate (Fasshauer, 2007).

1.6 Fundamentals of integrated radial basis function

Mai-Duy and Tran-Cong (2001a) reported the integrated radial basis function method (IRBF) for approximations of function and its derivatives on a set of discrete unstructured function values, u, and demonstrated that the IRBF method based on Multiquadric (MQ) RBF yields superior solution accuracy compared to that of the DRBF. For the sake of the present discussion, the working principles

of the two methods on a one-dimensional grid line (which is shown in Figure 1.4) are summarised in this section. When the mesh becomes tangled or degenerate during simulation

$$x_1 \quad x_2 \quad x_3 \qquad\qquad x_{m-2} \ x_{m-1} \ x_m$$

Figure 1.4 Example of 1D grid line with m nodal functions.

In this work, the chosen RBF is the MQ which is given by

$$G_i(x) = \sqrt{(x - c_i)^2 + a_i^2}, \tag{1.6}$$

where c_i and a_i are the centre and the width of the i-th MQ, respectively. The set of nodal points is taken to be the same as the set of MQ centres. We simply choose the MQ width as $a_i = \beta h_i$, where β, the shape parameter, is a positive scalar and h_i is the distance between the i-th node and its closest neighbour.

1.6.1 Direct method

In the direct method, DRBF, the decomposition of the function, u, can be written as

$$u(x) = \sum_{i=1}^{m} w_i G_i(x). \tag{1.7}$$

Once the weights, w_i, in (1.7) are found, the derivatives (e.g. up to second-order) are calculated by the differentiation processes

$$\frac{du(x)}{dx} = \sum_{i=1}^{m} w_i D_{1i}(x), \tag{1.8}$$

$$\frac{d^2u(x)}{dx^2} = \sum_{i=1}^{m} w_i D_{2i}(x), \tag{1.9}$$

where

$$D_{1i} = \frac{\partial G_i}{\partial x} = \frac{x - c_i}{[(x - c_i)^2 + a_i^2]^{1/2}}, \tag{1.10}$$

$$D_{2i} = \frac{\partial D_{1i}}{\partial x} = \frac{a_i^2}{[(x - c_i)^2 + a_i^2]^{3/2}}. \tag{1.11}$$

1.6.2 Indirect method

In the indirect method, IRBF, the formulation of the problem starts with the decomposition of the highest-order derivative of a function, u, into RBFs (e.g. second-order). The lower-order derivatives and finally the function itself are then obtained by integrating those RBFs as follows.

$$\frac{d^2u(x)}{dx^2} = \sum_{i=1}^{m} w_i G_i(x), \tag{1.12}$$

$$\frac{du(x)}{dx} = \sum_{i=1}^{m} w_i I_{1i}(x) + c_1, \tag{1.13}$$

$$u(x) = \sum_{i=1}^{m} w_i I_{2i}(x) + c_1 x + c_2, \tag{1.14}$$

where c_1 and c_2 are the constants of integration; and, I_1 and I_2 are defined as

$$I_{1i} = \int G_i dx = \frac{(x - c_i)}{2} A + \frac{a_i^2}{2} B, \tag{1.15}$$

$$I_{2i} = \int I_1 dx = \left(\frac{-a_i^2}{3} + \frac{(x - c_i)^2}{6} \right) A + \frac{a_i^2 (x - c_i)}{2} B, \tag{1.16}$$

where $A = \sqrt{(x - c_i)^2 + a_i^2}$ and $B = ln \left((x - c_i) + \sqrt{(x - c_i)^2 + a_i^2} \right)$. It is noted that the analytic forms of RBFs and IRBFs up to fourth-orders can be found in Appendix A.

1.7 Objectives of thesis

From the literature review mentioned above, it can be seen that the conforming mesh methods have limitations when dealing with large deformation or moving boundary problems due to mesh distortions, while, the non-conforming mesh ones have great capabilities to overcome these problems. The non-conforming mesh based IBM is one of the most useful computational methods in studying FSI. The IBM considers the structure as an immersed boundary, which can be represented by a singular force in the Navier-Stokes equations rather than a real body. It

eliminates difficulties associated with moving boundaries faced by conventional methods. The IBM can make use of efficient flow solvers for solving the governing equations on the stationary grid.

From the literature review on high-order approximation methods, the IRBFN method with the use of integration instead of traditional differentiation to construct the RBF approximations significantly improves the accuracy and stability of numerical solution. The IRBF approach is capable of achieving high level of accuracy with relatively coarse meshes.

This research project is mainly concerned with the development of new high-order approximation methods based on the IRBF for the discretisation of PDEs governing the motion of fluids. Then, the new approximation methods are implemented with the fully coupled approach for fluid flow problems and with the IBM procedure for FSI applications. The strength of IRBF methods lies in their ability to deal with scattered data. In the present work, this strength will be exploited in the context of Cartesian grid discretisations. It is noted that creating a Cartesian grid is generally much more efficient than creating a finite-element mesh, particularly for domains of non-rectangular shapes. Unlike the spectral method, the IRBF schemes can be directly applied to problems of irregular shapes, where the Cartesian grid used can be uniform or non-uniform. The main objectives of the research are outlined as follows.

- Developing a fully coupled velocity-pressure approach for fluid flow problems.

- Developing novel coupled and combined compact IRBF stencils for solving PDEs.

- Incorporating the high-order coupled compact IRBF into domain decomposition algorithms for large-scale fluid flow problems.

- Proposing a simple but effective preconditioning technique incorporated into compact IRBF approximation methods, which produces stable calculations for PDEs over a wide range of the shape parameters.

- Incorporating the coupled and combined compact IRBF approximation

schemes into the fluid flow and FSI solvers for highly accurate solutions.

1.8 Outline of thesis

The thesis has seven chapters including this chapter, Introduction. Each of the other six chapters is presented in a self-explanatory manner. The outline of the remaining chapters is as follows.

- Chapter 2 presents a numerical discretisation scheme, based on a direct fully coupled velocity-pressure approach and compact IRBF approximations, to simulate viscous flows in regular and irregular domains. The present scheme is verified through the solutions of several problems including Poisson equations, Taylor-Green vortices and lid driven cavity flows, defined on domains of different shapes.

- Chapter 3 proposes a three-point coupled compact IRBF approximation scheme for the discretisation of second-order differential problems in one and two dimensions. The essence of the coupled compact IRBF is to couple the extra information of the nodal first- and second-order derivative values via their identity equations. Owing to its coupling of the information of the nodal first- and second-order derivatives, the coupled compact IRBF becomes more accurate, stable and efficient than the normal compact IRBF schemes.

- Chapter 4 presents high-order coupled compact IRBF approximation based domain decomposition algorithms for the discretisation of second-order differential problems. Several numerical examples, including those governed by Poisson and Navier-Stokes equations are analysed to demonstrate the accuracy and efficiency of the serial and parallel algorithms implemented with the coupled compact IRBF. Numerical results show that the coupled compact IRBF-Serial and -Parallel algorithms have the capability to reach almost the same solution accuracy level of the coupled compact IRBF-Single domain, which is ideal in terms of computational calculations.

- Chapter 5 proposes a simple but effective preconditioning technique which

is employed in the process of converting the RBF coefficient space (RBF coefficients as unknowns) into the physical space (physical variables as unknowns) when implementing IRBF with large values of the shape parameter which are known to lead to severely ill-condition problems. Furthermore, to improve the solution accuracy, we propose a new combined compact IRBF approximation method for solving second-order partial differential equations.

- Chapter 6 presents a high-order numerical method based on a combined compact IRBF approximation for viscous flow and FSI problems. The fluid solver, in which the combined compact IRBF is employed with fully coupled velocity-pressure approach, is verified through various problems including heat, Burgers, convection-diffusion equations, Taylor-Green vortex and lid driven cavity flows. For FSI applications, we embed the fluid solver in the IBM procedure to simulate FSI problems in which an elastic structure is immersed in a viscous incompressible fluid. The numerical results obtained by the present scheme are highly accurate or in good agreement with those reported in earlier studies of the same problems.

- Chapter 7 concludes the thesis and suggests possible directions for future developments.

Chapter 2

Compact integrated RBF scheme for the fully discretised Navier-Stokes equations

This chapter presents a numerical discretisation scheme, based on a direct fully coupled velocity-pressure approach and compact integrated radial basis function approximations, to simulate viscous flows in regular and irregular domains. The governing equations are taken in the primitive form where the velocity and pressure fields are solved in a direct fully coupled approach. Compact local approximations, based on integrated radial basis functions, over 3-node stencils are introduced into the direct fully coupled approach to represent the field variables. The present scheme is verified through the solutions of several problems including Poisson equations, Taylor-Green vortices and lid driven cavity flows, defined on domains of different shapes. The numerical results obtained by the present scheme are highly accurate and in good agreement with those reported in earlier studies of the same problems.

The fully coupled velocity-pressure approach based on the high-order approximation methods developed in this chapter will be extensively used in Chapters 4 to 6 to simulate fluid flow and FSI problems.

2.1 Introduction

In the primitive variable discrete formulation of the incompressible Navier-Stokes equations, the treatment of the velocity-pressure coupling has a major influence on the convergence rate of the fluid flow simulation. In the incompressible Navier-Stokes equations, the pressure appears only through its gradient in the momentum equations and is only indirectly specified via the continuity equation. The lack of a dedicated equation for the pressure causes difficulty in solving the incompressible Navier-Stokes equations. Numerous approaches of coupling between the velocity and pressure fields have been studied to overcome this problem in the past decades. There are generally two approaches for the issue of the velocity-pressure storage and coupling: segregated approaches and fully coupled approaches.

The segregated approach, in which the continuity and momentum equations are solved sequentially, leads the most often to a so-called pressure correction method. The first attempt of the segregated method was introduced by Patankar and Spalding (1972), in which the pressure field is determined by two processes: first computing an intermediate field based on a guessed pressure field; then, conducting a correction process to ensure the new velocity satisfies the continuity equation. A difficulty of this approach lies in the lack of a pressure time derivative term in the continuity equation. Several methods have been proposed to overcome this drawback and they are classified by the way in which the incompressibility constraint is imposed. Among them, the commonly used methods are the so called pressure based schemes in which the velocity-pressure coupling is solved iteratively. The velocity variables are updated in the momentum equations and the pressure fields are computed in pressure equations. The updating procedure is processed by the well-known SIMPLE (Semi-Implicit Method for Pressure Linked Equations) or SIMPLEC (SIMPLE-Consistent) or SIMPLER (SIMPLE-Revisited) or PISO (Pressure-Implicit with Splitting of Operator) algorithm (Acharya et al., 2007). The algorithms improve the robustness of the pressure solver controlling its convergence rate and bring significant benefits for the overall method. However, the main shortcoming of these methods, where the velocity-pressure coupling is not enforced at each stage of iteration through

the solution of the linearised system, is that the convergence slows down when the number of grid points increases (Deng et al., 1994a; Pascau and Perez, 1996; Elman et al., 2003; Ammara and Masson, 2004; Darwish et al., 2009).

The fully coupled approach, in which the discretised equations of all variables are solved as one system, has been investigated as an alternative to the segregated approach. In these approaches, no explicit equation for pressure or for pressure correction is required and the momentum and continuity equations are discretised in a straight-forward manner. Caretto et al. (1972) proposed the coupled solution for the momentum equations and the continuity equation, the so-called SIVA (SImultaneous Variable Adjustments) algorithm. In this approach, the coupling between dependent variables is structured in small sub-domains. The resulting matrices in such approaches are easy to compute but poor convergence rates are obtained, due to the weak coupling between sub-domains, especially on fine grids. Multigrid methods (Vanka, 1986a; Bruneau and Jouron, 1990) have been developed to overcome this problem; however, they do not appear to bring significant improvement in comparison with standard pressure based methods (Deng et al., 1994a). Some other examples of the fully coupled algorithm include the SCGS (Symmetrical Coupled Gauss-Seidel) of Vanka (1986a), the UVP method of Karki and Mongia (1990), among others. The absence of a pressure equation in these fully coupled algorithms may lead to an ill-conditioned system of equations because zeros are present in the main diagonal of the discretised continuity equation (Henniger et al., 2010). Attempts have been made to deal with this issue, with various degrees of success, through the use of preconditioning (May and Moresi, 2008; Henniger et al., 2010), penalty methods (Braaten and Patankar, 1990; Pascau and Perez, 1996), or by algebraic manipulations (Zedan and Schneider, 1985; Galpin et al., 1985). These treatments may improve the stiffness of equations. Mazhar (2001) presents a fully coupled approach differing from the aforementioned approaches in the sense that a direct attempt is made to solve the primitive difference equations.

In (Hanby et al., 1996), a fully coupled procedure is presented and compared with the SIMPLEC solver. The comparison shows that a fully coupled solution gives quicker convergence with less nonlinear (or outer) iteration. Braaten and Shyy

(1986) investigated the effects of mesh skewness, Reynolds number and grid size on the iterative and direct solution methods. The results show the fully coupled fully implicit treatment of equations in the direct sparse matrix method leads to rates of convergence that are much more rapid than the iterative method. The work also indicates the importance of retaining the coupling between velocity and pressure fields in obtaining the superior convergence rate of the direct scheme. Whilst a fully coupled method requires more computer memory than a segregated approach, this is not a serious limitation on most current computers and it may offer advantages in terms of robustness, CPU time, and level of convergence.

Radial basis function networks (RBFNs) have emerged as a powerful numerical method for the approximation of scattered data (Fasshauer, 2007). Kansa (1990a,b) first proposed the concept of using direct/differential RBF (DRBF) approximation for solving partial differential equations (PDEs). In the DRBF method, the closed form RBF approximating function is first obtained from a set of training points and the derivative functions are then calculated directly from such closed form RBF (Mai-Duy and Tran-Cong, 2001a). Then, Mai-Duy and Tran-Cong (2001a,b, 2003) proposed the idea of using indirect/integrated RBF (IRBF) for the solution of PDEs. In the IRBF approach, the highest derivatives under interest are decomposed into RBFs; and, the expressions for the lower derivatives and its functions are then obtained through integration processes. Numerical studies in (Mai-Duy and Tran-Cong, 2001a,b, 2003, 2005; Sarra, 2006; Shu and Wu, 2007) have shown that the integral approach is more accurate than the differential approach because the integration process is averagely less sensitive to noise. To employ a larger number of collocation points, a one-dimensional IRBF scheme has been developed in literatures (Mai-Duy and Tanner, 2007; Mai-Duy and Tran-Cong, 2007). Recently, Mai-Duy and Tran-Cong (2013) have proposed a 3-point compact IRBF stencil where only nodal values of the second-order derivative (i.e. extra information) are incorporated into the approximations. Thai-Quang et al. (2012b) have proposed another 3-point compact IRBF stencil where the extra information includes nodal values of both the first- and second-order derivatives. The latter scheme with tri-diagonal matrices was reported to be more accurate and efficient (Thai-Quang et al., 2012b).

This chapter implements a direct fully coupled approach for the fluid flow simulation with the field variables being approximated on uniform/non-uniform Cartesian grids by the compact IRBF approximation scheme presented in (Thai-Quang et al., 2012b). The tight velocity-pressure coupling is developed on a collocated grid and one global system of equations involving the velocity and pressure is solved simultaneously in its primitive form. In this way, momentum and continuity conservation equations are satisfied implicitly and simultaneously over the whole grid points. The use of fully coupled fully implicit solver for Navier-Stokes equations exhibits rapid convergence and provides the stability for large time steps to be employed (Elman et al., 2003). A block preconditioning technique (Henniger et al., 2010) is used to refine the direct solution only when the coefficient matrix is ill-conditioned (e.g. the problem of irregular bottom lid driven cavity).

The remainder of this chapter is organised as follows: Section 2.2 outlines the governing equations and a fully coupled approach. Following this, a block preconditioning technique is briefly described in Section 2.3. Section 2.4 describes the spatial disretisation using compact IRBF stencils. In Section 2.5, numerical examples are presented and the compact IRBF results are compared with some benchmark solutions, where appropriate. Finally, concluding remarks are given in Section 2.6.

2.2 Mathematical model

The transient Navier-Stokes equations for an incompressible viscous fluid in the primitive variables are expressed in the dimensionless non-conservative forms as follows.

Conservation of x-momentum

$$\frac{\partial u}{\partial t} + \underbrace{\left\{ u\frac{\partial u}{\partial x} + v\frac{\partial u}{\partial y} \right\}}_{N(u)} = -\frac{\partial p}{\partial x} + \frac{1}{Re}\underbrace{\left\{ \frac{\partial^2 u}{\partial x^2} + \frac{\partial^2 u}{\partial y^2} \right\}}_{L(u)}, \tag{2.1}$$

conservation of y-momentum

$$\frac{\partial v}{\partial t} + \underbrace{\left\{ u\frac{\partial v}{\partial x} + v\frac{\partial v}{\partial y} \right\}}_{N(v)} = -\frac{\partial p}{\partial y} + \frac{1}{Re}\underbrace{\left\{ \frac{\partial^2 v}{\partial x^2} + \frac{\partial^2 v}{\partial y^2} \right\}}_{L(v)}, \tag{2.2}$$

conservation of mass (continuity)

$$\frac{\partial u}{\partial x} + \frac{\partial v}{\partial y} = 0, \tag{2.3}$$

where u, v and p are the velocity components in the x-, y-directions and static pressure, respectively; $Re = Ul/\nu$ is the Reynolds number, in which ν, l and U are the kinematic viscosity, characteristic length and characteristic speed of the flow, respectively. For simplicity, we employ notations $N(u)$ and $N(v)$ to represent the convective terms in x- and y-directions, respectively; and, $L(u)$ and $L(v)$ to denote the diffusive terms in x- and y-directions, respectively.

The temporal discretisations of (2.1)-(2.3), using the Adams-Bashforth scheme for the convective terms and Crank-Nicolson scheme for the diffusive terms, result in

$$\frac{u^n - u^{n-1}}{\Delta t} + \left\{ \frac{3}{2}N(u^{n-1}) - \frac{1}{2}N(u^{n-2}) \right\} = -G_x(p^{n-\frac{1}{2}}) + \frac{1}{2Re}\left\{ L(u^n) + L(u^{n-1}) \right\}, \tag{2.4}$$

$$\frac{v^n - v^{n-1}}{\Delta t} + \left\{ \frac{3}{2}N(v^{n-1}) - \frac{1}{2}N(v^{n-2}) \right\} = -G_y(p^{n-\frac{1}{2}}) + \frac{1}{2Re}\left\{ L(v^n) + L(v^{n-1}) \right\}, \tag{2.5}$$

$$D_x(u^n) + D_y(v^n) = 0, \tag{2.6}$$

where n denotes the current time level; G_x and G_y are gradients in x- and y-directions, respectively; and, D_x and D_y are gradients in x- and y-directions, respectively.

Taking the unknown quantities in (2.4)-(2.6) to the left hand side and the known quantities to the right hand side, and then collocating them at the interior nodal

points result in the matrix-vector form

$$
\begin{bmatrix}
\mathbf{K} & \mathbf{0} & \mathbf{G}_x \\
\mathbf{0} & \mathbf{K} & \mathbf{G}_y \\
\mathbf{D}_x & \mathbf{D}_y & \mathbf{0}
\end{bmatrix}
\begin{bmatrix}
\mathbf{u}^n \\
\mathbf{v}^n \\
\mathbf{p}^{n-\frac{1}{2}}
\end{bmatrix}
=
\begin{bmatrix}
\mathbf{r}_x^n \\
\mathbf{r}_y^n \\
\mathbf{0}
\end{bmatrix},
\tag{2.7}
$$

where

$$
\mathbf{K} = \frac{1}{\Delta t} \left\{ \mathbf{I} - \frac{\Delta t}{2Re} \mathbf{L} \right\},
\tag{2.8}
$$

$$
\mathbf{r}_x^n = \frac{1}{\Delta t} \left\{ \mathbf{I} + \frac{\Delta t}{2Re} \mathbf{L} \right\} \mathbf{u}^{n-1} - \left\{ \frac{3}{2} \mathbf{N}(\mathbf{u}^{n-1}) - \frac{1}{2} \mathbf{N}(\mathbf{u}^{n-2}) \right\},
\tag{2.9}
$$

$$
\mathbf{r}_y^n = \frac{1}{\Delta t} \left\{ \mathbf{I} + \frac{\Delta t}{2Re} \mathbf{L} \right\} \mathbf{v}^{n-1} - \left\{ \frac{3}{2} \mathbf{N}(\mathbf{v}^{n-1}) - \frac{1}{2} \mathbf{N}(\mathbf{v}^{n-2}) \right\},
\tag{2.10}
$$

$\mathbf{u}^n$ and $\mathbf{v}^n$ are vectors containing the nodal values of u^n and v^n at the boundary and interior nodes, respectively, while $\mathbf{p}^{n-\frac{1}{2}}$ is a vector containing the values of $p^{n-\frac{1}{2}}$ at the interior nodes only; $\mathbf{I}$ is the identity matrix; and, $\mathbf{N}$ and $\mathbf{L}$ are the matrix operators for the approximation of the convective and diffusive terms, respectively.

Since the velocities are given at the boundary, the goal of the fully coupled approach is to solve (2.7) for the values of the field variables simultaneously at the interior points. In (2.7), the approximation for the pressure involves the interior nodal points only. This is in accord with the fact that physics does not provide a prior boundary condition for pressure as it does for velocities (Moin and Kim, 1980). It is noted that the pressure is only determined up to an arbitrary constant because there exists no direct equation for pressure and the momentum equations only contain gradient terms for pressure (Moin and Kim, 1980; Vanka, 1986b; Bruneau and Jouron, 1990; Perot, 1993; May and Moresi, 2008).

2.3 Preconditioning technique

For simplicity, we define

$$
\widehat{\mathbf{K}} = \begin{bmatrix} \mathbf{K} & \mathbf{0} \\ \mathbf{0} & \mathbf{K} \end{bmatrix}, \quad \mathbf{G} = \begin{bmatrix} \mathbf{G}_x \\ \mathbf{G}_y \end{bmatrix}, \quad \mathbf{D} = \begin{bmatrix} \mathbf{D}_x & \mathbf{D}_y \end{bmatrix}, \quad \mathbf{U}^n = \begin{bmatrix} \mathbf{u}^n \\ \mathbf{v}^n \end{bmatrix}, \quad \mathbf{R}^n = \begin{bmatrix} \mathbf{r}_x^n \\ \mathbf{r}_y^n \end{bmatrix}.
$$
$$(2.11)$$

Substituting (2.11) into (2.7)

$$
\begin{bmatrix} \widehat{\mathbf{K}} & \mathbf{G} \\ \mathbf{D} & \mathbf{0} \end{bmatrix} \begin{bmatrix} \mathbf{U}^n \\ \mathbf{p}^{n-\frac{1}{2}} \end{bmatrix} = \begin{bmatrix} \mathbf{R}^n \\ \mathbf{0} \end{bmatrix}.
$$
$$(2.12)$$

Block-oriented preconditioning methods for the Navier-Stokes equations decompose the block 2×2 matrix in (2.12) using a block-LU decomposition

$$
\begin{bmatrix} \widehat{\mathbf{K}} & \mathbf{G} \\ \mathbf{D} & \mathbf{0} \end{bmatrix} = \begin{bmatrix} \mathbf{I} & \mathbf{0} \\ \mathbf{D}\widehat{\mathbf{K}}^{-1} & -\mathbf{I} \end{bmatrix} \begin{bmatrix} \widehat{\mathbf{K}} & \mathbf{G} \\ \mathbf{0} & \mathbf{D}\widehat{\mathbf{K}}^{-1}\mathbf{G} \end{bmatrix}.
$$
$$(2.13)$$

By defining Schur complement as $\mathbf{S} = \mathbf{D}\widehat{\mathbf{K}}^{-1}\mathbf{G}$ (Silvester et al., 2001), the block upper triangular preconditioner is expressed as

$$
\begin{bmatrix} \widehat{\mathbf{K}} & \mathbf{G} \\ \mathbf{0} & \mathbf{S} \end{bmatrix}.
$$
$$(2.14)$$

Substituting (2.13) into (2.12), we can obtain the Schur complement for the pressure (May and Moresi, 2008; Henniger et al., 2010; Furuichi et al., 2011). It yields the following block upper triangular system

$$
\begin{bmatrix} \widehat{\mathbf{K}} & \mathbf{G} \\ \mathbf{0} & \mathbf{S} \end{bmatrix} \begin{bmatrix} \mathbf{U}^n \\ \mathbf{p}^{n-\frac{1}{2}} \end{bmatrix} = \begin{bmatrix} \mathbf{R}^n \\ \mathbf{F}^n \end{bmatrix},
$$
$$(2.15)$$

where $\mathbf{F}^n = \mathbf{D}\widehat{\mathbf{K}}^{-1}\mathbf{R}^n$.

The velocity and pressure solutions are obtained via block back substitution in

(2.15), i.e. solving the following systems

$$\text{solve for } \mathbf{p}: \quad \mathbf{S}\mathbf{p}^{n-\frac{1}{2}} = \mathbf{F}^n. \tag{2.16}$$

$$\text{solve for } \mathbf{U}: \quad \widehat{\mathbf{K}}\mathbf{U}^n = \mathbf{R}^n - \mathbf{G}\mathbf{p}^{n-\frac{1}{2}}. \tag{2.17}$$

In this work, it is noted that the preconditioning technique is required whenever the coefficient matrix is ill-conditioned. In particular, it is only used to stiffen the coefficient matrix for the problem of an irregular bottom lid driven cavity in Section 2.5.6.

2.4 Spatial discretisation

For the approximation of the first- and second-order derivatives in (2.7), a compact IRBF scheme of Thai-Quang et al. (2012b) is employed in this chapter. It is represented as follows.

Consider a two-dimensional domain Ω, which is represented by a uniform Cartesian grid. The nodes are indexed in the x-direction by the subscript i ($i \in \{1, 2, ..., n_x\}$) and in y-direction by j ($j \in \{1, 2, ..., n_y\}$). For rectangular domains, let N be the total number of nodes (i.e. $N = n_x \times n_y$) and N_{ip} be the number of interior nodes (i.e. $N_{ip} = (n_x - 2) \times (n_y - 2)$). For non-rectangular domains, selection of interior nodes is detailed in Section 2.5.2. At an interior grid point $\mathbf{x}_{i,j} = (x_{(i,j)}, y_{(i,j)})^T$ where $i \in \{2, 3, ..., n_x - 1\}$ and $j \in \{2, 3, ..., n_y - 1\}$, the associated stencils to be considered here are two local stencils: $\{x_{(i-1,j)}, x_{(i,j)}, x_{(i+1,j)}\}$ in the x-direction and $\{y_{(i,j-1)}, y_{(i,j)}, y_{(i,j+1)}\}$ in the y-direction. Hereafter, for brevity, η denotes either x or y in a generic local stencil $\{\eta_1, \eta_2, \eta_3\}$, where $\eta_1 < \eta_2 < \eta_3$ and $\eta_2 \equiv \eta_{(i,j)}$, are illustrated in Figure 2.1. The integral ap-
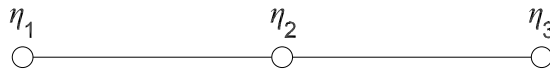
Figure 2.1 Compact 3-point 1D-IRBF stencil for interior nodes.

proach starts with the decomposition of the second-order derivative of a variable,

u, into RBFs

$$\frac{d^2 u(\eta)}{d\eta^2} = \sum_{i=1}^{m} w_i G_i(\eta),\tag{2.18}$$

where m is taken to be 3 for local stencils; $\{G_i(\eta)\}_{i=1}^{m}$ is the set of RBFs; and, $\{w_i\}_{i=1}^{m}$ is the set of weights/coefficients to be found. Approximate representations for the first-order derivative and the function itself are then obtained through the integration processes

$$\frac{du(\eta)}{d\eta} = \sum_{i=1}^{m} w_i I_{1i}(\eta) + c_1,\tag{2.19}$$

$$u(\eta) = \sum_{i=1}^{m} w_i I_{2i}(\eta) + c_1 \eta + c_2,\tag{2.20}$$

where $I_{1i}(\eta) = \int G_i(\eta) d\eta$; $I_{2i}(\eta) = \int I_{1i}(\eta) d\eta$; and, c_1 and c_2 are the constants of integration.

2.4.1 First-order derivative compact approximations

Extra information used in the compact approximation of the first-order derivative is chosen as $\frac{du_1}{d\eta}$ and $\frac{du_3}{d\eta}$. We construct the conversion system over a 3-point stencil associated with an interior node in the form

$$\begin{bmatrix} u_1 \\ u_2 \\ u_3 \\ \frac{du_1}{d\eta} \\ \frac{du_3}{d\eta} \end{bmatrix} = \underbrace{\begin{bmatrix} \mathbf{I}_2 \\ \mathbf{I}_1 \end{bmatrix}}_{\mathbf{C}_1} \begin{bmatrix} w_1 \\ w_2 \\ w_3 \\ c_1 \\ c_2 \end{bmatrix},\tag{2.21}$$

where $\frac{du_i}{d\eta} = \frac{du}{d\eta}(\eta_i)$ with $i \in \{1, 2, 3\}$; $\mathbf{C}_1$ is the conversion matrix; and, $\mathbf{I}_2$ and $\mathbf{I}_1$ are defined as

$$\mathbf{I}_2 = \begin{bmatrix} I_{21}(\eta_1) & I_{22}(\eta_1) & I_{23}(\eta_1) & \eta_1 & 1 \\ I_{21}(\eta_2) & I_{22}(\eta_2) & I_{23}(\eta_2) & \eta_2 & 1 \\ I_{21}(\eta_3) & I_{22}(\eta_3) & I_{23}(\eta_3) & \eta_3 & 1 \end{bmatrix}.\tag{2.22}$$

$$\mathbf{I}_1 = \begin{bmatrix} I_{11}(\eta_1) & I_{12}(\eta_1) & I_{13}(\eta_1) & 1 & 0 \\ I_{11}(\eta_3) & I_{12}(\eta_3) & I_{13}(\eta_3) & 1 & 0 \end{bmatrix}. \tag{2.23}$$

Solving (2.21) yields

$$\begin{bmatrix} w_1 \\ w_2 \\ w_3 \\ c_1 \\ c_2 \end{bmatrix} = \mathbf{C}_1^{-1} \begin{bmatrix} u_1 \\ u_2 \\ u_3 \\ \frac{du_1}{d\eta} \\ \frac{du_3}{d\eta} \end{bmatrix}, \tag{2.24}$$

which maps the vector of nodal values of the function and its first-order derivative to the vector of RBF coefficients including the two integration constants. Approximate expressions for the first-order derivative in the physical space are obtained by substituting (2.24) into (2.19)

$$\frac{du(\eta)}{d\eta} = \begin{bmatrix} I_{11}(\eta) & I_{12}(\eta) & I_{13}(\eta) & 1 & 0 \end{bmatrix} \mathbf{C}_1^{-1} \begin{bmatrix} \mathbf{u} \\ \frac{du_1}{d\eta} \\ \frac{du_3}{d\eta} \end{bmatrix}, \tag{2.25}$$

where $\eta_1 \le \eta \le \eta_3$ and $\mathbf{u} = [u_1, u_2, u_3]^T$. (2.25) can be rewritten as

$$\frac{du(\eta)}{d\eta} = \sum_{i=1}^{3} \frac{d\phi_i(\eta)}{d\eta} u_i + \frac{d\phi_4(\eta)}{d\eta}\frac{du_1}{d\eta} + \frac{d\phi_5(\eta)}{d\eta}\frac{du_3}{d\eta}, \tag{2.26}$$

where $\{\phi_i(\eta)\}_{i=1}^5$ is the set of IRBFs in the physical space. At the current time level n, (2.26) is taken as

$$\frac{du^n(\eta)}{d\eta} = \sum_{i=1}^{3} \frac{d\phi_i(\eta)}{d\eta} u_i^n + \frac{d\phi_4(\eta)}{d\eta}\frac{du_1^n}{d\eta} + \frac{d\phi_5(\eta)}{d\eta}\frac{du_3^n}{d\eta}, \tag{2.27}$$

where nodal values of the first-order derivative on the right hand side are treated as unknowns. Collocating (2.27) at $\eta = \eta_2$ results in

$$-\frac{d\phi_4(\eta_2)}{d\eta}\frac{du_1^n}{d\eta} + \frac{du_2^n}{d\eta} - \frac{d\phi_5(\eta_2)}{d\eta}\frac{du_3^n}{d\eta} = \frac{d\phi_1(\eta_2)}{d\eta}u_1^n + \frac{d\phi_2(\eta_2)}{d\eta}u_2^n + \frac{d\phi_3(\eta_2)}{d\eta}u_3^n, \tag{2.28}$$

or in the matrix-vector form

$$
\begin{bmatrix} -\frac{d\phi_4(\eta_2)}{d\eta} & 1 & -\frac{d\phi_5(\eta_2)}{d\eta} \end{bmatrix}
\begin{bmatrix} \frac{du_1^n}{d\eta} \\ \frac{du_2^n}{d\eta} \\ \frac{du_3^n}{d\eta} \end{bmatrix}
=
\begin{bmatrix} \frac{d\phi_1(\eta_2)}{d\eta} & \frac{d\phi_2(\eta_2)}{d\eta} & \frac{d\phi_3(\eta_2)}{d\eta} \end{bmatrix}
\begin{bmatrix} u_1^n \\ u_2^n \\ u_3^n \end{bmatrix}. \quad (2.29)
$$

At the boundary nodes, the first-order derivatives are approximated in special compact stencils. Consider the boundary node, e.g. η_1. Its associated stencil is $\{\eta_1, \eta_2, \eta_3, \eta_4\}$ as shown in Figure 2.2. The conversion system over this special

Figure 2.2 Special compact 4-point 1D-IRBF stencil for boundary nodes.

stencil is presented as the following matrix-vector multiplication

$$
\begin{bmatrix} u_1 \\ u_2 \\ u_3 \\ u_4 \\ \frac{du_2}{d\eta} \end{bmatrix}
=
\underbrace{\begin{bmatrix} \mathbf{I}_{2sp} \\ \mathbf{I}_{1sp} \end{bmatrix}}_{\mathbf{C}_{sp1}}
\begin{bmatrix} w_1 \\ w_2 \\ w_3 \\ w_4 \\ c_1 \\ c_2 \end{bmatrix}, \quad (2.30)
$$

where $\mathbf{C}_{sp1}$ is the conversion matrix; and, $\mathbf{I}_{2sp}$ and $\mathbf{I}_{1sp}$ are defined as

$$
\mathbf{I}_{2sp} =
\begin{bmatrix}
I_{21}(\eta_1) & I_{22}(\eta_1) & I_{23}(\eta_1) & I_{24}(\eta_1) & \eta_1 & 1 \\
I_{21}(\eta_2) & I_{22}(\eta_2) & I_{23}(\eta_2) & I_{24}(\eta_2) & \eta_2 & 1 \\
I_{21}(\eta_3) & I_{22}(\eta_3) & I_{23}(\eta_3) & I_{24}(\eta_3) & \eta_3 & 1 \\
I_{21}(\eta_4) & I_{22}(\eta_4) & I_{23}(\eta_4) & I_{24}(\eta_4) & \eta_4 & 1
\end{bmatrix}. \quad (2.31)
$$

$$
\mathbf{I}_{1sp} =
\begin{bmatrix} I_{11}(\eta_2) & I_{12}(\eta_2) & I_{13}(\eta_2) & I_{14}(\eta_2) & 1 & 0 \end{bmatrix}. \quad (2.32)
$$

Solving (2.30) yields

$$
\begin{bmatrix} w_1 \\ w_2 \\ w_3 \\ w_4 \\ c_1 \\ c_2 \end{bmatrix} = \mathbf{C}_{sp1}^{-1} \begin{bmatrix} u_1 \\ u_2 \\ u_3 \\ u_4 \\ \frac{du_2}{d\eta} \end{bmatrix}. \tag{2.33}
$$

The boundary value of the first-order derivative of u is thus obtained by substituting (2.33) into (2.19) and taking $\eta = \eta_1$

$$
\frac{du(\eta_1)}{d\eta} = \begin{bmatrix} I_{11}(\eta_1) & I_{12}(\eta_1) & I_{13}(\eta_1) & I_{14}(\eta_1) & 1 & 0 \end{bmatrix} \mathbf{C}_{sp1}^{-1} \begin{bmatrix} \mathbf{u} \\ \frac{du_2}{d\eta} \end{bmatrix}, \tag{2.34}
$$

where $\mathbf{u} = [u_1, u_2, u_3, u_4]^T$. (2.34) can be rewritten as

$$
\frac{du(\eta_1)}{d\eta} = \sum_{i=1}^{4} \frac{d\phi_{spi}(\eta_1)}{d\eta} u_i + \frac{d\phi_{sp5}(\eta_1)}{d\eta} \frac{du_2}{d\eta}. \tag{2.35}
$$

At the current time level n, (2.35) is taken as

$$
\frac{du^n(\eta_1)}{d\eta} = \sum_{i=1}^{4} \frac{d\phi_{spi}(\eta_1)}{d\eta} u_i^n + \frac{d\phi_{sp5}(\eta_1)}{d\eta} \frac{du_2^n}{d\eta}, \tag{2.36}
$$

or

$$
\frac{du_1^n}{d\eta} - \frac{d\phi_{sp5}(\eta_1)}{d\eta} \frac{du_2^n}{d\eta} = \frac{d\phi_{sp1}(\eta_1)}{d\eta} u_1^n + \frac{d\phi_{sp2}(\eta_1)}{d\eta} u_2^n + \frac{d\phi_{sp3}(\eta_1)}{d\eta} u_3^n + \frac{d\phi_{sp4}(\eta_1)}{d\eta} u_4^n, \tag{2.37}
$$

or in the matrix-vector form

$$
\begin{bmatrix} 1 & -\frac{d\phi_{sp5}(\eta_1)}{d\eta} & 0 & 0 \end{bmatrix} \begin{bmatrix} \frac{du_1^n}{d\eta} \\ \frac{du_2^n}{d\eta} \\ \frac{du_3^n}{d\eta} \\ \frac{du_4^n}{d\eta} \end{bmatrix} = \begin{bmatrix} \frac{d\phi_{sp1}(\eta_1)}{d\eta} & \frac{d\phi_{sp2}(\eta_1)}{d\eta} & \frac{d\phi_{sp3}(\eta_1)}{d\eta} & \frac{d\phi_{sp4}(\eta_1)}{d\eta} \end{bmatrix} \begin{bmatrix} u_1^n \\ u_2^n \\ u_3^n \\ u_4^n \end{bmatrix}. \tag{2.38}
$$

In a similar manner, one is able to calculate the first-order derivative of u at the boundary node η_{n_η}. The IRBF system on a grid line for the first-order derivative

of u is obtained by letting the interior node taking values from 2 to $(n_\eta - 1)$ in (2.29) and making use of (2.38) for the boundary nodes 1 and n_η, resulting in

$$\mathbf{Q}_\eta \mathbf{u}_\eta^n = \mathbf{R}_\eta \mathbf{u}^n,$$ (2.39)

where $\mathbf{Q}_\eta$ and $\mathbf{R}_\eta$ are $n_\eta \times n_\eta$ matrices.

2.4.2 Second-order derivative compact approximations

Extra information used in the compact approximation of the second-order derivative is chosen as $\frac{d^2 u_1}{d\eta^2}$ and $\frac{d^2 u_3}{d\eta^2}$. We construct the conversion system over a 3-point stencil associated with an interior node in the form

$$
\begin{bmatrix}
u_1 \\
u_2 \\
u_3 \\
\frac{d^2 u_1}{d\eta^2} \\
\frac{d^2 u_3}{d\eta^2}
\end{bmatrix}
=
\underbrace{
\begin{bmatrix}
\mathbf{I}_2 \\
\mathbf{G}
\end{bmatrix}
}_{\mathbf{C}_2}
\begin{bmatrix}
w_1 \\
w_2 \\
w_3 \\
c_1 \\
c_2
\end{bmatrix},
$$ (2.40)

where $\frac{d^2 u_i}{d\eta^2} = \frac{d^2 u}{d\eta^2}(\eta_i)$ with $i \in \{1, 2, 3\}$; $\mathbf{C}_2$ is the conversion matrix; $\mathbf{I}_2$ is defined as before (i.e. (2.22)); and, $\mathbf{G}$ is defined as

$$
\mathbf{G} =
\begin{bmatrix}
G_1(\eta_1) & G_2(\eta_1) & G_3(\eta_1) & 0 & 0 \\
G_1(\eta_3) & G_2(\eta_3) & G_3(\eta_3) & 0 & 0
\end{bmatrix}.
$$ (2.41)

Solving (2.40) yields

$$
\begin{bmatrix}
w_1 \\
w_2 \\
w_3 \\
c_1 \\
c_2
\end{bmatrix}
= \mathbf{C}_2^{-1}
\begin{bmatrix}
u_1 \\
u_2 \\
u_3 \\
\frac{d^2 u_1}{d\eta^2} \\
\frac{d^2 u_3}{d\eta^2}
\end{bmatrix},
$$ (2.42)

which maps the vector of nodal values of the function and its second-order derivative to the vector of RBF coefficients including the two integration constants. Approximate expressions for the second-order derivative in the physical space are

obtained by substituting (2.42) into (2.18)

$$\frac{d^2u(\eta)}{d\eta^2} = \begin{bmatrix} G_1(\eta) & G_2(\eta) & G_3(\eta) & 0 & 0 \end{bmatrix} \mathbf{C}_2^{-1} \begin{bmatrix} \mathbf{u} \\ \frac{d^2u_1}{d\eta^2} \\ \frac{d^2u_3}{d\eta^2} \end{bmatrix}, \qquad (2.43)$$

where $\eta_1 \le \eta \le \eta_3$ and $\mathbf{u} = [u_1, u_2, u_3]^T$. (2.43) can be rewritten as

$$\frac{d^2u(\eta)}{d\eta^2} = \sum_{i=1}^{3} \frac{d^2\phi_i(\eta)}{d\eta^2} u_i + \frac{d^2\phi_4(\eta)}{d\eta^2}\frac{d^2u_1}{d\eta^2} + \frac{d^2\phi_5(\eta)}{d\eta^2}\frac{d^2u_3}{d\eta^2}. \qquad (2.44)$$

At the current time level n

$$\frac{d^2u^n(\eta)}{d\eta^2} = \sum_{i=1}^{3} \frac{d^2\phi_i(\eta)}{d\eta^2} u_i^n + \frac{d^2\phi_4(\eta)}{d\eta^2}\frac{d^2u_1^n}{d\eta^2} + \frac{d^2\phi_5(\eta)}{d\eta^2}\frac{d^2u_3^n}{d\eta^2}, \qquad (2.45)$$

where nodal values of the second-order derivative on the right hand side are treated as unknowns. Collocating (2.45) at $\eta = \eta_2$ leads to

$$-\frac{d^2\phi_4(\eta_2)}{d\eta^2}\frac{d^2u_1^n}{d\eta^2} + \frac{d^2u_2^n}{d\eta^2} - \frac{d^2\phi_5(\eta_2)}{d\eta^2}\frac{d^2u_3^n}{d\eta^2} = \frac{d^2\phi_1(\eta_2)}{d\eta^2}u_1^n + \frac{d^2\phi_2(\eta_2)}{d\eta^2}u_2^n + \frac{d^2\phi_3(\eta_2)}{d\eta^2}u_3^n, \qquad (2.46)$$

or in the matrix-vector form

$$\begin{bmatrix} -\frac{d^2\phi_4(\eta_2)}{d\eta^2} & 1 & -\frac{d^2\phi_5(\eta_2)}{d\eta^2} \end{bmatrix} \begin{bmatrix} \frac{d^2u_1^n}{d\eta^2} \\ \frac{d^2u_2^n}{d\eta^2} \\ \frac{d^2u_3^n}{d\eta^2} \end{bmatrix} = \begin{bmatrix} \frac{d^2\phi_1(\eta_2)}{d\eta^2} & \frac{d^2\phi_2(\eta_2)}{d\eta^2} & \frac{d^2\phi_3(\eta_2)}{d\eta^2} \end{bmatrix} \begin{bmatrix} u_1^n \\ u_2^n \\ u_3^n \end{bmatrix}. \qquad (2.47)$$

At the boundary nodes, the second-order derivatives are approximated in special compact stencils. Consider the boundary node, e.g. η_1. Its associated stencil is $\{\eta_1, \eta_2, \eta_3, \eta_4\}$ as shown in Figure 2.2. The conversion system over this special

stencil is presented as the following matrix-vector multiplication

$$
\begin{bmatrix} u_1 \\ u_2 \\ u_3 \\ u_4 \\ \frac{d^2 u_2}{d\eta} \end{bmatrix} = \underbrace{\begin{bmatrix} \mathbf{I}_{2sp} \\ \mathbf{G}_{sp} \end{bmatrix}}_{\mathbf{C}_{sp2}} \begin{bmatrix} w_1 \\ w_2 \\ w_3 \\ w_4 \\ c_1 \\ c_2 \end{bmatrix},
\tag{2.48}
$$

where $\mathbf{C}_{sp2}$ is the conversion matrix; $\mathbf{I}_{2sp}$ is defined as before (i.e. (2.31)); and, $\mathbf{G}_{sp}$ is defined as

$$
\mathbf{G}_{sp} = \begin{bmatrix} G_1(\eta_2) & G_2(\eta_2) & G_3(\eta_2) & G_4(\eta_2) & 0 & 0 \end{bmatrix}.
\tag{2.49}
$$

Solving (2.48) yields

$$
\begin{bmatrix} w_1 \\ w_2 \\ w_3 \\ w_4 \\ c_1 \\ c_2 \end{bmatrix} = \mathbf{C}_{sp2}^{-1} \begin{bmatrix} u_1 \\ u_2 \\ u_3 \\ u_4 \\ \frac{d^2 u_2}{d\eta^2} \end{bmatrix}.
\tag{2.50}
$$

The boundary value of the second-order derivative of u is thus obtained by substituting (2.50) into (2.18) and taking $\eta = \eta_1$

$$
\frac{d^2 u(\eta_1)}{d\eta^2} = \begin{bmatrix} G_1(\eta_1) & G_2(\eta_1) & G_3(\eta_1) & G_4(\eta_1) & 0 & 0 \end{bmatrix} \mathbf{C}_{sp2}^{-1} \begin{bmatrix} \mathbf{u} \\ \frac{d^2 u_2}{d\eta^2} \end{bmatrix},
\tag{2.51}
$$

where $\mathbf{u} = [u_1, u_2, u_3, u_4]^T$. (2.51) can be rewritten as

$$
\frac{d^2 u(\eta_1)}{d\eta^2} = \sum_{i=1}^{4} \frac{d^2 \phi_{spi}(\eta_1)}{d\eta^2} u_i + \frac{d^2 \phi_{sp5}(\eta_1)}{d\eta^2} \frac{d^2 u_2}{d\eta^2}.
\tag{2.52}
$$

At the current time level n, (2.52) is taken as

$$
\frac{d^2 u^n(\eta_1)}{d\eta^2} = \sum_{i=1}^{4} \frac{d^2 \phi_{spi}(\eta_1)}{d\eta^2} u_i^n + \frac{d^2 \phi_{sp5}(\eta_1)}{d\eta^2} \frac{d^2 u_2^n}{d\eta^2},
\tag{2.53}
$$

or

$$\frac{d^2 u_1^n}{d\eta^2} - \frac{d^2 \phi_{sp5}(\eta_1)}{d\eta^2}\frac{d^2 u_2^n}{d\eta^2} = \frac{d^2 \phi_{sp1}(\eta_1)}{d\eta^2}u_1^n + \frac{d^2 \phi_{sp2}(\eta_1)}{d\eta^2}u_2^n + \frac{d^2 \phi_{sp3}(\eta_1)}{d\eta^2}u_3^n + \frac{d^2 \phi_{sp4}(\eta_1)}{d\eta^2}u_4^n,$$
(2.54)

or in the matrix-vector form

$$\begin{bmatrix} 1 & -\frac{d^2 \phi_{sp5}(\eta_1)}{d\eta^2} & 0 & 0 \end{bmatrix} \begin{bmatrix} \frac{d^2 u_1^n}{d\eta^2} \\ \frac{d^2 u_2^n}{d\eta^2} \\ \frac{d^2 u_3^n}{d\eta^2} \\ \frac{d^2 u_4^n}{d\eta^2} \end{bmatrix} = \begin{bmatrix} \frac{d^2 \phi_{sp1}(\eta_1)}{d\eta^2} & \frac{d^2 \phi_{sp2}(\eta_1)}{d\eta^2} & \frac{d^2 \phi_{sp3}(\eta_1)}{d\eta^2} & \frac{d^2 \phi_{sp4}(\eta_1)}{d\eta^2} \end{bmatrix} \begin{bmatrix} u_1^n \\ u_2^n \\ u_3^n \\ u_4^n \end{bmatrix}.$$
(2.55)

In a similar manner, one is able to calculate the second-order derivative of u at the boundary node η_{n_η}. The IRBF system on a grid line for the second-order derivative of u is obtained by letting the interior node taking values from 2 to $(n_\eta - 1)$ in (2.47) and making use of (2.55) for the boundary nodes 1 and n_η, resulting in

$$\mathbf{Q}_{\eta\eta}\mathbf{u}_{\eta\eta}^n = \mathbf{R}_{\eta\eta}\mathbf{u}^n,$$
(2.56)

where $\mathbf{Q}_{\eta\eta}$ and $\mathbf{R}_{\eta\eta}$ are $n_\eta \times n_\eta$ matrices.

It is noted that, for brevity, we use the same notations to represent the set of IRBFs and the RBF coefficients for the approximation of first- and second-order derivatives. In fact, for example, the basis functions $\{\phi_i(\eta)\}_{i=1}^5$ in (2.26) are different from those in (2.44); and, the coefficient set $[w_1, w_2, w_3, w_4, c_1, c_2]^T$ in (2.30) is not the same as that in (2.48).

2.5 Numerical examples

We chose the multiquadric (MQ) function, i.e. (1.6), as the basis function in the present calculations. The value of $\beta = 40$ is chosen for calculation in Section 2.5.4 and $\beta = 50$ for the rest of calculations in the present work. We evaluate the performance of the present scheme through the following measures.

i. The root mean square error (RMS) is defined as

$$RMS = \sqrt{\frac{\sum_{i=1}^{N}\left(f_i - \overline{f}_i\right)^2}{N}}, \tag{2.57}$$

where f_i and $\overline{f}_i$ are the computed and exact values of the solution f at the i-th node, respectively; and, N is the number of nodes over the whole domain.

ii. The maximum absolute error (L_∞) is defined as

$$L_\infty = \max_{i=1,\dots,N}|f_i - \overline{f}_i|. \tag{2.58}$$

iii. The global convergence rate, α, with respect to the grid refinement is defined through

$$RMS(h) \approx \gamma h^\alpha = O(h^\alpha), \tag{2.59}$$

where h is the grid size; and, γ and α are exponential model's parameters.

iv. A flow is considered as reaching its steady state when

$$\sqrt{\frac{\sum_{i=1}^{N}\left(f_i^n - f_i^{n-1}\right)^2}{N}} < 10^{-9}. \tag{2.60}$$

2.5.1 Poisson equation in rectangular domain

In order to study the spatial accuracy of the present compact IRBF approximation scheme in a rectangular domain, we consider the following Poisson equation (Mai-Duy and Tran-Cong, 2010)

$$\frac{d^2u}{dx_1^2} + \frac{d^2u}{dx_2^2} = 4(1-\pi^2)\{\sin(\pi(2x_1-1))\sinh(2x_2-1)$$
$$+4\cosh(2(2x_1-1))\cos(2\pi(2x_2-1))\}, \tag{2.61}$$

subject to the Dirichlet boundary condition derived from the following exact solution

$$\overline{u} = \sin(\pi(2x_1 - 1))\sinh(2x_2 - 1) + \cosh(2(2x_1 - 1))\cos(2\pi(2x_2 - 1)), \quad (2.62)$$

on a square domain $[0, 1]^2$. The calculations are carried out on a set of uniform grids of $\{41 \times 41, 51 \times 51, ..., 91 \times 91\}$. Figure 2.3 shows that present scheme outperforms the fourth-order compact finite difference method (HOC) by Tian et al. (2011) and the second-order standard finite difference method (FDM) in terms of both the solution accuracy and the convergence rate. The solutions converge as $O(h^{5.23})$ for the present scheme, $O(h^{4.56})$ for the HOC, and $O(h^{1.99})$ for the standard FDM. Figure 2.4 shows that the matrix condition number grows with approximately the same rate of $O(h^{-2.00})$ for the three methods.
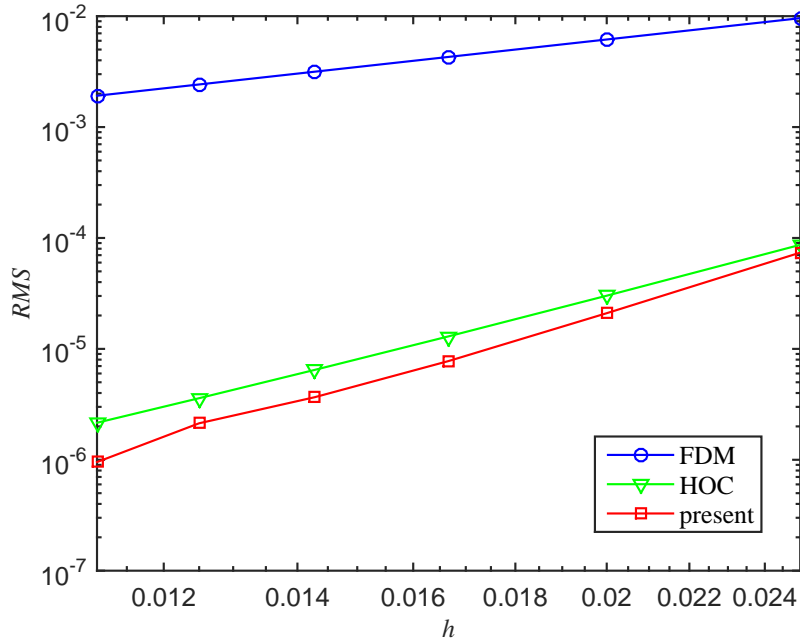
Figure 2.3 Poisson equation, rectangular domain, $\{41 \times 41, 51 \times 51, ..., 91 \times 91\}$: The effect of the grid size h on the solution accuracy RMS.

2.5.2 Poisson equation in non-rectangular domain

To study the spatial accuracy of the present compact IRBF approximation scheme in a non-rectangular domain, we consider the following Poisson equation (Mai-
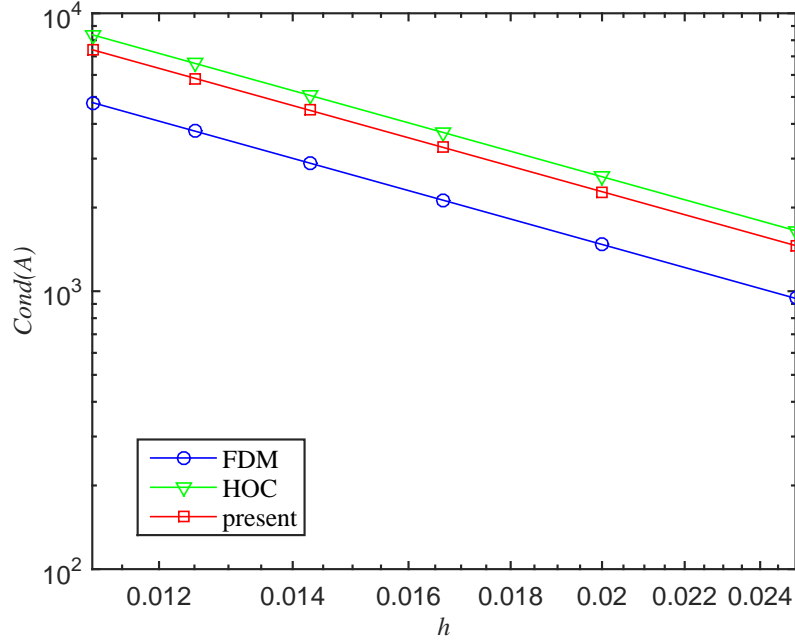
Figure 2.4 Poisson equation, rectangular domain, $\{41 \times 41, 51 \times 51, ..., 91 \times 91\}$: The effect of the grid size h on the matrix condition number.

Duy and Tran-Cong, 2010)

$$\frac{d^2 u}{dx_1^2} + \frac{d^2 u}{dx_2^2} = 4(1 - \pi^2) \left\{ \sin(2\pi x_1) \sinh(2x_2) + 4 \cosh(4x_1) \cos(4\pi x_2) \right\}, \quad (2.63)$$

subject to the Dirichlet boundary condition derived from the following exact solution

$$\overline{u} = \sin(2\pi x_1) \sinh(2x_2) + \cosh(4x_1) \cos(4\pi x_2), \quad (2.64)$$

on a circular domain with radius of $1/2$. The problem domain is embedded in a uniform Cartesian grid and the grid nodes exterior to the domain are removed. The interior nodes falling within a small distance $\delta = h/8$, where h is the grid size, to the boundary will also be discarded (Mai-Duy and Tran-Cong, 2010). The boundary nodes are generated through the intersection of the grid lines and the boundary as demonstrated in Figure 2.5. Calculations are carried out on a set of uniform grids, $\{20 \times 20, 30 \times 30, ..., 90 \times 90\}$. Figure 2.6 shows that the present compact IRBF has better performance than the second- and fourth-order HOC schemes proposed by Gamet et al. (1999). The present scheme yields a fast convergence rate of $O(h^{4.38})$ while the HOC produces a rate of $O(h^{3.99})$ for the fourth-order scheme and $O(h^{1.99})$ for the second-order scheme. Figure 2.7 shows

that the matrix condition number increases with approximately the same rate of $O(h^{-1.99})$ for the three methods.
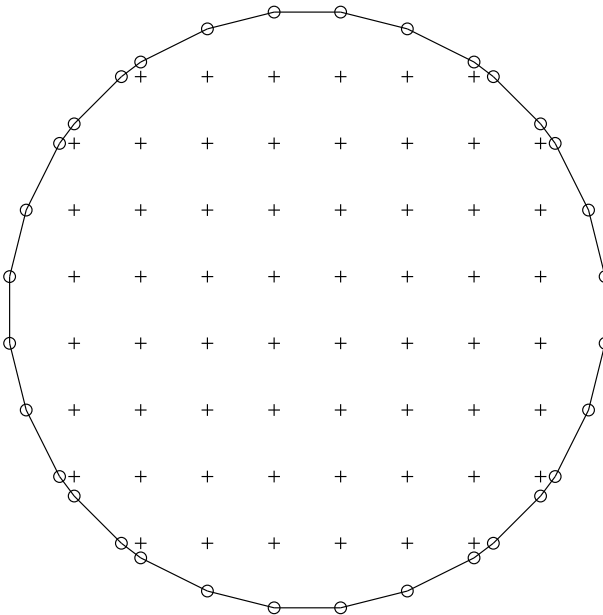
Figure 2.5 Poisson equation, non-rectangular domain, spatial discretisation: $+$, interior nodes; $\circ$, boundary nodes.
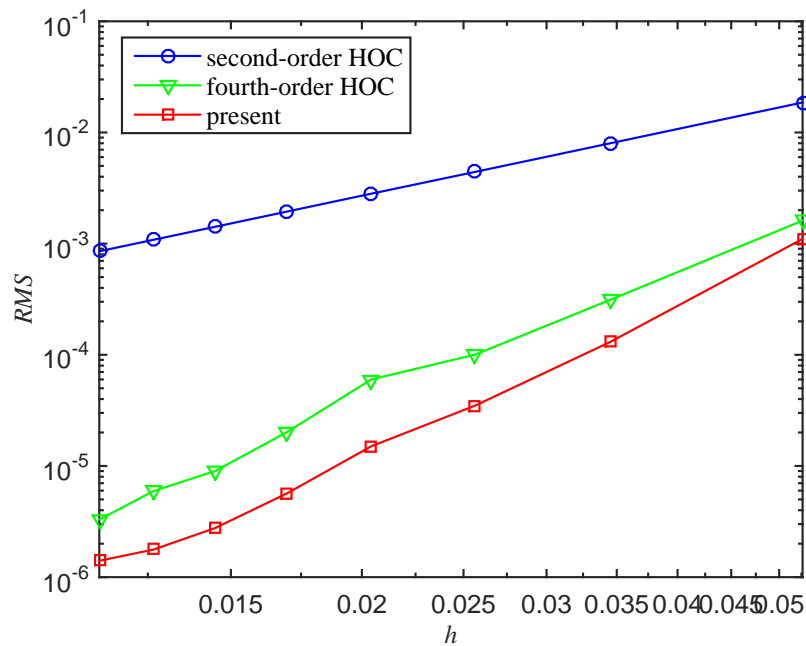
Figure 2.6 Poisson equation, non-rectangular domain, $\{20 \times 20, 30 \times 30, ..., 90 \times 90\}$: The effect of the grid size h on the solution accuracy RMS.
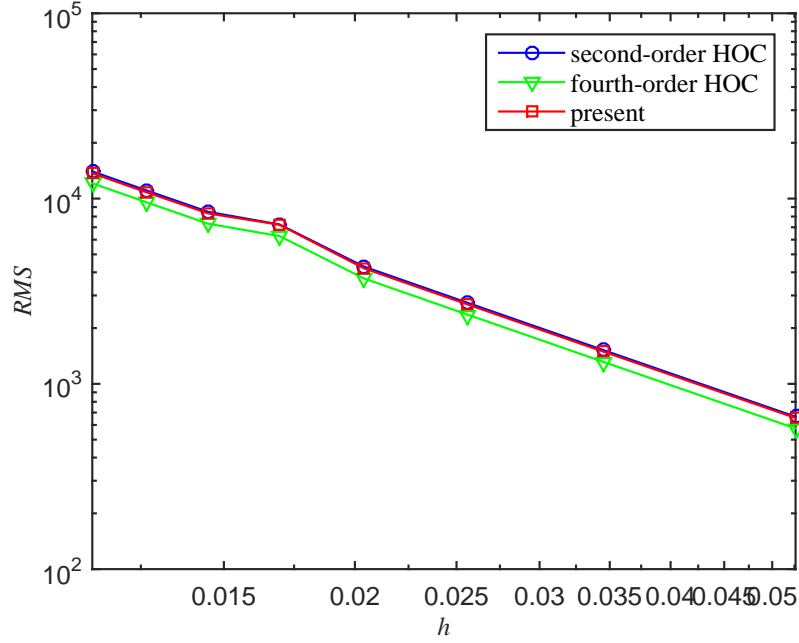
Figure 2.7 Poisson equation, non-rectangular domain, $\{20 \times 20, 30 \times 30, ..., 90 \times 90\}$: The effect of the grid size h on the matrix condition number.

2.5.3 Taylor-Green vortex in rectangular domain

To study the performance of the fully coupled velocity-pressure approach, based on the compact IRBF approximation, in simulating viscous flow in a rectangular domain, we consider a transient flow problem, namely Taylor-Green vortex (Tian et al., 2011). This problem is governed by the Navier-Stokes equations (2.4)-(2.6) and has the analytical solutions

$$\overline{u}(x_1, x_2, t) = -\cos(kx_1)\sin(kx_2)\exp(-2k^2 t/Re), \tag{2.65}$$

$$\overline{v}(x_1, x_2, t) = \sin(kx_1)\cos(kx_2)\exp(-2k^2 t/Re), \tag{2.66}$$

$$\overline{p}(x_1, x_2, t) = -1/4\left\{\cos(2kx_1) + \cos(2kx_2)\right\}\exp(-4k^2 t/Re), \tag{2.67}$$

where $0 \le x_1, x_2 \le 2\pi$. Calculations are carried out for $k = 2$ on a set of uniform grid, $\{11 \times 11, 21 \times 21, ..., 51 \times 51\}$. A fixed time step $\Delta t = 0.002$ and $Re = 100$ are employed. Numerical solutions are computed at $t = 2$. The exact solution, i.e. equations (2.65)-(2.67), provides the initial field at $t = 0$ and the time-dependent boundary conditions. Table 2.1 shows the accuracy comparison between the present scheme and the HOC scheme of Tian et al. (2011) in terms

of the RMS error and the convergence rate. It is seen that the present scheme produces better accuracy and better convergence rates than the scheme of the HOC, i.e. $O(h^{5.35})$ compared to $O(h^{2.92})$ for the velocity and $O(h^{4.48})$ compared to $O(h^{3.28})$ for the pressure.

2.5.4 Taylor-Green vortex in non-rectangular domain

In order to analyse the performance of the combination of the fully coupled approach and the compact IRBF approximation scheme in solving the transient viscous flow in a non-rectangular domain, we consider the case of an array of decaying vortices with the analytical solutions (Uhlmann, 2005) described by

$$\overline{u}(x_1, x_2, t) = \sin(\pi x_1) \cos(\pi x_2) \exp(-2\pi^2 t / Re), \tag{2.68}$$

$$\overline{v}(x_1, x_2, t) = -\sin(\pi x_2) \cos(\pi x_1) \exp(-2\pi^2 t / Re), \tag{2.69}$$

$$\overline{p}(x_1, x_2, t) = 1/2 \left\{ \cos^2(\pi x_2) - \sin^2(\pi x_1) \right\} \exp(-4\pi^2 t / Re). \tag{2.70}$$

The flow is computed in an embedded circular domain with radius of unity and centred at the origin of the computational domain $\Omega = [-1.5, 1.5] \times [-1.5, 1.5]$. The interior nodes are chosen and the boundary nodes are generated in a similar manner described in Section 2.5.2. Calculations are carried out on a set of uniform grids, $\{10 \times 10, 20 \times 20, ..., 50 \times 50\}$. The Reynolds number is set to be $Re = 5$ and numerical solutions are computed at $t = 0.3$ using a fixed time step $\Delta t = 0.001$. The initial field at $t = 0$ and the time-dependent boundary conditions are given by (2.68)-(2.70). Table 2.2 illustrates the accuracy comparison between the present scheme and the FDM approach of Uhlmann (2005) in terms of the maximum error and the convergence rate. It is observed that present scheme produces lower errors with better convergence rates, i.e. $O(h^{4.44})$ for the u-velocity and $O(h^{4.59})$ for the v-velocity in comparison with $O(h^{2.13})$ for both u- and v-velocities given by the approach of Uhlmann (2005).

Table 2.1 Taylor-Green Vortex, rectangular domain: *RMS* errors and convergence rates.

Grid	present			HOC (Tian et al., 2011)		
	u-error	v-error	p-error	u-error	v-error	p-error
11×11	1.7797233E-01	1.7797723E-01	3.0668704E-01	7.0070489E-02	7.0070489E-02	1.0764149E-01
21×21	4.6366355E-03	4.6366340E-03	8.5913505E-03	9.0692193E-03	9.0692193E-03	1.0567607E-02
31×31	5.3168859E-04	5.3168061E-04	2.6550518E-03	2.8851487E-03	2.8851487E-03	2.9103288E-03
41×41	1.0970214E-04	1.0968156E-04	3.4713723E-04	1.2238736E-03	1.2238736E-03	1.1356134E-03
51×51	3.2428099E-05	3.2378594E-05	2.6244035E-04	6.3063026E-04	6.3063026E-04	5.3933641E-04
Rate	$O(h^{5.35})$	$O(h^{5.35})$	$O(h^{4.48})$	$O(h^{2.92})$	$O(h^{2.92})$	$O(h^{3.28})$

Table 2.2 Taylor Green Vortex, non-rectangular domain: Maximum errors (L_∞) and convergence rates.

Grid	present			FDM (Uhlmann, 2005)		
	u-error	v-error	p-error	u-error	v-error	p-error
10×10	5.0940713E-02	3.9890094E-02	9.5986185E-02	–	–	–
20×20	1.1003665E-03	7.9266552E-04	2.2013746E-03	–	–	–
30×30	9.7670238E-05	8.1362620E-05	5.1711179E-04	≈1.056E-02	≈1.056E-02	–
40×40	5.8426984E-05	2.8665169E-05	2.1616129E-04	≈5.520E-03	≈5.520E-03	–
50×50	3.3759336E-05	2.3569385E-05	1.4680716E-04	≈3.441E-03	≈3.441E-03	–
Rate	$O(h^{4.44})$	$O(h^{4.59})$	$O(h^{3.88})$	$\approx O(h^{2.13})$	$\approx O(h^{2.13})$	$\approx O(h^{2.13})$

2.5.5 Lid driven cavity flow

The classical lid driven cavity flow has been considered as a test problem for the evaluation of numerical methods and the validation of fluid flow solvers for the past decades. Figure 2.8 shows the problem definition and boundary conditions. Uniform grids of $\{31 \times 31, 51 \times 51, 71 \times 71, 91 \times 91, 111 \times 111, 129 \times 129\}$ and a range of $Re \in \{100, 400, 1000, 3200\}$ are employed in the simulation. A fixed time step is chosen to be $\Delta t = 0.001$. Results of the present scheme are compared with those of some others (Ghia et al., 1982; Gresho et al., 1984; Bruneau and Jouron, 1990; Deng et al., 1994b; Botella and Peyret, 1998; Sahin and Owens, 2003; Thai-Quang et al., 2012a). From the literature, FDM results using very dense grids presented by Ghia et al. (1982) and pseudo-spectral results presented by Botella and Peyret (1998) have been referred to as "Benchmark" results for comparison purposes.

Tables 2.3, 2.4, 2.5, and 2.6 show the present results for the extrema of the vertical and horizontal velocity profiles along the horizontal and vertical centrelines of the cavity for several Reynolds numbers. For $Re = 100$ (Table 2.3) and $Re = 1000$ (Table 2.4), the "Errors" evaluated are relative to "Benchmark" results of Botella and Peyret (1998). The results obtained by the present scheme are generally better in comparison with those of the others.

Table 2.3 Lid driven cavity, $Re = 100$: Extrema of the vertical and horizontal velocity profiles along the horizontal and vertical centrelines of the cavity, respectively. "Errors" are relative to the "Benchmark" data.

Method	Grid	u_{min}	Error (%)	y_{min}	v_{max}	Error (%)	x_{max}	v_{min}	Error (%)	x_{min}
Present	31×31	-0.2132676	0.36	0.4586	0.1788936	0.38	0.2374	-0.2527995	0.40	0.8101
Present	51×51	-0.2139898	0.02	0.4581	0.1795821	0.01	0.2371	-0.2538354	0.01	0.8104
Present	71×71	-0.2140390	0.00	0.4581	0.1795960	0.01	0.2370	-0.2538423	0.02	0.8104
compact IRBF (u, v, p) (Thai-Quang et al., 2012a)	31×31	-0.2102259	1.78	0.4578	0.1768808	1.50	0.2370	-0.2501843	1.43	0.8107
compact IRBF (u, v, p) (Thai-Quang et al., 2012a)	51×51	-0.2121503	0.88	0.4579	0.1781849	0.77	0.2372	-0.2520400	0.69	0.8107
FVM (u, v, p) (Deng et al., 1994b)	64×64	-0.21315	0.42	—	0.17896	0.34	—	-0.25339	0.16	—
FDM $(\psi - \omega)$ (Ghia et al., 1982)	129×129	-0.21090	1.47	0.4531	0.17527	2.40	0.2344	-0.24533	3.34	0.8047
FDM (u, v, p) (Bruneau and Jouron, 1990)	129×129	-0.2106	1.61	0.4531	0.1786	0.54	0.2344	-0.2521	0.67	0.8125
FVM (u, v, p) (Sahin and Owens, 2003)	257×257	-0.213924	0.06	0.4598	0.180888	0.73	0.2354	-0.256603	1.10	0.8127
Benchmark (Botella and Peyret, 1998)		-0.2140424		0.4581	0.1795728		0.2370	-0.2538030		0.8104

Table 2.4 Lid driven cavity, $Re = 1000$: Extrema of the vertical and horizontal velocity profiles along the horizontal and vertical centrelines of the cavity, respectively. "Errors" are relative to the "Benchmark" data.

Method	Grid	u_{min}	Error (%)	y_{min}	v_{max}	Error (%)	x_{max}	v_{min}	Error (%)	x_{min}
Present	51×51	-0.3611357	7.06	0.1819	0.3481667	7.63	0.1621	-0.4853383	7.92	0.9025
Present	71×71	-0.3807425	2.01	0.1741	0.3685353	2.23	0.1593	-0.5156774	2.16	0.9079
Present	91×91	-0.3857664	0.72	0.1725	0.3738367	0.82	0.1585	-0.5231499	0.75	0.9089
Present	111×111	-0.3873278	0.32	0.1720	0.3755235	0.38	0.1582	-0.5254043	0.32	0.9091
compact IRBF (u, v, p) (Thai-Quang et al., 2012a)	71×71	-0.3755225	3.36	0.1753	0.3637009	3.51	0.1608	-0.5086961	3.49	0.9078
compact IRBF (u, v, p) (Thai-Quang et al., 2012a)	91×91	-0.3815923	1.80	0.1735	0.3698053	1.89	0.1594	-0.5174658	1.82	0.9085
compact IRBF (u, v, p) (Thai-Quang et al., 2012a)	111×111	-0.3840354	1.17	0.1728	0.3722634	1.24	0.1588	-0.5209683	1.16	0.9088
compact IRBF (u, v, p) (Thai-Quang et al., 2012a)	129×129	-0.3848064	0.97	0.1724	0.3729119	1.07	0.1586	-0.5223350	0.90	0.9089
FVM (u, v, p) (Deng et al., 1994b)	128×128	-0.38511	0.89	—	0.37369	0.86	—	-0.5228	0.81	—
FDM $(\psi - \omega)$ (Ghia et al., 1982)	129×129	-0.38289	1.46	0.1719	0.37095	1.59	0.1563	-0.5155	2.20	0.9063
FEM (u, v, p) (Gresho et al., 1984)	129×129	-0.375	3.49	0.160	0.362	3.96	0.160	-0.516	2.10	0.906
FDM (u, v, p) (Bruneau and Jouron, 1990)	256×256	-0.3764	3.13	0.1602	0.3665	2.77	0.1523	-0.5208	1.19	0.9102
FVM (u, v, p) (Sahin and Owens, 2003)	257×257	-0.388103	0.12	0.1727	0.376910	0.01	0.1573	-0.528447	0.26	0.9087
Benchmark (Botella and Peyret, 1998)		-0.3885698		0.1717	0.3769447		0.1578	-0.5270771		0.9092

Figure 2.9 displays velocity profiles along the vertical and horizontal centrelines for different grid sizes at $Re = 1000$, where a grid convergence of the present scheme is obviously observed (i.e. the present solution approaches the benchmark solution with a fast rate as the grid density is increased). The present scheme effectively achieves the benchmark results with a grid of only 91×91 in comparison with the grid of 129×129 used to obtain the benchmark results in (Ghia et al., 1982). In addition, those velocity profiles at $Re \in \{100, 400, 1000, 3200\}$ with the grid size of $\{51 \times 51, 71 \times 71, 91 \times 91, 129 \times 129\}$, respectively, are displayed in Figure 2.10, where the present solutions match the benchmark ones very well.
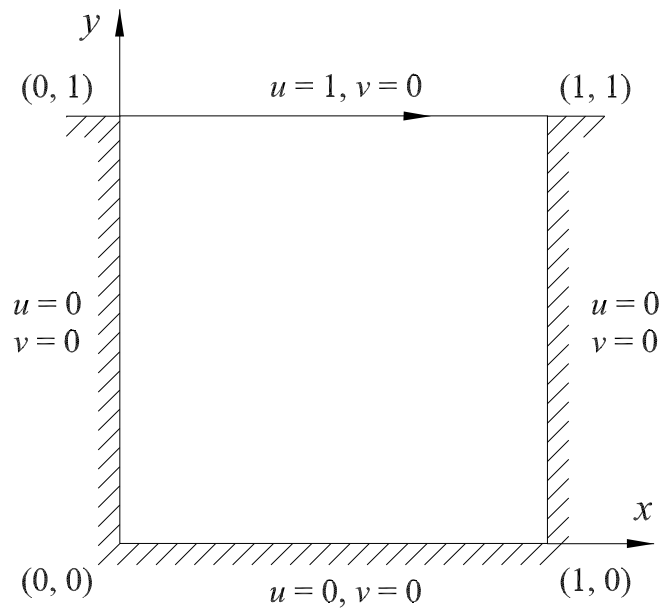
Figure 2.8 Lid driven cavity: problem configuration and boundary conditions.

To exhibit contour plots of the flow, a range of $Re \in \{100, 400, 1000, 3200\}$ and the grid of $\{51 \times 51, 71 \times 71, 91 \times 91, 129 \times 129\}$ are employed, respectively. Figures 2.11 and 2.12 show streamlines and iso-vorticity lines, which are derived from the velocity field. Figure 2.13 shows the pressure deviation contours of the present simulations. These plots are also in good agreement with those reported in the literature.

Table 2.5 Lid driven cavity, $Re = 400$: Extrema of the vertical and horizontal velocity profiles along the horizontal and vertical centrelines of the cavity, respectively.

Method	Grid	u_{min}	y_{min}	v_{max}	x_{max}	v_{min}	x_{min}
Present	51×51	-0.325864	0.2809	0.300815	0.2265	-0.450157	0.8619
Present	71×71	-0.328095	0.2801	0.303156	0.2257	-0.453380	0.8622
Present	91×91	-0.328548	0.2800	0.303655	0.2254	-0.453936	0.8623
compact IRBF (u, v, p) (Thai-Quang et al., 2012a)	51×51	-0.323158	0.2814	0.297493	0.2248	-0.442770	0.8605
compact IRBF (u, v, p) (Thai-Quang et al., 2012a)	71×71	-0.325168	0.2804	0.300818	0.2252	-0.449146	0.8620
FVM (u, v, p) (Deng et al., 1994b)	128×128	-0.32751	—	0.30271	—	-0.45274	—
FDM $(\psi - \omega)$ (Ghia et al., 1982)	129×129	-0.32726	0.2813	0.30203	0.2266	-0.44993	0.8594
FVM (u, v, p) (Sahin and Owens, 2003)	257×257	-0.328375	0.2815	0.304447	0.2253	-0.456316	0.8621

Table 2.6 Lid driven cavity, $Re = 3200$: Extrema of the vertical and horizontal velocity profiles along the horizontal and vertical centrelines of the cavity, respectively.

Method	Grid	u_{min}	y_{min}	v_{max}	x_{max}	v_{min}	x_{min}
Present	91×91	-0.390803	0.1042	0.390298	0.1001	-0.503019	0.9394
Present	111×111	-0.411768	0.0983	0.409752	0.0985	-0.533705	0.9438
Present	129×129	-0.421587	0.0960	0.419126	0.0979	-0.547987	0.9455
FEM (u, v, p) (Gresho et al., 1984)	129×129	-0.420	0.084	0.415	0.094	-0.560	0.945
FDM $(\psi - \omega)$ (Ghia et al., 1982)	129×129	-0.41933	0.1016	0.42768	0.0938	-0.54053	0.9453
FVM (u, v, p) (Sahin and Owens, 2003)	257×257	-0.435402	0.0921	0.432448	0.0972	-0.569145	0.9491
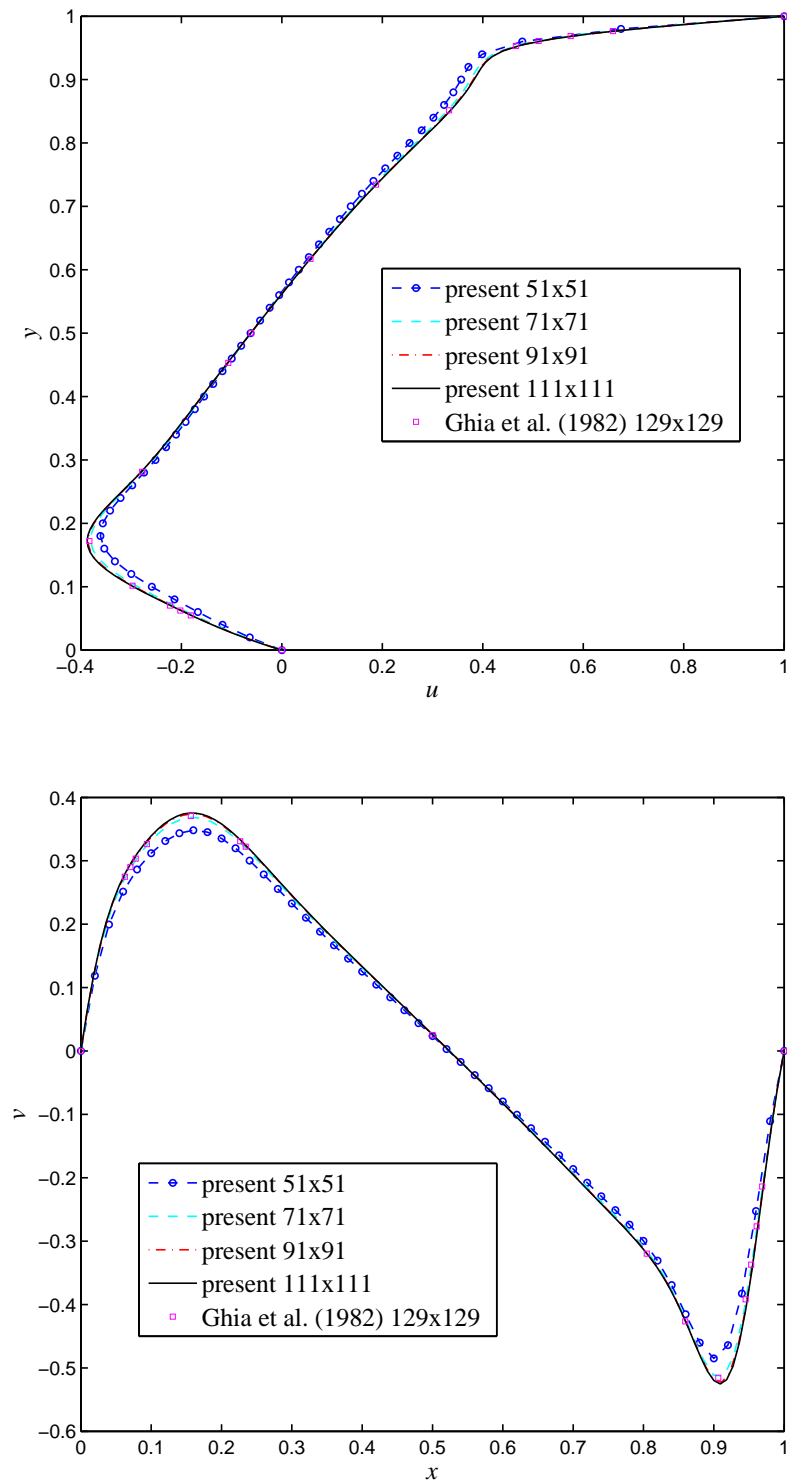
Figure 2.9 Lid driven cavity, $Re = 1000$: Profiles of the u-velocity along the vertical centreline and the v-velocity along the horizontal centreline as the grid density increases. It is noted that the curves for the last two grids are indistinguishable and in good agreement with the benchmark results of (Ghia et al., 1982).
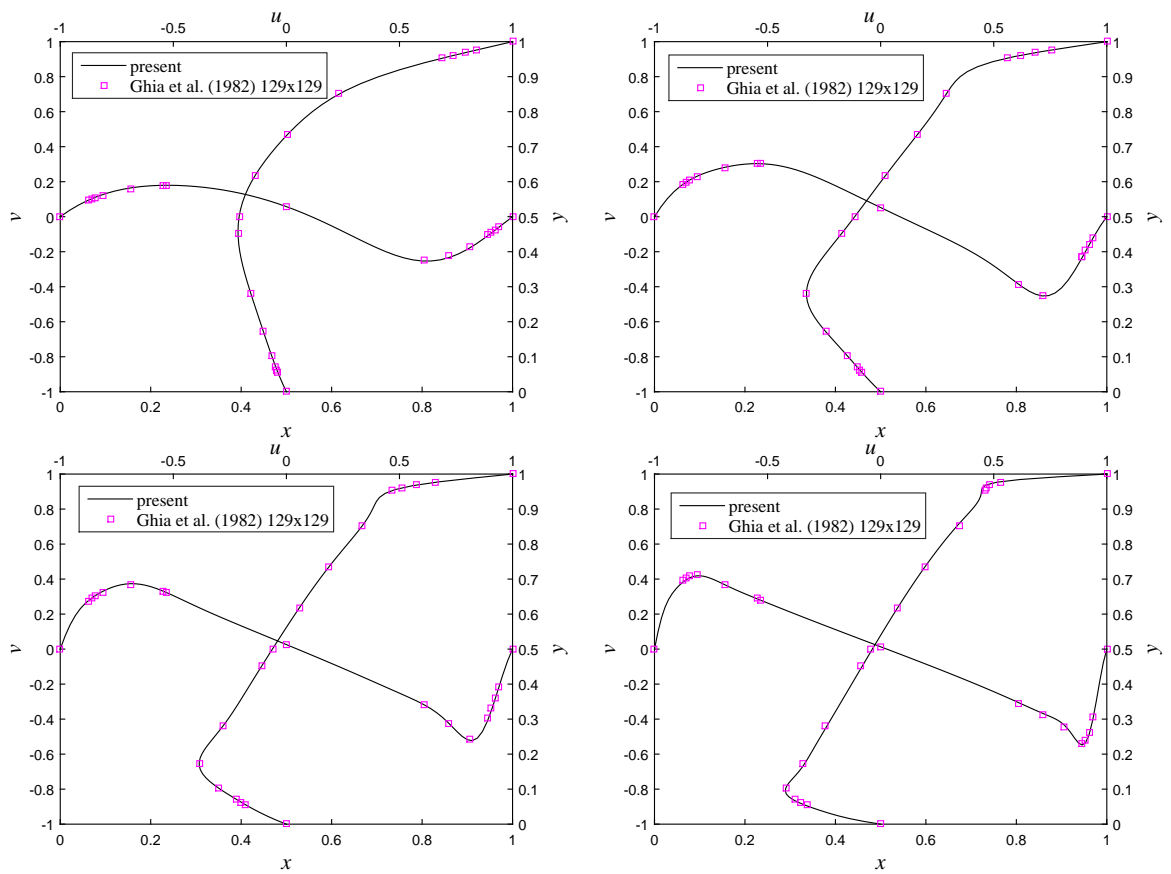
Figure 2.10 Lid driven cavity: Profiles of the u-velocity along the vertical centreline and the v-velocity along the horizontal centreline for $Re = 100$ (top-left), $Re = 400$ (top-right), $Re = 1000$ (bottom-left), and $Re = 3200$ (bottom-right) with the grid of 51×51, 71×71, 91×91, and 129×129, respectively.
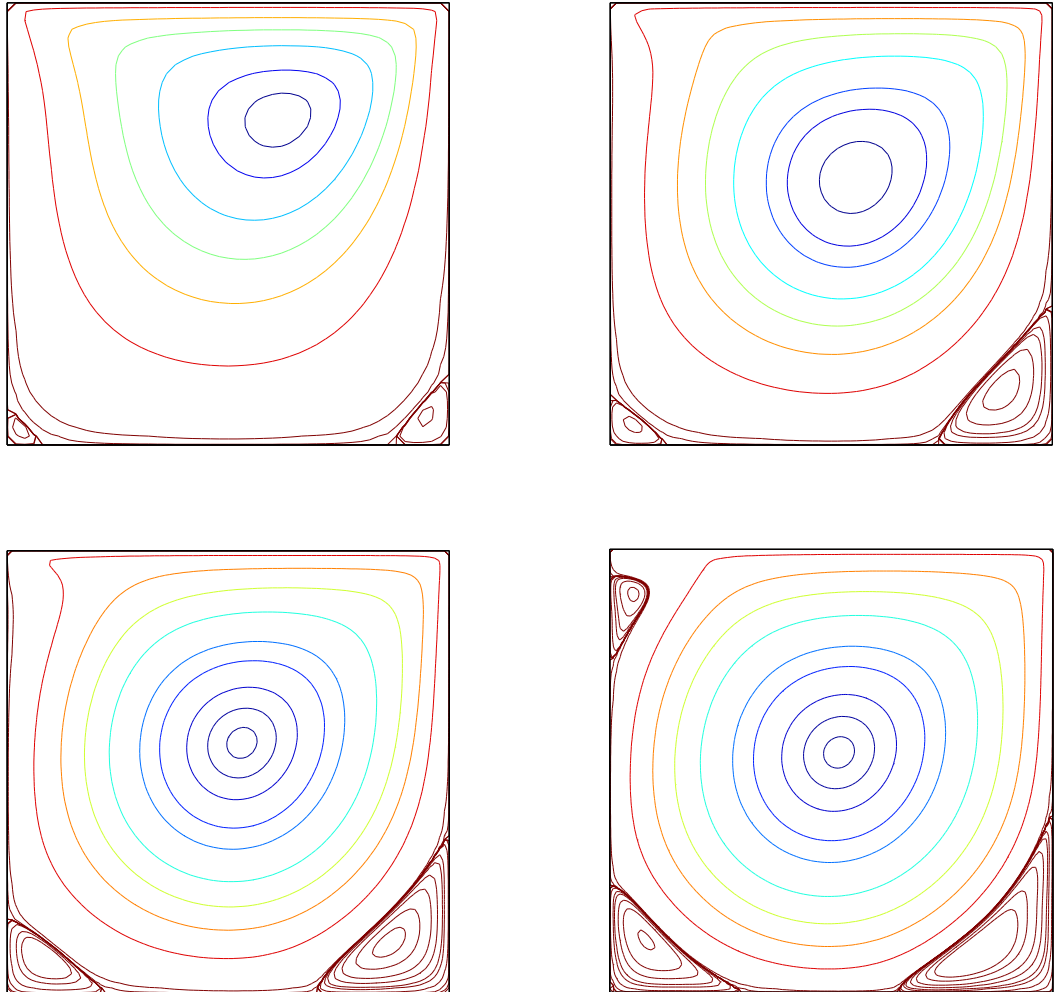
Figure 2.11 Lid driven cavity: Streamlines of the flow for $Re = 100$ (top-left), $Re = 400$ (top-right), $Re = 1000$ (bottom-left), and $Re = 3200$ (bottom-right) with the grid of 51×51, 71×71, 91×91, and 129×129, respectively. The contour values used here are taken to be the same as those in (Ghia et al., 1982).
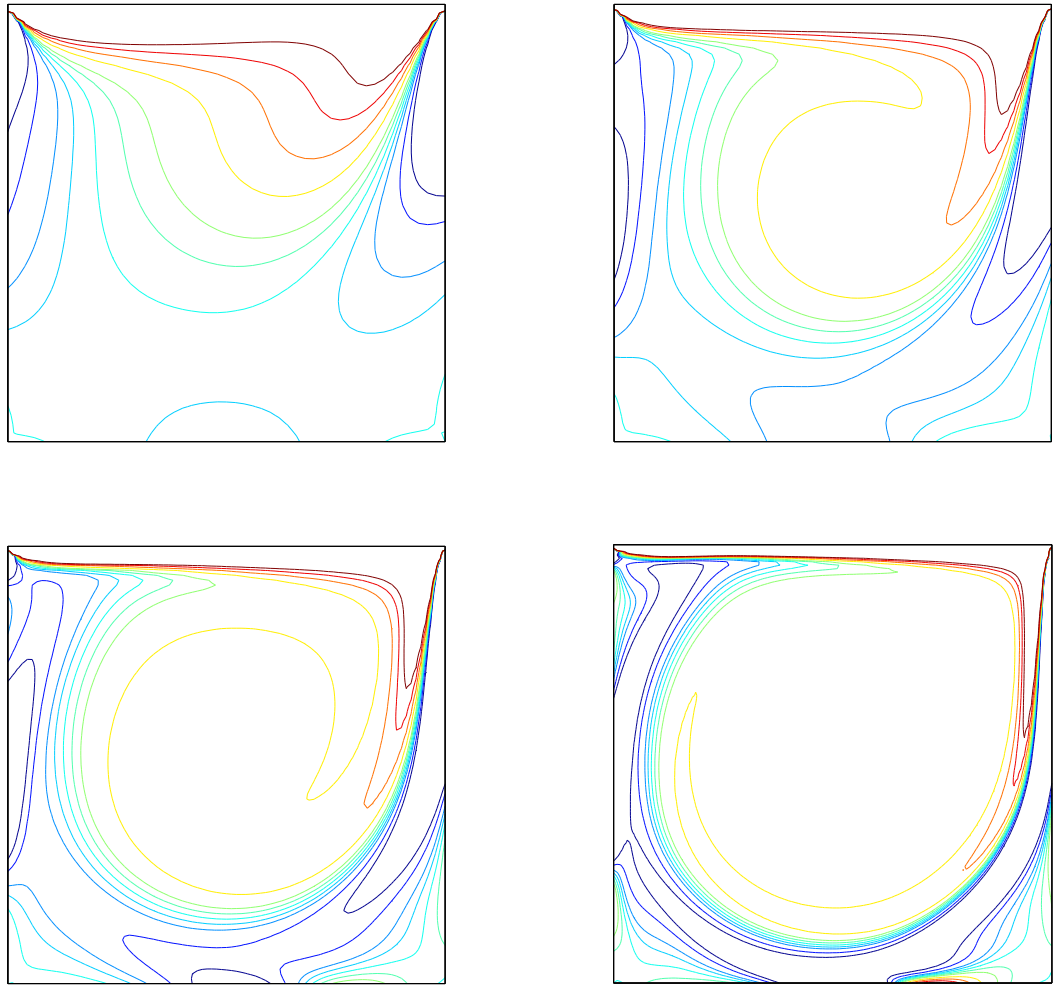
Figure 2.12 Lid driven cavity: Iso-vorticity lines of the flow for $Re = 100$ (top-left), $Re = 400$ (top-right), $Re = 1000$ (bottom-left), and $Re = 3200$ (bottom-right) with the grid of 51×51, 71×71, 91×91, and 129×129, respectively. The contour values used here are taken to be the same as those in (Ghia et al., 1982).
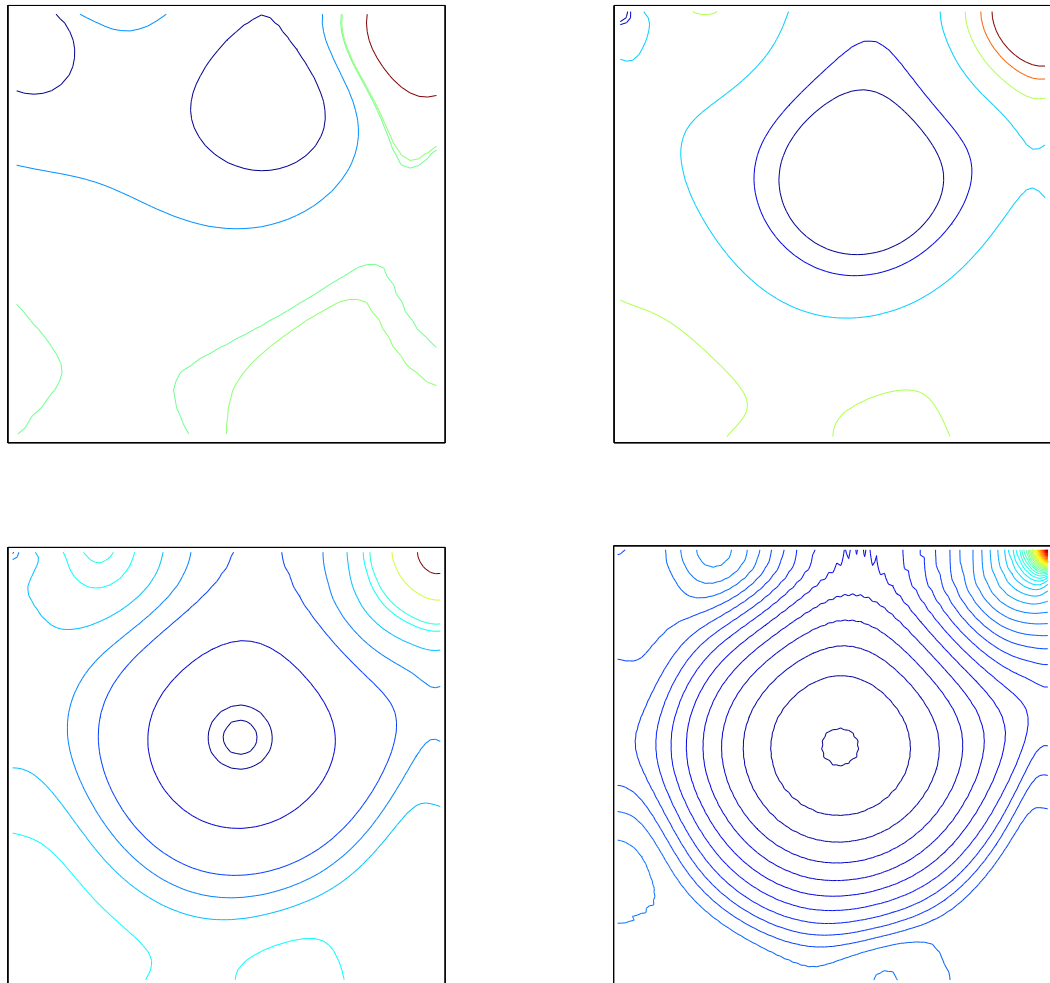
Figure 2.13 Lid driven cavity: Static pressure contours of the flow for $Re = 100$ (top-left), $Re = 400$ (top-right), $Re = 1000$ (bottom-left), and $Re = 3200$ (bottom-right) with the grid of 51×51, 71×71, 91×91, and 129×129, respectively. The contour values used here are taken to be the same as those in (Abdallah, 1987) for $Re = 100$ and $Re = 400$, (Botella and Peyret, 1998) for $Re = 1000$, and (Bruneau and Saad, 2006) for $Re = 3200$.

2.5.6 Irregular bottom lid driven cavity

The lid driven cavity with a deformed base presented in (Udaykumar et al., 1996; Shyy et al., 1996) is chosen to validate the performance of the present fluid flow solver in an irregular domain. The base is deformed sinusoidally with an amplitude of 10 percent of the base. The computational domain and boundary conditions are illustrated in Figure 2.14. The interior and boundary nodes are generated in a similar manner described in Section 2.5.2. The spatial discretisation is shown in Figure 2.15. A range of uniform grids, $\{53 \times 53, 63 \times 63, 83 \times 83, 93 \times 93\}$ is employed in the simulation. A fixed time step and Reynolds number are chosen to be $\Delta t = 0.001$ and $Re = 1000$, respectively. The results from the present method are compared with those presented in (Shyy et al., 1996; Mariani and Prata, 2008), where appropriate. From the literature, the FVM (Finite Volume Method) results using the well-tested body-fitted coordinate formulation and the dense grid of 121×121 presented in (Shyy et al., 1996) have been considered as "Benchmark" results for comparison purposes.
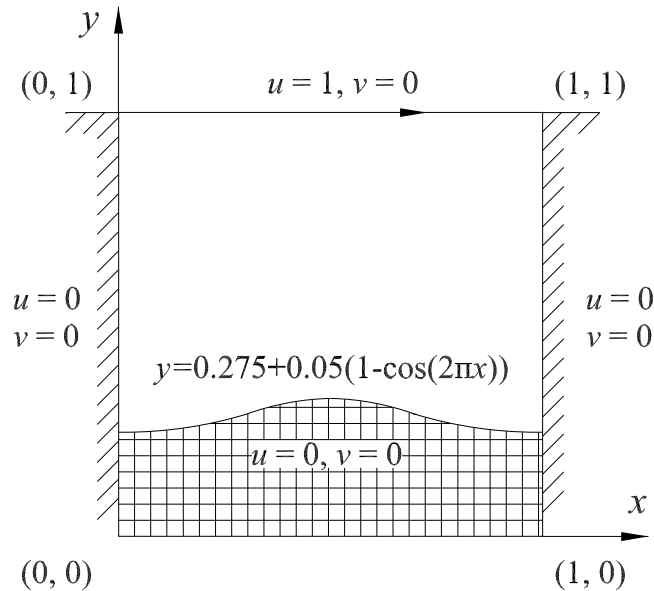
Figure 2.14 Irregular bottom lid driven cavity: problem configuration and boundary conditions.

Figure 2.16 displays horizontal and vertical velocity profiles along the vertical centreline for different grid sizes at $Re = 1000$, where the grid convergence of the present scheme is obviously observed (i.e. the present solution approaches the
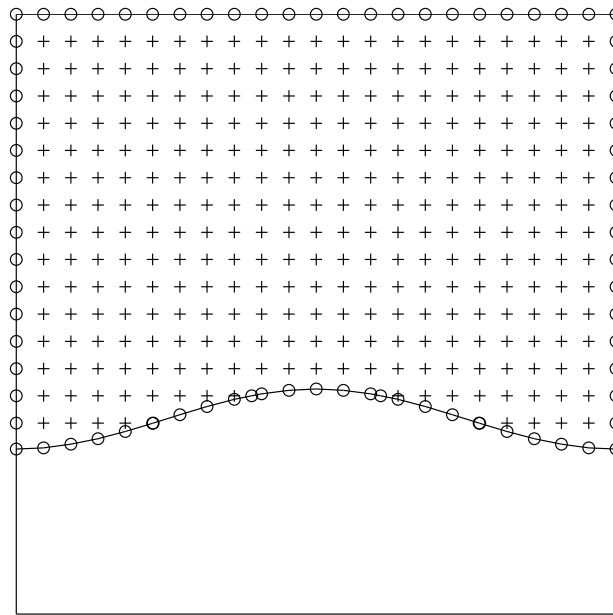
Figure 2.15 Irregular bottom lid driven cavity, spatial discretisation: +, interior nodes; ○, boundary nodes.

benchmark solution with a fast rate as the grid density is increased). The present scheme effectively achieves the benchmark results with a grid of only 83×83 in comparison with the grid of 121×121 used to obtain the benchmark results in (Shyy et al., 1996). In addition, the present results with a grid of only 53×53 outperform those of (Mariani and Prata, 2008) using the grid of 100×100. To exhibit contour plots of the flow, we employ the grid of 83×83 for $Re = 1000$. Figure 2.17 shows streamlines which are derived from the velocity field. Figure 2.18 shows the pressure deviation contours of the present simulation. These plots are in close agreement with those reported in the literature.
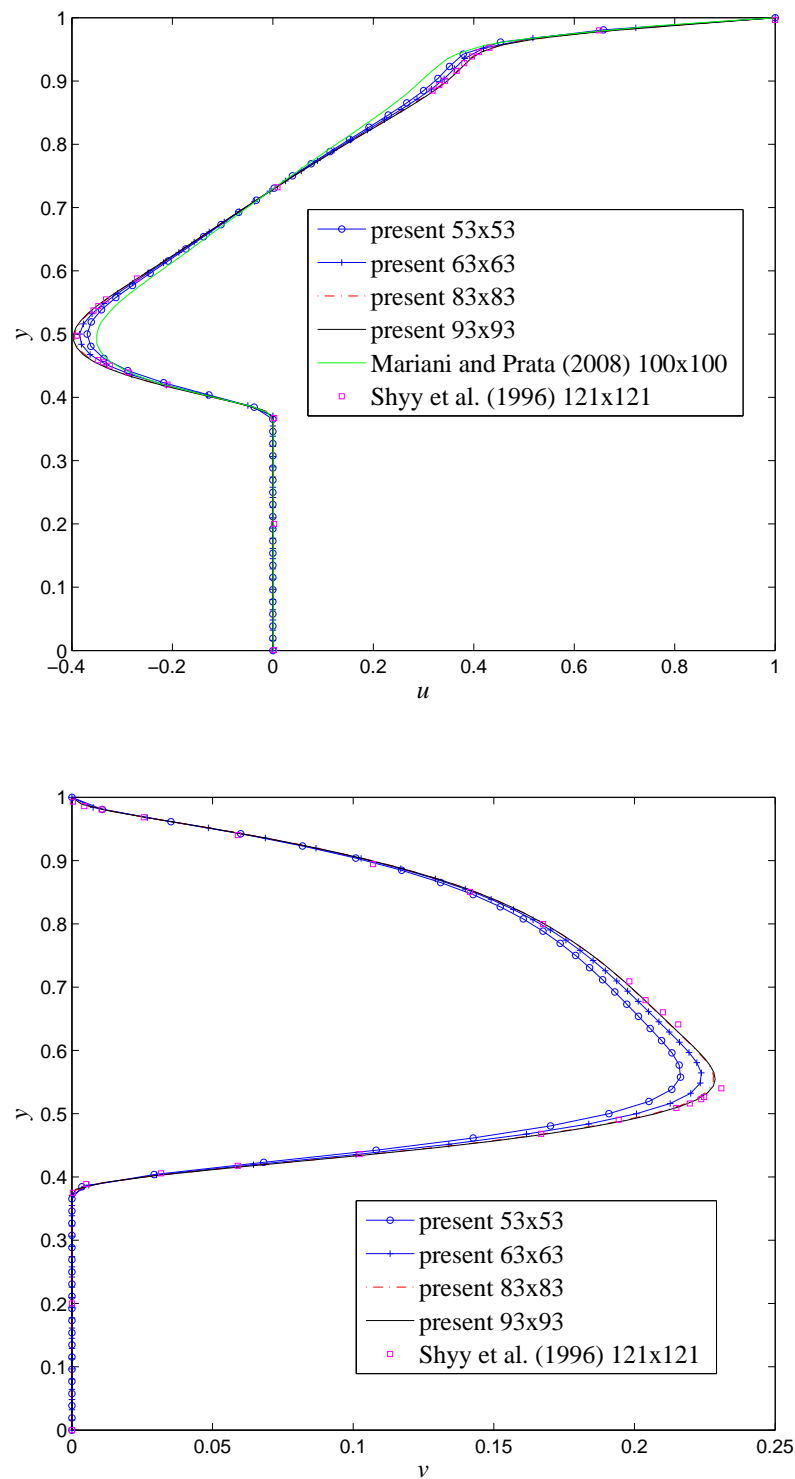
Figure 2.16 Irregular bottom lid driven cavity, $Re = 1000$: Profiles of the u-velocity (top) and v-velocity (bottom) along the vertical centreline as the grid density increases. It is noted that the curves for the last two grids are indistinguishable and in good agreement with the benchmark results of (Shyy et al., 1996).
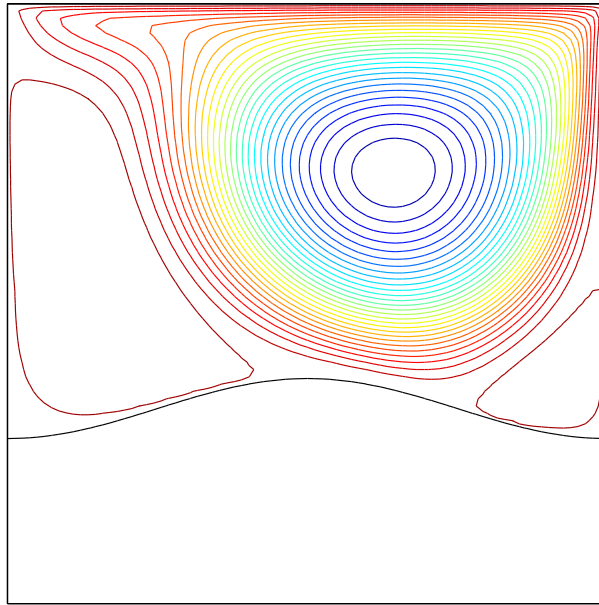
Figure 2.17 Irregular bottom lid driven cavity: Streamlines of the flow for $Re = 1000$ with the grid of 83×83. The plot contains 30 contour lines whose levels vary linearly from the minimum to maximum values; and, it is in good agreement with that of (Shyy et al., 1996).
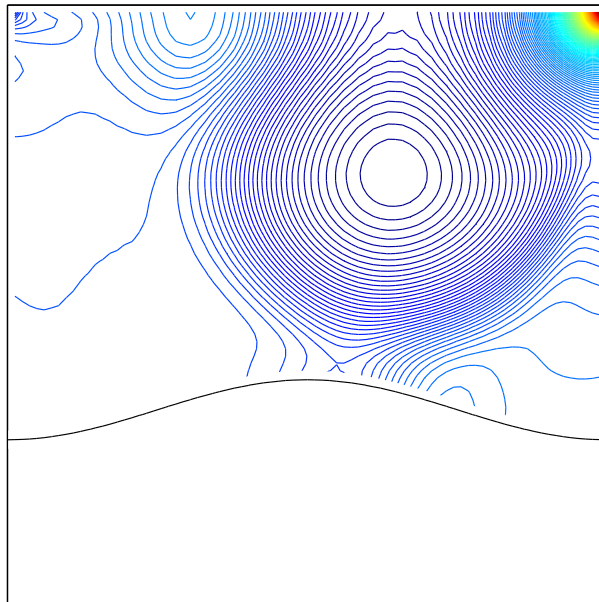
Figure 2.18 Irregular bottom lid driven cavity: Static pressure contours of the flow for $Re = 1000$ with the grid of 83×83. The plot contains 160 contour lines whose levels vary linearly from the minimum to maximum values.

2.6 Concluding remarks

In this chapter, we implement the high-order compact integrated radial basis function (IRBF) scheme, where first- and second-order derivative values of the field variables are included, in combination with the direct fully coupled velocity-pressure approach in the Cartesian-grid point-collocation structure. Like FDMs, the present approximation technique involves 3 nodes in each direction, which results in a sparse system matrix. Numerical examples indicate that the results of the present scheme are superior to those of the standard FDM scheme and the second- and fourth-order HOC schemes in terms of the solution accuracy and the convergence rate with the grid refinement. It is shown that the compact IRBF scheme produces up to fifth-order accuracy when approximating the Poisson equations in rectangular/non-rectangular domains. The combination of the compact IRBF and the direct fully coupled approach maintains the fourth-order accuracy in solving the transient flow problems of Taylor-Green vortices in rectangular/non-rectangular domains. In the fluid flow simulations with regular/irregular boundaries, the numerical results obtained by the present approach are highly accurate and in good agreement with the reported results in the literature.

In the next chapter, we will introduce a new coupled compact IRBF in order to improve the solution accuracy and efficiency of the compact IRBF in solving problems governed by differential equations.

Chapter 3

Coupled compact integrated RBF scheme for fluid flows

In this chapter, we propose a three-point coupled compact integrated radial basis function (IRBF) approximation scheme for the discretisation of second-order differential problems in one and two dimensions. The coupled compact scheme employs IRBFs to construct the approximations for its first- and second-order derivatives over a three-point stencil in each direction. Nodal values of the first- and second-order derivatives (i.e. extra information), incorporated into approximations by means of the constants of integration, are employed to compute the first- and second-order derivatives. The essence of the coupled compact IRBF scheme is to couple the extra information of the nodal first- and second-order derivative values via their identity equations. Owing to its coupling of the information of the nodal first- and second-order derivatives, the coupled compact IRBF scheme becomes more accurate, stable and efficient than the normal compact IRBF schemes proposed by Thai-Quang et al. (2012b). The main features of the coupled compact IRBF scheme include: three-point, high-order accuracy, stability, efficiency and inclusion of boundary values. Several analytic problems are considered to verify the present scheme and to compare its solution accuracy, stability and efficiency with those of the compact IRBF, higher-order compact (HOC) finite difference and some other high-order schemes. Numerical results show that highly accurate and stable results are obtained with the proposed

scheme. Additionally, the present scheme also takes less time to achieve a target accuracy in comparison with the compact IRBF and HOC schemes.

The coupled compact scheme developed in this chapter will also be used to simulate fluid flow problems presented in Chapter 4.

3.1 Introduction

Considerable progress has been made over the past decades on developing high-order accuracy schemes for solving second-order differential equations. The traditional first-order upwind and second-order central finite difference methods (FDMs) have low convergence rates and therefore require sufficiently fine meshes (Kun et al., 2012). The computational cost of those methods is thus relatively high, particularly for the case of high level of accuracy. One approach to alleviate these difficulties is to use high-order methods by which a comparable accuracy can be obtained with a much coarser discretisation.

Higher-order compact (HOC) finite difference methods (Hirsh, 1975; Rubin and Khosla, 1977; Adam, 1977; Noye and Tan, 1989), which require fewer grid points, have been widely used in numerical calculations with high accuracy for the small-scale problems. These approaches can provide a compromised way of combining the robustness of the FDM and the accuracy of spectral-like methods which converge exponentially towards the exact solution as the number of nodes is increased. In the HOC methods, the derivative values at a particular node are implicitly computed not only from the function values but also from the values of the derivatives at the neighboring nodes. In comparison with the FDM, these approaches give a higher order of accuracy for the same number of grid points. Lele (1992) proposed a family of spectral-like compact formulations and generalised its resolution characteristics on a uniform grid. Since then, the compact schemes have attained wide popularity in solving various problems involving the convection-diffusion and Navier-Stokes equations (Spotz and Carey, 1995; Mahesh, 1998; Ma et al., 1999; Li and Tang, 2001; Kalita et al., 2002; Karaa and Zhang, 2004; Tian and Ge, 2007; Tian et al., 2011).

Following the trend toward highly accurate numerical schemes for partial differential equations (PDEs), Kansa (1990a,b) first proposed the use of radial basis functions (RBFs) as approximants (here referred to as direct/differential RBF or DRBF methods). In the DRBF method, a closed form RBF approximating function is first obtained from a set of training points and the derivative functions are then calculated directly from the closed form RBF (Mai-Duy and Tran-Cong, 2001a). Mai-Duy and Tran-Cong (2001a, 2003) afterwards proposed the idea of using indirect/integrated radial basis functions (IRBFs) for the solution of PDEs. In the IRBF approach, the highest-order derivatives under interest are decomposed into a set of RBFs; and expressions for the lower derivatives and its function are then obtained through integration processes. Extensive numerical studies in (Mai-Duy and Tran-Cong, 2001a,b, 2003, 2005; Sarra, 2006; Shu and Wu, 2007) have shown that the integral approach is more accurate than the differential approach because the integration process is averagely less sensitive to noise. The integration process gives rise to integration constants through which extra equations can be employed. A one-dimensional IRBF scheme has been developed in (Mai-Duy and Tanner, 2007). This global RBF scheme has advantages of fast convergence, meshless nature and simple implementation, however its RBF matrices are fully populated and thus tend to be much more ill-conditioned as the number of the RBF is increased. To resolve these drawbacks, Mai-Duy and Tran-Cong (2011) developed a five-point compact IRBF scheme that is capable of solving second-order elliptic PDEs. Recently, Mai-Duy and Tran-Cong (2013) have proposed a three-point compact IRBF scheme where only nodal values of second-order derivatives (i.e. extra information) are incorporated into the approximations. Thai-Quang et al. (2012b) have proposed another three-point compact IRBF scheme where the extra information includes nodal values of the first- and second-order derivatives for the computation of the first- and second-order derivatives, respectively. The latter scheme was reported to be more accurate (Thai-Quang et al., 2012b). Several other approaches using RBFs for solving engineering and scientific problems have been recently reported, see for example (Kosec et al., 2011; Ngo-Cong et al., 2012; Sellountos et al., 2012; Thai-Quang et al., 2013; Mramor et al., 2013; Elgohary et al., 2014a,b; Hon et al., 2015) and

the references therein.

This chapter develops a new three-point coupled compact IRBF scheme for solving second-order PDEs. In the proposed coupled compact IRBF scheme, the first- and second-order derivatives at a particular node are implicitly obtained from the function values at the stencil points and from the nodal values of not only first- but also second-order derivatives (i.e. extra information) at two neighboring points. Coupling processes of the extra information of the nodal first- and second-order derivatives are performed by means of coupling identity equations. The coupled compact IRBF scheme is more accurate, stable and efficient than the normal compact IRBF schemes developed in (Thai-Quang et al., 2012b), which is achieved by the coupling of the first- and second-order derivatives. Major features of the coupled compact IRBF scheme are: three-point, implicit, high-order accuracy, stability, efficiency and inclusion of boundary values. Numerical solutions of PDEs, including Poisson equation, heat equation, Burgers equation, and steady/non-steady convection-diffusion equations, are used to illustrate the accuracy, stability and efficiency of the proposed coupled compact IRBF scheme. Results obtained are also compared with those obtained by the compact IRBF, HOC and some other high-order schemes. Greater accuracy and stability are obtained with the present scheme. Furthermore, it also achieves a prescribed accuracy with smaller amount of time compared with the compact IRBF and HOC schemes. The proposed coupled compact IRBF scheme appears to be an attractive alternative to the normal compact IRBF scheme for computations of second-order PDEs.

The remainder of this chapter is organised as follows: the coupled compact IRBF scheme is proposed in Section 3.2. Section 3.3 outlines the ADI solution for convection-diffusion equations. In Section 3.4, numerical examples are presented and coupled compact IRBF results are compared with some published solutions, where appropriate. Finally, concluding remarks are given in Section 3.5.

3.2 Coupled compact IRBF scheme

To improve the performance of compact local approximations, a coupled compact integrated radial basis function scheme is developed in this chapter as follows.

Consider a two-dimensional domain Ω, which is represented by a uniform Cartesian grid. The nodes are indexed in the x-direction by the subscript i ($i \in \{1, 2, ..., n_x\}$) and in the y-direction by j ($j \in \{1, 2, ..., n_y\}$). For rectangular domains, let N be the total number of nodes ($N = n_x \times n_y$) and N_{ip} be the number of interior nodes ($N_{ip} = (n_x - 2) \times (n_y - 2)$). At an interior grid point $\mathbf{x}_{i,j} = (x_{(i,j)}, y_{(i,j)})^T$ where $i \in \{2, 3, ..., n_x - 1\}$ and $j \in \{2, 3, ..., n_y - 1\}$, the associated stencils to be considered here are two local stencils: $\{x_{(i-1,j)}, x_{(i,j)}, x_{(i+1,j)}\}$ in the x-direction and $\{y_{(i,j-1)}, y_{(i,j)}, y_{(i,j+1)}\}$ in the y-direction. Hereafter, for brevity, η denotes either x or y in a generic local stencil $\{\eta_1, \eta_2, \eta_3\}$, where $\eta_1 < \eta_2 < \eta_3$ and $\eta_2 \equiv \eta_{(i,j)}$, are illustrated in Figure 3.1.

Figure 3.1 Compact three-point 1D-IRBF stencil for interior nodes.

The integral approach starts with the decomposition of second-order derivatives of a variable, u, into RBFs

$$\frac{d^2 u(\eta)}{d\eta^2} = \sum_{i=1}^{m} w_i G_i(\eta), \tag{3.1}$$

where m is taken to be 3 for local stencils; $\{G_i(\eta)\}_{i=1}^{m}$ is the set of RBFs; and $\{w_i\}_{i=1}^{m}$ is the set of weights/coefficients to be found. Approximate representations for the first-order derivatives and the functions itself are then obtained through the integration processes

$$\frac{du(\eta)}{d\eta} = \sum_{i=1}^{m} w_i I_{1i}(\eta) + c_1, \tag{3.2}$$

$$u(\eta) = \sum_{i=1}^{m} w_i I_{2i}(\eta) + c_1 \eta + c_2, \tag{3.3}$$

where $I_{1i}(\eta) = \int G_i(\eta)d\eta$; $I_{2i}(\eta) = \int I_{1i}(\eta)d\eta$; and, c_1 and c_2 are the constants of integration.

3.2.1 First-order derivatives at interior nodes

For the coupled compact approximation of the first-order derivatives at interior nodes, nodal derivative values (i.e. extra information) are chosen as not only $\left\{ \frac{du_1}{d\eta}; \frac{du_3}{d\eta} \right\}$ but also $\left\{ \frac{d^2u_1}{d\eta^2}; \frac{d^2u_3}{d\eta^2} \right\}$. At a particular interior node, the approximation is processed through three steps: (i) we first approximate its first-order derivative over its associated three-point stencil involving $\left\{ \frac{du_1}{d\eta}; \frac{du_3}{d\eta} \right\}$; (ii) we then approximate its first-order derivative over the same stencil used in step (i) involving $\left\{ \frac{d^2u_1}{d\eta^2}; \frac{d^2u_3}{d\eta^2} \right\}$; (iii) an identity equation of the first-order derivative is employed to enhance the level of compactness of the stencil. Both $\left\{ \frac{du_1}{d\eta}; \frac{du_3}{d\eta} \right\}$ and $\left\{ \frac{d^2u_1}{d\eta^2}; \frac{d^2u_3}{d\eta^2} \right\}$ are incorporated into the first-order derivative approximation.

First-order derivatives at interior nodes involving $\left\{ \frac{du_1}{d\eta}; \frac{du_3}{d\eta} \right\}$

We construct a conversion system over a three-point stencil associated with an interior node involving $\left\{ \frac{du_1}{d\eta}; \frac{du_3}{d\eta} \right\}$ in the form

$$
\begin{bmatrix} u_1 \\ u_2 \\ u_3 \\ \frac{du_1}{d\eta} \\ \frac{du_3}{d\eta} \end{bmatrix} = \underbrace{\begin{bmatrix} \mathbf{I}_2 \\ \mathbf{I}_1 \end{bmatrix}}_{\mathbf{C}_{1\mathrm{F}}} \begin{bmatrix} w_1 \\ w_2 \\ w_3 \\ c_1 \\ c_2 \end{bmatrix}, \tag{3.4}
$$

where $\frac{du_i}{d\eta} = \frac{du}{d\eta}(\eta_i)$ with $i \in \{1, 2, 3\}$; $\mathbf{C}_{1\mathrm{F}}$ is the conversion matrix, where the subscript 1 and F stand for the 1st derivatives to be approximated and the extra information of the nodal first-order derivative values chosen, respectively; and, $\mathbf{I}_2$

and $\mathbf{I}_1$ are defined as

$$\mathbf{I}_2 = \begin{bmatrix} I_{21}(\eta_1) & I_{22}(\eta_1) & I_{23}(\eta_1) & \eta_1 & 1 \\ I_{21}(\eta_2) & I_{22}(\eta_2) & I_{23}(\eta_2) & \eta_2 & 1 \\ I_{21}(\eta_3) & I_{22}(\eta_3) & I_{23}(\eta_3) & \eta_3 & 1 \end{bmatrix}, \tag{3.5}$$

$$\mathbf{I}_1 = \begin{bmatrix} I_{11}(\eta_1) & I_{12}(\eta_1) & I_{13}(\eta_1) & 1 & 0 \\ I_{11}(\eta_3) & I_{12}(\eta_3) & I_{13}(\eta_3) & 1 & 0 \end{bmatrix}. \tag{3.6}$$

Solving (3.4) yields

$$\begin{bmatrix} w_1 \\ w_2 \\ w_3 \\ c_1 \\ c_2 \end{bmatrix} = \mathbf{C}_{1F}^{-1} \begin{bmatrix} u_1 \\ u_2 \\ u_3 \\ \frac{du_1}{d\eta} \\ \frac{du_3}{d\eta} \end{bmatrix}, \tag{3.7}$$

which maps the vector of nodal values of the function and first-order derivative to the vector of RBF coefficients including the two integration constants. Approximate expressions for the first-order derivative in the physical space are obtained by substituting (3.7) into (3.2)

$$\frac{du(\eta)}{d\eta} = \begin{bmatrix} I_{11}(\eta) & I_{12}(\eta) & I_{13}(\eta) & 1 & 0 \end{bmatrix} \mathbf{C}_{1F}^{-1} \begin{bmatrix} \mathbf{u} \\ \frac{du_1}{d\eta} \\ \frac{du_3}{d\eta} \end{bmatrix}, \tag{3.8}$$

where $\eta_1 \leq \eta \leq \eta_3$ and $\mathbf{u} = [u_1, u_2, u_3]^T$. (3.8) can be rewritten as

$$\frac{du(\eta)}{d\eta} = \sum_{i=1}^{3} \frac{d\phi_{1Fi}(\eta)}{d\eta} u_i + \frac{d\phi_{1F4}(\eta)}{d\eta} \frac{du_1}{d\eta} + \frac{d\phi_{1F5}(\eta)}{d\eta} \frac{du_3}{d\eta}, \tag{3.9}$$

where $\{\phi_{1Fi}(\eta)\}_{i=1}^{5}$ is the set of IRBFs in the physical space. Collocating (3.9) at $\eta = \eta_2$ results in

$$\frac{du(\eta_2)}{d\eta} = \sum_{i=1}^{3} \frac{d\phi_{1Fi}(\eta_2)}{d\eta} u_i + \frac{d\phi_{1F4}(\eta_2)}{d\eta} \frac{du_1}{d\eta} + \frac{d\phi_{1F5}(\eta_2)}{d\eta} \frac{du_3}{d\eta}. \tag{3.10}$$

For brevity, we rewrite expression (3.10) as

$$u_2' = \sum_{i=1}^{3} \mu_{1\mathrm{Fi}} u_i + \mu_{1\mathrm{F4}} u_1' + \mu_{1\mathrm{F5}} u_3', \tag{3.11}$$

where $\{\mu_{1\mathrm{Fi}}\}_{i=1}^{5} = \left\{ \frac{d\phi_{1\mathrm{Fi}}(\eta_2)}{d\eta} \right\}_{i=1}^{5}$; $u_1' = \frac{du_1}{d\eta}$; $u_2' = \frac{du(\eta_2)}{d\eta}$; and, $u_3' = \frac{du_3}{d\eta}$. At the current time level n, (3.11) is taken as

$$u_2'^{\,n} = \sum_{i=1}^{3} \mu_{1\mathrm{Fi}} u_i{}^{n} + \mu_{1\mathrm{F4}} u_1'^{\,n} + \mu_{1\mathrm{F5}} u_3'^{\,n}, \tag{3.12}$$

where the nodal values of the first-order derivatives on the right hand side are treated as unknowns. Rearranging (3.12) in the matrix-vector form

$$\begin{bmatrix} -\mu_{1\mathrm{F4}} & 1 & -\mu_{1\mathrm{F5}} \end{bmatrix} \mathbf{u}'^{n} + \begin{bmatrix} 0 & 0 & 0 \end{bmatrix} \mathbf{u}''^{n} = \begin{bmatrix} \mu_{1\mathrm{F1}} & \mu_{1\mathrm{F2}} & \mu_{1\mathrm{F3}} \end{bmatrix} \mathbf{u}^{n}, \tag{3.13}$$

where $\mathbf{u}'^{n} = [u_1'^{\,n}, u_2'^{\,n}, u_3'^{\,n}]^{T}$; $\mathbf{u}''^{n} = [u_1''^{n}, u_2''^{n}, u_3''^{n}]^{T}$; and, $\mathbf{u}^{n} = [u_1{}^{n}, u_2{}^{n}, u_3{}^{n}]^{T}$. It is noted that $\mathbf{u}''^{n}$ is introduced here to produce a general form for the coupling task which is mentioned later on.

First-order derivatives at interior nodes involving $\left\{ \frac{d^2 u_1}{d\eta^2}; \frac{d^2 u_3}{d\eta^2} \right\}$

We construct a conversion system over a three-point stencil associated with an interior node involving $\left\{ \frac{d^2 u_1}{d\eta^2}; \frac{d^2 u_3}{d\eta^2} \right\}$ in the form

$$\begin{bmatrix} u_1 \\ u_2 \\ u_3 \\ \frac{d^2 u_1}{d\eta^2} \\ \frac{d^2 u_3}{d\eta^2} \end{bmatrix} = \underbrace{\begin{bmatrix} \mathbf{I}_2 \\ \mathbf{G} \end{bmatrix}}_{\mathbf{C}_{1\mathrm{S}}} \begin{bmatrix} w_1 \\ w_2 \\ w_3 \\ c_1 \\ c_2 \end{bmatrix}, \tag{3.14}$$

where $\frac{d^2 u_i}{d\eta^2} = \frac{d^2 u}{d\eta^2}(\eta_i)$ with $i \in \{1, 2, 3\}$; $\mathbf{C}_{1\mathrm{S}}$ is the conversion matrix, where the subscript 1 and S stand for the 1st derivatives to be approximated and the extra information of the nodal second-order derivative values chosen, respectively; $\mathbf{I}_2$ is

defined as before, i.e. (3.5); and, $\mathbf{G}$ is defined as

$$\mathbf{G} = \begin{bmatrix} G_1(\eta_1) & G_2(\eta_1) & G_3(\eta_1) & 0 & 0 \\ G_1(\eta_3) & G_2(\eta_3) & G_3(\eta_3) & 0 & 0 \end{bmatrix}. \tag{3.15}$$

Solving (3.14) yields

$$\begin{bmatrix} w_1 \\ w_2 \\ w_3 \\ c_1 \\ c_2 \end{bmatrix} = \mathbf{C}_{1S}^{-1} \begin{bmatrix} u_1 \\ u_2 \\ u_3 \\ \frac{d^2 u_1}{d\eta^2} \\ \frac{d^2 u_3}{d\eta^2} \end{bmatrix}, \tag{3.16}$$

which maps the vector of nodal values of the function and second-order derivative to the vector of RBF coefficients including the two integration constants. Approximate expressions for the first-order derivative in the physical space are obtained by substituting (3.16) into (3.2)

$$\frac{du(\eta)}{d\eta} = \begin{bmatrix} I_{11}(\eta) & I_{12}(\eta) & I_{13}(\eta) & 1 & 0 \end{bmatrix} \mathbf{C}_{1S}^{-1} \begin{bmatrix} \mathbf{u} \\ \frac{d^2 u_1}{d\eta^2} \\ \frac{d^2 u_3}{d\eta^2} \end{bmatrix}, \tag{3.17}$$

where $\eta_1 \le \eta \le \eta_3$ and $\mathbf{u} = [u_1, u_2, u_3]^T$. (3.17) can be rewritten as

$$\frac{du(\eta)}{d\eta} = \sum_{i=1}^{3} \frac{d\phi_{1Si}(\eta)}{d\eta} u_i + \frac{d\phi_{1S4}(\eta)}{d\eta} \frac{d^2 u_1}{d\eta^2} + \frac{d\phi_{1S5}(\eta)}{d\eta} \frac{d^2 u_3}{d\eta^2}, \tag{3.18}$$

where $\{\phi_{1Si}(\eta)\}_{i=1}^{5}$ is the set of IRBFs in the physical space. Collocating (3.18) at $\eta = \eta_2$ results in

$$\frac{du(\eta_2)}{d\eta} = \sum_{i=1}^{3} \frac{d\phi_{1Si}(\eta_2)}{d\eta} u_i + \frac{d\phi_{1S4}(\eta_2)}{d\eta} \frac{d^2 u_1}{d\eta^2} + \frac{d\phi_{1S5}(\eta_2)}{d\eta} \frac{d^2 u_3}{d\eta^2}. \tag{3.19}$$

For brevity, we rewrite expression (3.19) as

$$u_2' = \sum_{i=1}^{3} \mu_{1Si} u_i + \mu_{1S4} u_1'' + \mu_{1S5} u_3'', \tag{3.20}$$

where $\{\mu_{1\text{Si}}\}_{i=1}^5 = \left\{ \frac{d\phi_{1\text{Si}}(\eta_2)}{d\eta} \right\}_{i=1}^5$; $u_2' = \frac{du(\eta_2)}{d\eta}$; $u_1'' = \frac{d^2 u_1}{d\eta^2}$; and, $u_3'' = \frac{d^2 u_3}{d\eta^2}$. At the current time level n, (3.20) is taken as

$$u_2'^{\,n} = \sum_{i=1}^3 \mu_{1\text{Si}} u_i^{\,n} + \mu_{1\text{S4}} u_1''^{\,n} + \mu_{1\text{S5}} u_3''^{\,n}, \qquad (3.21)$$

where the nodal values of the second-order derivatives on the right hand side are treated as unknowns. Rearranging (3.21) in the matrix-vector form

$$\begin{bmatrix} 0 & 1 & 0 \end{bmatrix} \mathbf{u}'^n + \begin{bmatrix} -\mu_{1\text{S4}} & 0 & -\mu_{1\text{S5}} \end{bmatrix} \mathbf{u}''^n = \begin{bmatrix} \mu_{1\text{S1}} & \mu_{1\text{S2}} & \mu_{1\text{S3}} \end{bmatrix} \mathbf{u}^n, \quad (3.22)$$

where $\mathbf{u}'^n = [u_1'^{\,n}, u_2'^{\,n}, u_3'^{\,n}]^T$; $\mathbf{u}''^n = [u_1''^{\,n}, u_2''^{\,n}, u_3''^{\,n}]^T$; and, $\mathbf{u}^n = [u_1^{\,n}, u_2^{\,n}, u_3^{\,n}]^T$.

First-order derivative couplings at interior nodes

For the first-order derivative coupling at each interior node, e.g. $\eta = \eta_2$, we set the right hand side of (3.11) to be equal to that of (3.20) to couple the nodal first-order derivative information, i.e. $\left\{ \frac{du_1}{d\eta}; \frac{du_3}{d\eta} \right\}$, and the nodal second-order derivative information, i.e. $\left\{ \frac{d^2 u_1}{d\eta^2}; \frac{d^2 u_3}{d\eta^2} \right\}$, as follow

$$\sum_{i=1}^3 \mu_{1\text{Fi}} u_i^{\,n} + \mu_{1\text{F4}} u_1'^{\,n} + \mu_{1\text{F5}} u_3'^{\,n} = \sum_{i=1}^3 \mu_{1\text{Si}} u_i^{\,n} + \mu_{1\text{S4}} u_1''^{\,n} + \mu_{1\text{S5}} u_3''^{\,n}, \qquad (3.23)$$

or in the matrix-vector form

$$\begin{bmatrix} \mu_{1\text{F4}} & 0 & \mu_{1\text{F5}} \end{bmatrix} \mathbf{u}'^n + \begin{bmatrix} -\mu_{1\text{S4}} & 0 & -\mu_{1\text{S5}} \end{bmatrix} \mathbf{u}''^n$$
$$= \begin{bmatrix} (\mu_{1\text{S1}} - \mu_{1\text{F1}}) & (\mu_{1\text{S2}} - \mu_{1\text{F2}}) & (\mu_{1\text{S3}} - \mu_{1\text{F3}}) \end{bmatrix} \mathbf{u}^n, \quad (3.24)$$

where $\mathbf{u}'^n = [u_1'^{\,n}, u_2'^{\,n}, u_3'^{\,n}]^T$; $\mathbf{u}''^n = [u_1''^{\,n}, u_2''^{\,n}, u_3''^{\,n}]^T$; and, $\mathbf{u}^n = [u_1^{\,n}, u_2^{\,n}, u_3^{\,n}]^T$.

3.2.2 First-order derivatives at boundary nodes

At the boundary nodes, the first-order derivatives are approximated in special compact stencils. Consider a boundary node, e.g. η_1. Its associated stencil is $\{\eta_1, \eta_2, \eta_3, \eta_4\}$ as shown in Figure 3.2. For the coupled compact approximation

of the first-order derivative at the boundary node η_1, nodal derivative values (i.e. extra information) are chosen as both $\frac{du_2}{d\eta}$ and $\frac{d^2u_2}{d\eta^2}$. The approximation is processed through three steps: (i) we first approximate its first-order derivative over its associated four-point stencil involving $\frac{du_2}{d\eta}$; (ii) we then approximate its first-order derivative over the same stencil used in step (i) involving $\frac{d^2u_2}{d\eta^2}$; (iii) an identity equation of the first-order derivative is introduced to incorporate both $\frac{du_2}{d\eta}$ and $\frac{d^2u_2}{d\eta^2}$ into the first-order derivative approximation.

Figure 3.2 Special compact four-point 1D-IRBF stencil for boundary nodes.

First-order derivatives at boundary node η_1 involving $\frac{du_2}{d\eta}$

We construct a conversion system over the special four-point stencil associated with the boundary node η_1 involving $\frac{du_2}{d\eta}$ in the form

$$
\begin{bmatrix} u_1 \\ u_2 \\ u_3 \\ u_4 \\ \frac{du_2}{d\eta} \end{bmatrix} = \underbrace{\begin{bmatrix} \mathbf{I}_{2\text{sp}} \\ \mathbf{I}_{1\text{sp}} \end{bmatrix}}_{\mathbf{C}_{\text{sp1F}}} \begin{bmatrix} w_1 \\ w_2 \\ w_3 \\ w_4 \\ c_1 \\ c_2 \end{bmatrix}, \tag{3.25}
$$

where $\mathbf{C}_{\text{sp1F}}$ is the conversion matrix and $\mathbf{I}_{2\text{sp}}$, $\mathbf{I}_{1\text{sp}}$ are defined as

$$
\mathbf{I}_{2\text{sp}} = \begin{bmatrix} I_{21}(\eta_1) & I_{22}(\eta_1) & I_{23}(\eta_1) & I_{24}(\eta_1) & \eta_1 & 1 \\ I_{21}(\eta_2) & I_{22}(\eta_2) & I_{23}(\eta_2) & I_{24}(\eta_2) & \eta_2 & 1 \\ I_{21}(\eta_3) & I_{22}(\eta_3) & I_{23}(\eta_3) & I_{24}(\eta_3) & \eta_3 & 1 \\ I_{21}(\eta_4) & I_{22}(\eta_4) & I_{23}(\eta_4) & I_{24}(\eta_4) & \eta_4 & 1 \end{bmatrix}, \tag{3.26}
$$

$$
\mathbf{I}_{1\text{sp}} = \begin{bmatrix} I_{11}(\eta_2) & I_{12}(\eta_2) & I_{13}(\eta_2) & I_{14}(\eta_2) & 1 & 0 \end{bmatrix}. \tag{3.27}
$$

Solving (3.25) yields

$$
\begin{bmatrix} w_1 \\ w_2 \\ w_3 \\ w_4 \\ c_1 \\ c_2 \end{bmatrix} = \mathbf{C}_{\text{sp1F}}^{-1} \begin{bmatrix} u_1 \\ u_2 \\ u_3 \\ u_4 \\ \frac{du_2}{d\eta} \end{bmatrix}. \tag{3.28}
$$

The boundary value of the first-order derivative is thus obtained by substituting (3.28) into (3.2) and taking $\eta = \eta_1$

$$
\frac{du(\eta_1)}{d\eta} = \begin{bmatrix} I_{11}(\eta_1) & I_{12}(\eta_1) & I_{13}(\eta_1) & I_{14}(\eta_1) & 1 & 0 \end{bmatrix} \mathbf{C}_{\text{sp1F}}^{-1} \begin{bmatrix} \mathbf{u} \\ \frac{du_2}{d\eta} \end{bmatrix}, \tag{3.29}
$$

where $\mathbf{u} = [u_1, u_2, u_3, u_4]^T$. (3.29) can be rewritten as

$$
\frac{du(\eta_1)}{d\eta} = \sum_{i=1}^{4} \frac{d\phi_{\text{sp1Fi}}(\eta_1)}{d\eta} u_i + \frac{d\phi_{\text{sp1F5}}(\eta_1)}{d\eta} \frac{du_2}{d\eta}. \tag{3.30}
$$

For brevity, we rewrite expression (3.30) as

$$
u_1' = \sum_{i=1}^{4} \mu_{\text{sp1Fi}} u_i + \mu_{\text{sp1F5}} u_2', \tag{3.31}
$$

where $\{\mu_{\text{sp1Fi}}\}_{i=1}^{5} = \left\{ \frac{d\phi_{\text{sp1Fi}}(\eta_1)}{d\eta} \right\}_{i=1}^{5}$; $u_1' = \frac{du(\eta_1)}{d\eta}$; and, $u_2' = \frac{du_2}{d\eta}$. At the current time level n, (3.31) is taken as

$$
{u_1'}^{n} = \sum_{i=1}^{4} \mu_{\text{sp1Fi}} {u_i}^{n} + \mu_{\text{sp1F5}} {u_2'}^{n}, \tag{3.32}
$$

where the nodal value of the first-order derivative on the right hand side is treated as unknowns. Rearranging (3.32) in the matrix-vector form

$$
\begin{bmatrix} 1 & -\mu_{\text{sp1F5}} & 0 & 0 \end{bmatrix} \mathbf{u}'^{n} + \begin{bmatrix} 0 & 0 & 0 & 0 \end{bmatrix} \mathbf{u}''^{n}
$$
$$
= \begin{bmatrix} \mu_{\text{sp1F1}} & \mu_{\text{sp1F2}} & \mu_{\text{sp1F3}} & \mu_{\text{sp1F4}} \end{bmatrix} \mathbf{u}^{n}, \tag{3.33}
$$

where $\mathbf{u}'^{n} = [{u_1'}^{n}, {u_2'}^{n}, {u_3'}^{n}, {u_4'}^{n}]^T$; $\mathbf{u}''^{n} = [{u_1''}^{n}, {u_2''}^{n}, {u_3''}^{n}, {u_4''}^{n}]^T$; and, $\mathbf{u}^{n} = [{u_1}^{n}, {u_2}^{n}, {u_3}^{n}, {u_4}^{n}]^T$.

First-order derivatives at boundary node η_1 involving $\frac{d^2 u_2}{d\eta^2}$

We construct a conversion system over the special four-point stencil associated with the boundary node η_1 involving $\frac{d^2 u_2}{d\eta^2}$ in the form

$$
\begin{bmatrix} u_1 \\ u_2 \\ u_3 \\ u_4 \\ \frac{d^2 u_2}{d\eta^2} \end{bmatrix} = \underbrace{\begin{bmatrix} \mathbf{I}_{2\mathrm{sp}} \\ \mathbf{G}_{\mathrm{sp}} \end{bmatrix}}_{\mathbf{C}_{\mathrm{sp1S}}} \begin{bmatrix} w_1 \\ w_2 \\ w_3 \\ w_4 \\ c_1 \\ c_2 \end{bmatrix},
\tag{3.34}
$$

where $\mathbf{C}_{\mathrm{sp1S}}$ is the conversion matrix; $\mathbf{I}_{2\mathrm{sp}}$ is defined as before, i.e. (3.26); and, $\mathbf{G}_{\mathrm{sp}}$ is defined as

$$
\mathbf{G}_{\mathrm{sp}} = \begin{bmatrix} G_1(\eta_2) & G_2(\eta_2) & G_3(\eta_2) & G_4(\eta_2) & 0 & 0 \end{bmatrix}.
\tag{3.35}
$$

Solving (3.34) yields

$$
\begin{bmatrix} w_1 \\ w_2 \\ w_3 \\ w_4 \\ c_1 \\ c_2 \end{bmatrix} = \mathbf{C}_{\mathrm{sp1S}}^{-1} \begin{bmatrix} u_1 \\ u_2 \\ u_3 \\ u_4 \\ \frac{d^2 u_2}{d\eta^2} \end{bmatrix}.
\tag{3.36}
$$

The boundary value of the first-order derivative is thus obtained by substituting (3.36) into (3.2) and taking $\eta = \eta_1$

$$
\frac{du(\eta_1)}{d\eta} = \begin{bmatrix} I_{11}(\eta_1) & I_{12}(\eta_1) & I_{13}(\eta_1) & I_{14}(\eta_1) & 1 & 0 \end{bmatrix} \mathbf{C}_{\mathrm{sp1S}}^{-1} \begin{bmatrix} \mathbf{u} \\ \frac{d^2 u_2}{d\eta^2} \end{bmatrix},
\tag{3.37}
$$

where $\mathbf{u} = [u_1, u_2, u_3, u_4]^T$. (3.37) can be rewritten as

$$
\frac{du(\eta_1)}{d\eta} = \sum_{i=1}^{4} \frac{d\phi_{\mathrm{sp1Si}}(\eta_1)}{d\eta} u_i + \frac{d\phi_{\mathrm{sp1S5}}(\eta_1)}{d\eta} \frac{d^2 u_2}{d\eta^2}.
\tag{3.38}
$$

For brevity, we rewrite expression (3.38) as

$$u_1' = \sum_{i=1}^{4} \mu_{\text{sp1Si}} u_i + \mu_{\text{sp1S5}} u_2'', \qquad (3.39)$$

where $\{\mu_{\text{sp1Si}}\}_{i=1}^{5} = \left\{ \frac{d\phi_{\text{sp1Si}}(\eta_1)}{d\eta} \right\}_{i=1}^{5}$; $u_1' = \frac{du(\eta_1)}{d\eta}$; and, $u_2'' = \frac{d^2 u_2}{d\eta^2}$. At the current time level n, (3.39) is taken as

$$u_1'^{\,n} = \sum_{i=1}^{4} \mu_{\text{sp1Si}} u_i^{\,n} + \mu_{\text{sp1S5}} u_2''^{\,n}, \qquad (3.40)$$

where the nodal value of the second-order derivative on the right hand side is treated as unknowns. Rearranging (3.40) in the matrix-vector form

$$\begin{bmatrix} 1 & 0 & 0 & 0 \end{bmatrix} \mathbf{u}'^n + \begin{bmatrix} 0 & -\mu_{\text{sp1S5}} & 0 & 0 \end{bmatrix} \mathbf{u}''^n$$
$$= \begin{bmatrix} \mu_{\text{sp1S1}} & \mu_{\text{sp1S2}} & \mu_{\text{sp1S3}} & \mu_{\text{sp1S4}} \end{bmatrix} \mathbf{u}^n, \quad (3.41)$$

where $\mathbf{u}'^n = [u_1'^{\,n}, u_2'^{\,n}, u_3'^{\,n}, u_4'^{\,n}]^T$; $\mathbf{u}''^n = [u_1''^{\,n}, u_2''^{\,n}, u_3''^{\,n}, u_4''^{\,n}]^T$; and, $\mathbf{u}^n = [u_1^{\,n}, u_2^{\,n}, u_3^{\,n}, u_4^{\,n}]^T$.

First-order derivative coupling at boundary node η_1

For the first-order derivative coupling at each boundary node, e.g. $\eta = \eta_1$, we set the right hand side of (3.31) to be equal to that of (3.39) to couple the nodal first-order derivative information, i.e. $\frac{du_2}{d\eta}$, and the nodal second-order derivative information, i.e. $\frac{d^2 u_2}{d\eta^2}$, as follows.

$$\sum_{i=1}^{4} \mu_{\text{sp1Fi}} u_i^{\,n} + \mu_{\text{sp1F5}} u_2'^{\,n} = \sum_{i=1}^{4} \mu_{\text{sp1Si}} u_i^{\,n} + \mu_{\text{sp1S5}} u_2''^{\,n}, \qquad (3.42)$$

or in the matrix-vector form

$$\begin{bmatrix} 0 & \mu_{\text{sp1F5}} & 0 & 0 \end{bmatrix} \mathbf{u}'^n + \begin{bmatrix} 0 & -\mu_{\text{sp1S5}} & 0 & 0 \end{bmatrix} \mathbf{u}''^n$$
$$= \begin{bmatrix} (\mu_{\text{sp1S1}} - \mu_{\text{sp1F1}}) & (\mu_{\text{sp1S2}} - \mu_{\text{sp1F2}}) & (\mu_{\text{sp1S3}} - \mu_{\text{sp1F3}}) & (\mu_{\text{sp1S4}} - \mu_{\text{sp1F4}}) \end{bmatrix} \mathbf{u}^n,$$
$$(3.43)$$

where $\mathbf{u}'^n = [u_1'^n, u_2'^n, u_3'^n, u_4'^n]^T$; $\mathbf{u}''^n = [u_1''^n, u_2''^n, u_3''^n, u_4''^n]^T$; and, $\mathbf{u}^n = [u_1{}^n, u_2{}^n, u_3{}^n, u_4{}^n]^T$.

In a similar manner, one is able to calculate the first-order derivative at the boundary node η_{n_η}.

3.2.3   Second-order derivatives at interior nodes

For the coupled compact approximation of the second-order derivatives at interior nodes, nodal derivative values (i.e. extra information) are chosen to be the same as those used for the approximation of the first-order derivatives, i.e. $\left\{ \frac{du_1}{d\eta}; \frac{du_3}{d\eta} \right\}$ and $\left\{ \frac{d^2 u_1}{d\eta^2}; \frac{d^2 u_3}{d\eta^2} \right\}$. At a particular interior node, the approximation of its second-order derivative is processed through three steps: (i) we first approximate its second-order derivative over its associated three-point stencil involving $\left\{ \frac{du_1}{d\eta}; \frac{du_3}{d\eta} \right\}$; (ii) we then approximate its second-order derivative over the same stencil used in step (i) involving $\left\{ \frac{d^2 u_1}{d\eta^2}; \frac{d^2 u_3}{d\eta^2} \right\}$; (iii) an identity equation of the second-order derivative is employed to enhance the level of compactness of the stencil. Both $\left\{ \frac{du_1}{d\eta}; \frac{du_3}{d\eta} \right\}$ and $\left\{ \frac{d^2 u_1}{d\eta^2}; \frac{d^2 u_3}{d\eta^2} \right\}$ are incorporated into the second-order derivative approximation.

Second-order derivatives at interior nodes involving $\left\{ \frac{du_1}{d\eta}; \frac{du_3}{d\eta} \right\}$

Because we employ the same extra information used in the approximation of the first-order derivatives involving $\left\{ \frac{du_1}{d\eta}; \frac{du_3}{d\eta} \right\}$, approximate expressions for the second-order derivative in the physical space are obtained by simply substituting (3.7) into (3.1)

$$\frac{d^2 u(\eta)}{d\eta^2} = \begin{bmatrix} G_1(\eta) & G_2(\eta) & G_3(\eta) & 0 & 0 \end{bmatrix} \mathbf{C}_{1F}^{-1} \begin{bmatrix} \mathbf{u} \\ \frac{du_1}{d\eta} \\ \frac{du_3}{d\eta} \end{bmatrix}, \qquad (3.44)$$

where $\eta \in \{\eta_1, \eta_2, \eta_3\}$ and $\mathbf{u} = [u_1, u_2, u_3]^T$. (3.44) can be rewritten as

$$\frac{d^2 u(\eta)}{d\eta^2} = \sum_{i=1}^{3} \frac{d^2 \phi_{2Fi}(\eta)}{d\eta^2} u_i + \frac{d^2 \phi_{2F4}(\eta)}{d\eta^2} \frac{du_1}{d\eta} + \frac{d^2 \phi_{2F5}(\eta)}{d\eta^2} \frac{du_3}{d\eta}, \qquad (3.45)$$

where $\{\phi_{2\text{Fi}}(\eta)\}_{i=1}^5$ is the set of IRBFs in the physical space, in which 2 and F stand for the 2nd derivatives to be approximated and the extra information of the first-order derivatives, respectively. Collocating (3.45) at $\eta = \eta_2$ results in

$$\frac{d^2u(\eta_2)}{d\eta^2} = \sum_{i=1}^{3} \frac{d^2\phi_{2\text{Fi}}(\eta_2)}{d\eta^2}u_i + \frac{d^2\phi_{2\text{F4}}(\eta_2)}{d\eta^2}\frac{du_1}{d\eta} + \frac{d^2\phi_{2\text{F5}}(\eta_2)}{d\eta^2}\frac{du_3}{d\eta}. \qquad (3.46)$$

For brevity, we rewrite expression (3.46) as

$$u_2'' = \sum_{i=1}^{3} \nu_{2\text{Fi}}u_i + \nu_{2\text{F4}}u_1' + \nu_{2\text{F5}}u_3', \qquad (3.47)$$

where $\{\nu_{2\text{Fi}}\}_{i=1}^5 = \left\{\frac{d^2\phi_{2\text{Fi}}(\eta_2)}{d\eta^2}\right\}_{i=1}^5$; $u_1' = \frac{du_1}{d\eta}$; $u_3' = \frac{du_3}{d\eta}$; and, $u_2'' = \frac{d^2u(\eta_2)}{d\eta^2}$. At the current time level n, (3.47) is taken as

$$u_2''^n = \sum_{i=1}^{3} \nu_{2\text{Fi}}u_i{}^n + \nu_{2\text{F4}}u_1'{}^n + \nu_{2\text{F5}}u_3'{}^n, \qquad (3.48)$$

where the nodal values of the first-order derivatives on the right hand side are treated as unknowns. Rearranging (3.48) in the matrix-vector form

$$\begin{bmatrix} -\nu_{2\text{F4}} & 0 & -\nu_{2\text{F5}} \end{bmatrix}\mathbf{u}'^n + \begin{bmatrix} 0 & 1 & 0 \end{bmatrix}\mathbf{u}''^n = \begin{bmatrix} \nu_{2\text{F1}} & \nu_{2\text{F2}} & \nu_{2\text{F3}} \end{bmatrix}\mathbf{u}^n, \qquad (3.49)$$

where $\mathbf{u}'^n = [u_1'{}^n, u_2'{}^n, u_3'{}^n]^T$; $\mathbf{u}''^n = [u_1''^n, u_2''^n, u_3''^n]^T$; and, $\mathbf{u}^n = [u_1{}^n, u_2{}^n, u_3{}^n]^T$.

Second-order derivatives at interior nodes involving $\left\{\frac{d^2u_1}{d\eta^2}; \frac{d^2u_3}{d\eta^2}\right\}$

Because we employ the same extra information used in the approximation of the first-order derivatives involving $\left\{\frac{d^2u_1}{d\eta^2}; \frac{d^2u_3}{d\eta^2}\right\}$, approximate expressions for the second-order derivative in the physical space are obtained by simply substituting (3.16) into (3.1)

$$\frac{d^2u(\eta)}{d\eta^2} = \begin{bmatrix} G_1(\eta) & G_2(\eta) & G_3(\eta) & 0 & 0 \end{bmatrix}\mathbf{C}_{1\text{S}}^{-1}\begin{bmatrix} \mathbf{u} \\ \frac{d^2u_1}{d\eta^2} \\ \frac{d^2u_3}{d\eta^2} \end{bmatrix}, \qquad (3.50)$$

where $\eta_1 \leq \eta \leq \eta_3$ and $\mathbf{u} = [u_1, u_2, u_3]^T$. (3.50) can be rewritten as

$$\frac{d^2 u(\eta)}{d\eta^2} = \sum_{i=1}^{3} \frac{d^2 \phi_{2\mathrm{S}i}(\eta)}{d\eta^2} u_i + \frac{d^2 \phi_{2\mathrm{S}4}(\eta)}{d\eta^2} \frac{d^2 u_1}{d\eta^2} + \frac{d^2 \phi_{2\mathrm{S}5}(\eta)}{d\eta^2} \frac{d^2 u_3}{d\eta^2}, \qquad (3.51)$$

where $\{\phi_{2\mathrm{S}i}(\eta)\}_{i=1}^{5}$ is the set of IRBFs in the physical space, in which 2 and S stand for the 2nd derivatives to be approximated and the extra information of the second-order derivatives, respectively. Collocating (3.51) at $\eta = \eta_2$ results in

$$\frac{d^2 u(\eta_2)}{d\eta^2} = \sum_{i=1}^{3} \frac{d^2 \phi_{2\mathrm{S}i}(\eta_2)}{d\eta^2} u_i + \frac{d^2 \phi_{2\mathrm{S}4}(\eta_2)}{d\eta^2} \frac{d^2 u_1}{d\eta^2} + \frac{d^2 \phi_{2\mathrm{S}5}(\eta_2)}{d\eta^2} \frac{d^2 u_3}{d\eta^2}. \qquad (3.52)$$

For brevity, we rewrite expression (3.52) as

$$u_2'' = \sum_{i=1}^{3} \nu_{2\mathrm{S}i} u_i + \nu_{2\mathrm{S}4} u_1'' + \nu_{2\mathrm{S}5} u_3'', \qquad (3.53)$$

where $\{\nu_{2\mathrm{S}i}\}_{i=1}^{5} = \left\{ \frac{d^2 \phi_{2\mathrm{S}i}(\eta_2)}{d\eta^2} \right\}_{i=1}^{5}$; $u_1'' = \frac{d^2 u_1}{d\eta^2}$; $u_2'' = \frac{d^2 u(\eta_2)}{d\eta^2}$; and, $u_3'' = \frac{d^2 u_3}{d\eta^2}$. At the current time level n, (3.53) is taken as

$$u_2''^{n} = \sum_{i=1}^{3} \nu_{2\mathrm{S}i} u_i^{n} + \nu_{2\mathrm{S}4} u_1''^{n} + \nu_{2\mathrm{S}5} u_3''^{n}, \qquad (3.54)$$

where the nodal values of the second-order derivatives on the right hand side are treated as unknowns. Rearranging (3.54) in the matrix-vector form

$$\begin{bmatrix} 0 & 0 & 0 \end{bmatrix} \mathbf{u}'^{n} + \begin{bmatrix} -\nu_{2\mathrm{S}4} & 1 & -\nu_{2\mathrm{S}5} \end{bmatrix} \mathbf{u}''^{n} = \begin{bmatrix} \nu_{2\mathrm{S}1} & \nu_{2\mathrm{S}2} & \nu_{2\mathrm{S}3} \end{bmatrix} \mathbf{u}^{n}, \qquad (3.55)$$

where $\mathbf{u}'^{n} = [u_1'^{n}, u_2'^{n}, u_3'^{n}]^T$; $\mathbf{u}''^{n} = [u_1''^{n}, u_2''^{n}, u_3''^{n}]^T$; and, $\mathbf{u}^{n} = [u_1^{n}, u_2^{n}, u_3^{n}]^T$.

Second-order derivative couplings at interior nodes

For the second-order derivative coupling at each interior node, e.g. $\eta = \eta_2$, we set the right hand side of (3.47) to be equal to that of (3.53) to couple the nodal first-order derivative information, i.e. $\left\{ \frac{du_1}{d\eta}; \frac{du_3}{d\eta} \right\}$, and the nodal second-order

derivative information, i.e. $\left\{ \frac{d^2 u_1}{d\eta^2}; \frac{d^2 u_3}{d\eta^2} \right\}$, as follows.

$$\sum_{i=1}^{3} \nu_{2\mathrm{Fi}} u_i{}^n + \nu_{2\mathrm{F}4} u_1'{}^n + \nu_{2\mathrm{F}5} u_3'{}^n = \sum_{i=1}^{3} \nu_{2\mathrm{Si}} u_i{}^n + \nu_{2\mathrm{S}4} u_1''{}^n + \nu_{2\mathrm{S}5} u_3''{}^n, \qquad (3.56)$$

or in the matrix-vector form

$$\begin{bmatrix} \nu_{2\mathrm{F}4} & 0 & \nu_{2\mathrm{F}5} \end{bmatrix} \mathbf{u}'^n + \begin{bmatrix} -\nu_{2\mathrm{S}4} & 0 & -\nu_{2\mathrm{S}5} \end{bmatrix} \mathbf{u}''^n$$
$$= \begin{bmatrix} (\nu_{2\mathrm{S}1} - \nu_{2\mathrm{F}1}) & (\nu_{2\mathrm{S}2} - \nu_{2\mathrm{F}2}) & (\nu_{2\mathrm{S}3} - \nu_{2\mathrm{F}3}) \end{bmatrix} \mathbf{u}^n, \quad (3.57)$$

where $\mathbf{u}'^n = [u_1'{}^n, u_2'{}^n, u_3'{}^n]^T$; $\mathbf{u}''^n = [u_1''^n, u_2''^n, u_3''^n]^T$; and, $\mathbf{u}^n = [u_1{}^n, u_2{}^n, u_3{}^n]^T$.

3.2.4 Second-order derivatives at boundary nodes

At the boundary nodes, the second-order derivatives are approximated in special compact stencils. Consider the boundary node, e.g. η_1. Its associated stencil is $\{\eta_1, \eta_2, \eta_3, \eta_4\}$ as shown in Figure 3.2. For the coupled compact approximation of the second-order derivative at the boundary node η_1, nodal derivative values (i.e. extra information) are chosen to be the same as those used for the approximation of the first-order derivatives, i.e. $\frac{du_2}{d\eta}$ and $\frac{d^2 u_2}{d\eta^2}$. The approximation of its second-order derivative is processed through three steps: (i) we first approximate its second-order derivative over its associated four-point stencil involving $\frac{du_2}{d\eta}$; (ii) we then approximate its second-order derivative over the same stencil used in step (i) involving $\frac{d^2 u_2}{d\eta^2}$; (iii) an identity equation of the second-order derivative is introduced to incorporate both $\frac{du_2}{d\eta}$ and $\frac{d^2 u_2}{d\eta^2}$ into the second-order derivative approximation.

Second-order derivatives at boundary node η_1 involving $\frac{du_2}{d\eta}$

Because we employ the same extra information used in the approximation of the first-order derivatives involving $\frac{du_2}{d\eta}$, approximate expression for the second-order derivative at η_1 in the physical space is obtained by simply substituting (3.28)

into (3.1) and taking $\eta = \eta_1$

$$\frac{d^2 u(\eta_1)}{d\eta^2} = \begin{bmatrix} G_1(\eta_1) & G_2(\eta_1) & G_3(\eta_1) & G_4(\eta_1) & 0 & 0 \end{bmatrix} \mathbf{C}_{\mathrm{sp1F}}^{-1} \begin{bmatrix} \mathbf{u} \\ \frac{du_2}{d\eta} \end{bmatrix}, \quad (3.58)$$

where $\mathbf{u} = [u_1, u_2, u_3, u_4]^T$. (3.58) can be rewritten as

$$\frac{d^2 u(\eta_1)}{d\eta^2} = \sum_{i=1}^{4} \frac{d^2 \phi_{\mathrm{sp2Fi}}(\eta_1)}{d\eta^2} u_i + \frac{d^2 \phi_{\mathrm{sp2F5}}(\eta_1)}{d\eta^2} \frac{du_2}{d\eta}. \quad (3.59)$$

For brevity, we rewrite expression (3.59) as

$$u_1'' = \sum_{i=1}^{4} \nu_{\mathrm{sp2Fi}} u_i + \nu_{\mathrm{sp2F5}} u_2', \quad (3.60)$$

where $\{\nu_{\mathrm{sp2Fi}}\}_{i=1}^{5} = \left\{ \frac{d^2 \phi_{\mathrm{sp2Fi}}(\eta_1)}{d\eta^2} \right\}_{i=1}^{5}$; $u_2' = \frac{du_2}{d\eta}$; and, $u_1'' = \frac{d^2 u(\eta_1)}{d\eta^2}$. At the current time level n, (3.60) is taken as

$$u_1''^n = \sum_{i=1}^{4} \nu_{\mathrm{sp2Fi}} u_i^n + \nu_{\mathrm{sp2F5}} u_2'^n, \quad (3.61)$$

where the nodal value of the first-order derivative on the right hand side is treated as unknowns. Rearranging (3.61) in the matrix-vector form

$$\begin{bmatrix} 0 & -\nu_{\mathrm{sp2F5}} & 0 & 0 \end{bmatrix} \mathbf{u}'^n + \begin{bmatrix} 1 & 0 & 0 & 0 \end{bmatrix} \mathbf{u}''^n$$
$$= \begin{bmatrix} \nu_{\mathrm{sp2F1}} & \nu_{\mathrm{sp2F2}} & \nu_{\mathrm{sp2F3}} & \nu_{\mathrm{sp2F4}} \end{bmatrix} \mathbf{u}^n, \quad (3.62)$$

where $\mathbf{u}'^n = [u_1'^n, u_2'^n, u_3'^n, u_4'^n]^T$; $\mathbf{u}''^n = [u_1''^n, u_2''^n, u_3''^n, u_4''^n]^T$; and, $\mathbf{u}^n = [u_1^n, u_2^n, u_3^n, u_4^n]^T$.

Second-order derivatives at boundary node η_1 involving $\frac{d^2 u_2}{d\eta^2}$

Because we employ the same extra information used in the approximation of the first-order derivatives involving $\frac{d^2 u_2}{d\eta^2}$, approximate expression for the second-order derivative at η_1 in the physical space is obtained by simply substituting (3.36)

into (3.1) and taking $\eta = \eta_1$

$$\frac{d^2 u(\eta_1)}{d\eta^2} = \begin{bmatrix} G_1(\eta_1) & G_2(\eta_1) & G_3(\eta_1) & G_4(\eta_1) & 0 & 0 \end{bmatrix} \mathbf{C}_{\text{sp1S}}^{-1} \begin{bmatrix} \mathbf{u} \\ \frac{d^2 u_2}{d\eta^2} \end{bmatrix}, \quad (3.63)$$

where $\mathbf{u} = [u_1, u_2, u_3, u_4]^T$. (3.63) can be rewritten as

$$\frac{d^2 u(\eta_1)}{d\eta^2} = \sum_{i=1}^{4} \frac{d^2 \phi_{\text{sp2Si}}(\eta_1)}{d\eta^2} u_i + \frac{d^2 \phi_{\text{sp2S5}}(\eta_1)}{d\eta^2} \frac{d^2 u_2}{d\eta^2}. \quad (3.64)$$

For brevity, we rewrite expression (3.64) as

$$u_1'' = \sum_{i=1}^{4} \nu_{\text{sp2Si}} u_i + \nu_{\text{sp2S5}} u_2'', \quad (3.65)$$

where $\{\nu_{\text{sp2Si}}\}_{i=1}^{5} = \left\{ \frac{d^2 \phi_{\text{sp2Si}}(\eta_1)}{d\eta^2} \right\}_{i=1}^{5}$; $u_1'' = \frac{d^2 u(\eta_1)}{d\eta^2}$; and, $u_2'' = \frac{d^2 u_2}{d\eta^2}$. At the current time level n, (3.65) is taken as

$$u_1''^n = \sum_{i=1}^{4} \nu_{\text{sp2Si}} u_i{}^n + \nu_{\text{sp2S5}} u_2''^n, \quad (3.66)$$

where the nodal value of the second-order derivative on the right hand side is treated as unknowns. Rearranging (3.66) in the matrix-vector form

$$\begin{bmatrix} 0 & 0 & 0 & 0 \end{bmatrix} \mathbf{u}'^n + \begin{bmatrix} 1 & -\nu_{\text{sp2S5}} & 0 & 0 \end{bmatrix} \mathbf{u}''^n$$
$$= \begin{bmatrix} \nu_{\text{sp2S1}} & \nu_{\text{sp2S2}} & \nu_{\text{sp2S3}} & \nu_{\text{sp2S4}} \end{bmatrix} \mathbf{u}^n, \quad (3.67)$$

where $\mathbf{u}'^n = [u_1'{}^n, u_2'{}^n, u_3'{}^n, u_4'{}^n]^T$; $\mathbf{u}''^n = [u_1''^n, u_2''^n, u_3''^n, u_4''^n]^T$; and, $\mathbf{u}^n = [u_1{}^n, u_2{}^n, u_3{}^n, u_4{}^n]^T$.

Second derivative coupling at boundary node η_1

For the second-order derivative coupling at each boundary node, e.g. $\eta = \eta_1$, we set the right hand side of (3.60) to be equal to that of (3.65) to couple the nodal first-order derivative information, i.e. $\frac{du_2}{d\eta}$, and the nodal second-order derivative

information, i.e. $\frac{d^2 u_2}{d\eta^2}$, as follow

$$\sum_{i=1}^{4} \nu_{\text{sp2Fi}} u_i{}^n + \nu_{\text{sp2F5}} u_2'{}^n = \sum_{i=1}^{4} \nu_{\text{sp2Si}} u_i{}^n + \nu_{\text{sp2S5}} u_2''{}^n, \tag{3.68}$$

or in the matrix-vector form

$$\begin{bmatrix} 0 & \nu_{\text{sp2F5}} & 0 & 0 \end{bmatrix} \mathbf{u}'^n + \begin{bmatrix} 0 & -\nu_{\text{sp2S5}} & 0 & 0 \end{bmatrix} \mathbf{u}''^n$$
$$= \begin{bmatrix} (\nu_{\text{sp2S1}} - \nu_{\text{sp2F1}}) & (\nu_{\text{sp2S2}} - \nu_{\text{sp2F2}}) & (\nu_{\text{sp2S3}} - \nu_{\text{sp2F3}}) & (\nu_{\text{sp2S4}} - \nu_{\text{sp2F4}}) \end{bmatrix} \mathbf{u}^n, \tag{3.69}$$

where $\mathbf{u}'^n = [u_1'{}^n, u_2'{}^n, u_3'{}^n, u_4'{}^n]^T$; $\mathbf{u}''^n = [u_1''{}^n, u_2''{}^n, u_3''{}^n, u_4''{}^n]^T$; and, $\mathbf{u}^n = [u_1{}^n, u_2{}^n, u_3{}^n, u_4{}^n]^T$.

In a similar manner, one is able to calculate the second-order derivative at the boundary node η_{n_η}.

3.2.5 Matrix assembly for first and second-order derivative expressions

The IRBF system on a grid line for the first-order derivative is obtained by letting the interior node taking values from 2 to $(n_\eta - 1)$ in (3.13), (3.22), and (3.24); and, making use of (3.33), (3.41), and (3.43) for the boundary nodes 1 and n_η. In a similar manner, the IRBF system on a grid line for the second-order derivative is obtained by letting the interior node taking values from 2 to $(n_\eta - 1)$ in (3.49), (3.55), and (3.57); and, making use of (3.62), (3.67), and (3.69) for the boundary nodes 1 and n_η. The resultant matrix assembly is expressed as

$$\underbrace{\begin{bmatrix} \mathbf{A}_{1F} & \mathbf{0} \\ \mathbf{A}_{1S} & \mathbf{B}_{1S} \\ \mathbf{A}_{1FS} & \mathbf{B}_{1FS} \\ \mathbf{A}_{2F} & \mathbf{B}_{2F} \\ \mathbf{0} & \mathbf{B}_{2S} \\ \mathbf{A}_{2FS} & \mathbf{B}_{2FS} \end{bmatrix}}_{\text{Coefficient matrix}} \begin{bmatrix} \mathbf{u}'^n \\ \mathbf{u}''^n \end{bmatrix} = \begin{bmatrix} \mathbf{R}_{1F} \\ \mathbf{R}_{1S} \\ \mathbf{R}_{1FS} \\ \mathbf{R}_{2F} \\ \mathbf{R}_{2S} \\ \mathbf{R}_{2FS} \end{bmatrix} \mathbf{u}^n, \tag{3.70}$$

where $\mathbf{A}_{1F}$, $\mathbf{A}_{1S}$, $\mathbf{B}_{1S}$, $\mathbf{A}_{1FS}$, $\mathbf{B}_{1FS}$, $\mathbf{A}_{2F}$, $\mathbf{B}_{2F}$, $\mathbf{B}_{2S}$, $\mathbf{A}_{2FS}$, $\mathbf{B}_{2FS}$, and $\mathbf{0}$ are $n_\eta \times n_\eta$ matrices; $\mathbf{u}'^n = \left\{ u'^{\,n}_1, u'^{\,n}_2, ..., u'^{\,n}_{n_\eta} \right\}^T$; $\mathbf{u}''^n = \left\{ u''^{\,n}_1, u''^{\,n}_2, ..., u''^{\,n}_{n_\eta} \right\}^T$; and, $\mathbf{u}^n = \left\{ u_1^{\,n}, u_2^{\,n}, ..., u_{n_\eta}^{\,n} \right\}^T$. The coefficient matrix is sparse with diagonal, bi-diagonal, and tri-diagonal sub-matrices. Solving (3.70) yields

$$\mathbf{u}'^n = \mathbf{D}_\eta \mathbf{u}^n, \tag{3.71}$$

$$\mathbf{u}''^n = \mathbf{D}_{\eta\eta} \mathbf{u}^n, \tag{3.72}$$

where $\mathbf{D}_\eta$ and $\mathbf{D}_{\eta\eta}$ are $n_\eta \times n_\eta$ matrices.

It is noted that, for brevity, we use the same notations to represent the RBF coefficients for the approximation of first- and second-order derivatives. In fact, for example, the coefficient set $[w_1, w_2, w_3, c_1, c_2]^T$ in (3.4) is not the same as that in (3.14).

3.3   ADI method for convection-diffusion equations

We consider a two-dimensional (2D) unsteady convection-diffusion equation for a variable u

$$\frac{\partial u}{\partial t} + c_x \frac{\partial u}{\partial x} + c_y \frac{\partial u}{\partial y} = d_x \frac{\partial^2 u}{\partial x^2} + d_y \frac{\partial^2 u}{\partial y^2} + f_b, \quad (x, y, t) \in \Omega \times [0, T], \tag{3.73}$$

subject to the initial condition

$$u(x, y, 0) = u_0(x, y), \quad (x, y) \in \Omega, \tag{3.74}$$

and the Dirichlet boundary condition

$$u(x, y, t) = u_\Gamma(x, y, t), \quad (x, y) \in \Gamma, \tag{3.75}$$

where Ω is a two-dimensional rectangular domain; Γ is the boundary of Ω; $[0, T]$ is the time interval; f_b is the driving function; and, u_0 and u_Γ are some given functions. In (3.73), c_x and c_y are the convective velocities, and d_x and d_y are

the positive diffusive coefficients. For the steady-state case, (3.73) reduces to

$$c_x \frac{\partial u}{\partial x} + c_y \frac{\partial u}{\partial y} = d_x \frac{\partial^2 u}{\partial x^2} + d_y \frac{\partial^2 u}{\partial y^2} + f_b. \tag{3.76}$$

(3.73) and (3.76) are known as a simplified version of the Navier-Stokes equation. They have been widely used in computational fluid dynamics (CFD) and physical sciences to describe the transport of mass, momentum, vorticity, heat and energy, the modeling of semiconductors, *etc*. In this chapter, we implement the alternating direction implicit (ADI) method proposed by You (2006) in the context of coupled compact IRBF approximations for the solution of the convection-diffusion equation.

3.3.1 You's ADI temporal discretisation

You (2006) proposed the following ADI factorisation to (3.73)

$$\left(1 + \frac{\Delta t}{2} c_x \frac{\partial}{\partial x}\right) \left(1 - \frac{\Delta t}{2} d_x \frac{\partial^2}{\partial x^2}\right) \left(1 + \frac{\Delta t}{2} c_y \frac{\partial}{\partial y}\right) \left(1 - \frac{\Delta t}{2} d_y \frac{\partial^2}{\partial y^2}\right) u^n$$
$$= \left(1 - \frac{\Delta t}{2} c_x \frac{\partial}{\partial x}\right) \left(1 + \frac{\Delta t}{2} d_x \frac{\partial^2}{\partial x^2}\right) \left(1 - \frac{\Delta t}{2} c_y \frac{\partial}{\partial y}\right) \left(1 + \frac{\Delta t}{2} d_y \frac{\partial^2}{\partial y^2}\right) u^{n-1}$$
$$+ \Delta t f_b^{n-1/2} + O(\Delta t^2). \tag{3.77}$$

We rewrite (3.77)

$$T_x^+ T_{xx}^- T_y^+ T_{yy}^- u^n = T_x^- T_{xx}^+ T_y^- T_{yy}^+ u^{n-1}, \tag{3.78}$$

where

$$T_x^\pm = \left(1 \pm \frac{\Delta t}{2} c_x \frac{\partial}{\partial x}\right), \qquad T_{xx}^\pm = \left(1 \pm \frac{\Delta t}{2} d_x \frac{\partial^2}{\partial x^2}\right), \tag{3.79}$$
$$T_y^\pm = \left(1 \pm \frac{\Delta t}{2} c_y \frac{\partial}{\partial y}\right), \qquad T_{yy}^\pm = \left(1 \pm \frac{\Delta t}{2} d_y \frac{\partial^2}{\partial y^2}\right).$$

(3.78) can be solved by the following two steps

$$T_x^+ T_{xx}^- u^* = T_x^- T_{xx}^+ T_y^- T_{yy}^+ u^{n-1}, \tag{3.80}$$
$$T_y^+ T_{yy}^- u^n = u^*. \tag{3.81}$$

3.3.2 ADI spatial-temporal discretisation

We incorporate the coupled compact IRBF approximations derived in Section 3.2 into the ADI equation by substituting (3.71) and (3.72), nodal value of the first- and second-order derivatives, respectively, into (3.77), resulting in the matrix-vector form

$$\mathbf{T}_x^+\mathbf{T}_{xx}^-\mathbf{T}_y^+\mathbf{T}_{yy}^-\mathbf{u}^n = \mathbf{T}_x^-\mathbf{T}_{xx}^+\mathbf{T}_y^-\mathbf{T}_{yy}^+\mathbf{u}^{n-1} + \Delta t\mathbf{f}_b^{n-1/2}, \tag{3.82}$$

where

$$\mathbf{T}_x^\pm = \left(\mathbf{I} \pm \frac{\Delta t}{2}c_x\mathbf{D}_x\right), \qquad \mathbf{T}_{xx}^\pm = \left(\mathbf{I} \pm \frac{\Delta t}{2}d_x\mathbf{D}_{xx}\right), \tag{3.83}$$

$$\mathbf{T}_y^\pm = \left(\mathbf{I} \pm \frac{\Delta t}{2}c_y\mathbf{D}_y\right), \qquad \mathbf{T}_{yy}^\pm = \left(\mathbf{I} \pm \frac{\Delta t}{2}d_y\mathbf{D}_{yy}\right),$$

and $\mathbf{I}$ is the $n_\eta \times n_\eta$ identity matrix.

3.3.3 ADI calculation procedure

Equation (3.82) is equivalent to

$$\mathbf{T}_x^+\mathbf{T}_{xx}^-\mathbf{u}^* = \mathbf{T}_x^-\mathbf{T}_{xx}^+\mathbf{T}_y^-\mathbf{T}_{yy}^+\mathbf{u}^{n-1} + \Delta t\mathbf{f}_b^{n-1/2}, \tag{3.84}$$

$$\mathbf{T}_y^+\mathbf{T}_{yy}^-\mathbf{u}^n = \mathbf{u}^*, \tag{3.85}$$

which can be solved by the following two steps.

Step 1: This step involves two sub-steps

- Sub-step 1: Compute the nodal values of $\mathbf{u}^*$ at the left and right boundaries of the computational domain via (3.85) for $x = x_1$ and $x = x_{n_x}$ with the given boundary condition (3.75).

- Sub-step 2: Solve (3.84) on the x-grid lines ($y = y_j$, $j \in \{2, 3, \cdots, n_y - 1\}$) for the values of $\mathbf{u}^*$ at the interior nodes.

Step 2: Solve (3.85) on the y-grid lines ($x = x_i$, $i \in \{2, 3, \cdots, n_x - 1\}$) for the

values of $\mathbf{u}^n$ at the interior nodes.

3.4 Numerical examples

We choose the multiquadric (MQ) function as the basis function, i.e. (1.6), in the present calculations. The value of $\beta = 50$ is employed in the present work. We evaluate the performance of the present scheme through the following measures.

i. The root mean square error (RMS) is defined as

$$RMS = \sqrt{\frac{\sum_{i=1}^{N} \left(f_i - \overline{f}_i\right)^2}{N}}, \qquad (3.86)$$

where f_i and $\overline{f}_i$ are the computed and exact values of the solution f at the i-th node, respectively; and, N is the number of nodes over the whole domain.

ii. The average absolute error (L_1) is defined as

$$L_1 = \frac{1}{N} \sum_{i=1}^{N} |f_i - \overline{f}_i|. \qquad (3.87)$$

iii. The maximum absolute error (L_∞) is defined as

$$L_\infty = \max_{i=1,\dots,N} |f_i - \overline{f}_i|. \qquad (3.88)$$

iv. The global convergence rate, α, with respect to the grid refinement is defined through

$$Error(h) \approx \gamma h^\alpha = O(h^\alpha), \qquad (3.89)$$

where h is the grid size; and, γ and α are exponential model's parameters.

v. A solution is considered to reach its steady state when

$$\sqrt{\frac{\sum_{i=1}^{N} \left(f_i^n - f_i^{n-1}\right)^2}{N}} < 10^{-9}. \qquad (3.90)$$

For comparison purposes, we also use the HOC scheme of Tian et al. (2011) and the compact IRBF scheme of Thai-Quang et al. (2012b) for calculations.

In this work, calculations are done with a Dell computer Optiplex 9010 version 2013. Its specifications are intel(R) core(TM) i7-3770 CPU 3.40 GHz 3.40 GHz, memory(RAM) of 8GB(7.89 usable) and 64-bit operating system. The Matlab(R) version 2012 is utilised.

3.4.1 Poisson equation

In order to study the spatial accuracy of the present coupled compact IRBF approximation scheme, we consider the following Poisson equation

$$\frac{d^2u}{dx_1^2} + \frac{d^2u}{dx_2^2} = -18\pi^2 \sin(3\pi x_1)\sin(3\pi x_2), \qquad (3.91)$$

on a square domain $[0,1]^2$, subjected to the Dirichlet boundary condition derived from the following exact solution

$$\overline{u} = \sin(3\pi x_1)\sin(3\pi x_2), \qquad (3.92)$$

The calculations are carried out on a set of uniform grids of $\{21 \times 21, 31 \times 31, ..., 111 \times 111\}$. Table 3.1 shows that the proposed scheme outperforms the HOC and compact IRBF schemes in terms of the solution accuracy. Figure 3.3 illustrates the matrix condition number grows with approximately the rate of $O(h^{-2.00})$ for the HOC and the compact IRBF, and $O(h^{-1.90})$ for the coupled compact IRBF.

Table 3.1 Poisson equation: The effect of the grid size h on the solution accuracy RMS.

Grid ($n_x \times n_y$)	HOC Tian et al. (2011) RMS	compact IRBF Thai-Quang et al. (2012b) RMS	present RMS
21×21	3.3579E-04	3.3492E-04	2.5405E-04
31×31	5.6856E-05	5.6674E-05	4.2362E-05
41×41	1.4589E-05	1.4594E-05	1.0997E-05
51×51	4.9330E-06	4.7158E-06	3.7709E-06
61×61	2.0151E-06	1.9227E-06	1.5371E-06
71×71	9.4467E-07	9.2935E-07	7.1799E-07
81×81	4.9199E-07	4.6935E-07	3.8210E-07
91×91	2.7850E-07	3.0597E-07	2.0317E-07
101×101	1.6869E-07	1.5204E-07	1.3230E-07
111×111	1.0805E-07	1.4662E-07	7.8442E-08
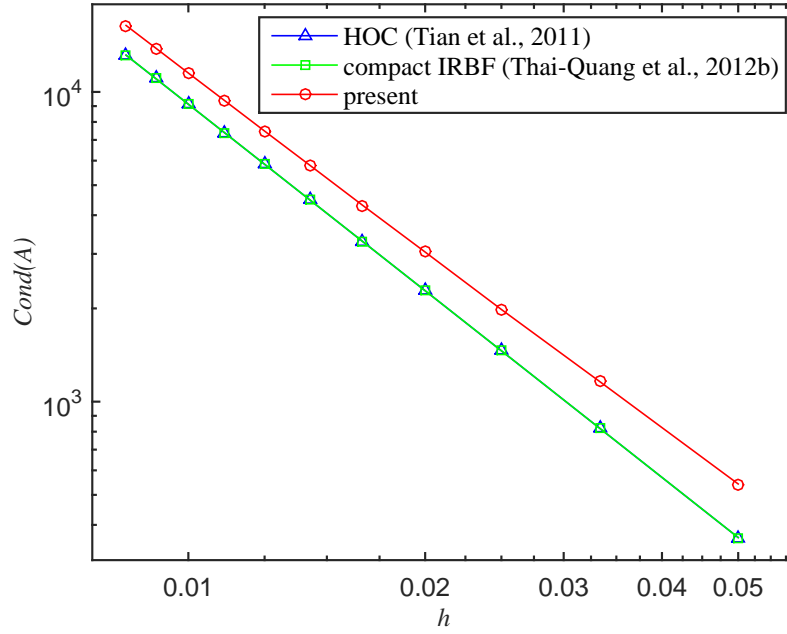
Figure 3.3 Poisson equation, $\{21 \times 21, 31 \times 31, ..., 111 \times 111\}$: The effect of the grid size h on the matrix condition number. It is noted that the curves for the HOC and the compact IRBF are indistinguishable.

To compare the computational efficiency of the coupled compact IRBF, compact IRBF and HOC schemes, we let the grid increase as $\{21 \times 21, 23 \times 23, ...\}$ until the solution accuracy achieves a target RMS level of 10^{-6}. Figure 3.4 shows that the present scheme takes much less time to reach the target accuracy than the compact IRBF and the HOC. It is noted that the final grid used to achieve the target accuracy is 71×71 for the HOC and the compact IRBF and 67×67 for the coupled compact IRBF.

The effect of the MQ width on the solution accuracy for three different grids $\{21 \times 21, 51 \times 51, 81 \times 81\}$ is illustrated in Figure 3.5. It can be seen that the present scheme has better accuracy and is more stable than the compact IRBF scheme.

3.4.2 Heat equation

By selecting the following heat equation, the performance of the proposed scheme can be studied for the diffusive term only as

$$\frac{\partial u}{\partial t} = \frac{\partial^2 u}{\partial x^2}, \quad a \leq x \leq b, \quad t \geq 0, \tag{3.93}$$
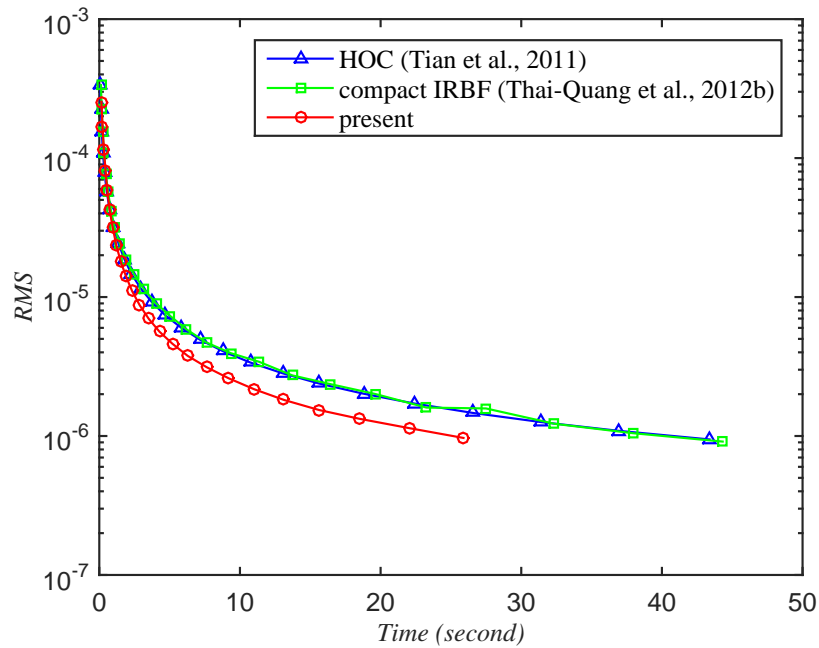
Figure 3.4 Poisson equation, $\{21 \times 21, 23 \times 23, ...\}$: The computational cost to achieve the target accuracy of 10^{-6}. The final grid is 71×71 for the HOC and the compact IRBF and 67×67 for the present.
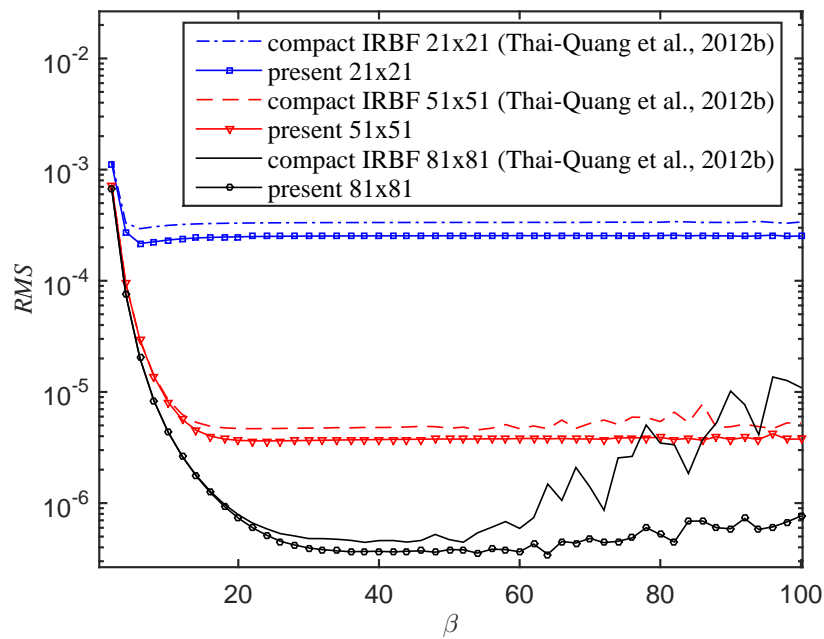
Figure 3.5 Poisson equation, $\{21 \times 21, 51 \times 51, 81 \times 81\}$: The effect of the MQ width β on the solution accuracy RMS.

$$u(x, 0) = u_0(x), \quad a \leq x \leq b, \tag{3.94}$$

$$u(a, t) = u_{\Gamma_1}(t) \quad \text{and} \quad u(b, t) = u_{\Gamma_2}(t), \quad t \geq 0, \tag{3.95}$$

where u and t are the field variable and time, respectively; and, $u_0(x)$, $u_{\Gamma_1}(t)$, and $u_{\Gamma_2}(t)$ are prescribed functions. The temporal discretisation of (3.93) with a Crank-Nicolson scheme gives

$$\frac{u^n - u^{n-1}}{\Delta t} = \frac{1}{2}\left\{\frac{\partial^2 u^n}{\partial x^2} + \frac{\partial^2 u^{n-1}}{\partial x^2}\right\}, \tag{3.96}$$

where the superscript n denotes the current time step. (3.96) can be rewritten as

$$\left\{1 - \frac{\Delta t}{2}\frac{\partial^2}{\partial x^2}\right\} u^n = \left\{1 + \frac{\Delta t}{2}\frac{\partial^2}{\partial x^2}\right\} u^{n-1}. \tag{3.97}$$

Consider (3.93) on a segment $[0, \pi]$ with the initial and boundary conditions $u(x, 0) = \sin(2x)$, $0 < x < \pi$ and $u(0, t) = u(\pi, t) = 0$, $t \geq 0$, respectively. The exact solution of this problem can be verified to be $\bar{u}(x, t) = \sin(2x)e^{-4t}$. The spatial accuracy of the proposed scheme is tested on various uniform grids $\{11, 21, ..., 111\}$. We employ here a small time step, $\Delta t = 10^{-6}$, to minimise the effect of the approximation error in time. The solution is computed at $t = 0.0125$. Table 3.2 shows that the coupled compact IRBF outperforms the HOC and the compact IRBF in terms of both the solution accuracy and the convergence rate. At the two finest grids, it can be seen that the coupled compact IRBF maintains its high convergence rates and produces highly accurate and stable results while the convergence rates of the compact IRBF fall dramatically. Figure 3.6 illustrates a similar trend of the matrix condition number for the three schemes.

To study the computational efficiency of the coupled compact IRBF, compact IRBF and HOC schemes, we increase the number of grids as $\{11, 13, ...\}$ until the solution accuracy achieves a target RMS level of 10^{-6}. We also use a small time step, $\Delta t = 10^{-6}$, and the solution is computed at $t = 0.0125$. Figure 3.7 shows that the present scheme uses a smaller amount of time to reach the target accuracy than the compact IRBF and the HOC. It is noted that the final grid used to achieve the target accuracy is 43 for the HOC and the compact IRBF and 41 for the coupled compact IRBF.

Table 3.2 Heat equation, $\Delta t = 10^{-6}$, $t = 0.0125$: The effect of the grid size h on the solution accuracy RMS. LCR stands for "*Local Convergence Rate*".

Grid ($n_x \times n_y$)	HOC Tian et al. (2011)		compact IRBF Thai-Quang et al. (2012b)		present	
	RMS	$LCR^{(*)}$	RMS	$LCR^{(*)}$	RMS	$LCR^{(*)}$
11×11	1.9029E-04	—	1.8980E-04	—	1.6692E-04	—
21×21	2.1464E-05	3.37	2.1213E-05	3.39	1.5704E-05	3.66
31×31	4.1528E-06	3.69	4.0418E-06	3.72	2.9809E-06	3.89
41×41	1.1631E-06	3.87	1.1049E-06	3.91	8.2778E-07	4.03
51×51	4.1535E-07	3.99	3.8564E-07	4.04	2.8916E-07	4.15
61×61	1.7581E-07	4.08	1.5638E-07	4.15	1.1851E-07	4.23
71×71	8.4228E-08	4.14	7.2009E-08	4.22	5.7172E-08	4.28
81×81	4.4304E-08	4.19	3.6360E-08	4.29	3.2741E-08	4.28
91×91	2.5062E-08	4.23	1.8962E-08	4.36	1.3035E-08	4.48
101×101	1.5025E-08	4.26	1.8306E-08	4.17	7.5240E-09	4.51
111×111	9.4465E-09	4.29	2.1701E-08	3.93	4.9223E-09	4.51

$^{(*)}LCR$=-log$[RMS(n_x)/RMS(11)]$/log$[n_x/11]$.
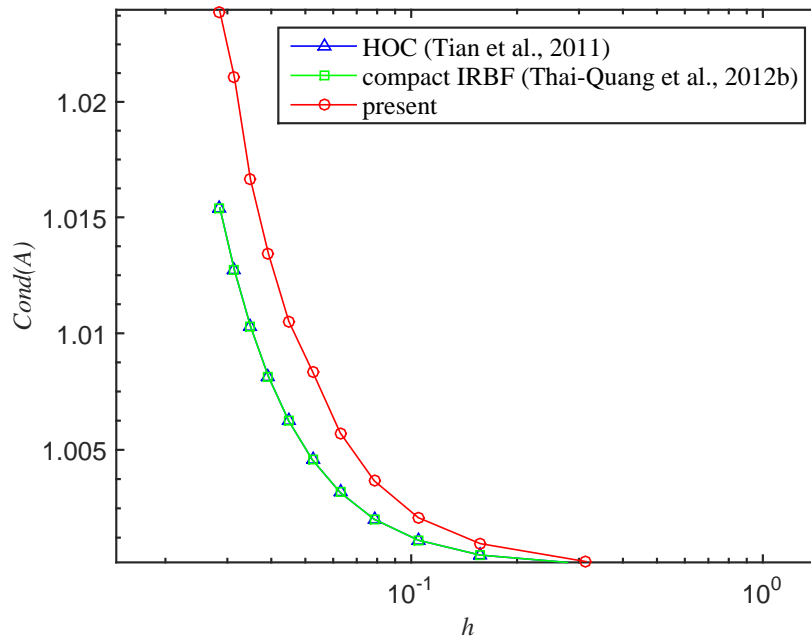
Figure 3.6 Heat equation, $\{11, 21, ..., 111\}$, $\Delta t = 10^{-6}$, $t = 0.0125$: The effect of the grid size h on the matrix condition number. It is noted that the curves for the HOC and the compact IRBF are indistinguishable.
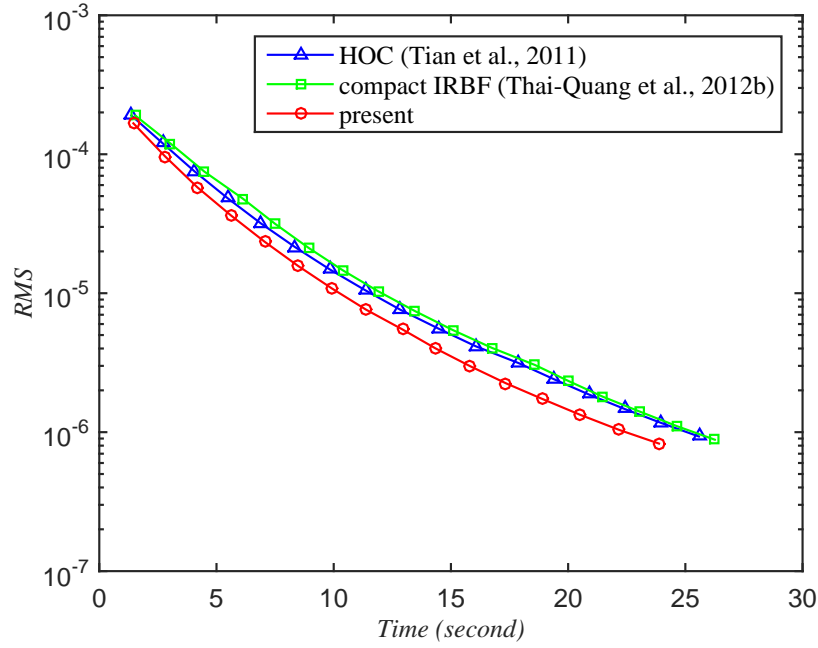
Figure 3.7 Heat equation, $\{11, 13, ...\}$: The computational cost to achieve the target accuracy of 10^{-6}. The final grid is 43 for the HOC and the compact IRBF and 41 for the coupled compact IRBF.

The effect of the MQ width on the solution accuracy for three different grids $\{11, 41, 71\}$ is illustrated in Figure 3.8 where it can be observed that the present scheme has better accuracy than the compact IRBF scheme.
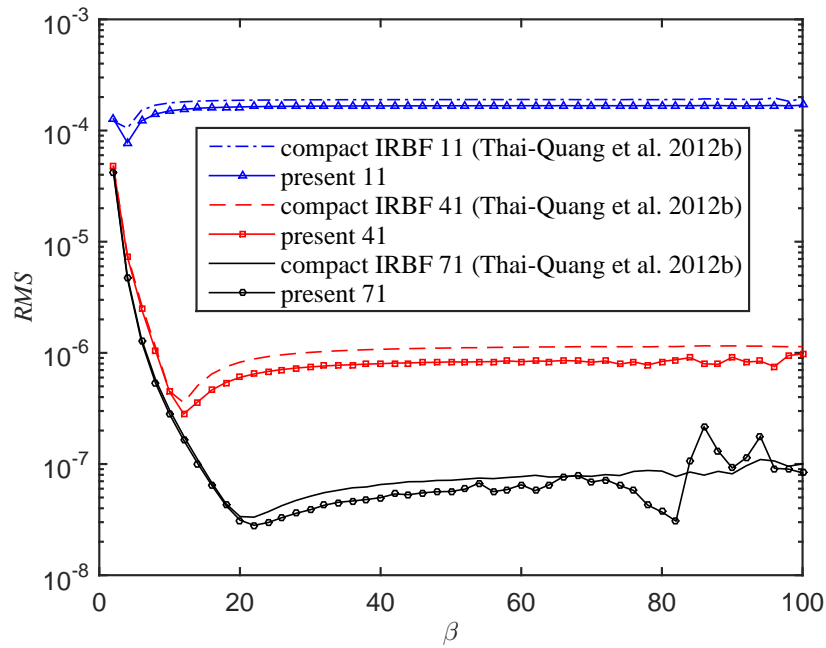
Figure 3.8 Heat equation, $\{11, 41, 71\}$, $\Delta t = 10^{-6}$, $t = 0.0125$: The effect of the MQ width β on the solution accuracy RMS.

3.4.3 Burgers equation

With Burgers equation, the performance of the proposed scheme can be investigated for both convective and diffusive terms as

$$\frac{\partial u}{\partial t} + u\frac{\partial u}{\partial x} = \frac{1}{Re}\frac{\partial^2 u}{\partial x^2}, \quad a \le x \le b, \quad t \ge 0, \tag{3.98}$$

$$u(x,0) = u_0(x), \quad a \le x \le b, \tag{3.99}$$

$$u(a,t) = u_{\Gamma_1}(t) \quad \text{and} \quad u(b,t) = u_{\Gamma_2}(t), \quad t \ge 0, \tag{3.100}$$

where $Re > 0$ is the Reynolds number; and, $u_0(x)$, $u_{\Gamma_1}(t)$, and $u_{\Gamma_2}(t)$ are prescribed functions. The temporal discretisations of (3.98) using the Adams-Bashforth scheme for the convective term and Crank-Nicolson scheme for the diffusive term, result in

$$\frac{u^n - u^{n-1}}{\Delta t} + \left\{\frac{3}{2}\left(u\frac{\partial u}{\partial x}\right)^{n-1} - \frac{1}{2}\left(u\frac{\partial u}{\partial x}\right)^{n-2}\right\} = \frac{1}{2Re}\left\{\frac{\partial^2 u^n}{\partial x^2} + \frac{\partial^2 u^{n-1}}{\partial x^2}\right\}, \tag{3.101}$$

or

$$\left\{1 - \frac{\Delta t}{2Re}\frac{\partial^2}{\partial x^2}\right\}u^n = \left\{1 + \frac{\Delta t}{2Re}\frac{\partial^2}{\partial x^2}\right\}u^{n-1} - \Delta t\left\{\frac{3}{2}\left(u\frac{\partial u}{\partial x}\right)^{n-1} - \frac{1}{2}\left(u\frac{\partial u}{\partial x}\right)^{n-2}\right\}. \tag{3.102}$$

The problem is considered on a segment $0 \le x \le 1$, $t \ge 0$ in the form (Hassanien et al., 2005)

$$\bar{u}(x,t) = \frac{\alpha_0 + \mu_0 + (\mu_0 - \alpha_0)\exp(\eta)}{1 + \exp(\eta)}, \tag{3.103}$$

where $\eta = \alpha_0 Re(x - \mu_0 t - \beta_0)$, $\alpha_0 = 0.4$, $\beta_0 = 0.125$, $\mu_0 = 0.6$, and $Re = 100$. The initial and boundary conditions can be derived from the analytic solution (3.103). The calculations are carried out on a set of uniform grids $\{31, 41, ..., 191\}$. The time step $\Delta t = 10^{-6}$ is chosen. The errors of the solution are calculated at the time $t = 0.0125$. Figure 3.9 displays that the present scheme has lower errors than the HOC and the compact IRBF. At high grid densities, it can be also seen that the coupled compact IRBF is more accurate and stable than the compact IRBF. A similar trend of the matrix condition number for the three schemes is

observed in Figure 3.10.
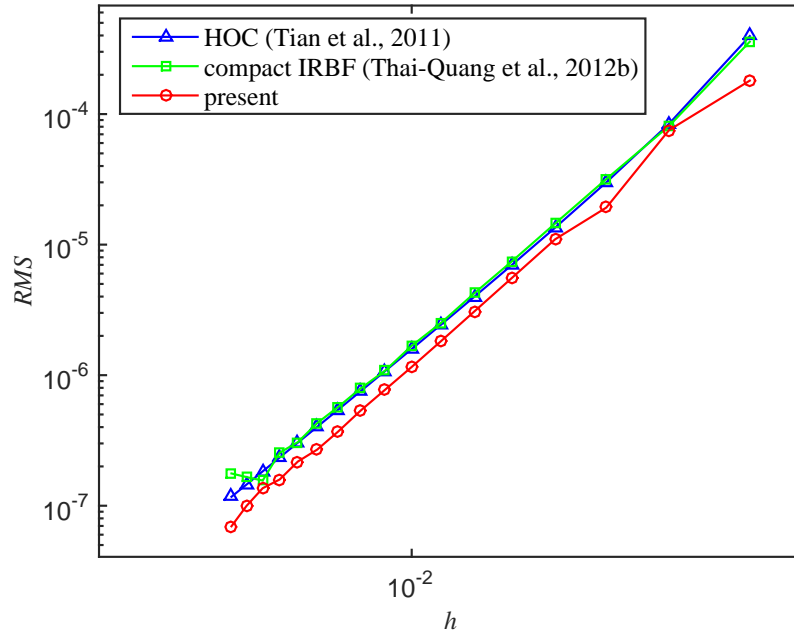
Figure 3.9 Burgers equation, $\{31, 41, ..., 191\}$, $Re = 100$, $\Delta t = 10^{-6}$, $t = 0.0125$: The effect of the grid size h on the solution accuracy RMS. The solution converges as $O(h^{4.29})$ for the HOC, $O(h^{4.21})$ for the compact IRBF, and $O(h^{4.27})$ for the coupled compact IRBF.
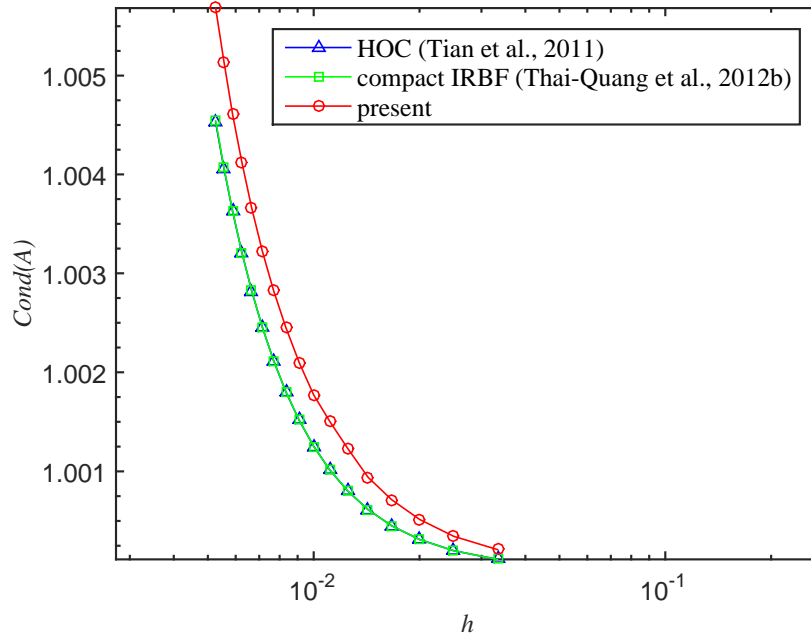
Figure 3.10 Burgers equation, $\{31, 41, ..., 191\}$, $Re = 100$, $\Delta t = 10^{-6}$, $t = 0.0125$: The effect of the grid size h on the matrix condition number. It is noted that the curves for the HOC and the compact IRBF are indistinguishable.

To study the computational efficiency of the coupled compact IRBF, compact IRBF and HOC schemes, we increase the number of grids as $\{31, 41, ...\}$ until the

solution accuracy achieves a target RMS level of 10^{-6}. The time step $\Delta t = 10^{-6}$ is chosen and the errors of the solution are calculated at the time $t = 0.0125$. Figure 3.11 shows that the present scheme takes less time to reach the target accuracy than the compact IRBF and the HOC. It is noted that the final grid used to achieve the target accuracy is 121 for the HOC and the compact IRBF and 111 for the coupled compact IRBF.
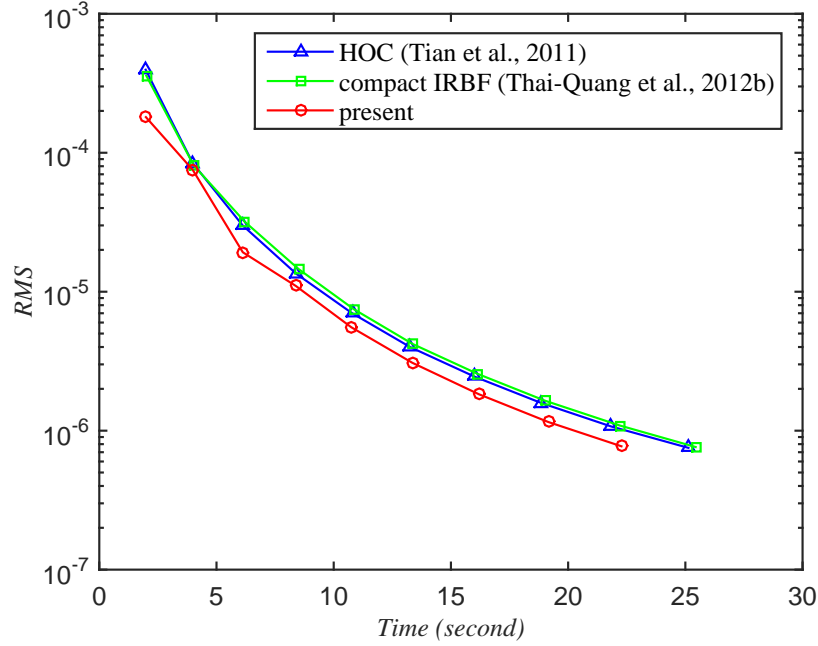
Figure 3.11 Burgers equation, $\{31, 41, ...\}$: The computational cost to achieve the target accuracy of 10^{-6}. The final grid is 121 for the HOC and the compact IRBF and 111 for the coupled compact IRBF.

Figure 3.12 shows the effect of the MQ width on the solution accuracy, where the present scheme produces better accuracy than the compact IRBF scheme over a wide range of β for three different grids $\{31, 71, 101\}$.

3.4.4 Steady convection-diffusion equation

Consider (3.76) with $c_x = c_y = 0.1$, $d_x = d_y = 1$ in a square $\Omega = [0, L] \times [0, L]$ and apply the Dirichlet boundary condition. The analytic solution takes the form (Sheu et al., 2011)

$$\overline{u} = \frac{u_0}{e^{r+} - e^{r-}} e^{\delta_x/2} \sin(\pi x) \left(e^{r+y} - e^{r-y} \right), \qquad (3.104)$$
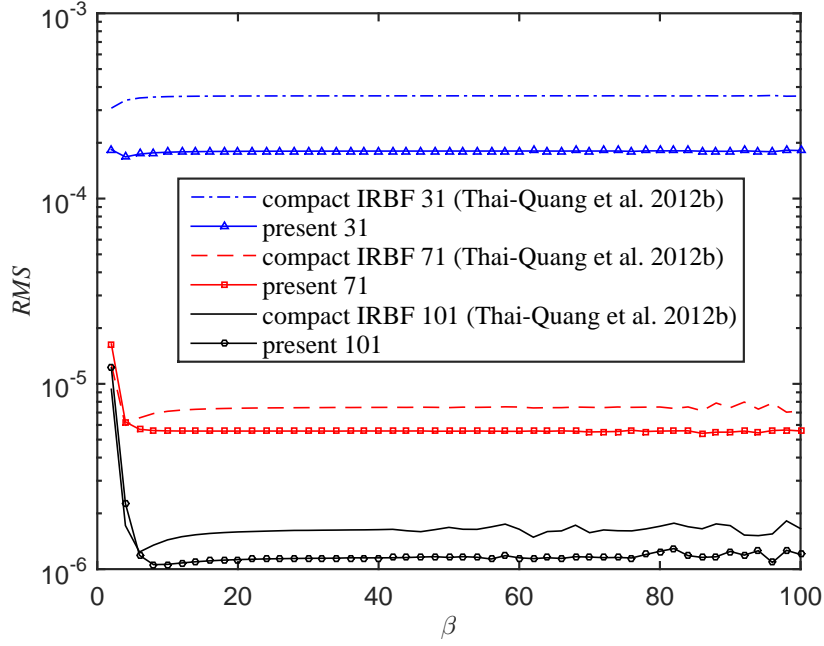
Figure 3.12 Burgers equation, $\{31, 71, 101\}$, $Re = 100$, $\Delta t = 10^{-6}$, $t = 0.0125$: The effect of the MQ width β on the solution accuracy RMS.

where $u_0 = 1$, $\delta_x = c_x L / d_x$, $\delta_y = c_y L / d_y$, $L = 1$, and

$$r_\pm = \frac{1}{2}\delta_y \pm \frac{1}{2}\sqrt{\left(\delta_y^2 + 4W\right)}, \quad W = 4\pi^2 + \delta_x^2/4. \tag{3.105}$$

The driving function f_b is given by

$$f_b = c_x \frac{\partial \overline{u}}{\partial x} + c_y \frac{\partial \overline{u}}{\partial y} - d_x \frac{\partial^2 \overline{u}}{\partial x^2} - d_y \frac{\partial^2 \overline{u}}{\partial y^2}. \tag{3.106}$$

To solve the steady equation (3.76), we make use of the unsteady form (3.73) where $\frac{\partial u}{\partial t}$ is considered as a pseudo time-derivative term to facilitate an iterative calculation. The steady equation (3.76) thus has the same form as the unsteady equation (3.73). When the difference of u between two successive time levels is small, i.e. less than a given tolerance (3.90), the obtained solution is the solution to (3.76).

In order to study the solution accuracy with the grid refinement, we employ a set of uniform grids $\{11 \times 11, 16 \times 16, ..., 51 \times 51\}$ and a time step of 0.0005. Figure 3.13 displays the present results are better than those of the HOC and the compact IRBF.
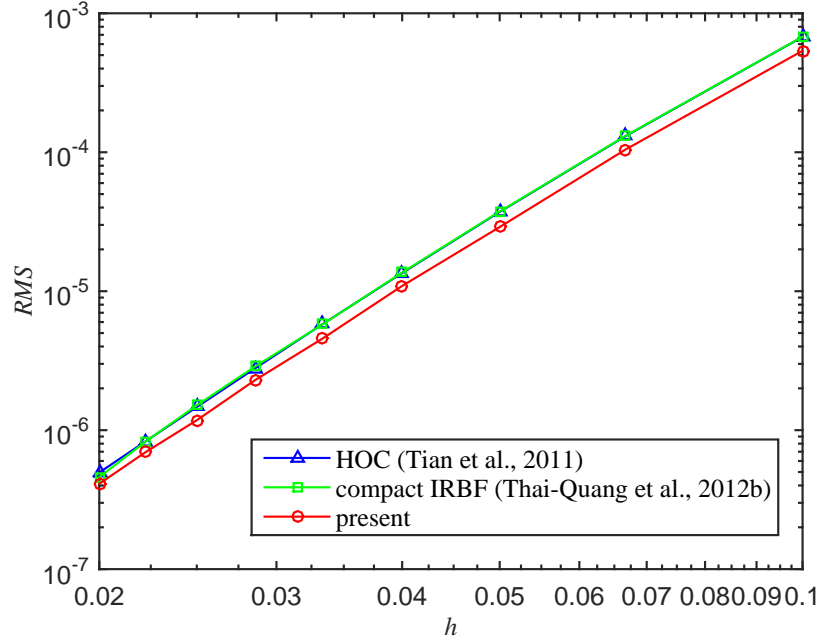
Figure 3.13 Steady convection-diffusion equation, $\{11 \times 11, 16 \times 16, ..., 51 \times 51\}$: The effect of the grid size h on the solution accuracy RMS. The present solution is more accurate than those of the HOC and the compact IRBF.

To investigate the computational efficiency of the coupled compact IRBF, compact IRBF and HOC schemes, we let the number of grids increase as $\{11 \times 11, 13 \times 13, ...\}$ until the solution accuracy achieves a target RMS level of 10^{-6}. The time step is 0.0005. Figure 3.14 shows that the present scheme takes less time to reach the target accuracy than the compact IRBF and the HOC. It is noted that the final grid used to achieve the target accuracy is 47×47 for the compact IRBF, 45×45 for the HOC and 43×43 for the coupled compact IRBF.

Figure 3.15 illustrates the solution accuracy versus the MQ width for three different grids $\{31 \times 31, 41 \times 41, 51 \times 51\}$. It is observed that the coupled compact IRBF is more accurate and stable than the compact IRBF.

3.4.5 Unsteady diffusion equation

Consider a diffusion equation by setting the parameters in (3.73) as $c_x = c_y = 0$, $d_x = d_y = 1$ and $f_b = 0$. The analytic solution is taken here as (Tian and Ge, 2007)

$$\overline{u}(x, y, t) = e^{-2\pi^2 t} \sin(\pi x) \sin(\pi y). \tag{3.107}$$
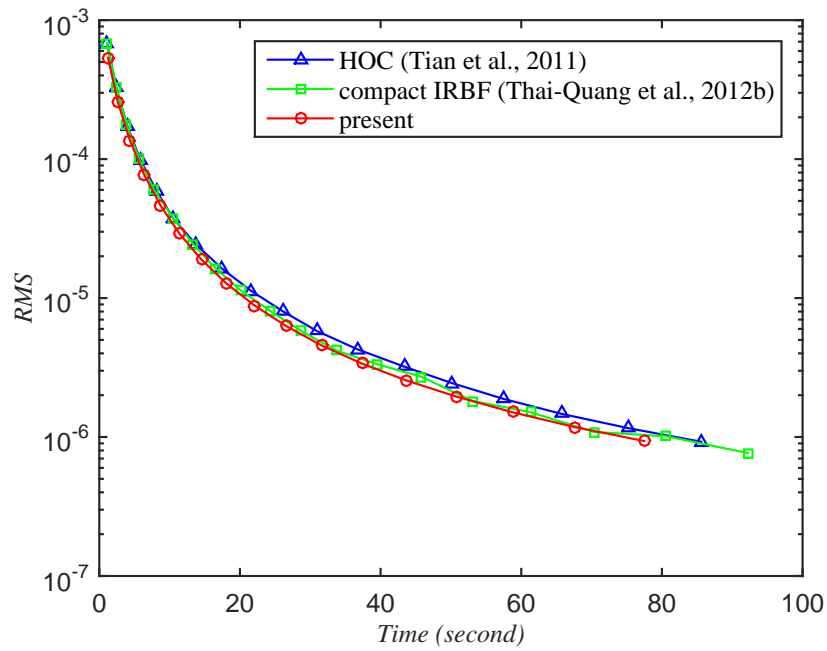
Figure 3.14 Steady convection-diffusion equation, $\{11 \times 11, 13 \times 13, ...\}$: The computational cost to achieve the target accuracy of 10^{-6}. The final grid is 47×47 for the compact IRBF, 45×45 for the HOC and 43×43 for the coupled compact IRBF.
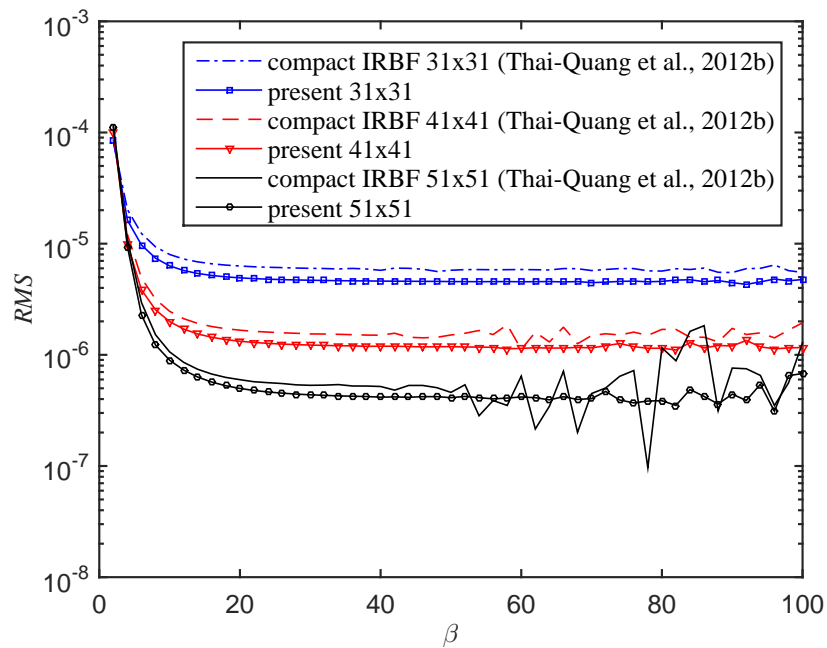
Figure 3.15 Steady convection-diffusion equation, $\{31 \times 31, 41 \times 41, 51 \times 51\}$: The effect of the MQ width β on the solution accuracy RMS.

The problem domain is chosen to be a unit square $\Omega = [0,1] \times [0,1]$ and the initial and Dirichlet boundary conditions are derived from (3.107).

We employ a set of uniform grids $\{11 \times 11, 16 \times 16, ..., 41 \times 41\}$ to study the solution accuracy with the grid refinement. Results computed at $t = 0.0125$ using $\Delta t = 10^{-5}$ are displayed in Figure 3.16, showing that the coupled compact IRBF gives lower errors than the HOC and the compact IRBF.
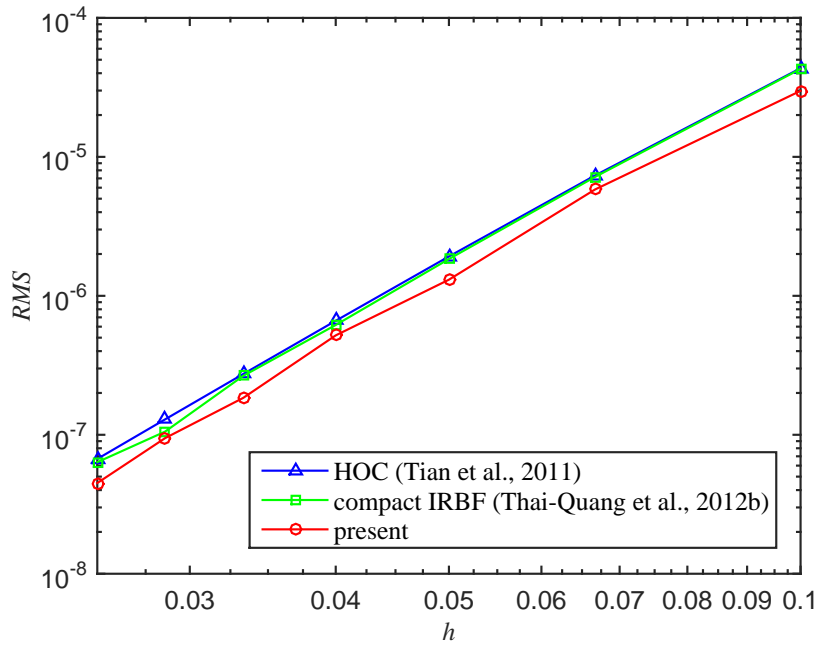
Figure 3.16 Unsteady diffusion equation, $\{11 \times 11, 16 \times 16, ..., 41 \times 41\}, \Delta t = 10^{-5}, t = 0.0125$: The effect of the grid size h on the solution accuracy RMS. The present solution is more accurate than those of the HOC and the compact IRBF.

In order to investigate the computational efficiency of the coupled compact IRBF, compact IRBF and HOC schemes, we increase the number of grids as $\{11 \times 11, 13 \times 13, ...\}$ until the solution accuracy achieves a target RMS level of 10^{-6}. Results are also computed at $t = 0.0125$ using $\Delta t = 10^{-5}$. Figure 3.17 shows that the present scheme reaches the target accuracy using less time than the compact IRBF and the HOC. It is noted that the final grid used to achieve the target accuracy is 25×25 for the HOC and the compact IRBF and 23×23 for the coupled compact IRBF.

We employ a set of time steps $\Delta t = \{0.05, 0.025, 0.0125, 0.00625\}$ to test the temporal accuracy. Results computed at $t = 1.25$ using a uniform grid of 81×81
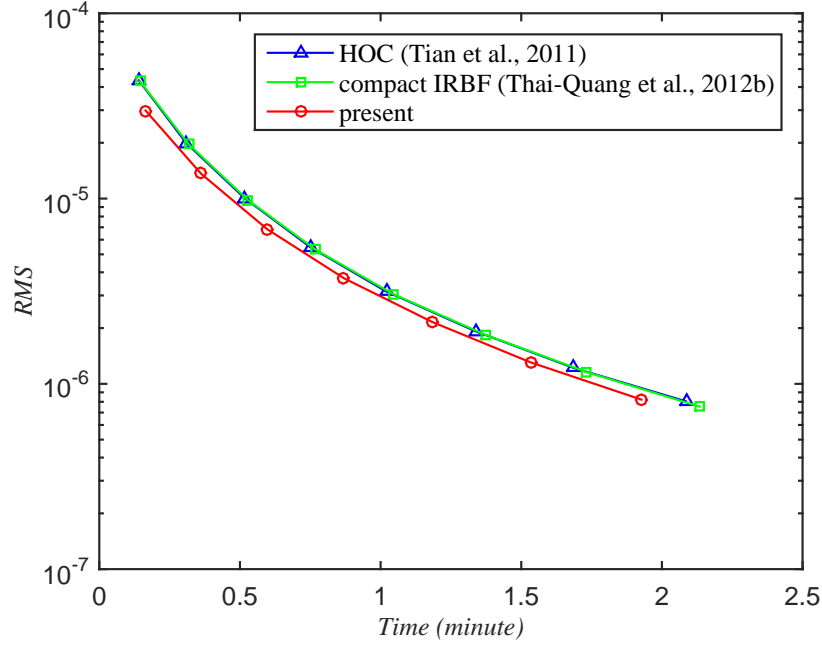
Figure 3.17 Unsteady diffusion equation, $\{11 \times 11, 13 \times 13, ...\}$: The computational cost to achieve the target accuracy of 10^{-6}. The final grid is 25×25 for the HOC and the compact IRBF and 23×23 for the coupled compact IRBF.

are shown in Table 3.3.

Table 3.3 Unsteady diffusion equation, $t = 1.25$, grid of 81×81: Solution accuracy of the three schemes against time step.

Δt	HOC Tian et al. (2011)		compact IRBF Thai-Quang et al. (2012b)		present	
	RMS	Rate	RMS	Rate	RMS	Rate
0.05	3.8518E-12	—	3.8518E-12	—	3.8519E-12	—
0.025	1.1276E-12	1.77	1.1276E-12	1.77	1.1277E-12	1.77
0.0125	2.9340E-13	1.94	2.9337E-13	1.94	2.9351E-13	1.94
0.00625	7.4089E-14	1.99	7.4054E-14	1.99	7.4199E-14	1.98

To facilitate a further comparison with the exponential high-order compact scheme (EHOC) of Tian and Ge (2007), we now choose $\Delta t = h^2$ and $t = 0.125$. Table 3.4 indicates that the present coupled compact IRBF scheme is more accurate than the HOC and compact IRBF schemes and comparable with the EHOC scheme. The four schemes yield similar local convergence rates of about 4.

Figure 3.18 plots the RMS error against time with $\Delta t = 10^{-4}$ and $t = 0.125$ using a grid of 21×21. The plot shows that the coupled compact IRBF is more accurate than both the HOC and the compact IRBF.

The effect of the MQ width on the solution accuracy for three different grids

Table 3.4 Unsteady diffusion equation, $t = 0.125$, $\Delta t = h^2$: Effect of the grid size, h, on the solution accuracy RMS.

Grid	EHOC Tian and Ge (2007) RMS	HOC Tian et al. (2011) RMS	compact IRBF Thai-Quang et al. (2012b) RMS	present RMS
11×11	8.5513E-05	9.4741E-05	9.3942E-05	8.7048E-05
21×21	5.1916E-06	5.7865E-06	5.8195E-06	5.5153E-06
41×41	3.1748E-07	3.3969E-07	4.0291E-07	3.3936E-07
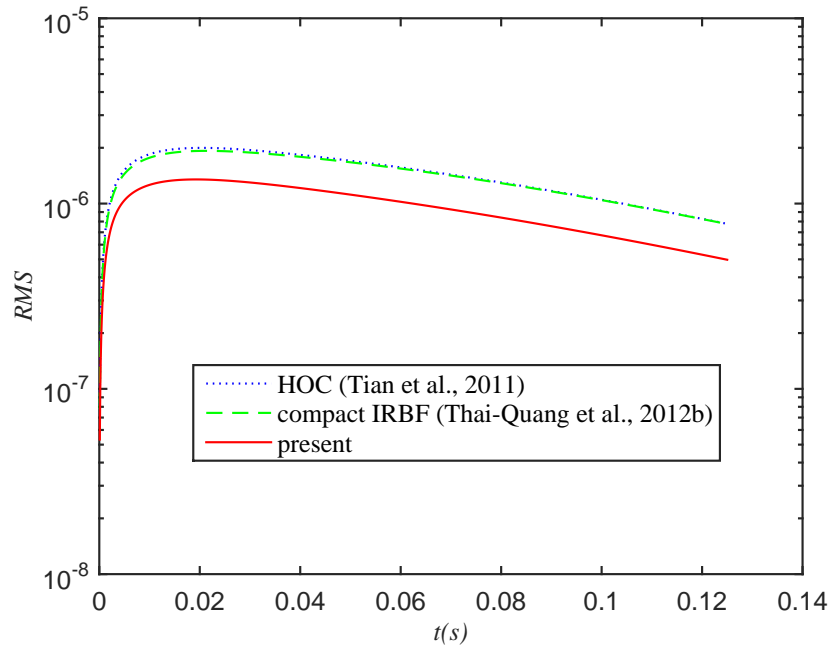
Figure 3.18 Unsteady diffusion equation, grid of 21×21, $\Delta t = 10^{-4}$, $t = 0.125$: The solution accuracy RMS against time.

$\{21 \times 21, 31 \times 31, 41 \times 41\}$ is illustrated in Figure 3.19.
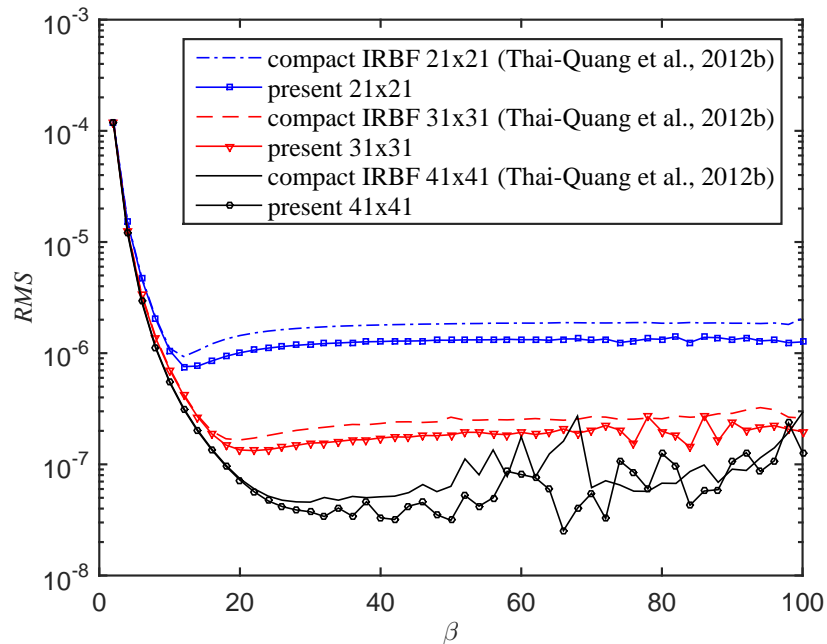
Figure 3.19 Unsteady diffusion equation, $\{21 \times 21, 31 \times 31, 41 \times 41\}$, $\Delta t = 10^{-4}$, $t = 0.125$: The effect of the MQ width β on the solution accuracy RMS.

3.4.6 Unsteady convection-diffusion equation

Consider the unsteady convection-diffusion equation (3.73), where $f_b = 0$, in a square $\Omega = [0,2] \times [0,2]$ with the following analytic solution (Noye and Tan, 1989)

$$\overline{u}(x,y,t) = \frac{1}{4t+1} exp \left[-\frac{(x-c_x t - 0.5)^2}{d_x(4t+1)} - \frac{(y-c_y t - 0.5)^2}{d_y(4t+1)} \right], \qquad (3.108)$$

and the Dirichlet boundary conditions are used. From (3.108), one can derive the initial and boundary conditions. The problem parameters are chosen as $c_x = c_y = 0.8$ and $d_x = d_y = 0.01$.

To study the solution accuracy with the grid refinement, we employ a set of uniform grids $\{31 \times 31, 41 \times 41, ..., 81 \times 81\}$. The solution is calculated at $t = 1.25$ using $\Delta t = 10^{-4}$. Figure 3.20 describes that the proposed scheme has better performance than the HOC and compact IRBF schemes.
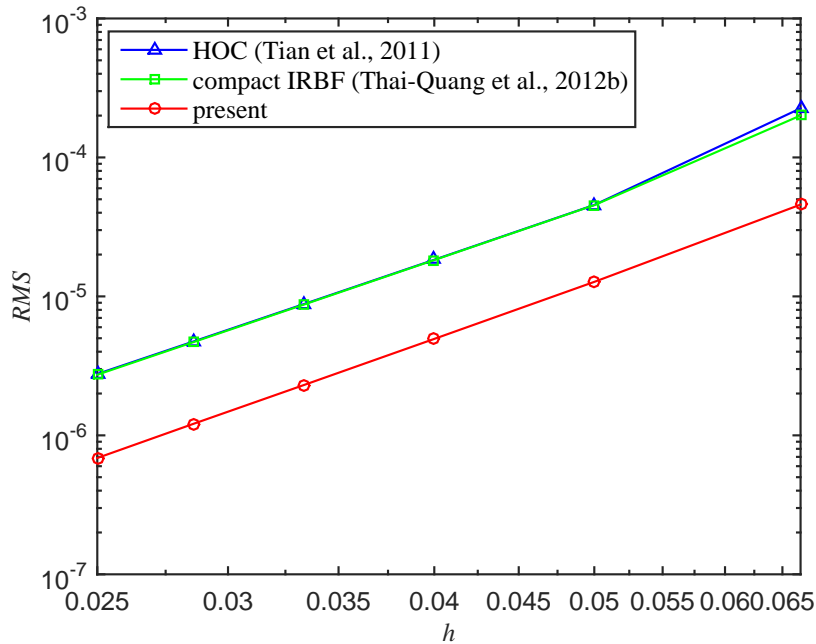
Figure 3.20 Unsteady convection-diffusion equation, $c_x = c_y = 0.8$ and $d_x = d_y = 0.01$, $\{31 \times 31, 41 \times 41, ..., 81 \times 81\}$, $\Delta t = 10^{-4}$, $t = 1.25$: The effect of the grid size h on the solution accuracy RMS. The solution converges as $O(h^{4.41})$ for the HOC, $O(h^{4.32})$ for the compact IRBF, and $O(h^{4.27})$ for the coupled compact IRBF.

To investigate the computational cost in achieving an accuracy of interest, we increase the grid $\{33 \times 33, 35 \times 35, ...\}$ until the solution accuracy reaches the target accuracy which is chosen to be $RMS = 10^{-5}$. The solution is also calculated at

$t = 1.25$ using $\Delta t = 10^{-4}$. Figure 3.21 illustrates that for a given level of accuracy, the proposed scheme is more efficient than the HOC and compact IRBF schemes. It is noted that the final grid used to achieve the target accuracy is 61×61 for the HOC and the compact IRBF and 45×45 for the coupled compact IRBF.
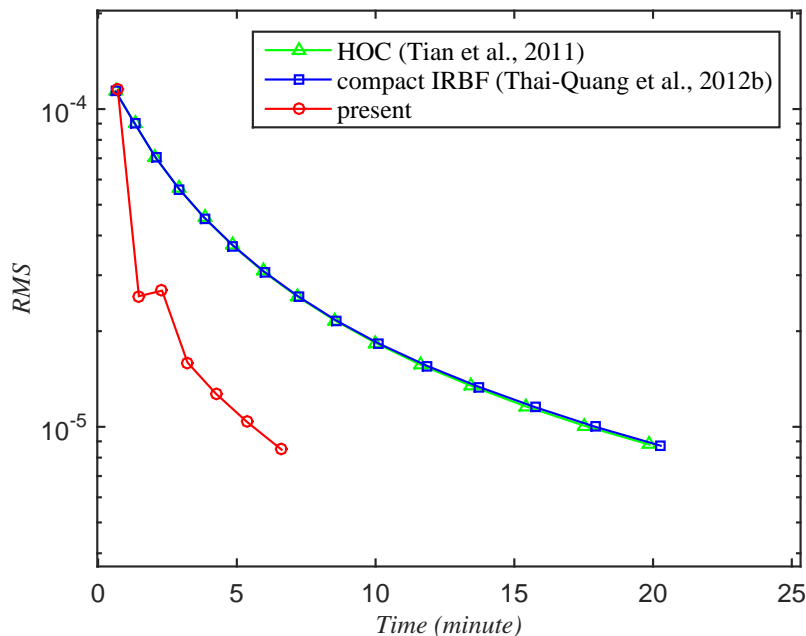
**Figure 3.21** Unsteady convection-diffusion equation, $\{33 \times 33, 35 \times 35, ...\}$: The computational cost to achieve the target accuracy of 10^{-5}. The final grid is 61×61 for the HOC and the compact IRBF and 45×45 for the coupled compact IRBF.

Table 3.5 shows a comparison of L_1, RMS and L_∞ errors between the present scheme and the third-order nine-point compact scheme of Noye and Tan (1989), the fourth-order nine-point compact scheme of (Kalita et al., 2002), the HOC scheme of Karaa and Zhang (2004), the EHOC scheme of Tian and Ge (2007), the high-order compact boundary value method (HOC-BVM) of Dehghan and Mohebbi (2008), the HOC scheme of Tian et al. (2011), and the compact IRBF of Thai-Quang et al. (2012b). It can be seen that the present scheme yields the most accurate solution. Furthermore, Figure 3.22 plots the solution accuracy against time for these schemes (except for EHOC whose data is not available). It illustrates that all of these curves have similar shapes and the present scheme produces smaller error for every time step.

Ma et al. (2012) proposed a high-order hybrid Padé (HPD) method for the convection-dominated diffusion problem and examined the performance of the

Table 3.5 Unsteady convection-diffusion equation, $c_x = c_y = 0.8$ and $d_x = d_y = 0.01$, grid of 81×81, $t = 1.25$, $\Delta t = 0.00625$: Comparison of the solution accuracy between the present scheme and some others.

Method	$L_1(u)$	$RMS(u)$	$L_\infty(u)$
third-order nine-point compact (Noye and Tan, 1989)	1.971E-05	1.280E-04	6.509E-04
fourth-order nine-point compact (Kalita et al., 2002)	1.597E-05	1.024E-04	4.477E-04
HOC (Karaa and Zhang, 2004)	9.218E-06	5.931E-05	2.500E-04
EHOC (Tian and Ge, 2007)	9.663E-06	6.194E-05	2.664E-04
HOC-BVM (Dehghan and Mohebbi, 2008)	9.493E-06	—	2.477E-04
HOC (Tian et al., 2011)	6.754E-06	2.200E-05	1.706E-04
compact IRBF (Thai-Quang et al., 2012b)	6.742E-06	2.197E-05	1.703E-04
present	5.989E-06	1.904E-05	1.427E-04
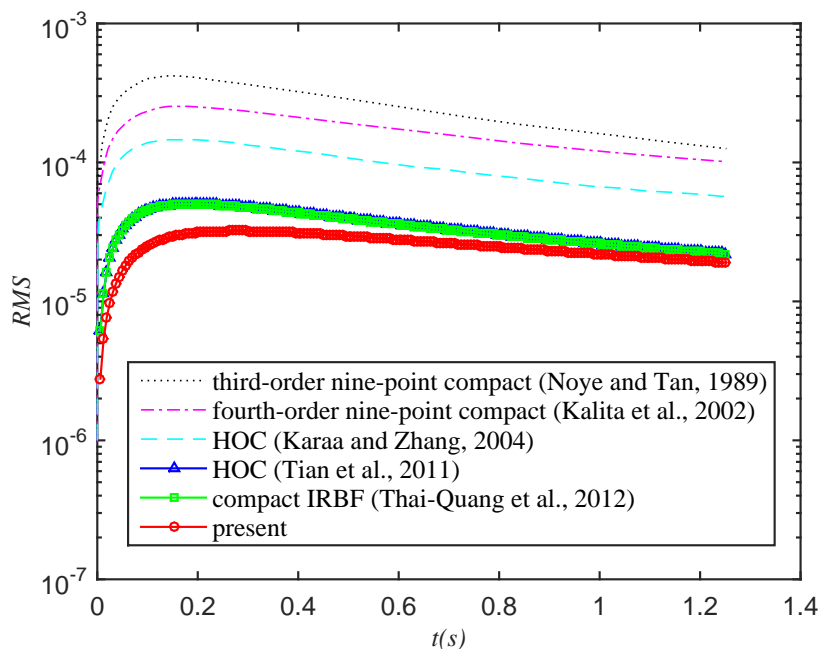
Figure 3.22 Unsteady convection-diffusion equation, $c_x = c_y = 0.8$ and $d_x = d_y = 0.01$, grid of 81×81, $\Delta t = 0.00625$, $t = 1.25$: The solution accuracy RMS against time. It is noted that the curves for the HOC and the compact IRBF are indistinguishable.

HPD scheme via this example, which is also considered in (Thai-Quang et al., 2012b). For comparison purposes, we also consider two sets of parameters used in their articles

Case I: $c_x = c_y = 0.8$, $d_x = d_y = 0.01$, $t = 1.25$, $\Delta t = 2.5E - 4$.

Case II: $c_x = c_y = 80$, $d_x = d_y = 0.01$, $t = 0.0125$, $\Delta t = 2.5E - 6$.

The corresponding Peclet number is thus $Pe = 2$ for case I and $Pe = 200$ for case II. Results concerning RMS and L_∞ errors are presented in Tables 3.6-3.8. In the case of low P_e, the present scheme is superior to the HPD and also other schemes (Table 3.6). In the case of high P_e (i.e. convection dominated), the coupled compact IRBF yields the best performance: higher degrees of accuracy (Table 3.7) and higher convergence rates (Table 3.8).

Table 3.6 Unsteady convection-diffusion equation, case I, grid of 81×81: Comparison of the solution accuracy between the present coupled compact IRBF scheme and some other techniques.

Method	$RMS(u)$	$L_\infty(u)$
HOC (Karaa and Zhang, 2004)	2.73E-05	2.46E-04
PDE (You, 2006)	2.20E-05	1.71E-04
HPD (Ma et al., 2012)	6.38E-05	6.54E-04
HOC (Tian et al., 2011)	2.79E-06	2.40E-05
compact IRBF (Thai-Quang et al., 2012b)	2.75E-06	2.37E-05
present	6.68E-07	6.43E-06

Table 3.7 Unsteady convection-diffusion equation, case II, grid of 81×81: Comparison of the solution accuracy between the present coupled compact IRBF scheme and some other techniques.

Method	$RMS(u)$	$L_\infty(u)$
HOC (Karaa and Zhang, 2004)	1.47E-02	2.42E-01
PDE (You, 2006)	5.49E-04	1.22E-02
HPD (Ma et al., 2012)	5.49E-04	1.24E-02
HOC (Tian et al., 2011)	5.46E-04	1.06E-02
compact IRBF (Thai-Quang et al., 2012b)	5.45E-04	1.06E-02
present	1.55E-04	2.93E-03

The effect of the MQ width on the solution accuracy is also plotted in Figure 3.23 for case I and in Figure 3.24 for case II. In both plots, it can be seen that the coupled compact IRBF gives much more accurate results than the compact IRBF.

Table 3.8 Unsteady convection-diffusion equation, case II: The solution accuracy of the present coupled compact IRBF scheme and some other techniques against the grid size. *LCR* stands for "*Local Convergence Rate*".

Grid ($n_x \times n_y$)	PDE You (2006)		HPD Ma et al. (2012)		HOC Tian et al. (2011)		compact IRBF Thai-Quang et al. (2012b)		present	
	RMS	$LCR^{(*)}$	RMS	$LCR^{(*)}$	RMS	$LCR^{(*)}$	RMS	$LCR^{(*)}$	RMS	$LCR^{(*)}$
31×31	1.93E-02	—	1.91E-02	—	2.42E-02	—	2.42E-02	—	1.19E-02	—
41×41	8.41E-03	2.98	8.30E-03	2.97	8.46E-03	3.76	8.45E-03	3.45	3.98E-03	3.92
51×51	3.74E-03	3.30	3.70E-03	3.29	3.74E-03	3.75	3.74E-03	3.58	1.41E-03	4.28
61×61	1.80E-03	3.51	1.78E-03	3.50	1.80E-03	3.84	1.79E-03	3.71	5.85E-04	4.45
71×71	9.51E-04	3.63	9.48E-04	3.62	9.49E-04	3.91	9.47E-04	3.80	2.84E-04	4.51
81×81	5.49E-04	3.69	5.49E-04	3.69	5.46E-04	3.95	5.45E-04	3.86	1.55E-04	4.52
101×101	2.21E-04	3.78	2.23E-04	3.76	2.19E-04	3.99	2.18E-04	3.91	5.80E-05	4.51
121×121	1.07E-04	3.81	1.10E-04	3.79	1.05E-04	4.00	1.04E-04	3.94	2.62E-05	4.49

$^{(*)} LCR = -\log[RMS(n_x)/RMS(31)]/\log[n_x/31]$.
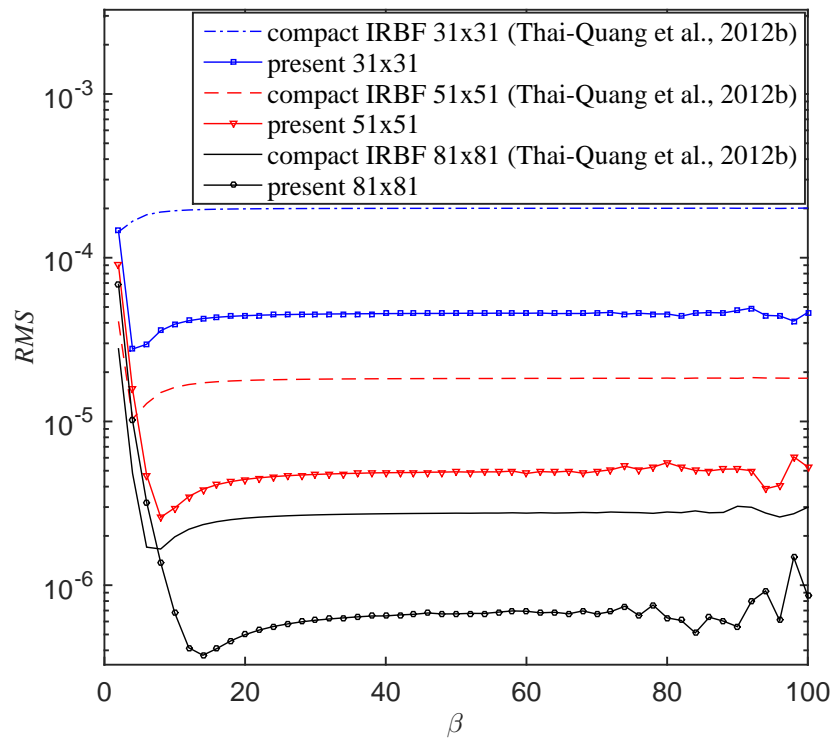
Figure 3.23 Unsteady convection-diffusion equation, case I, $\{31 \times 31, 51 \times 51, 81 \times 81\}$: The effect of the MQ width β on the solution accuracy RMS.
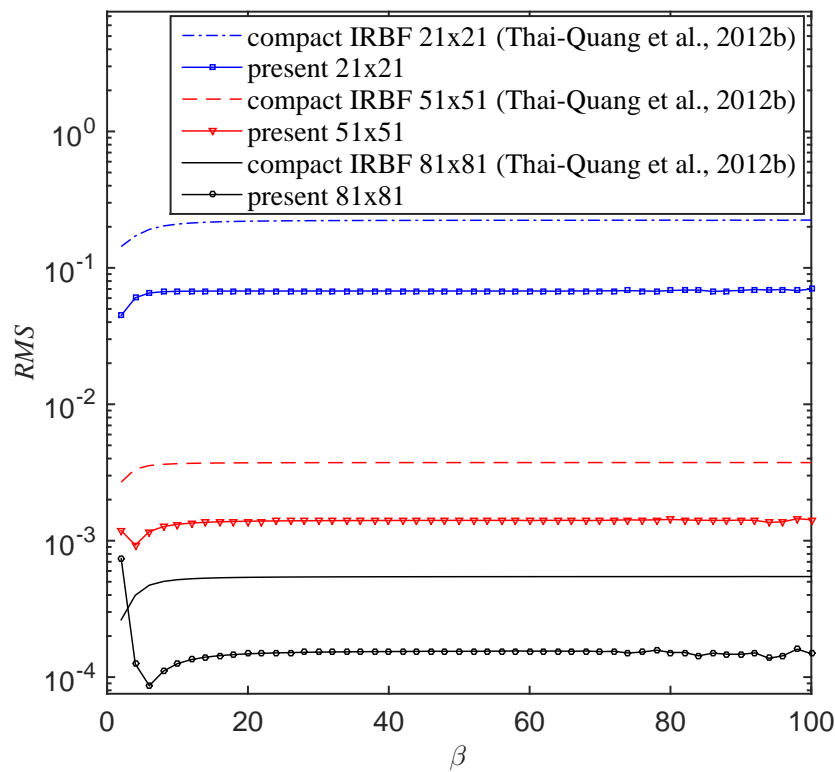
Figure 3.24 Unsteady convection-diffusion equation, case II, $\{21 \times 21, 51 \times 51, 81 \times 81\}$: The effect of the MQ width β on the solution accuracy RMS.

3.5 Concluding remarks

A coupled compact integrated radial basis function (IRBF) scheme has been proposed in this chapter. The proposed scheme is constructed over a three-point stencil, where nodal first- and second-order derivative values of the field variable are both incorporated into the approximation by means of their identity equations. This leads to a significant improvement in the solution accuracy and stability in comparison with the normal compact IRBF. Numerical examples indicate that the results obtained by the present scheme are superior to those of the compact IRBF, HOC and some other high-order schemes. Moreover, the enhanced convergence rate of the present scheme provides the present scheme with an ability to obtain a prescribed accuracy using smaller amount of time compared with the compact IRBF and HOC schemes. It can be stated that the coupled compact IRBF scheme is a stable, efficient and promising highly accurate method for both derivative computation and second-order differential solutions.

In the next chapter, we will integrate this coupled compact scheme into domain decomposition methods for solving large-scale fluid flow problems. The solution accuracy and efficiency of the serial and parallel algorithms implemented with the coupled compact IRBF will be presented.

Chapter 4

Coupled compact integrated RBF and domain decomposition scheme for fluid flows

This chapter presents a high-order coupled compact integrated RBF (IRBF) approximation based domain decomposition (DD) algorithms for the discretisation of second-order differential problems. Several Schwarz DD algorithms, including one-level additive/ multiplicative and two-level additive/ multiplicative/ hybrid, are employed. The coupled compact IRBF based DD algorithms are analysed with different grid sizes, numbers of sub-domains and overlap sizes for Poisson problems. Our convergence analysis shows that the coupled compact IRBF two-level multiplicative version is the most effective algorithm among various schemes employed here. Especially, the present coupled compact IRBF two-level method converges quite rapidly even when the domain is divided into many sub-domains, which shows great promise for either serial or parallel computing. For practical tests, we then incorporate the coupled compact IRBF into serial and parallel two-level multiplicative Schwarz. Several numerical examples, including those governed by Poisson and Navier-Stokes equations are analysed to demonstrate the accuracy and efficiency of the serial and parallel algorithms implemented with the coupled compact IRBF. Numerical results show: (i) the coupled compact IRBF-Serial and -Parallel algorithms have the capability to reach almost the same solution accuracy level of the coupled compact IRBF-Single domain, which is ideal in terms of computational calculations; (ii) the coupled compact

IRBF-Serial and -Parallel algorithms are highly accurate in comparison with standard finite difference, compact finite difference and some other schemes; (iii) the proposed coupled compact IRBF-Serial and -Parallel algorithms may be used as alternatives to solve large-size problems which the coupled compact IRBF-Single domain may not be able to deal with. The ability of producing stable and highly accurate results of the proposed serial and parallel schemes is believed to be the contribution of the coarse mesh of the two-level domain decomposition and the coupled compact IRBF approximation. It is noted that the focus of this chapter is on the derivation of highly accurate serial and parallel algorithms for second-order differential problems. The scope of this work does not cover a thorough analysis of computational time.

4.1 Introduction

Traditional techniques such as the finite difference method (FDM), finite volume method (FVM), finite element method (FEM) and boundary element method (BEM) are among the most popular numerical solution methods for partial differential equations (PDEs) governing many problems in engineering and sciences. These methods are based on some discretisation of a problem domain into small elements. These elements are not overlapping each other. If an element is heavily distorted, approximations on this element are of poor quality, leading to unacceptable accuracy or possibly failed computation. Element-free methods are developed to address the issues associated with element distortions by using different approximation methods over a cluster of scattered nodes. The smooth particle hydrodynamics method (SPH) (Lucy, 1977) is one of the initial and well developed element-free methods. The diffusive element method (DEM) (Nayroles et al., 1992) was the first element-free method to employ moving least squares (MLS) approximation (Lancaster and Salkauskas, 1981) in constructing their shape functions over scattered nodes. Several element-free methods have been proposed since then, including the element-free Galerkin method (EFG) (Belytschko et al., 1994), the reproducing kernel particle method (RKPM) (Liu et al., 1996), the partition of unity (PU) method (Babuska and Melenk, 1997)

and the meshless local Petrov-Galerkin method (MLPG) (Atluri and Zhu, 1998). For an overview on these element-free methods, readers may find more details in (Belytschko et al., 1994; Chen et al., 2006) and references therein.

In the last three decades, there has been great interest in using element-free radial basis function (RBF) methods for the numerical solutions of various types of PDEs. Kansa (1990a,b) introduced a new approach for this kind of problems, using radial basis functions (here referred as differential/direct RBF or DRBF) for the approximate solutions of PDEs. Mai-Duy and Tran-Cong (2001a,b, 2003) then proposed an idea of using indirect/integrated radial basis functions (IRBFs) for the solution of PDEs. Numerical examples in Mai-Duy and Tran-Cong (2001a,b, 2003, 2005) show that the IRBF approach achieves a greater accuracy than the DRBF approach. It has been shown that these RBF methods are more accurate than the traditional techniques such as the FDM, FVM and FEM (Zerroukat et al., 1998; Li et al., 2003b; Thai-Quang et al., 2012b). Furthermore, the RBF approaches can work with simple discretisation based on a Cartesian grid. However, when dealing with large-scale problems, a big obstacle for the global RBF method is that the system matrix is generally ill-conditioned, non-symmetric and dense. Therefore, the RBF method needs to be combined with the domain decomposition (DD) method to reduce the density and ill-conditioning of the matrix for an accurate solution.

The earliest idea of DD was introduced as a classical Schwarz alternating algorithm by Schwarz in 1870. Generally, DD methods can be classified into two major methods: overlapping methods, which are referred to as Schwarz methods, and non-overlapping methods, which are referred to as iterative sub-structuring or Schur complement methods (Smith et al., 1996; Quarteroni and Valli, 1999; Toselli and Widlund, 2005). In this work, we will concentrate on iterative Schwarz DD methods using overlapping sub-domains. The overlapping DD methods have a simple algorithmic structure because there is no need to solve the continuity problem across sub-domain interfaces (Cai, 2003). The overlapping methods provide parallel, potentially fast and robust algorithms for the solution of linear or nonlinear systems of equations resulting usually from the discretisation of PDEs.

It is noted that the convergence characteristics of the DD based methods are sensitive to the choice of the number of sub-domains, mesh sizes and overlap sizes. In particular, having too many sub-domains leads to a very large coarse mesh problem, while having too few sub-domains requires the solution of large problems for each sub-domain. Furthermore, having too small overlaps usually leads to a large number of iterations, while having too large overlaps leads to the solution of large problems for each sub-domain. In this point of view, efficient DD based methods should stably converge with a small number of iterations for a wide range of numbers of sub-domains and mesh sizes, using a small number of overlaps. For most of overlapping domain decomposition algorithms, it was reported that the overlapping ratio cannot be fixed a priori without a preliminary study. Indeed, if the ratio is too small, the error at the frontiers will increase, affecting the quality of the overall results, and if the ratio is too large, the quality will also be degraded due to a larger size of the sub-domains and a potentially higher complexity of the sub-functions to approximate. Although there is no analytical way to compute the optimal value of the overlapping ratio at the present, in practice it generally falls in between 10% and 20% of the width of a sub-domain (Smith et al., 1996; Palma et al., 2008).

In this chapter, we investigate convergence characteristics of the recently developed three-point coupled compact integrated RBF (IRBF) approximation scheme proposed in (Tien et al., 2015c) when incorporated into the Schwarz DD algorithms for solving Poisson problems. Different types of Schwarz DD algorithms are utilised, including the one-level additive/ multiplicative and two-level additive/ multiplicative/ hybrid. In the one-level algorithm, a fine mesh problem on each sub-domain is solved and the sub-domain solutions are interpolated back to the global grid. The two-level algorithm is formulated by adding the coarse mesh problem to the one-level problem. The use of the coarse mesh generally reduces the number of iterations. The present coupled compact IRBF based Schwarz DD algorithms are investigated with various grid sizes, numbers of sub-domains and overlap sizes. It is found that the present coupled compact IRBF two-level multiplicative version is far better than the other coupled compact IRBF based DD versions in terms of the iteration count. The present coupled compact IRBF

two-level multiplicative version shows a great promise for both serial and parallel computing because it is stable with various numbers of sub-domains and grid sizes while being able to converge quickly with very small overlap sizes.

Then, we incorporate the coupled compact IRBF into serial and parallel two-level multiplicative Schwarz algorithms for practical tests. We parallelise problems which are decomposed by the two-level multiplicative Schwarz with a colouring technique. The serial and parallel algorithms are so called coupled compact IRBF-Serial and -Parallel, respectively. To analyse their accuracy and efficiency, analytical examples including Poisson and Navier-Stokes equations are performed. Lid driven cavity problems, in which Taylor-series type boundary condition for vorticity is first implemented in the context of the coupled compact IRBF, are also analysed as practical applications. Numerical results show: (i) the results produced by the coupled compact IRBF-Serial and -Parallel have almost the same solution accuracy with those calculated by the coupled compact IRBF-Single domain, which is computationally ideal; (ii) the coupled compact IRBF-Serial and -Parallel algorithms are highly accurate in comparison with standard FDM, higher-order compact finite difference (HOC) and some other schemes; (iii) the proposed coupled compact IRBF-Serial and -Parallel algorithms can efficiently solve large-size problems which the single domain algorithms are struggling to handle.

This chapter is organised as follows. Section 4.2 reviews the coupled compact IRBF approximation scheme. In Section 4.3, we briefly describe the one-level additive/ multiplicative and two-level additive/ multiplicative/ hybrid. In Section 4.4, the GMRES iterative method is briefly mentioned. Section 4.5 explains the serial and parallel two-level multiplicative Schwarz DD methods, followed by Section 4.6 which details the parallel technique. Numerical examples demonstrating the convergence analysis and effectiveness of the algorithms are presented in Section 4.8. Finally, the concluding remarks of the chapter are given in Section 4.9.

4.2 Coupled compact IRBF scheme

The coupled compact integrated radial basis function (coupled compact IRBF) approximation scheme developed by Tien et al. (2015c) is utilised in this chapter. Readers may find more details about coupled compact IRBF scheme in (Tien et al., 2015c), which are summarised here for convenience.

The essence of the coupled compact IRBF scheme is to couple extra information of the nodal first- and second-order derivative values via their identity equations, which makes the scheme more accurate, stable and efficient. Hereafter, for brevity, η denotes either x or y in a generic local stencil $\{\eta_1, \eta_2, \eta_3\}$, where $\eta_1 < \eta_2 < \eta_3$ and $\eta_2 \equiv \eta_{(i,j)}$, are illustrated in Figure 4.1
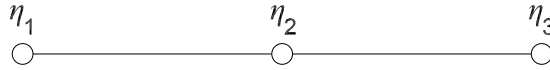
Figure 4.1 Compact three-point 1D-IRBF stencil for interior nodes.

4.2.1 First-order derivatives at interior nodes

For the coupled compact approximation of the first-order derivatives at interior nodes, nodal derivative values (i.e. extra information) are chosen as not only $\left\{\frac{du_1}{d\eta}; \frac{du_3}{d\eta}\right\}$ but also $\left\{\frac{d^2u_1}{d\eta^2}; \frac{d^2u_3}{d\eta^2}\right\}$. At a particular interior node, the approximation is processed through three steps: (i) we first approximate its first-order derivative over its associated three-point stencil involving $\left\{\frac{du_1}{d\eta}; \frac{du_3}{d\eta}\right\}$; (ii) we then approximate its first-order derivative over the same stencil used in step (i) involving $\left\{\frac{d^2u_1}{d\eta^2}; \frac{d^2u_3}{d\eta^2}\right\}$; (iii) an identity equation of the first-order derivative is employed to enhance the level of compactness of the stencil. Both $\left\{\frac{du_1}{d\eta}; \frac{du_3}{d\eta}\right\}$ and $\left\{\frac{d^2u_1}{d\eta^2}; \frac{d^2u_3}{d\eta^2}\right\}$ are incorporated into the first-order derivative approximation.

First-order derivatives at interior nodes involving $\left\{ \frac{du_1}{d\eta}; \frac{du_3}{d\eta} \right\}$

At $\eta = \eta_2$, the approximation formulation of the stencil is expressed in the matrix-vector form as

$$\begin{bmatrix} -\mu_{1F4} & 1 & -\mu_{1F5} \end{bmatrix} \mathbf{u}'^n + \begin{bmatrix} 0 & 0 & 0 \end{bmatrix} \mathbf{u}'''^n = \begin{bmatrix} \mu_{1F1} & \mu_{1F2} & \mu_{1F3} \end{bmatrix} \mathbf{u}^n, \quad (4.1)$$

where $\{\mu_{1Fi}\}_{i=1}^{5}$ is the set of IRBFs in the physical space, in which 1 and F stand for the 1st derivatives to be approximated and the extra information of the nodal first-order derivative values chosen, respectively; $\mathbf{u}'^n = [u_1'^n, u_2'^n, u_3'^n]^T$; $\mathbf{u}'''^n = [u_1'''^n, u_2'''^n, u_3'''^n]^T$; and, $\mathbf{u}^n = [u_1{}^n, u_2{}^n, u_3{}^n]^T$. It is noted that $\mathbf{u}'''^n$ is introduced here to produce a general form for the coupling task which is mentioned later on.

First-order derivatives at interior nodes involving $\left\{ \frac{d^2u_1}{d\eta^2}; \frac{d^2u_3}{d\eta^2} \right\}$

At $\eta = \eta_2$, the approximation formulation of the stencil is expressed in the matrix-vector form as

$$\begin{bmatrix} 0 & 1 & 0 \end{bmatrix} \mathbf{u}'^n + \begin{bmatrix} -\mu_{1S4} & 0 & -\mu_{1S5} \end{bmatrix} \mathbf{u}'''^n = \begin{bmatrix} \mu_{1S1} & \mu_{1S2} & \mu_{1S3} \end{bmatrix} \mathbf{u}^n, \quad (4.2)$$

where $\{\mu_{1Si}\}_{i=1}^{5}$ is the set of IRBFs in the physical space, in which 1 and S stand for the 1st derivatives to be approximated and the extra information of the nodal second-order derivative values chosen, respectively; $\mathbf{u}'^n = [u_1'^n, u_2'^n, u_3'^n]^T$; $\mathbf{u}'''^n = [u_1'''^n, u_2'''^n, u_3'''^n]^T$; and, $\mathbf{u}^n = [u_1{}^n, u_2{}^n, u_3{}^n]^T$.

First-order derivative couplings at interior nodes

At $\eta = \eta_2$, a coupling equation in matrix-vector form is described as

$$\begin{bmatrix} \mu_{1F4} & 0 & \mu_{1F5} \end{bmatrix} \mathbf{u}'^n + \begin{bmatrix} -\mu_{1S4} & 0 & -\mu_{1S5} \end{bmatrix} \mathbf{u}'''^n$$
$$= \begin{bmatrix} (\mu_{1S1} - \mu_{1F1}) & (\mu_{1S2} - \mu_{1F2}) & (\mu_{1S3} - \mu_{1F3}) \end{bmatrix} \mathbf{u}^n, \quad (4.3)$$

where $\mathbf{u}'^n = [u_1'^n, u_2'^n, u_3'^n]^T$; $\mathbf{u}'''^n = [u_1'''^n, u_2'''^n, u_3'''^n]^T$; and, $\mathbf{u}^n = [u_1{}^n, u_2{}^n, u_3{}^n]^T$.

4.2.2 First-order derivatives at boundary nodes

At the boundary nodes, the first-order derivatives are approximated in special compact stencils. Consider the boundary node, e.g. η_1. Its associated stencil is $\{\eta_1, \eta_2, \eta_3, \eta_4\}$ as shown in Figure 4.2. For the coupled compact approximation of the first-order derivative at the boundary node η_1, nodal derivative values (i.e. extra information) are chosen as both $\frac{du_2}{d\eta}$ and $\frac{d^2u_2}{d\eta^2}$. The approximation is processed through three steps: (i) we first approximate its first-order derivative over its associated four-point stencil involving $\frac{du_2}{d\eta}$; (ii) we then approximate its first-order derivative over the same stencil used in step (i) involving $\frac{d^2u_2}{d\eta^2}$; (iii) an identity equation of the first-order derivative is employed to enhance the level of compactness of the stencil. Both $\frac{du_2}{d\eta}$ and $\frac{d^2u_2}{d\eta^2}$ are incorporated into the second-order derivative approximation.

Figure 4.2 Special compact four-point 1D-IRBF stencil for boundary nodes.

First-order derivatives at boundary node η_1 involving $\frac{du_2}{d\eta}$

$$\begin{bmatrix} 1 & -\mu_{\mathrm{sp1F5}} & 0 & 0 \end{bmatrix} \mathbf{u}'^n + \begin{bmatrix} 0 & 0 & 0 & 0 \end{bmatrix} \mathbf{u}''^n$$
$$= \begin{bmatrix} \mu_{\mathrm{sp1F1}} & \mu_{\mathrm{sp1F2}} & \mu_{\mathrm{sp1F3}} & \mu_{\mathrm{sp1F4}} \end{bmatrix} \mathbf{u}^n, \quad (4.4)$$

where $\mathbf{u}'^n = [u_1'^n, u_2'^n, u_3'^n, u_4'^n]^T$; $\mathbf{u}''^n = [u_1''^n, u_2''^n, u_3''^n, u_4''^n]^T$; and, $\mathbf{u}^n = [u_1^n, u_2^n, u_3^n, u_4^n]^T$.

First-order derivatives at boundary node η_1 involving $\frac{d^2u_2}{d\eta^2}$

$$\begin{bmatrix} 1 & 0 & 0 & 0 \end{bmatrix} \mathbf{u}'^n + \begin{bmatrix} 0 & -\mu_{\mathrm{sp1S5}} & 0 & 0 \end{bmatrix} \mathbf{u}''^n$$
$$= \begin{bmatrix} \mu_{\mathrm{sp1S1}} & \mu_{\mathrm{sp1S2}} & \mu_{\mathrm{sp1S3}} & \mu_{\mathrm{sp1S4}} \end{bmatrix} \mathbf{u}^n, \quad (4.5)$$

where $\mathbf{u}'^n = [u_1'{}^n, u_2'{}^n, u_3'{}^n, u_4'{}^n]^T$; $\mathbf{u}''^n = [u_1''{}^n, u_2''{}^n, u_3''{}^n, u_4''{}^n]^T$; and, $\mathbf{u}^n = [u_1{}^n, u_2{}^n, u_3{}^n, u_4{}^n]^T$.

First-order derivative coupling at boundary node η_1

$$
\begin{bmatrix} 0 & \mu_{\mathrm{sp1F5}} & 0 & 0 \end{bmatrix} \mathbf{u}'^n + \begin{bmatrix} 0 & -\mu_{\mathrm{sp1S5}} & 0 & 0 \end{bmatrix} \mathbf{u}''^n
$$
$$
= \begin{bmatrix} (\mu_{\mathrm{sp1S1}} - \mu_{\mathrm{sp1F1}}) & (\mu_{\mathrm{sp1S2}} - \mu_{\mathrm{sp1F2}}) & (\mu_{\mathrm{sp1S3}} - \mu_{\mathrm{sp1F3}}) & (\mu_{\mathrm{sp1S4}} - \mu_{\mathrm{sp1F4}}) \end{bmatrix} \mathbf{u}^n,
$$
$$
(4.6)
$$

where $\mathbf{u}'^n = [u_1'{}^n, u_2'{}^n, u_3'{}^n, u_4'{}^n]^T$; $\mathbf{u}''^n = [u_1''{}^n, u_2''{}^n, u_3''{}^n, u_4''{}^n]^T$; and, $\mathbf{u}^n = [u_1{}^n, u_2{}^n, u_3{}^n, u_4{}^n]^T$.

In a similar manner, one is able to calculate the first-order derivative at the boundary node η_{n_η}.

4.2.3 Second-order derivatives at interior nodes

In a similar manner as in Section 4.2.1, one is able to calculate the coupled compact approximation of the second-order derivatives at interior nodes as follows.

Second-order derivatives at interior nodes involving $\left\{ \frac{du_1}{d\eta}; \frac{du_3}{d\eta} \right\}$

At $\eta = \eta_2$, the approximation formulation of the stencil is expressed in the matrix-vector form as

$$
\begin{bmatrix} -\nu_{\mathrm{2F4}} & 0 & -\nu_{\mathrm{2F5}} \end{bmatrix} \mathbf{u}'^n + \begin{bmatrix} 0 & 1 & 0 \end{bmatrix} \mathbf{u}''^n = \begin{bmatrix} \nu_{\mathrm{2F1}} & \nu_{\mathrm{2F2}} & \nu_{\mathrm{2F3}} \end{bmatrix} \mathbf{u}^n, \quad (4.7)
$$

where $\{\nu_{\mathrm{2Fi}}\}_{i=1}^5$ is the set of IRBFs in the physical space, in which 2 and F stand for the 2nd derivatives to be approximated and the extra information of the first-order derivatives, respectively; $\mathbf{u}'^n = [u_1'{}^n, u_2'{}^n, u_3'{}^n]^T$; $\mathbf{u}''^n = [u_1''{}^n, u_2''{}^n, u_3''{}^n]^T$; and, $\mathbf{u}^n = [u_1{}^n, u_2{}^n, u_3{}^n]^T$.

Second-order derivatives at interior nodes involving $\left\{ \frac{d^2 u_1}{d\eta^2}; \frac{d^2 u_3}{d\eta^2} \right\}$

At $\eta = \eta_2$, the approximation formulation of the stencil is expressed in the matrix-vector form as

$$\begin{bmatrix} 0 & 0 & 0 \end{bmatrix} \mathbf{u}'^n + \begin{bmatrix} -\nu_{2S4} & 1 & -\nu_{2S5} \end{bmatrix} \mathbf{u}''^n = \begin{bmatrix} \nu_{2S1} & \nu_{2S2} & \nu_{2S3} \end{bmatrix} \mathbf{u}^n, \quad (4.8)$$

where $\{\nu_{2Si}\}_{i=1}^{5}$ is is the set of IRBFs in the physical space, in which 2 and S stand for the 2nd derivatives to be approximated and the extra information of the second-order derivatives, respectively; $\mathbf{u}'^n = [u_1'^n, u_2'^n, u_3'^n]^T$; $\mathbf{u}''^n = [u_1''^n, u_2''^n, u_3''^n]^T$; and, $\mathbf{u}^n = [u_1{}^n, u_2{}^n, u_3{}^n]^T$.

Second-order derivative couplings at interior nodes

At $\eta = \eta_2$, a coupling equation in the matrix-vector form is described as

$$\begin{bmatrix} \nu_{2F4} & 0 & \nu_{2F5} \end{bmatrix} \mathbf{u}'^n + \begin{bmatrix} -\nu_{2S4} & 0 & -\nu_{2S5} \end{bmatrix} \mathbf{u}''^n$$
$$= \begin{bmatrix} (\nu_{2S1} - \nu_{2F1}) & (\nu_{2S2} - \nu_{2F2}) & (\nu_{2S3} - \nu_{2F3}) \end{bmatrix} \mathbf{u}^n, \quad (4.9)$$

where $\mathbf{u}'^n = [u_1'^n, u_2'^n, u_3'^n]^T$; $\mathbf{u}''^n = [u_1''^n, u_2''^n, u_3''^n]^T$; and $\mathbf{u}^n = [u_1{}^n, u_2{}^n, u_3{}^n]^T$.

4.2.4 Second-order derivatives at boundary nodes

In a similar manner as in Section 4.2.2, one is able to calculate the coupled compact approximation of the second-order derivatives at boundary nodes as follows.

Second-order derivatives at boundary node η_1 **involving** $\frac{du_2}{d\eta}$

$$\begin{bmatrix} 0 & -\nu_{sp2F5} & 0 & 0 \end{bmatrix} \mathbf{u}'^n + \begin{bmatrix} 1 & 0 & 0 & 0 \end{bmatrix} \mathbf{u}''^n$$
$$= \begin{bmatrix} \nu_{sp2F1} & \nu_{sp2F2} & \nu_{sp2F3} & \nu_{sp2F4} \end{bmatrix} \mathbf{u}^n, \quad (4.10)$$

where $\mathbf{u}'^n = [u'^n_1, u'^n_2, u'^n_3, u'^n_4]^T$; $\mathbf{u}''^n = [u''^n_1, u''^n_2, u''^n_3, u''^n_4]^T$; and, $\mathbf{u}^n = [u_1{}^n, u_2{}^n, u_3{}^n, u_4{}^n]^T$.

Second-order derivatives at boundary node η_1 involving $\frac{d^2 u_2}{d\eta^2}$

$$\begin{bmatrix} 0 & 0 & 0 & 0 \end{bmatrix} \mathbf{u}'^n + \begin{bmatrix} 1 & -\nu_{\text{sp2S5}} & 0 & 0 \end{bmatrix} \mathbf{u}''^n$$
$$= \begin{bmatrix} \nu_{\text{sp2S1}} & \nu_{\text{sp2S2}} & \nu_{\text{sp2S3}} & \nu_{\text{sp2S4}} \end{bmatrix} \mathbf{u}^n, \quad (4.11)$$

where $\mathbf{u}'^n = [u'^n_1, u'^n_2, u'^n_3, u'^n_4]^T$; $\mathbf{u}''^n = [u''^n_1, u''^n_2, u''^n_3, u''^n_4]^T$; and, $\mathbf{u}^n = [u_1{}^n, u_2{}^n, u_3{}^n, u_4{}^n]^T$.

Second-order derivative coupling at boundary node η_1

$$\begin{bmatrix} 0 & \nu_{\text{sp2F5}} & 0 & 0 \end{bmatrix} \mathbf{u}'^n + \begin{bmatrix} 0 & -\nu_{\text{sp2S5}} & 0 & 0 \end{bmatrix} \mathbf{u}''^n$$
$$= \begin{bmatrix} (\nu_{\text{sp2S1}} - \nu_{\text{sp2F1}}) & (\nu_{\text{sp2S2}} - \nu_{\text{sp2F2}}) & (\nu_{\text{sp2S3}} - \nu_{\text{sp2F3}}) & (\nu_{\text{sp2S4}} - \nu_{\text{sp2F4}}) \end{bmatrix} \mathbf{u}^n,$$
$$(4.12)$$

where $\mathbf{u}'^n = [u'^n_1, u'^n_2, u'^n_3, u'^n_4]^T$; $\mathbf{u}''^n = [u''^n_1, u''^n_2, u''^n_3, u''^n_4]^T$; and, $\mathbf{u}^n = [u_1{}^n, u_2{}^n, u_3{}^n, u_4{}^n]^T$.

In an similar manner, one is able to calculate the second-order derivative at the boundary node η_{n_η}.

4.2.5 Matrix assembly for first- and second-order derivative expressions

The IRBF system on a grid line for the first-order derivative is obtained by letting the interior node taking values from 2 to $(n_\eta - 1)$ in (4.1), (4.2), and (4.3); and, making use of (4.4), (4.5), and (4.6) for the boundary nodes 1 and n_η. In a similar manner, the IRBF system on a grid line for the second-order derivative is obtained by letting the interior node taking values from 2 to $(n_\eta - 1)$ in (4.7), (4.8), and (4.9); and, making use of (4.10), (4.11), and (4.12) for the boundary

nodes 1 and n_η. The resultant matrix assembly is expressed as

$$
\underbrace{\begin{bmatrix}
\mathbf{A}_{1F} & \mathbf{0} \\
\mathbf{A}_{1S} & \mathbf{B}_{1S} \\
\mathbf{A}_{1FS} & \mathbf{B}_{1FS} \\
\mathbf{A}_{2F} & \mathbf{B}_{2F} \\
\mathbf{0} & \mathbf{B}_{2S} \\
\mathbf{A}_{2FS} & \mathbf{B}_{2FS}
\end{bmatrix}}_{\text{Coefficient matrix}}
\begin{bmatrix}
\mathbf{u}'^n \\
\mathbf{u}''^n
\end{bmatrix}
=
\begin{bmatrix}
\mathbf{R}_{1F} \\
\mathbf{R}_{1S} \\
\mathbf{R}_{1FS} \\
\mathbf{R}_{2F} \\
\mathbf{R}_{2S} \\
\mathbf{R}_{2FS}
\end{bmatrix}
\mathbf{u}^n ,
\tag{4.13}
$$

where $\mathbf{A}_{1F}$, $\mathbf{A}_{1S}$, $\mathbf{B}_{1S}$, $\mathbf{A}_{1FS}$, $\mathbf{B}_{1FS}$, $\mathbf{A}_{2F}$, $\mathbf{B}_{2F}$, $\mathbf{B}_{2S}$, $\mathbf{A}_{2FS}$, $\mathbf{B}_{2FS}$, and $\mathbf{0}$ are $n_\eta \times n_\eta$ matrices; $\mathbf{u}'^n = \left\{ u_1'^n, u_2'^n, ..., u_{n_\eta}'^n \right\}^T$; $\mathbf{u}''^n = \left\{ u_1''^n, u_2''^n, ..., u_{n_\eta}''^n \right\}^T$; and, $\mathbf{u}^n = \left\{ u_1^n, u_2^n, ..., u_{n_\eta}^n \right\}^T$. The coefficient matrix is sparse with diagonal, bi-diagonal, and tri-diagonal sub-matrices. Solving (4.13) yields

$$
\mathbf{u}'^n = \mathbf{D}_\eta \mathbf{u}^n,
\tag{4.14}
$$

$$
\mathbf{u}''^n = \mathbf{D}_{\eta\eta} \mathbf{u}^n,
\tag{4.15}
$$

where $\mathbf{D}_\eta$ and $\mathbf{D}_{\eta\eta}$ are $n_\eta \times n_\eta$ matrices. The approximations of the first- and second-order derivatives, $\mathbf{u}'$ and $\mathbf{u}''$, respectively, are will be used for calculations in the following sections.

4.3 Domain decomposition preconditioners

This chapter presents the implementation of the Schwarz domain decomposition (DD) preconditioned GMRES techniques using the coupled compact IRBF approximation scheme for the convergence analysis for Poisson problems. In order to describe the working principles of the Schwarz DD methods, we will first reintroduce the classical alternating and parallel Schwarz algorithms for Poisson problems as below. For more information about the Schwarz DD methods, readers are referred to the literature in (Smith et al., 1996; Danaila, 2007).

4.3.1 Classical Schwarz

In one dimension, the Poisson problem is expressed as follows.

$$
\begin{cases}
-u''(x) = f(x) & \text{for} \quad x \in (a, b), \\
u(a) = u_a, \\
u(b) = u_b,
\end{cases}
\tag{4.16}
$$

where u'' are the operators of the approximation of the second-order derivative; f are given right hand side values; u are solutions; and, u_a and u_b are boundary values. The computational interval $[a, b]$ is discretised on $n + 2$ points $x_i = a + ih$ for $i = 0, ..., n + 1$ with a uniform step $h = \frac{b-a}{n+1}$. For simplicity, we decompose the computational interval $[a, b]$ into two sub-intervals with overlapping: we choose an odd value n and two integer values i_l and i_r symmetric with respect to $\frac{n+1}{2}$ such that $i_l < \frac{n+1}{2} < i_r$. We set $x_l = i_l h$ and $x_r = i_r h$, thus defining two intervals $[a, x_r]$ and $[x_l, b]$ with a nonempty overlap $[a, x_r] \cap [x_l, b] = [x_l, x_r] = \Omega_0 \neq \varnothing$. The problem domain and sub-domains become $\Omega = (a, b)$, $\Omega_1 = (a, x_r)$, and $\Omega_2 = (x_l, b)$, respectively. It is noted that the domains Ω, Ω_1 and Ω_2 do not include their boundaries and $\cup_{i=1}^{2}\Omega_i = \Omega$.

We now compute the solution u to the problem (4.16) by solving two problems on sub-intervals $[a, x_r]$ and $[x_l, b]$. The solution u_1 (respectively u_2) is expected to be the restriction on the $[a, x_r]$ (respectively $[x_l, b]$) of the solution u to the problem on the full interval $[a, b]$. The two solutions u_1 and u_2 must therefore be identical within the overlapping region $[x_l, x_r]$, which allows us to define the boundary conditions in x_l and x_r

$$
u_1(x_r) = \beta = u_2(x_r) \quad \text{and} \quad u_1(x_l) = \alpha = u_2(x_l),
\tag{4.17}
$$

Initially, the values of α and β are "guessed" by linear interpolation of the global boundary conditions

$$
\alpha = \frac{1}{b-a} \left\{ u_a(b - x_l) + u_b(x_l - a) \right\},
\tag{4.18}
$$

$$\beta = \frac{1}{b-a} \left\{ u_a(b - x_r) + u_b(x_r - a) \right\}.$$ (4.19)

Classical alternating Schwarz

In alternating Schwarz method, a sequence (u_1^n, u_2^n) for $n \geq 0$ is built by solving alternatively the same equations (4.16) in $[a, x_r]$ and $[x_l, b]$ with the values on the boundary defined by the previously computed values in the other sub-domain. The alternating Schwarz method begins by selecting an initial guess $u_2{}^0(x_r) = \beta$. Then, iteratively for $n = 1, 2, 3...$, one solves the boundary value problem

$$[a, x_r] \begin{cases} -u_1''^n(x) = f(x) \quad \text{for} \quad x \in \Omega_1 = (a, x_r), \\ u_1{}^n(a) = u_a, \\ u_1{}^n(x_r) = u_2{}^{n-1}(x_r), \end{cases}$$ (4.20)

for solution $u_1{}^n$. This is followed by the solution of the boundary value problem

$$[x_l, b] \begin{cases} -u_2''^n(x) = f(x) \quad \text{for} \quad x \in \Omega_2 = (x_l, b), \\ u_2{}^n(x_l) = u_1{}^n(x_l), \\ u_2{}^n(b) = u_b, \end{cases}$$ (4.21)

for solution $u_2{}^n$.

Classical parallel Schwarz

In parallel Schwarz method, we set $u_1{}^0(x_l) = \alpha$ and $u_2{}^0(x_r) = \beta$. The computations in $[a, x_r]$ and $[x_l, b]$ are made in parallel

$$[a, x_r] \begin{cases} -u_1''^n(x) = f(x) \quad \text{for} \quad x \in (a, x_r), \\ u_1{}^n(a) = u_a, \\ u_1{}^n(x_r) = u_2{}^{n-1}(x_r), \end{cases}$$ (4.22)

and

$$[x_l, b] \begin{cases} -u_2''^n(x) = f(x) \text{ for } x \in (x_l, b), \\ u_2{}^n(x_l) = u_1{}^{n-1}(x_l), \\ u_2{}^n(b) = u_b, \end{cases} \tag{4.23}$$

for solution $u_1{}^n$ and $u_2{}^n$.

The two classical algorithms described above can be modified to get additive, multiplicative and hybrid DD preconditioners used in a Krylov subspace solver such as GMRES. For convenience, we only summarise those DD preconditioners in this chapter as below. For more details, readers refer to (Smith et al., 1996).

4.3.2 Addictive, multiplicative and hybrid Schwarz preconditioners

Figure 4.3 illustrates the decomposition of the global domain Ω into two sub-domains Ω_i, where Ω_i are overlapping sub-domains.
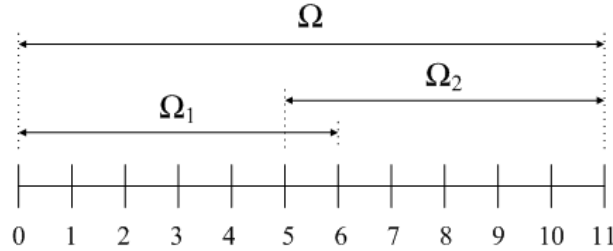
Figure 4.3 An example of decomposition of a domain into two sub-domains.

We define the restriction map $\mathbf{R}_i$ from global domain Ω to sub-domain Ω_i as follows.

$$\mathbf{R}_1 = \begin{bmatrix} \mathbf{I}_{\Omega_1} & \mathbf{0} \end{bmatrix}, \tag{4.24}$$

$$\mathbf{R}_2 = \begin{bmatrix} \mathbf{0} & \mathbf{I}_{\Omega_2} \end{bmatrix}, \tag{4.25}$$

where $\mathbf{I}$ are identity matrices. Then, sub-domain matrix is defined as

$$\mathbf{A}_i = \mathbf{R}_i \mathbf{A} \mathbf{R}_i^T, \tag{4.26}$$

where $\mathbf{A}$ is the problem system matrix and $\mathbf{R}_i^T$ is the interpolation map from global domain Ω to sub-domain Ω_i. For general description, we assume that the

global domain Ω is divided into q sub-domains, where $q \geq 2$.

One-level additive Schwarz preconditioner

The one-level additive Schwarz preconditioner is simply formulated as.

Algorithm 1 : one-level additive Schwarz preconditioner

$$\mathbf{v} \leftarrow \sum_{i=1}^{q} \mathbf{B}_i \mathbf{r}, \tag{4.27}$$

where $\mathbf{r}$ is the residual; $\mathbf{B}_i = \mathbf{R}_i^T \mathbf{A}_i^{-1} \mathbf{R}_i$ restricts the residual $\mathbf{r}$ to sub-domain Ω_i; and, $\mathbf{v}$ is Krylov vector in the GMRES algorithm.

One-level multiplicative Schwarz preconditioner

One-level multiplicative Schwarz preconditioner, the sequential version of the one-level additive Schwarz preconditioner, is expressed as follows.

Algorithm 2 : one-level multiplicative Schwarz preconditioner

$$\mathbf{v} \leftarrow \mathbf{B}_1 \mathbf{r}, \tag{4.28}$$

$$\mathbf{v} \leftarrow \mathbf{v} + \mathbf{B}_2 (\mathbf{r} - \mathbf{A}\mathbf{v}), \tag{4.29}$$

$$...$$

$$\mathbf{v} \leftarrow \mathbf{v} + \mathbf{B}_q (\mathbf{r} - \mathbf{A}\mathbf{v}). \tag{4.30}$$

Partition of unity coarse meshes for two-level algorithms : In the two-level methods, coarse meshes need to be constructed. We define the coarse mesh on the existing fine mesh (Jenkins et al., 2001). By this way, we do not need to create the coarse mesh geometry or use the geometric information about sub-domains. Figure 4.4 shows the discretisation of a fine mesh into two coarse meshes with one coarse mesh map per sub-domain Ω_i, where $\Omega_0 = \Omega_1 \cap \Omega_2$ is an overlapping region.
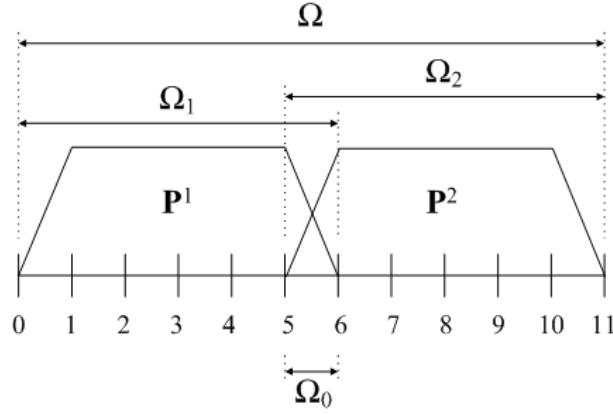
Figure 4.4 An example of discretisation of two coarse meshes.

We use the partition of unity (PU), i.e. to sum up to one everywhere in the domain of calculation, and let $\mathbf{P}^i$ be a PU subordinate to the covering partition Ω_i of Ω with the following conditions

$$\begin{cases} \mathbf{P}^1 + \mathbf{P}^2 = \mathbf{1}, \\ \mathbf{0} \leq \mathbf{P}^1, \mathbf{P}^2 \leq \mathbf{1}, \\ \mathbf{P}^1 \equiv \mathbf{1} \text{ on } \Omega_1 \setminus \Omega_0 \text{ and } \mathbf{P}^1 \equiv \mathbf{0} \text{ on } \Omega_2 \setminus \Omega_0, \\ \mathbf{P}^2 \equiv \mathbf{1} \text{ on } \Omega_2 \setminus \Omega_0 \text{ and } \mathbf{P}^2 \equiv \mathbf{0} \text{ on } \Omega_1 \setminus \Omega_0. \end{cases} \tag{4.31}$$

Similarly to the one-level, we will choose $\mathbf{R}_0$, a coarse mesh restriction map from fine to coarse meshes, such that it has the form

$$\mathbf{R}_0 = \begin{bmatrix} \mathbf{W}^1 \\ \mathbf{W}^2 \end{bmatrix}, \tag{4.32}$$

where $\mathbf{W}^1$ and $\mathbf{W}^2$ are defined as

$$\mathbf{W}_1 = \mathbf{P}^1 / \|\mathbf{P}^1\|_2 \text{ and } \mathbf{W}_2 = \mathbf{P}^2 / \|\mathbf{P}^2\|_2, \tag{4.33}$$

$\|\cdot\|_2$ denotes Euclidean norm. A Galerkin or variational coarse grid correction uses the fine grid matrix to obtain the coarse mesh matrix as follows.

$$\mathbf{A}_0 = \mathbf{R}_0 \mathbf{A} \mathbf{R}_0^T, \tag{4.34}$$

where $\mathbf{R}_0^T$ is a coarse mesh interpolation map from fine to coarse meshes. For general description, we again assume that the global domain Ω is divided into q sub-domains, where $q \geq 2$.

Two-level additive Schwarz preconditioner

The two-level additive Schwarz is formed by adding the coarse mesh problem to the one-level additive problem.

Algorithm 3 : two-level additive Schwarz preconditioner

$$\mathbf{v} \leftarrow \left(\mathbf{R}_0^T \mathbf{A}_0^{-1} \mathbf{R}_0 + \sum_{i=1}^{q} \mathbf{B}_i \right) \mathbf{r}. \tag{4.35}$$

Two-level multiplicative Schwarz preconditioner

The two-level multiplicative Schwarz is formed by adding the coarse mesh problem to the one-level multiplicative as follows. It is noted that the coarse mesh problem is solved only once at the beginning of calculation.

Algorithm 4 : two-level multiplicative Schwarz preconditioner

$$\mathbf{v} \leftarrow \mathbf{R}_0^T \mathbf{A}_0^{-1} \mathbf{R}_0 \mathbf{r}, \tag{4.36}$$

$$\mathbf{v} \leftarrow \mathbf{v} + \mathbf{B}_1(\mathbf{r} - \mathbf{A}\mathbf{v}), \tag{4.37}$$

$$...$$

$$\mathbf{v} \leftarrow \mathbf{v} + \mathbf{B}_q(\mathbf{r} - \mathbf{A}\mathbf{v}). \tag{4.38}$$

Two-level hybrid I Schwarz preconditioner

The two-level hybrid I is formulated on the basis of the one-level multiplicative by adding the coarse mesh problem to its last stage.

Algorithm 5 : two-level hybrid I Schwarz preconditioner

$$\mathbf{v} \leftarrow \mathbf{B}_1\mathbf{r}, \tag{4.39}$$

$$\mathbf{v} \leftarrow \mathbf{v} + \mathbf{B}_2(\mathbf{r} - \mathbf{A}\mathbf{v}), \tag{4.40}$$

$$...$$

$$\mathbf{v} \leftarrow \mathbf{v} + \mathbf{B}_q(\mathbf{r} - \mathbf{A}\mathbf{v}). \tag{4.41}$$

$$\mathbf{v} \leftarrow \mathbf{v} + \mathbf{R}_0^T\mathbf{A}_0^{-1}\mathbf{R}_0\mathbf{r}. \tag{4.42}$$

Two-level hybrid II Schwarz preconditioner

The two-level hybrid II is formulated on the basis of the one-level additive by adding the coarse mesh problem to its last stage.

Algorithm 6 : two-level hybrid II Schwarz preconditioner

$$\mathbf{v} \leftarrow \sum_{i=1}^{q} \mathbf{B}_i\mathbf{r}, \tag{4.43}$$

$$\mathbf{v} \leftarrow \mathbf{v} + \mathbf{R}_0^T\mathbf{A}_0^{-1}\mathbf{R}_0(\mathbf{r} - \mathbf{A}\mathbf{v}). \tag{4.44}$$

4.4 GMRES

We utilise a generalised minimal residual algorithm (GMRES) for solving non-symmetric linear systems. More information about GMRES may be found in (Saad and Schultz, 1986; Strang, 2007). Consider the linear system

$$\mathbf{A}\mathbf{u} = \mathbf{f}, \tag{4.45}$$

where $\mathbf{f}$ are given right hand side values; $\mathbf{u}$ are unknowns; and, $\mathbf{A}$ is the problem system matrix. The GMRES algorithm is outlined in Table 4.1, where *Algorithm*★ is used to represent one of the six preconditioning algorithms mentioned above and ε is the GMRES tolerance.

Table 4.1 GMRES Algorithm.

Initialisation	
$\mathbf{r}_0 \leftarrow \mathbf{f} - \mathbf{A}\mathbf{u}_0$	compute initial residual
$\beta \leftarrow \|\mathbf{r}_0\|_2$	compute initial residual norm
$\mathbf{v}_1 \leftarrow \mathbf{r}_0/\beta$	define first Krylov vector
$\mathbf{g} \leftarrow \beta \mathbf{e}_1$	initialise right hand side
Iteration	
1. **for** $j = 1, 2, ..., k, ...,$ **until satisfied do**	
2. $\quad \mathbf{v}_{j+1} \leftarrow Algorithm\bigstar\ (\mathbf{v}_j)$	preconditioning step
3. $\quad \mathbf{v}_{j+1} \leftarrow \mathbf{A}\mathbf{v}_{j+1}$	matrix-vector product
4. $\quad$ **for** $i = 1, 2, ..., j$	modified Gramm-Schmidt orthogonalisation
5. $\qquad h_{i,j} \leftarrow (\mathbf{v}_i, \mathbf{v}_{j+1})$	
6. $\qquad \mathbf{v}_{j+1} \leftarrow \mathbf{v}_{j+1} - h_{i,j}\mathbf{v}_i$	
7. $\quad h_{j+1,j} \leftarrow \|\mathbf{v}_{j+1}\|_2$	
8. $\quad \mathbf{v}_{j+1} \leftarrow \mathbf{v}_{j+1}/h_{j+1,j}$	define next Krylov vector
9. $\quad$ **for** $i = 1, 2, ..., j$	previous Givens rotation on $\mathbf{H}$
10. $\quad \begin{cases} h_{i,j} \leftarrow c_i h_{i,j} + s_i h_{i+1,j} \\ h_{i+1,j} \leftarrow -s_i h_{i,j} + c_i h_{i+1,j} \end{cases}$	
11. $\quad \gamma \leftarrow \sqrt{h_{j,j}^2 + h_{j+1,j}^2}$	compute next Givens rotation
12. $\quad c_j \leftarrow h_{j,j}/\gamma; \quad s_j \leftarrow h_{j+1,j}/\gamma$	
13. $\quad \begin{cases} h_{j,j} \leftarrow \gamma \\ h_{j+1,j} \leftarrow 0 \end{cases}$	Givens rotation on $\mathbf{H}$
14. $\quad \begin{cases} g_j \leftarrow c_j g_j \\ g_{j+1} \leftarrow -s_j g_j \end{cases}$	Givens rotation on $\mathbf{g}$
15. $\quad$ **if** $|g_{j+1}| \leq \varepsilon$ **exit loop**	loop convergence check
Form approximate solution	
$\begin{Bmatrix} y_1 \\ \vdots \\ y_j \end{Bmatrix} \leftarrow \begin{bmatrix} h_{1,1} & \cdots & h_{1,j} \\ \vdots & \ddots & \vdots \\ 0 & \cdots & h_{j,j} \end{bmatrix}^{-1} \begin{Bmatrix} g_1 \\ \vdots \\ g_j \end{Bmatrix}$	back substitution
$\mathbf{u}_k \leftarrow \mathbf{u}_0 + \mathbf{V}_k \mathbf{y}_k.$	form approximate solution

Note: *Algorithm*$\bigstar$ is used to represent one of the six preconditioning algorithms mentioned in Section 4.3.2.

4.5 Serial and parallel two-level multiplicative Schwarz DD methods

For numerical examples, we incorporate the coupled compact IRBF into serial and parallel two-level multiplicative Schwarz DD methods to solve the linear system (4.45) as follows.

4.5.1 Serial two-level multiplicative Schwarz

First, solve the coarse mesh problem once at the beginning

$$\mathbf{u} \leftarrow \mathbf{B}_0(\mathbf{f} - \mathbf{A}\mathbf{u}), \tag{4.46}$$

Then, solve the fine mesh problem

$$\mathbf{u} \leftarrow \mathbf{u} + \mathbf{B}_1(\mathbf{f} - \mathbf{A}\mathbf{u}), \tag{4.47}$$

$$...$$

$$\mathbf{u} \leftarrow \mathbf{u} + \mathbf{B}_q(\mathbf{f} - \mathbf{A}\mathbf{u}), \tag{4.48}$$

where $\mathbf{B}_i = \mathbf{R}_i^T \mathbf{A}_i^{-1} \mathbf{R}_i$.

4.5.2 Parallel two-level multiplicative Schwarz

The serial two-level multiplicative Schwarz method mentioned above has very little potential for parallelism. This is easily fixed. It is noted that there are often many sub-domains which share no common grid points as shown in Figure 4.5. The numerical solution on these sub-domains, therefore, could be updated simultaneously, in parallel.

Define a colouring of the sub-domains in the way described in (Smith et al., 1996). For each sub-domain, we associate a colour in the way that no two sub-domains sharing common grid points have the same colour. Let i be the number of colours used.
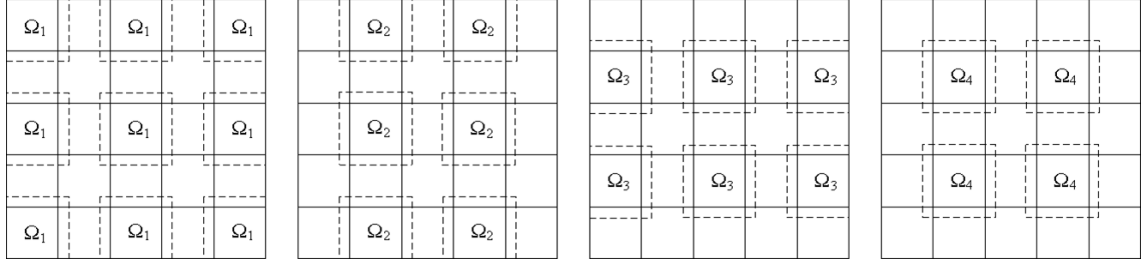
Figure 4.5 Colouring of 5×5 sub-domains into four classes.

In this chapter, we introduce the coarse mesh problem into the original colouring technique of Smith et al. (1996). We can now generate a i-step method as follows.

First, solve the coarse mesh problem once at the beginning

$$\mathbf{u}^n \leftarrow \mathbf{B}_0 \left(\mathbf{f} - \mathbf{A}\mathbf{u}^n \right), \tag{4.49}$$

Then, solve the fine mesh problem

$$\mathbf{u}^{n+1/i} \leftarrow \mathbf{u}^n + \sum_{i \in \Omega_1} \mathbf{B}_i \left(\mathbf{f} - \mathbf{A}\mathbf{u}^n \right), \tag{4.50}$$

$$\mathbf{u}^{n+2/i} \leftarrow \mathbf{u}^{n+1/i} + \sum_{i \in \Omega_2} \mathbf{B}_i \left(\mathbf{f} - \mathbf{A}\mathbf{u}^{n+1/i} \right), \tag{4.51}$$

$$...$$

$$\mathbf{u}^{n+1} \leftarrow \mathbf{u}^{n+(i-1)/i} + \sum_{i \in \Omega_4} \mathbf{B}_i \left(\mathbf{f} - \mathbf{A}\mathbf{u}^{n+(i-1)/i} \right), \tag{4.52}$$

where $(n + 1)$ is the current time level.

4.6 Parallelism

The parallel implementation is based on the colouring technique explained in Section 4.5.2. As shown in Figure 4.5, four colours are used to mark colours of sub-domains so that sub-domains with the same colour do not overlap each other. In each sub-step from (4.50) to (4.52), when one colour is considered, each CPU is assigned to solve the problem in each sub-domain within that colour. Then, the results from sub-domains will be exchanged between themselves in order for

each sub-domain to obtain a unique copy of the whole domain solution. In next sub-step, the next colour is considered and this process keeps going until the convergence measurement reaches a predefined value.

In this implementation, the broadcast communication is used because each sub-domain needs to send information to and receive it from all other sub-domains. As whole domain solution is kept in each sub-domain and updated after each sub-step, the convergence measurement calculated in each sub-domain is consistent with all other sub-domains. This ensures the concurrent convergence of sub-domains and thus alleviate the need of a dedicated termination algorithm for the whole system.

4.7 Stream function-vorticity formulation

The transient Navier-Stokes equations for an incompressible viscous fluid in the stream function-vorticity formulation are expressed in the dimensionless conservative forms as follows.

$$\frac{\partial \omega}{\partial t} + \frac{\partial (u\omega)}{\partial x} + \frac{\partial (v\omega)}{\partial y} = \frac{1}{Re}\left(\frac{\partial^2}{\partial x^2} + \frac{\partial^2}{\partial y^2}\right)\omega, \tag{4.53}$$

$$\left(\frac{\partial^2}{\partial x^2} + \frac{\partial^2}{\partial y^2}\right)\psi = -\omega. \tag{4.54}$$

It is well known that equations in the conservative form generally produce more accurate results compared to those in the non-conservative form (Niyogi et al., 2009). In equations (4.53) and (4.54), ψ is the stream function; ω is the vorticity; $Re = Ul/\nu$ is the Reynolds number, in which ν, l and U are the kinematic viscosity, characteristic length and characteristic speed of the flow, respectively; and, u and v velocity components in x- and y-directions, respectively, are given by

$$u = \frac{\partial \psi}{\partial y} \quad \text{and} \quad v = -\frac{\partial \psi}{\partial x}. \tag{4.55}$$

At current time level, n, stream function equation is expressed as

$$\left(\frac{\partial^2}{\partial x^2} + \frac{\partial^2}{\partial y^2}\right)\psi^n = -\omega^{n-1}, \tag{4.56}$$

; and, velocities are expressed as

$$u^n = \frac{\partial \psi^n}{\partial y} \quad \text{and} \quad v^n = -\frac{\partial \psi^n}{\partial x}. \tag{4.57}$$

The temporal discretisation of (4.53) results in

$$\frac{\omega^n - \omega^{n-1}}{\partial t} = \frac{1}{Re} \left(\frac{\partial^2}{\partial x^2} + \frac{\partial^2}{\partial x^2} \right) \omega^{n-1} - \frac{\partial(u^n \omega^{n-1})}{\partial x} - \frac{\partial(v^n \omega^{n-1})}{\partial y}. \tag{4.58}$$

4.8 Numerical examples

We chose the MQ function as the basis function, i.e. (1.6), in the present calculations.

Measurement Criteria: We evaluate the performance of the present schemes through the following measures.

i. The root mean square error (RMS) is defined as

$$RMS = \sqrt{\frac{\sum_{i=1}^{N} \left(f_i - \overline{f}_i \right)^2}{N}}, \tag{4.59}$$

where f_i and $\overline{f}_i$ are the computed and exact values of the solution f at the i-th node, respectively; and, N is the number of nodes over the whole domain.

ii. The average absolute error (L_1) is defined as

$$L_1 = \frac{1}{N} \sum_{i=1}^{N} |f_i - \overline{f}_i|. \tag{4.60}$$

iii. The global convergence rate, α, with respect to the grid refinement is defined through

$$RMS(h) \approx \gamma h^\alpha = O(h^\alpha), \tag{4.61}$$

where h is the grid size; and, γ and α are exponential model's parameters.

iv. A flow is considered to reach its steady state when

$$\sqrt{\frac{\sum_{i=1}^{N} \left(f_i^n - f_i^{n-1}\right)^2}{N}} < 10^{-8}. \tag{4.62}$$

v. Speed-up, S, and efficiency, E are defined as

$$S = \frac{T_s}{T_p}, \tag{4.63}$$

$$E = \frac{S}{p} \times 100, \tag{4.64}$$

where T_s is computation time on a single CPU; T_p is computation time on parallel CPUs; and, p is the number of parallel CPUs. In particular, T_s is defined as the computation time of the coupled compact IRBF-Single domain in this chapter.

Subdomain partition: Referring the sub-domain partition presented in (Jenkins et al., 2001), we let $h = 2^{-m}$ be the scale of the fine mesh and let the overlap o be the nearest integer larger than

$$2^m o_1, \tag{4.65}$$

where o_1 is the overlap that depends on the physical sub-domain. For example, overlap of 1% is determined by letting $o_1 = 0.01$. The global grid is an $n \times n$ mesh where $n = 2^m + o$. We will use 2^p sub-divisions in each direction so there will be 2^{p+1} sub-domains, each of size $m \times m$, where

$$m = 2^{m-p} + o - 1. \tag{4.66}$$

The scale H of the sub-domains is defined as 2^{-p}. This way of partition allows for a perfect split with all intervals having equal length. Figure 4.6 illustrates an example of decomposition of the 2D domain Ω.

In this work, calculations are done with a Dell computer, Precision T7600. Its specifications are Intel(R) Xeon(R) CPU E5-2687W 0 3.10 GHz 3.10 GHz (2 pro-
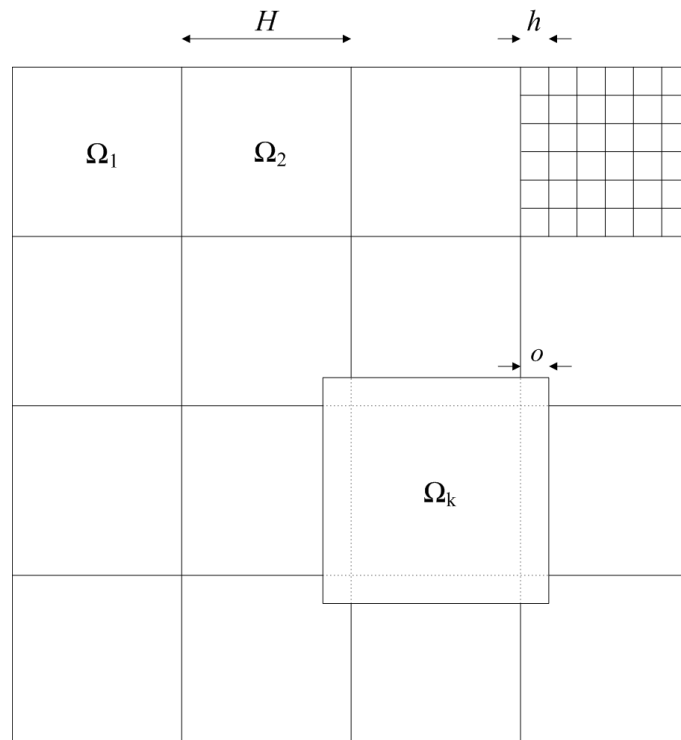
Figure 4.6 An example of decomposition of Ω into sub-domains $\Omega_1, \Omega_2, ..., \Omega_k, ...$

cessors), memory(RAM) of 128GB and 64-bit operating system. The Matlab(R) version 2014 is utilised. In serial and parallel algorithms, the overlapping is chosen between 1% to 25%. In parallel computing, the percentage of communication time is calculated with respect to its total computation time.

4.8.1 Convergence analysis of coupled compact IRBF based additive/ multiplicative/ hybrid Schwarz for 2D Poisson

We now apply the GMRES algorithm described in Section 4.4 for the 2D case. The Poisson problem becomes $-(u''_{xx} + u''_{yy}) = f$. We consider the right hand side f equal to $-2\pi^2 sin(\pi x)sin(\pi y)$ and the solution is required to be zero on the boundary of $[0,1]^2$. Calculations are carried out on coarse meshes of size $H = 1/4, 1/8$ and $1/16$ and fine meshes of size roughly $h = 1/32, 1/64$ and $1/128$. The value of $\beta = 50$ is simply chosen. We terminate calculations when the GMRES residual is smaller than 0.01. We tabulate iteration counts upon termination. In Tables 4.2-4.7, H is decreased by a factor of two going down the columns and h is similarly decreased going across the rows. We increase the overlap size as

$\{1\%, 5\%, 10\%, 15\%, 20\%, 25\%\}$. We consider calculations having the number of iteration larger than 100 to be not stable and unlikely to converge. For plots of iteration count versus overlap percentage and of GMRES residual versus iteration count, we deliberately choose the case where $H = 1/8$ and $h = 1/128$ to be a representative case for each overlap case because calculations with $H = 1/8$ and $h = 1/128$ are reasonably stable in our experiments.

One-level additive Schwarz preconditioner

Table 4.2 shows the iteration counts of the one-level additive preconditioned GM-RES using the present coupled compact IRBF. More details about convergence characteristics of the present one-level additive algorithm are shown in Figure 4.7. It appears that the present coupled compact IRBF one-level additive algorithm performs best with an overlap around 20%.

Table 4.2 One-level additive preconditioned GMRES using the present coupled compact IRBF: number of iteration required to achieve convergence.

$H \setminus h$	one-level additive		
	1/32	1/64	1/128
overlap $= 1\%$			
1/4	17	23	20
1/8	23	29	19
1/16	32	39	18
overlap $= 5\%$			
1/4	12	13	18
1/8	13	13	21
1/16	11	13	26
overlap $= 10\%$			
1/4	10	14	14
1/8	10	17	16
1/16	13	16	18
overlap $= 15\%$			
1/4	12	10	10
1/8	15	13	14
1/16	18	16	17
overlap $= 20\%$			
1/4	12	12	9
1/8	15	16	13
1/16	23	23	19
overlap $= 25\%$			
1/4	9	10	11
1/8	13	14	15
1/16	20	21	21
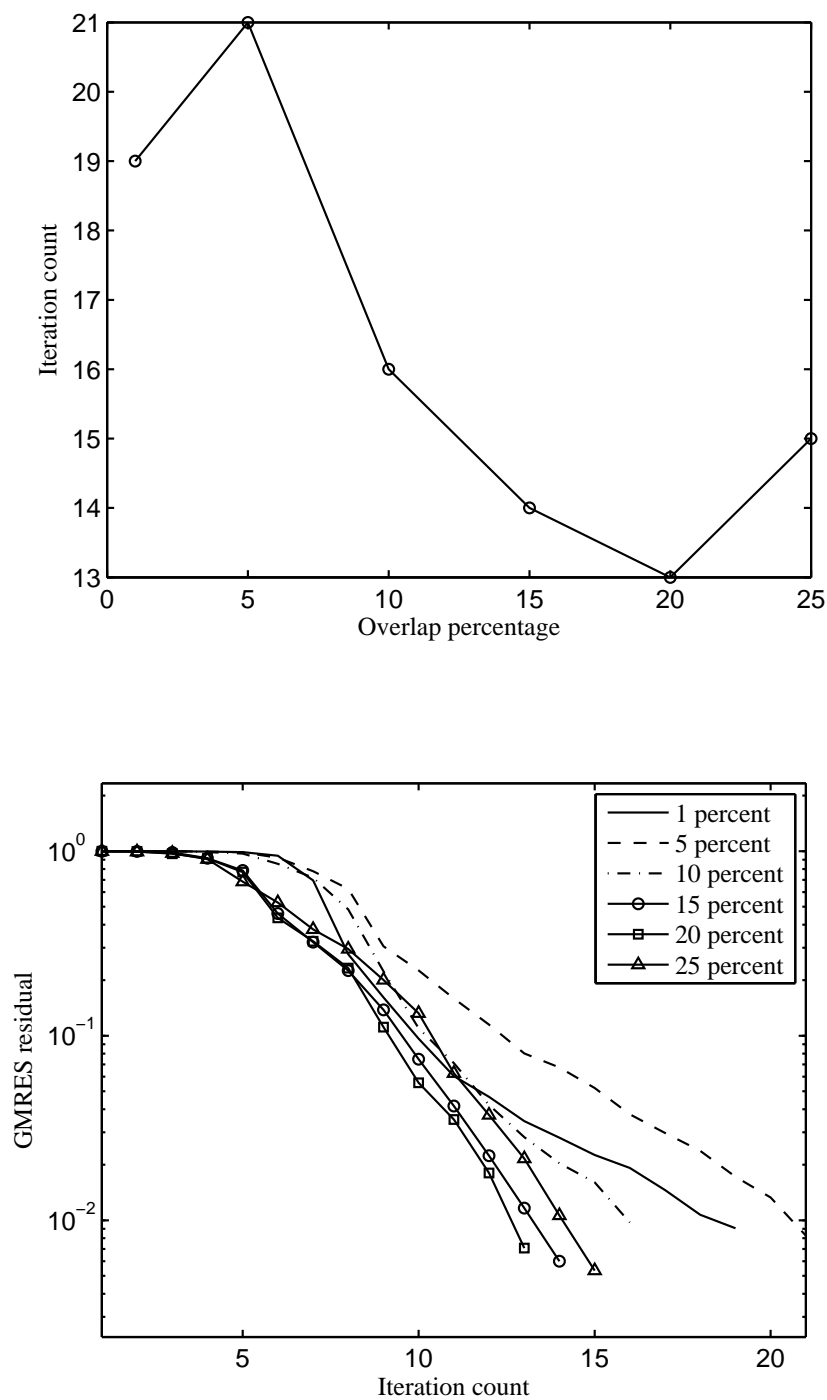
Figure 4.7 One-level additive preconditioned GMRES using the present coupled compact IRBF: Iteration count versus overlap percentage (top) and GMRES residual versus iteration count (bottom).

One-level multiplicative Schwarz preconditioner

The iteration counts of the one-level multiplicative preconditioned GMRES using the present coupled compact IRBF are provided in Table 4.3. The iteration counts of the present one-level multiplicative algorithm are much smaller than those of the present one-level additive algorithm tabulated in Tables 4.2, except for the case of 1% overlap. Especially, with cases where $H = 1/16$, the iteration counts of the present one-level multiplicative algorithm are much smaller than those figures of the present one-level additive algorithm in Tables 4.2. Plots of iteration count versus overlap percentage and GMRES residual versus iteration count are illustrated in Figure 4.8. It can be seen that the present coupled compact IRBF one-level multiplicative algorithm performs best with the overlap between 15% and 20%.

Table 4.3 One-level multiplicative preconditioned GMRES using the present coupled compact IRBF: number of iteration required to achieve convergence.

$H \setminus h$	one-level multiplicative		
	1/32	1/64	1/128
	overlap = 1%		
1/4	51	25	11
1/8	19	95	12
1/16	19	34	17
	overlap = 5%		
1/4	8	7	8
1/8	9	9	11
1/16	9	10	16
	overlap = 10%		
1/4	6	7	7
1/8	7	9	9
1/16	7	12	12
	overlap = 15%		
1/4	6	6	6
1/8	8	6	7
1/16	12	7	8
	overlap = 20%		
1/4	6	6	6
1/8	7	7	6
1/16	8	7	7
	overlap = 25%		
1/4	5	5	5
1/8	5	5	6
1/16	5	6	6
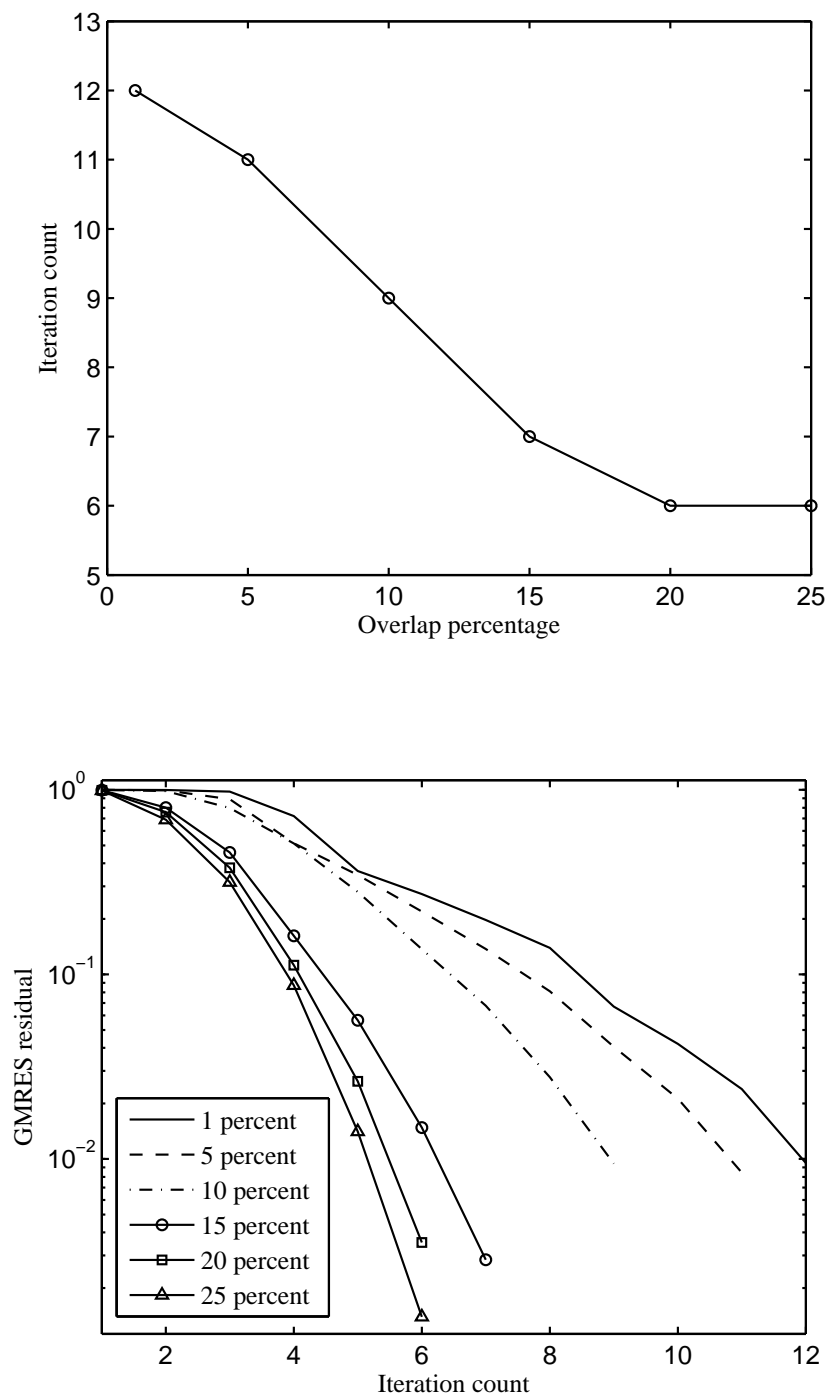
Figure 4.8 One-level multiplicative preconditioned GMRES using the present coupled compact IRBF: Iteration count versus overlap percentage (top) and GMRES residual versus iteration count (bottom).

Two-level additive Schwarz preconditioner

Table 4.4 shows the iteration counts of the two-level additive preconditioned GMRES using the present coupled compact IRBF. The present two-level additive scheme is comparable with the present one-level additive scheme shown in Table 4.2. As shown in Figure 4.9, the present coupled compact IRBF two-level additive scheme performs best with an overlap of around 10%.

Table 4.4 Two-level additive preconditioned GMRES using the present coupled compact IRBF: number of iteration required to achieve convergence.

$H \setminus h$	two-level additive		
	1/32	1/64	1/128
	overlap = 1%		
1/4	16	21	21
1/8	15	19	20
1/16	11	16	16
	overlap = 5%		
1/4	11	13	17
1/8	11	11	15
1/16	16	17	10
	overlap = 10%		
1/4	9	12	13
1/8	12	10	11
1/16	15	16	18
	overlap = 15%		
1/4	10	9	9
1/8	16	15	15
1/16	15	16	16
	overlap = 20%		
1/4	9	10	8
1/8	14	14	13
1/16	22	21	19
	overlap = 25%		
1/4	11	11	12
1/8	14	14	14
1/16	21	21	21

Two-level multiplicative Schwarz preconditioner

Table 4.5 shows the iteration statistics of the two-level multiplicative preconditioned GMRES using the present coupled compact IRBF. In comparison with the present one-level additive/ multiplicative and two-level additive algorithms shown in Table 4.2, 4.3 and 4.4, respectively, the present two-level multiplicative algorithm is superior with much smaller iterations. Figure 4.10 depicts fast con-
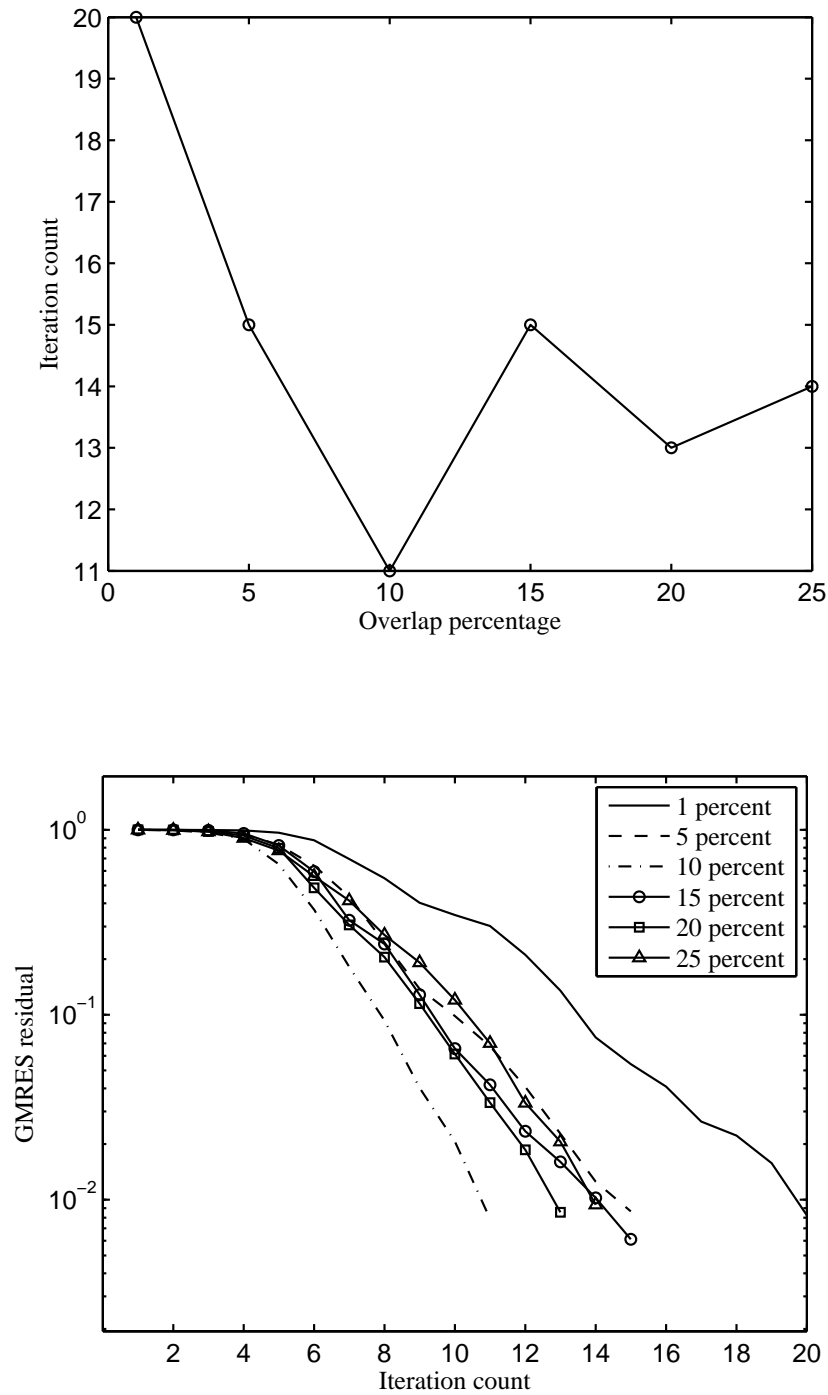
Figure 4.9 Two-level additive preconditioned GMRES using the present coupled compact IRBF: Iteration count versus overlap percentage (top) and GMRES residual versus iteration count (bottom).

vergence of the present two-level multiplicative algorithm for overlap from 10% up to 25%. Moreover, the smaller the overlap size, the faster the calculation, and therefore, the overlap of 10% is recommended for the present coupled compact IRBF two-level multiplicative.

Table 4.5 Two-level multiplicative preconditioned GMRES using the HOC and the present coupled compact IRBF: number of iteration required to achieve convergence.

	HOC Tian et al. (2011)			two-level multiplicative		
$H \setminus h$	1/32	1/64	1/128	1/32	1/64	1/128
	overlap $= 1\%$					
1/4	100+	100+	59	10	13	12
1/8	100+	100+	88	9	13	11
1/16	–	100+	100+	5	9	8
	overlap $= 5\%$					
1/4	20	5	6	7	6	7
1/8	8	4	5	5	5	7
1/16	30	6	2	8	7	4
	overlap $= 10\%$					
1/4	3	4	5	4	5	5
1/8	4	2	3	5	5	4
1/16	4	5	5	5	8	8
	overlap $= 15\%$					
1/4	3	3	3	5	4	4
1/8	4	4	4	6	5	4
1/16	2	3	4	9	5	5
	overlap $= 20\%$					
1/4	2	2	3	4	4	3
1/8	4	4	4	5	5	4
1/16	3	3	3	6	6	4
	overlap $= 25\%$					
1/4	5	5	6	4	4	3
1/8	6	6	7	5	4	4
1/16	6	6	6	4	4	4

For comparison purposes, we incorporate the high order compact (HOC) finite difference of (Tian et al., 2011) into the DD two-level multiplicative Schwarz preconditioned GMRES algorithm. It can be seen that the present coupled compact IRBF two-level multiplicative scheme produces much better results than those of the HOC two-level multiplicative scheme at the overlap of 1% and 25%. For other overlap cases, the present coupled compact IRBF two-level multiplicative algorithm is comparable with the HOC two-level multiplicative algorithm.
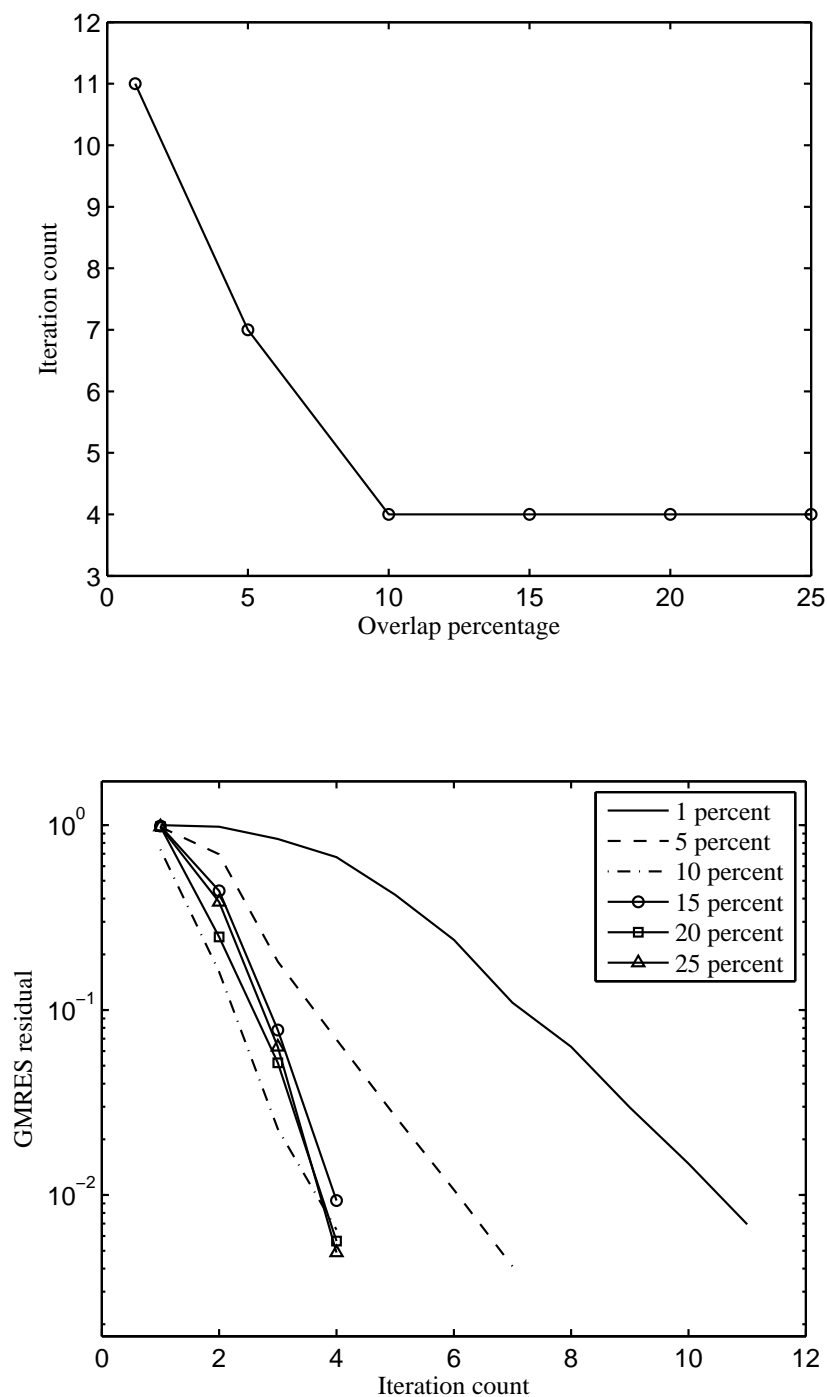
Figure 4.10 Two-level multiplicative preconditioned GMRES using the present coupled compact IRBF: Iteration count versus overlap percentage (top) and GMRES residual versus iteration count (bottom).

Two-level hybrid I Schwarz preconditioner

The iteration statistics of the two-level hybrid I preconditioned GMRES using the present coupled compact IRBF are presented in Table 4.6. In comparison with the present two-level multiplicative shown in Table 4.5, the present two-level hybrid I is less effective with larger iteration counts. Plots of iteration count versus overlap percent and GMRES residual versus iteration count for the present two-level hybrid I are depicted in Figure 4.11. It can be seen that the present coupled compact IRBF two-level hybrid I performs best around an overlap of 10%.

Table 4.6 Two-level hybrid-I preconditioned GMRES using the present coupled compact IRBF: number of iteration required to achieve convergence.

$H \setminus h$	two-level hybrid-I		
	1/32	1/64	1/128
	overlap = 1%		
1/4	15	17	14
1/8	13	28	16
1/16	6	15	14
	overlap = 5%		
1/4	9	9	10
1/8	8	8	9
1/16	10	11	6
	overlap = 10%		
1/4	6	7	8
1/8	8	6	6
1/16	8	10	11
	overlap = 15%		
1/4	8	6	6
1/8	8	7	7
1/16	12	8	8
	overlap = 20%		
1/4	7	6	6
1/8	7	7	7
1/16	9	8	7
	overlap = 25%		
1/4	6	6	6
1/8	7	7	7
1/16	7	7	7

Two-level hybrid II Schwarz preconditioner

Table 4.7 reports the iteration counts of the two-level hybrid-II preconditioned GMRES using the present coupled compact IRBF. At the overlap of 1%, 5%, 10%
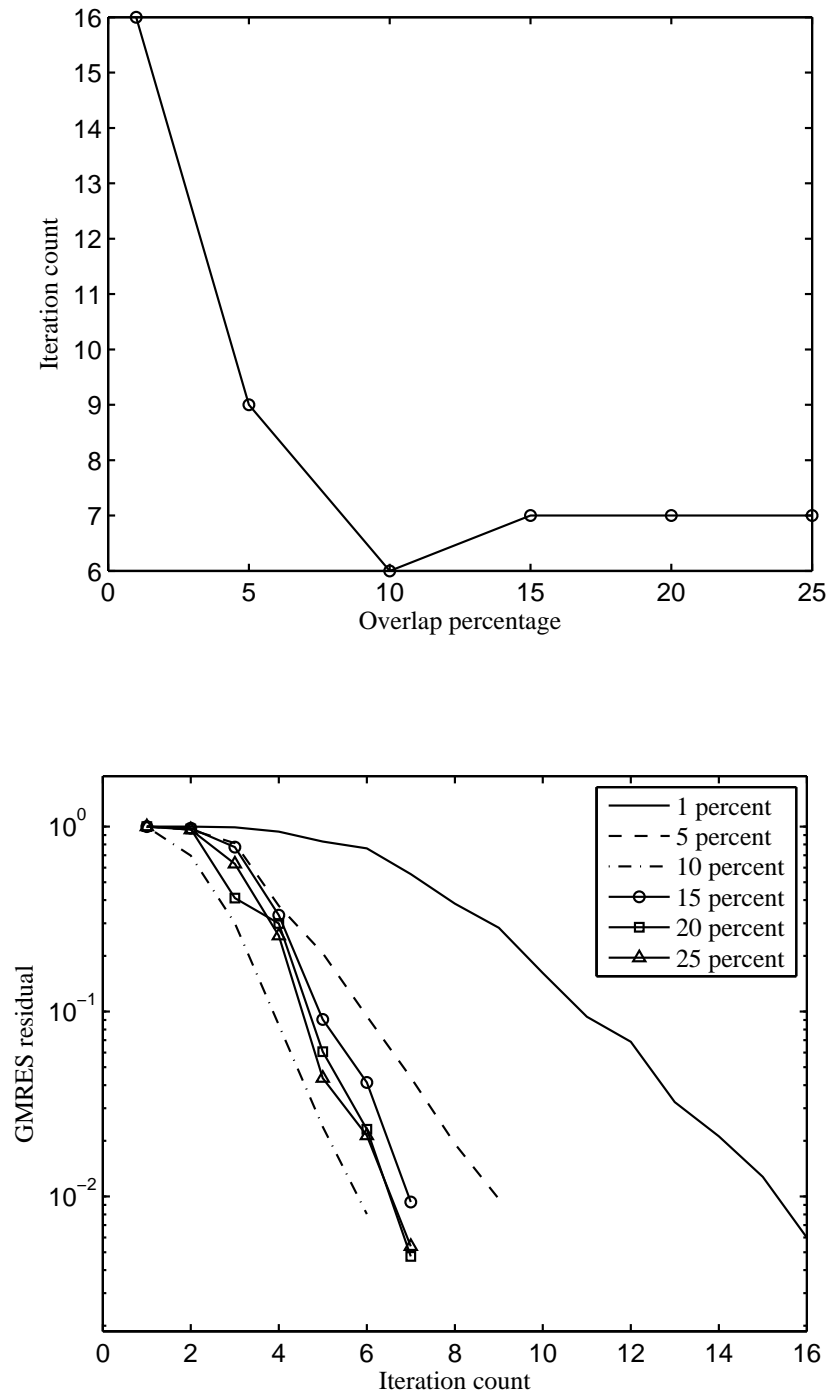
Figure 4.11 Two-level hybrid I preconditioned GMRES using the present coupled compact IRBF: Iteration count versus overlap percentage (top) and GMRES residual versus iteration count (bottom).

and 15%, the present two-level hybrid-II shows better results compared to those of the present one- and two-level additive in Tables 4.2 and 4.4, respectively. For other overlap cases where $H = 1/16$, the iteration counts of the present two-level hybrid-II algorithm are much smaller than those figures of the present one- and two-level additive algorithms in Tables 4.2 and 4.4, respectively. Figure 4.12 plots the iteration count versus the overlap percent and the GMRES residual versus the iteration count, from which it can be observed that the present coupled compact IRBF two-level hybrid-II performs best around an overlap of 10%.

Table 4.7 Two-level hybrid-II preconditioned GMRES using the present coupled compact IRBF: number of iteration required to achieve convergence.

$H \setminus h$	two-level hybrid-II		
	1/32	1/64	1/128
	overlap = 1%		
1/4	12	16	16
1/8	12	14	13
1/16	11	12	12
	overlap = 5%		
1/4	10	10	13
1/8	10	10	12
1/16	14	14	10
	overlap = 10%		
1/4	9	11	12
1/8	12	10	11
1/16	15	16	16
	overlap = 15%		
1/4	10	9	9
1/8	14	13	13
1/16	15	16	17
	overlap = 20%		
1/4	10	10	8
1/8	15	15	14
1/16	19	20	18
	overlap = 25%		
1/4	11	11	12
1/8	14	15	15
1/16	18	19	19

Final comparison of the six algorithms using the present coupled compact IRBF

For comparison purpose, at $H = 1/8$ and $h = 1/128$, we finally choose the overlap percentages at which each of the six algorithms using the present coupled compact IRBF gives its best performance. Figure 4.13 shows the comparison of the six algorithms in terms of the GMRES residual versus the iteration count. It
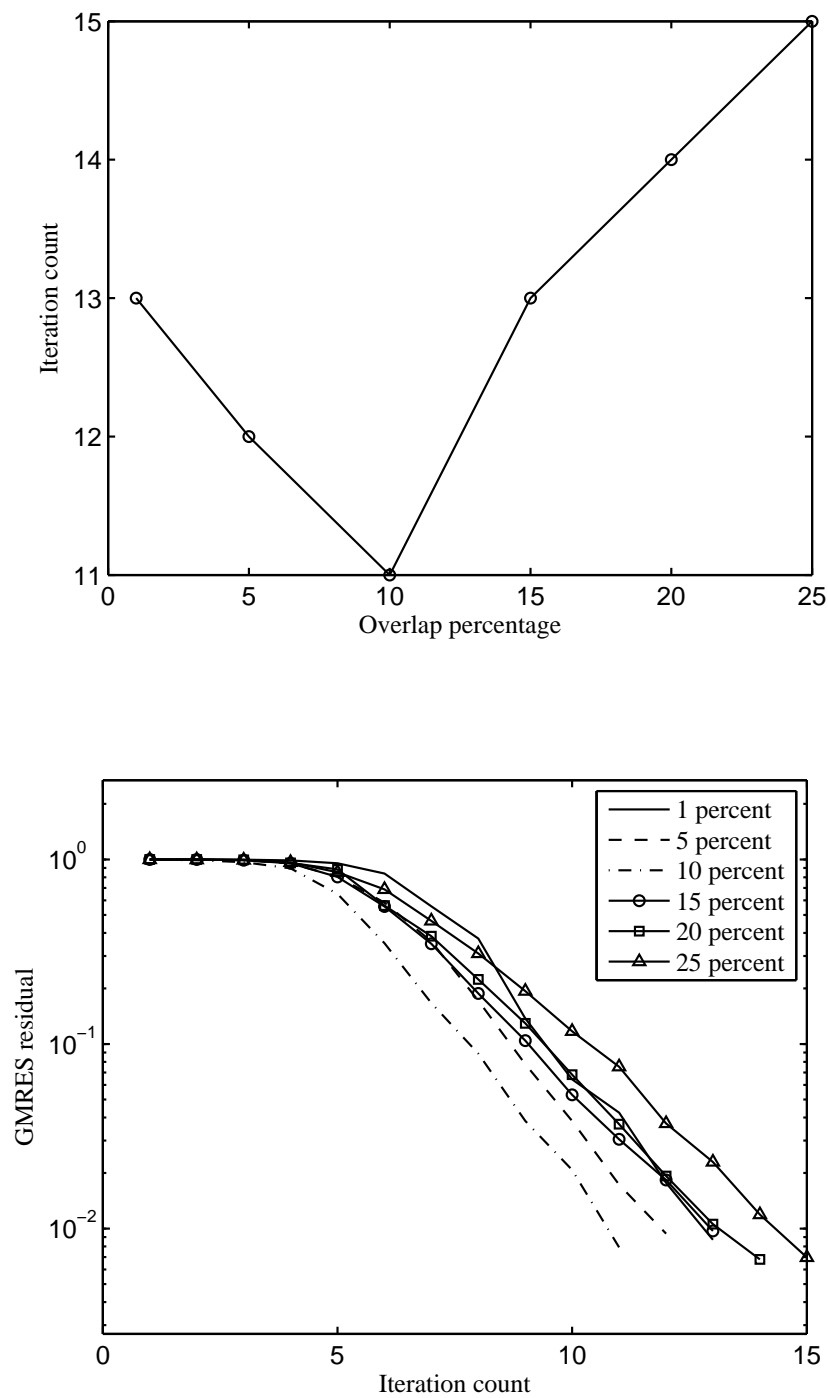
Figure 4.12 Two-level hybrid II preconditioned GMRES using the present coupled compact IRBF: Iteration count versus overlap percentage (top) and GMRES residual versus iteration count (bottom).

can be seen that the present two-level multiplicative at 10% overlap reaches the prescribed residual with the least iterations of only 4. After that, both the present one-level multiplicative at 20% overlap and the present two-level hybrid I at 10% overlap require 6 iterations to reach the prescribed GMRES residual. Then, both the present two-level additive at 10% overlap and the present two-level hybrid II at 10% overlap take 11 iterations to get to the target GMRES residual.
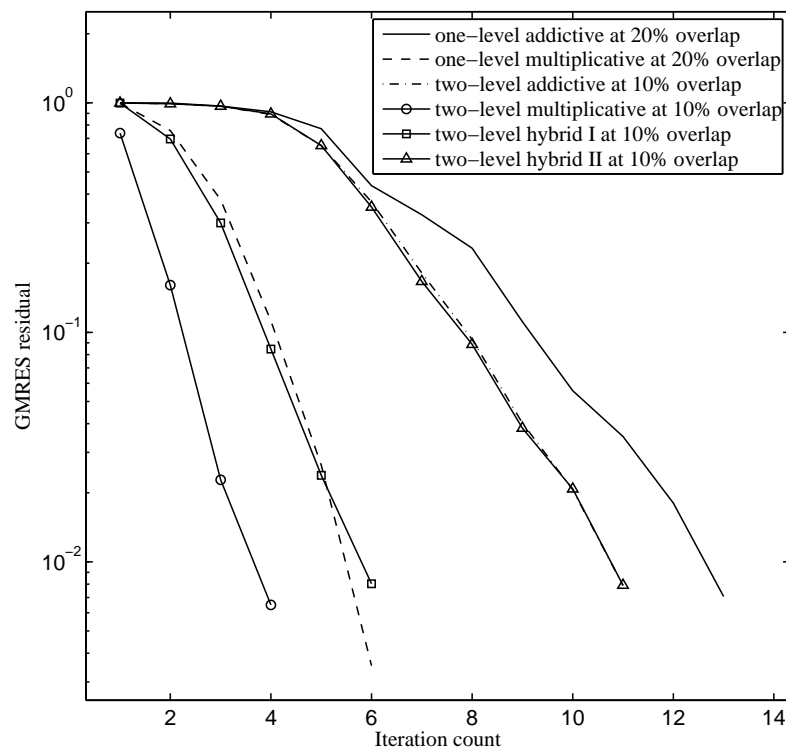
Figure 4.13 Comparison of the six algorithms using the present coupled compact IRBF: GMRES residual versus iteration count.

Because of the great performance of the present coupled compact IRBF two-level multiplicative algorithm, we will incorporate it into the serial and parallel structures as detailed in Section 4.5 for the computation in the following examples.

4.8.2 Poisson equation

In order to study the spatial accuracy of the present coupled compact IRBF-Serial and -Parallel algorithms, we consider the following Poisson equation

$$\frac{d^2u}{dx_1^2} + \frac{d^2u}{dx_2^2} = -18\pi^2 \sin(3\pi x_1)\sin(3\pi x_2), \qquad (4.67)$$

subject to the Dirichlet boundary condition derived from the following exact solution

$$\overline{u} = \sin(3\pi x_1)\sin(3\pi x_2), \qquad (4.68)$$

on a square domain $[0,1]^2$. The calculations are carried out on a set of uniform grids of $\{21 \times 21, 32 \times 32, 42 \times 42, 53 \times 53, 63 \times 63, 74 \times 74, 84 \times 84, 95 \times 95, 105 \times 105\}$. The coupled compact IRBF-Serial and -Parallel are considered to reach its steady state when its RMS is smaller than 10^{-9}. The value of $\beta = 50$ is chosen for calculations. Table 4.8 illustrates the proposed coupled compact IRBF-Serial using 2×2 sub-domains and coupled compact IRBF-Parallel using 4×4 sub-domains are able to produce the same solution accuracy to those of the coupled compact IRBF-Single domain. For comparison purposes, we incorporate the standard central FDM and the HOC of Tian et al. (2011) into the two-level DD. Figure 4.14 shows that the proposed coupled compact IRBF-Serial and -Parallel outperform the FDM-Serial and HOC-Serial in terms of solution accuracy. The solutions converge as $O(h^{4.7})$ for the coupled compact IRBF-Single domain, -Serial and -Parallel, $O(h^{4.8})$ for the HOC-Serial, and $O(h^{2.0})$ for the FDM-Serial.

An analysis of the computational efficiency of the three algorithms, coupled compact IRBF-Single domain, -Serial and -Parallel are illustrated in Table 4.9 which shows that the coupled compact IRBF-Serial and -Parallel are generally much more efficient than the coupled compact IRBF-Single domain. In term of computation time, the coupled compact IRBF-Parallel generally uses less time to reach the same accuracy than the coupled compact IRBF-Serial does. In term of efficiency, the coupled compact IRBF-Serial is much more efficient than the coupled compact IRBF-Parallel at low numbers of grids. However, the efficiency of the coupled compact IRBF-Parallel increases and becomes better than that of

Table 4.8 Poisson equation, $\beta = 50$: The effect of the grid size h on the solution accuracy RMS. LCR stands for *"Local Convergence Rate"*.

Grid $(n_x \times n_y)$	coupled compact IRBF-Single domain		present coupled compact IRBF-Serial		present coupled compact IRBF-Parallel	
	RMS	$LCR^{(*)}$	RMS	$LCR^{(*)}$	RMS	$LCR^{(*)}$
21×21	2.5405E-04	—	2.5405E-04	—	2.5405E-04	—
32×32	4.1526E-05	4.30	4.1526E-05	4.30	4.1526E-05	4.30
42×42	1.1130E-05	4.51	1.1130E-05	4.51	1.1130E-05	4.51
53×53	3.1203E-06	4.75	3.1203E-06	4.75	3.1203E-06	4.75
63×63	1.3301E-06	4.78	1.3301E-06	4.78	1.3301E-06	4.78
74×74	6.5607E-07	4.73	6.5607E-07	4.73	6.5607E-07	4.73
84×84	3.4805E-07	4.76	3.4805E-07	4.76	3.4805E-07	4.76
95×95	1.9210E-07	4.76	1.9210E-07	4.76	1.9210E-07	4.76
105×105	1.1548E-07	4.78	1.1548E-07	4.78	1.1548E-07	4.78

$^{(*)}LCR = -\log[RMS(n_x)/RMS(21)]/\log[n_x/21]$.
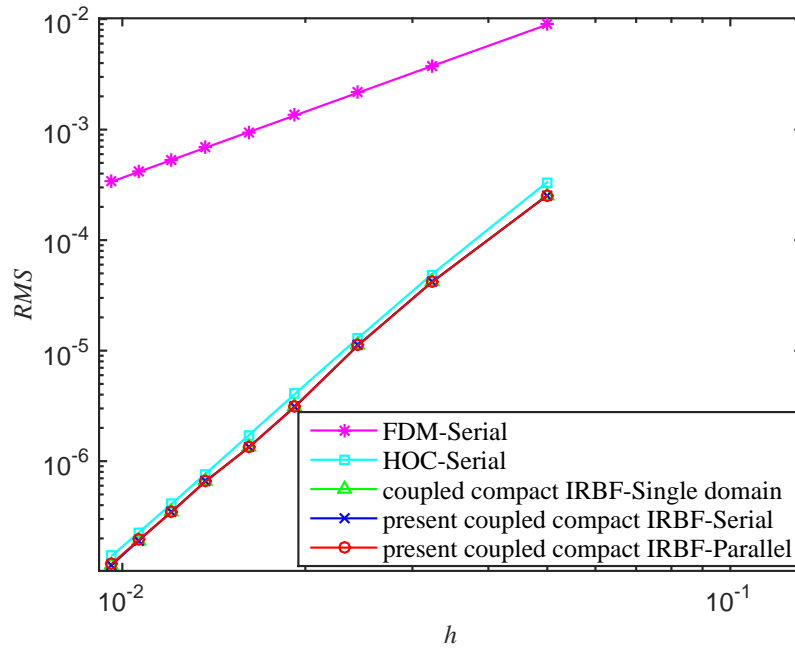
Figure 4.14 Poisson equation, $\beta = 50$: The effect of the grid size h on the solution accuracy RMS. It is noted that the results for the coupled compact IRBF-Single domain, coupled compact IRBF-Serial and coupled compact IRBF-Parallel are indistinguishable.

the coupled compact IRBF-Serial as the number of grids increases. In general, when the number of sub-domains is increased, the iteration count and the communication time will accordingly increase, which deteriorates the speed-up and the efficiency of the parallel algorithm. The possible reason is that the larger the number of sub-domains, the more time and iteration count it will take for the parallel algorithm to satisfy the convergence criteria set on every sub-domain. It is recommended that increasing the number of sub-domains is only considered when necessary, for example the simulation of a large-scale flooding problem.

Table 4.9 Poisson equation, $\beta = 50$: computational efficiency of the three algorithms, coupled compact IRBF-Single domain, -Serial and -Parallel. It is noted that "Comm." is the abbreviation of "Communication".

Grid ($n_x \times n_y$)	Methods	Sub-domains	CPUs	RMS	Iterations	Comm. time Second(%)	Total time Second	Speed-up, S	Efficiency, E %
53 × 53	coupled compact IRBF-Single domain	—	1	3.1203e-06	—	—	6.7	—	—
	present coupled compact IRBF-Serial	2 × 2	1	3.1203e-06	71	—	1.1	6.1	610
	present coupled compact IRBF-Serial	4 × 4	1	3.1203e-06	125	—	3.5	1.9	190
	present coupled compact IRBF-Parallel	4 × 4	4	3.1203e-06	321	0.4(22)	1.8	3.7	93
	present coupled compact IRBF-Parallel	6 × 6	9	3.1203e-06	391	1.1(23)	4.7	1.4	16
84 × 84	coupled compact IRBF-Single domain	—	1	3.4805E-07	—	—	19.2	—	—
	present coupled compact IRBF-Serial	2 × 2	1	3.4805E-07	73	—	6.3	3.0	300
	present coupled compact IRBF-Serial	4 × 4	1	3.4805E-07	23	—	6.5	3.0	300
	present coupled compact IRBF-Parallel	4 × 4	4	3.4805E-07	75	0.3(16)	1.9	10.1	253
	present coupled compact IRBF-Parallel	6 × 6	9	3.4805E-07	370	1.1(10)	10.5	1.8	20
95 × 95	coupled compact IRBF-Single domain	—	1	1.9210E-07	—	—	36.0	—	—
	present coupled compact IRBF-Serial	2 × 2	1	1.9210E-07	73	—	9.6	3.8	380
	present coupled compact IRBF-Serial	4 × 4	1	1.9210E-07	29	—	11.2	3.2	320
	present coupled compact IRBF-Parallel	4 × 4	4	1.9210E-07	101	0.6(17)	3.5	10.3	258
	present coupled compact IRBF-Parallel	6 × 6	9	1.9210E-07	287	1.2(10)	12.1	3.0	33
105 × 105	coupled compact IRBF-Single domain	—	1	1.1548E-07	—	—	59.4	—	—
	present coupled compact IRBF-Serial	2 × 2	1	1.1548E-07	96	—	16.3	3.6	360
	present coupled compact IRBF-Serial	4 × 4	1	1.1548E-07	43	—	21.7	2.7	270
	present coupled compact IRBF-Parallel	4 × 4	4	1.1548E-07	143	1.3(19)	6.7	8.9	223

	present coupled compact IRBF-Parallel	6 × 6	9	1.1548E-07	201	1.0(9)	11.6	5.1	57
	coupled compact IRBF-Single domain	—	1	7.8865E-08	—	—	2469.8	—	—
	present coupled compact IRBF-Serial	2 × 2	1	7.8865E-08	67	—	177.4	13.9	139
205 × 205	present coupled compact IRBF-Serial	4 × 4	1	7.8865E-08	51	—	243.1	10.2	102
	present coupled compact IRBF-Parallel	4 × 4	4	7.8865E-08	230	16.2(17)	93.8	26.3	658
	present coupled compact IRBF-Parallel	6 × 6	9	7.8865E-08	468	13.8(6)	230.4	10.7	119
	coupled compact IRBF-Single domain	—	—	—	—	—	—	—	—
	present coupled compact IRBF-Serial	2 × 2	1	1.3785E-07	111	—	1102.5	—	—
305 × 305	present coupled compact IRBF-Serial	4 × 4	1	1.3785E-07	117	—	2386.2	—	—
	present coupled compact IRBF-Parallel	4 × 4	4	1.3785E-07	620	151.1(17)	876.5	—	—
	present coupled compact IRBF-Parallel	6 × 6	9	1.3785E-07	786	101.8(7)	1468.3	—	—

4.8.3 Navier-Stokes equation

To construct a test problem of the stream function-vorticity formulation with analytic solutions, we specify the stream function described in (Richards and Crane, 1979)

$$\psi = \frac{(x^2 + y^2)}{4} \left(ln \left(x^2 + y^2 \right) - 2 \right), \tag{4.69}$$

on the unit square. The corresponding vorticity function, derived from (4.54), results in

$$\omega = ln \left(x^2 + y^2 \right), \tag{4.70}$$

The calculations are carried out on a uniform grid of 21×21. A wide range of Reynolds numbers, $Re = [10, 30, 50, 70, 90, 120, 150, 200]$, is employed. The value of $\beta = 50$ is chosen for calculations. Starting values of ω are analytic values of (4.70). To solve the steady vorticity equation, we utilise the vorticity equation (4.53), where $\frac{\partial u}{\partial t}$ is a pseudo time-derivative term. The vorticity equation (4.53) is subjected to the Dirichlet boundary condition derived from the exact solution of (4.70). We deliberately employ a small time step, $\Delta t = 10^{-6}$, to minimise the effect of the approximate error in time. The criterion to be satisfied for termination of iteration is given

$$\left| \frac{\omega^n - \omega^{n-1}}{\omega^{n-1}} \right| < 10^{-6}. \tag{4.71}$$

Figure 4.15 shows numerical results produced by coupled compact IRBF-Single domain, -Serial and -Parallel are much more accurate than those computed by the standard central FDM in (Richards and Crane, 1979). Table 4.10 shows the present coupled compact IRBF-Serial and -Parallel produce the same results with those of the coupled compact IRBF-Single domain.

4.8.4 Lid driven cavity

The classical lid driven cavity has been considered as the test problem for the valuation of numerical methods and the validation of fluid flow solvers for the past decades. Figure 4.16 shows the problem definition and boundary conditions.
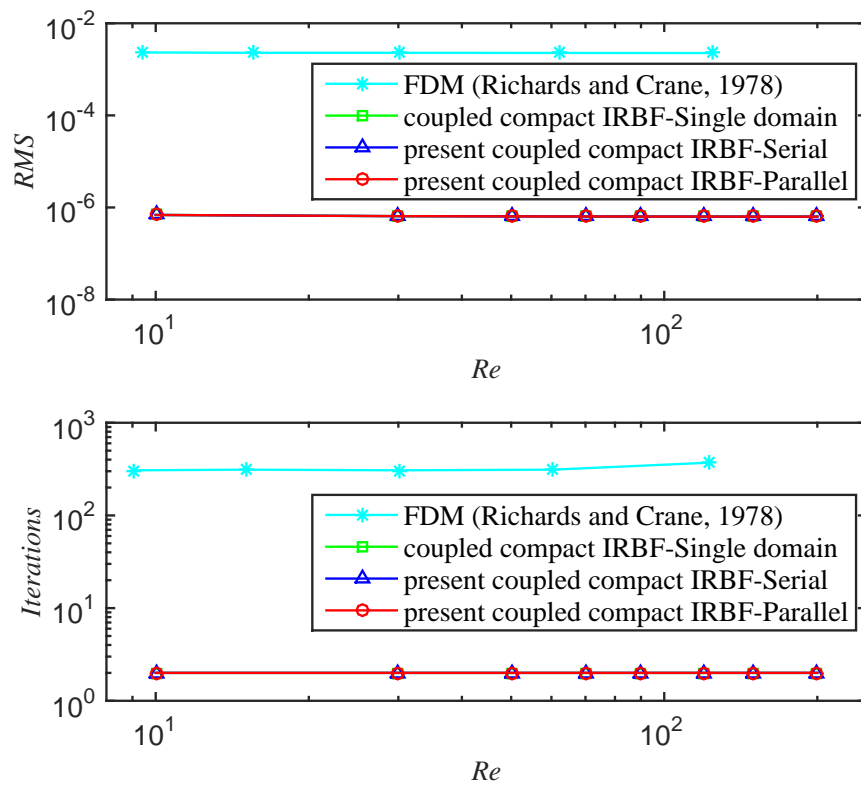
Figure 4.15 Navier-Stokes problem with analytic solutions, numerical solutions using a grid of 21×21, $\beta = 50$: The effect of the Reynolds number Re on the solution accuracy L_1 of the vorticity (top) and on the iteration number (bottom). It is noted that the results for the coupled compact IRBF-Single domain, -Serial and -Parallel are indistinguishable.

Table 4.10 Navier-Stokes problem with analytic solutions, $\beta = 50$: The effect of the Reynolds number Re on the solution accuracy RMS of the vorticity.

Re	coupled compact IRBF-Single domain L_1	present coupled compact IRBF-Serial L_1	present coupled compact IRBF-Parallel L_1
10	6.8802E-07	6.8802E-07	6.8802E-07
30	6.4819E-07	6.4819E-07	6.4819E-07
50	6.4047E-07	6.4047E-07	6.4047E-07
70	6.3717E-07	6.3717E-07	6.3717E-07
90	6.3534E-07	6.3534E-07	6.3534E-07
120	6.3374E-07	6.3374E-07	6.3374E-07
150	6.3278E-07	6.3278E-07	6.3278E-07
200	6.3182E-07	6.3182E-07	6.3182E-07

The discretisation of the cavity domain is shown in Figure 4.17.
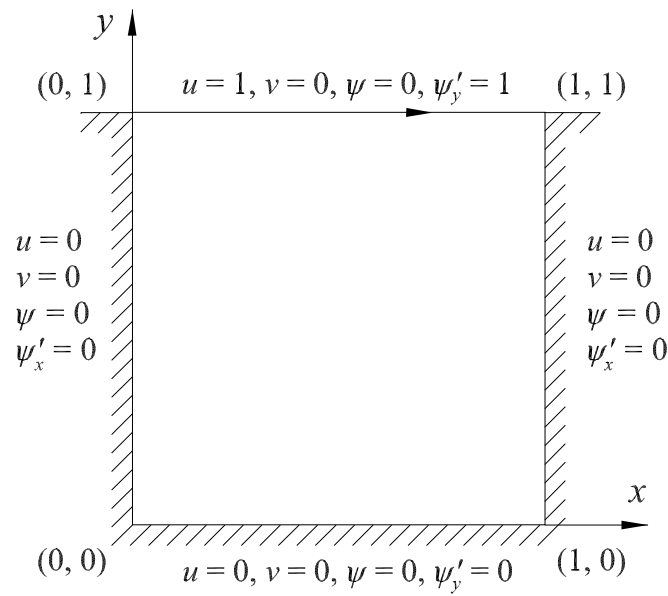
Figure 4.16 Lid driven cavity: problem configuration and boundary conditions in terms of the stream function.
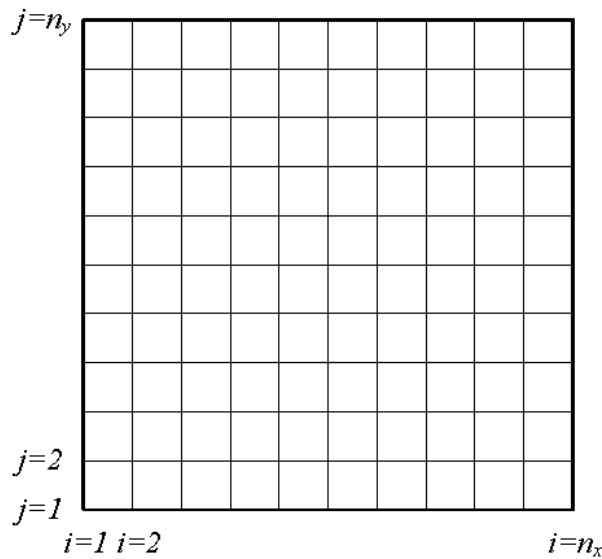
Figure 4.17 Lid driven cavity: domain discretisation.

To derive the boundary conditions of the vorticity, the grid arrangement close to the bottom wall ($j = 1$) is illustrated in Figure 4.18.

Apply Taylor series up to second order for $\psi_{i,j=2}$ (Biringen and Chow, 2011)

$$\psi_{i,j=2} = \psi_{i,j=1} + \frac{\partial \psi_{i,j=1}}{\partial y} h + \frac{\partial^2 \psi_{i,j=1}}{\partial y^2} \frac{h^2}{2}, \tag{4.72}$$
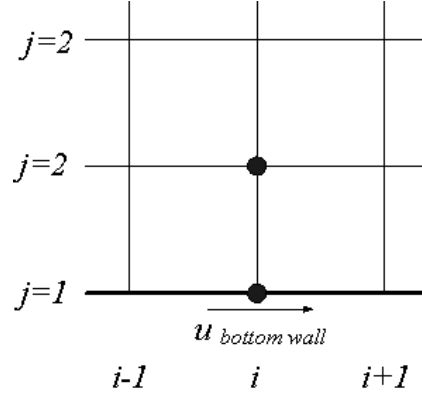
Figure 4.18 Lid driven cavity: Grid arrangement close to the bottom wall.

using

$$-\frac{\partial^2 \psi i, j = 1}{\partial y^2} = \omega_{i,j=1} = \omega_{\text{bottom wall}}; \text{ and } \frac{\partial \psi_{i,j=1}}{\partial y} = u_{i,j=1} = u_{\text{bottom wall}}, \quad (4.73)$$

Equation (4.72) becomes

$$\psi_{i,j=2} = \psi_{i,j=1} + u_{\text{bottom wall}}h - \omega_{\text{bottom wall}}\frac{h^2}{2}, \quad (4.74)$$

or

$$\omega_{\text{bottom wall}} = \left(\psi_{i,j=1} - \psi_{i,j=2}\right)\frac{2}{h^2} + u_{\text{bottom wall}}\frac{2}{h}. \quad (4.75)$$

Similarly, at the top wall $(j = n_y)$

$$\omega_{\text{top wall}} = \left(\psi_{i,j=n_y} - \psi_{i,j=n_y-1}\right)\frac{2}{h^2} - u_{\text{top wall}}\frac{2}{h}. \quad (4.76)$$

At the left wall $(i = 1)$

$$\omega_{\text{left wall}} = \left(\psi_{i=1,j} - \psi_{i=2,j}\right)\frac{2}{h^2} - u_{\text{left wall}}\frac{2}{h}. \quad (4.77)$$

At the right wall $(i = n_x)$

$$\omega_{\text{right wall}} = \left(\psi_{i=n_x,j} - \psi_{i=n_x-1,j}\right)\frac{2}{h^2} + u_{\text{right wall}}\frac{2}{h}. \quad (4.78)$$

The numerical integration is done according to the following steps.

1. Set initial conditions at $t = 0$ (e.g., at all interior points set $\omega_{i,j}^{n-1} = 0$).

2. Obtain interior values of $\psi_{i,j}^n$ by solving

$$\left(\frac{\partial^2}{\partial x^2} + \frac{\partial^2}{\partial y^2}\right)\psi_{i,j}^n = -\omega_{i,j}^{n-1}. \tag{4.79}$$

3. Compute interior points of velocities by calculating

$$u_{i,j}^n = \frac{\partial \psi_{i,j}^n}{\partial y} \quad \text{and} \quad v_{i,j}^n = -\frac{\partial \psi_{i,j}^n}{\partial x}. \tag{4.80}$$

4. Calculate (4.75) to (4.78) for boundary values of $\omega_{i,j}^n$ using $\psi_{i,j}^n$.

5. Find right hand side (RHS) of vorticity equation (4.58)

$$RHS_{i,j}^n = \frac{1}{Re}\left(\frac{\partial^2}{\partial x^2} + \frac{\partial^2}{\partial x^2}\right)\omega_{i,j}^{n-1} - \frac{\partial(u_{i,j}^n \omega_{i,j}^{n-1})}{\partial x} - \frac{\partial(v_{i,j}^n \omega_{i,j}^{n-1})}{\partial y}. \tag{4.81}$$

6. Compute interior values of $\omega_{i,j}^n$ using (4.58)

$$\omega_{i,j}^n = \omega_{i,j}^{n-1} + \Delta t RHS_{i,j}^n. \tag{4.82}$$

7. If a prescribed convergence criterion is reached, terminate the calculation; otherwise, go back to step 2.

Uniform grids of $\{11 \times 11, 31 \times 31, 41 \times 41, 51 \times 51\}$ and a range of $Re \in \{100, 400, 1000\}$ are employed in the simulation. A fixed time step is chosen to be $\Delta t = 0.0001$. Results of the present schemes are compared with some others (Ghia et al., 1982; Gresho et al., 1984; Bruneau and Jouron, 1990; Deng et al., 1994b; Botella and Peyret, 1998; Sahin and Owens, 2003; Thai-Quang et al., 2012b). From the literature, the FDM results using very dense grids presented by Ghia et al. (1982) and the pseudo-spectral results presented by Botella and Peyret (1998) have been referred as "Benchmark" results for comparison purposes. Tables 4.11, 4.12 and 4.13 show the present results for the extrema of the vertical and horizontal velocity profiles along the horizontal and vertical centrelines of the cavity for several Reynolds numbers. For $Re = 100$ (Table 4.11) and $Re = 1000$ (Table 4.13), the "Errors" evaluated are relative to the "Benchmark" results of Botella and Peyret

(1998). The results obtained by the present schemes are very comparable with others.

From Tables 4.11, 4.12 and 4.13, we can observe the present scheme effectively achieves the benchmark results with fewer grids in comparison with the grids of some other methods used to obtain the benchmark results. In addition, those velocity profiles at $Re \in \{100, 400, 1000\}$ with the grid of 51×51, are displayed in Figure 4.19, where the present solutions match the benchmark ones very well. The present scheme effectively achieves the benchmark results with the grid of only 51×51 in comparison with the grid of 129×129 used to obtain the benchmark results in (Ghia et al., 1982).

To exhibit contour plots of the flow, a range of $Re \in \{100, 400, 1000\}$ and the grid of 91×91 are employed. Figures 4.20 and 4.21 show streamlines and iso-vorticity lines, which are derived from the velocity field. These plots are also in good agreement with those reported in the literature.

For simplicity, the results of coupled compact IRBF-Parallel are chosen to be plotted in Figures 4.19, 4.20 and 4.21. It is noted that the results of coupled compact IRBF-Serial and -Parallel are indistinguishable.

Table 4.11 Lid driven cavity, $\beta = 10$, $Re = 100$: Extrema of the vertical and horizontal velocity profiles along the horizontal and vertical centrelines of the cavity, respectively. "Errors" are relative to the "Benchmark" data.

Method	Grid	u_{min}	Error (%)	y_{min}	v_{max}	Error (%)	x_{max}	v_{min}	Error (%)	x_{min}
coupled compact IRBF-Single domain	11×11	-0.1856399	13.27	0.4590	0.1486491	17.22	0.2574	-0.2393795	5.68	0.8379
coupled compact IRBF-Single domain	31×31	-0.2115965	1.14	0.4596	0.1772869	1.27	0.2385	-0.2505319	1.29	0.8109
coupled compact IRBF-Single domain	51×51	-0.2132844	0.35	0.4588	0.1789250	0.36	0.2372	-0.2526019	0.47	0.8105
present coupled compact IRBF-Serial	31×31	-0.2115965	1.14	0.4596	0.1772869	1.27	0.2385	-0.2505319	1.29	0.8109
present coupled compact IRBF-Serial	51×51	-0.2132844	0.35	0.4588	0.1789250	0.36	0.2372	-0.2526019	0.47	0.8105
present coupled compact IRBF-Parallel	31×31	-0.2115980	1.14	0.4596	0.1772881	1.27	0.2385	-0.2505346	1.29	0.8109
present coupled compact IRBF-Parallel	51×51	-0.2132822	0.36	0.4588	0.1789225	0.36	0.2372	-0.2525999	0.47	0.8105
compact IRBF (u, v, p), (Thai-Quang et al., 2012a)	31×31	-0.2102259	1.78	0.4578	0.1768808	1.50	0.2370	-0.2501843	1.43	0.8107
compact IRBF (u, v, p), (Thai-Quang et al., 2012a)	51×51	-0.2121503	0.88	0.4579	0.1781849	0.77	0.2372	-0.2520400	0.69	0.8107
FVM (u, v, p), (Deng et al., 1994b)	64×64	-0.21315	0.42	—	0.17896	0.34	—	-0.25339	0.16	—
FDM (ψ, ω), (Ghia et al., 1982)	129×129	-0.21090	1.47	0.4531	0.17527	2.40	0.2344	-0.24533	3.34	0.8047
FDM (u, v, p), (Bruneau and Jouron, 1990)	129×129	-0.2106	1.61	0.4531	0.1786	0.54	0.2344	-0.2521	0.67	0.8125
FVM (u, v, p), (Sahin and Owens, 2003)	257×257	-0.213924	0.06	0.4598	0.180888	0.73	0.2354	-0.256603	1.10	0.8127
Benchmark, (Botella and Peyret, 1998)		-0.2140424		0.4581	0.1795728		0.2370	-0.2538030		0.8104

Table 4.12 Lid driven cavity, $\beta = 2$, $Re = 400$: Extrema of the vertical and horizontal velocity profiles along the horizontal and vertical centrelines of the cavity, respectively.

Method	Grid	u_{min}	y_{min}	v_{max}	x_{max}	v_{min}	x_{min}
coupled compact IRBF-Single domain	31×31	-0.3047737	0.2873	0.2771614	0.2255	-0.4220126	0.8568
coupled compact IRBF-Single domain	41×41	-0.3201692	0.2814	0.2938922	0.2222	-0.4433914	0.8601
coupled compact IRBF-Single domain	51×51	-0.3296499	0.2799	0.3030723	0.2265	-0.4537653	0.8621
present coupled compact IRBF-Serial	31×31	-0.3047737	0.2873	0.2771614	0.2255	-0.4220126	0.8568
present coupled compact IRBF-Serial	41×41	-0.3201424	0.2811	0.2939847	0.2219	-0.4434279	0.8601
present coupled compact IRBF-Serial	51×51	-0.3296499	0.2799	0.3030723	0.2265	-0.4537653	0.8621
present coupled compact IRBF-Parallel	31×31	-0.3047736	0.2873	0.2771612	0.2255	-0.4220121	0.8568
present coupled compact IRBF-Parallel	41×41	-0.3201424	0.2811	0.2939846	0.2219	-0.4434277	0.8601
present coupled compact IRBF-Parallel	51×51	-0.3296498	0.2799	0.3030722	0.2265	-0.4537652	0.8621
compact IRBF (u, v, p), (Thai-Quang et al., 2012a)	31×31	-0.316205	0.2833	0.293696	0.2236	-0.435578	0.8583
compact IRBF (u, v, p), (Thai-Quang et al., 2012a)	51×51	-0.323158	0.2814	0.297493	0.2248	-0.442770	0.8605
compact IRBF (u, v, p), (Thai-Quang et al., 2012a)	71×71	-0.325168	0.2804	0.300818	0.2252	-0.449146	0.8620
FVM (u, v, p), (Deng et al., 1994b)	128×128	-0.32751	—	0.30271	—	-0.45274	—
FDM (ψ, ω), (Ghia et al., 1982)	129×129	-0.32726	0.2813	0.30203	0.2266	-0.44993	0.8594
FVM (u, v, p), (Sahin and Owens, 2003)	257×257	-0.328375	0.2815	0.304447	0.2253	-0.456316	0.8621

Table 4.13 Lid driven cavity, $\beta = 1$, $Re = 1000$: Extrema of the vertical and horizontal velocity profiles along the horizontal and vertical centrelines of the cavity, respectively. "Errors" are relative to the "Benchmark" data.

Method	Grid	u_{min}	Error (%)	y_{min}	v_{max}	Error (%)	x_{max}	v_{min}	Error (%)	x_{min}
coupled compact IRBF-Single domain	31×31	-0.3602892	7.28	0.2135	0.3398357	9.84	0.1697	-0.4642615	11.92	0.8879
coupled compact IRBF-Single domain	41×41	-0.3824678	1.57	0.2015	0.3654459	3.05	0.1646	-0.4973683	5.64	0.8913
coupled compact IRBF-Single domain	51×51	-0.3915410	0.76	0.1925	0.3770969	0.04	0.1618	-0.5162784	2.05	0.8955
present coupled compact IRBF-Serial	41×41	-0.3823441	1.60	0.2015	0.3653190	3.08	0.1646	-0.4972672	5.66	0.8913
present coupled compact IRBF-Serial	51×51	-0.3915274	0.76	0.1925	0.3770822	0.04	0.1618	-0.5162669	2.05	0.8955
present coupled compact IRBF-Parallel	41×41	-0.3823440	1.60	0.2015	0.3653189	3.08	0.1646	-0.4972672	5.66	0.8913
present coupled compact IRBF-Parallel	51×51	-0.3915273	0.76	0.1925	0.3770822	0.04	0.1618	-0.5162668	2.05	0.8955
compact IRBF (u, v, p), (Thai-Quang et al., 2012a)	71×71	-0.3755225	3.36	0.1753	0.3637009	3.51	0.1608	-0.5086961	3.49	0.9078
compact IRBF (u, v, p), (Thai-Quang et al., 2012a)	91×91	-0.3815923	1.80	0.1735	0.3698053	1.89	0.1594	-0.5174658	1.82	0.9085
compact IRBF (u, v, p), (Thai-Quang et al., 2012a)	111×111	-0.3840354	1.17	0.1728	0.3722634	1.24	0.1588	-0.5209683	1.16	0.9088
compact IRBF (u, v, p), (Thai-Quang et al., 2012a)	129×129	-0.3848064	0.97	0.1724	0.3729119	1.07	0.1586	-0.5223350	0.90	0.9089
FVM (u, v, p), (Deng et al., 1994b)	128×128	-0.38511	0.89	—	0.37369	0.86	—	-0.5228	0.81	—
FDM (ψ, ω), (Ghia et al., 1982)	129×129	-0.38289	1.46	0.1719	0.37095	1.59	0.1563	-0.5155	2.20	0.9063
FEM (u, v, p), (Gresho et al., 1984)	129×129	-0.375	3.49	0.160	0.362	3.96	0.160	-0.516	2.10	0.906
FDM (u, v, p), (Bruneau and Jouron, 1990)	256×256	-0.3764	3.13	0.1602	0.3665	2.77	0.1523	-0.5208	1.19	0.9102
FVM (u, v, p), (Sahin and Owens, 2003)	257×257	-0.388103	0.12	0.1727	0.376910	0.01	0.1573	-0.528447	0.26	0.9087
Benchmark, (Botella and Peyret, 1998)		-0.3885698		0.1717	0.3769447		0.1578	-0.5270771		0.9092

Figure 4.19 Lid driven cavity: Profiles of the u-velocity along the vertical centreline and the v-velocity along the horizontal centreline for $Re = 100$ (top), $Re = 400$ (middle) and $Re = 1000$ (bottom) with the grid of 51×51.
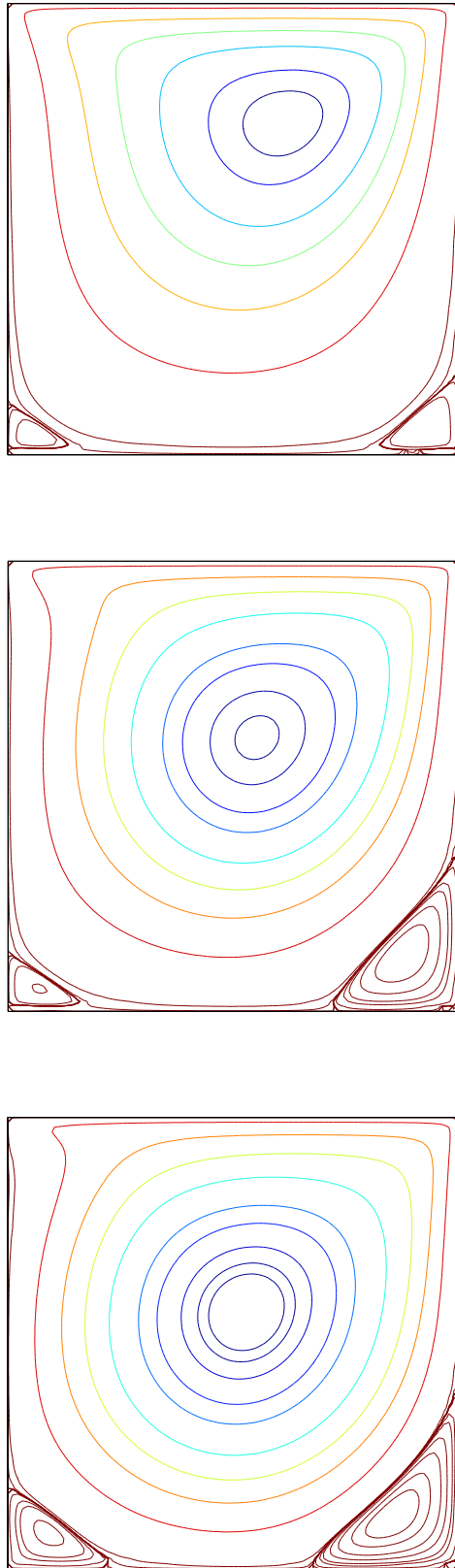
Figure 4.20 Lid driven cavity: Streamlines of the flow for $Re = 100$ (top), $Re = 400$ (middle) and $Re = 1000$ (bottom) with the grid of 91×91. The contour values used here are taken to be the same as those in (Ghia et al., 1982).

Table 4.14 shows the indicative comparison of the computational efficiency of the coupled compact IRBF-Single domain, -Serial and - Parallel for the case of $Re = 100$ with a variety of grid sizes. The coupled compact IRBF-Serial and -Parallel are more efficient in comparison with the coupled compact IRBF-Single domain.
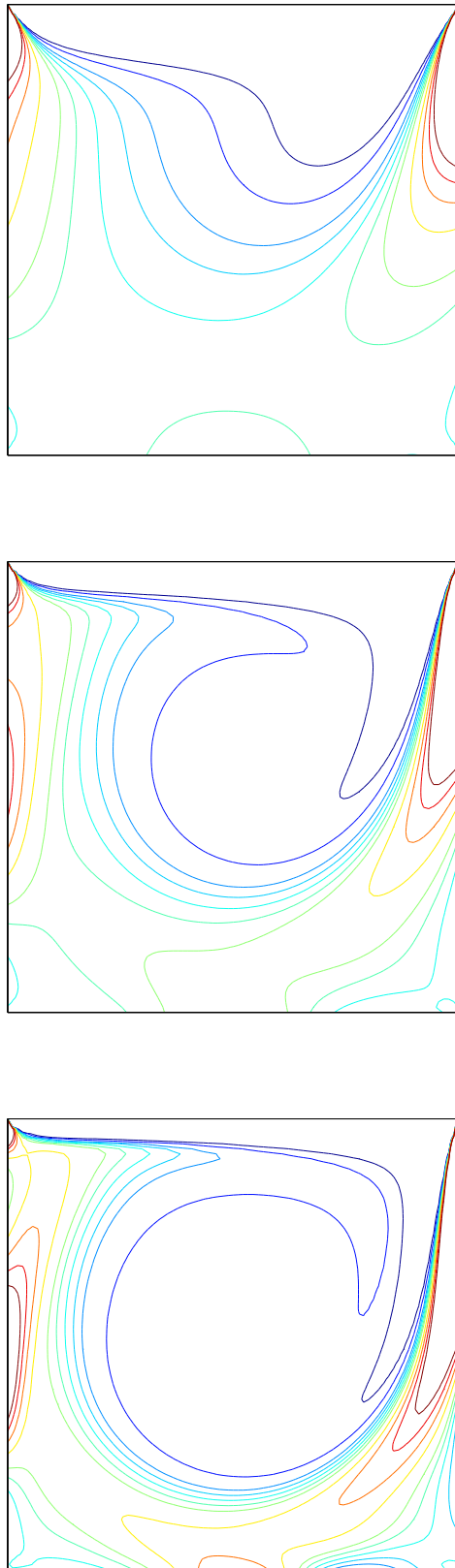
Figure 4.21 Lid driven cavity: Iso-vorticity lines of the flow for $Re = 100$ (top), $Re = 400$ (middle) and $Re = 1000$ (bottom) with the grid of 91×91. The contour values used here are taken to be the same as those in (Ghia et al., 1982).

Table 4.14 Lid driven cavity, $\beta = 10$, $Re = 100$: computational efficiency of the three algorithms, coupled compact IRBF-Single domain, -Serial and -Parallel. It is noted that "Comm." is the abbreviation of "Communication".

Grid ($n_x \times n_y$)	Methods	Sub-domains	CPUs	Iterations	Comm. time Minute(%)	Total time Minute	Speed-up, S	Efficiency, E %
	coupled compact IRBF-Single domain	—	1	169	—	19.7	—	—
	present coupled compact IRBF-Serial	2 × 2	1	502	—	16.3	1.2	120
51 × 51	present coupled compact IRBF-Serial	4 × 4	1	820	—	30.4	0.6	—
	present coupled compact IRBF-Parallel	4 × 4	4	1972	2.7(13)	20.4	1.0	25
	present coupled compact IRBF-Parallel	6 × 6	9	2384	4.3(11)	37.5	0.5	—
	coupled compact IRBF-Single domain	—	1	1067	—	238.1	—	—
	present coupled compact IRBF-Serial	2 × 2	1	2153	—	92.2	2.6	260
101 × 101	present coupled compact IRBF-Serial	4 × 4	1	1475	—	103.0	2.3	230
	present coupled compact IRBF-Parallel	4 × 4	4	4181	5.6(15)	36.5	6.5	163
	present coupled compact IRBF-Parallel	6 × 6	9	3936	4.9(9)	55.2	4.3	48
	coupled compact IRBF-Single domain	—	1	969	—	285.9	—	—
	present coupled compact IRBF-Serial	2 × 2	1	2049	—	105.3	2.7	270
151 × 151	present coupled compact IRBF-Serial	4 × 4	1	1341	—	112.4	2.5	250
	present coupled compact IRBF-Parallel	4 × 4	4	4562	6.1(16)	38.2	7.5	188
	present coupled compact IRBF-Parallel	6 × 6	9	4256	5.2(9)	58.2	4.9	54
	coupled compact IRBF-Single domain	—	1	3509	—	2476.3	—	—
	present coupled compact IRBF-Serial	2 × 2	1	1444	—	639.2	3.9	390
201 × 201	present coupled compact IRBF-Serial	4 × 4	1	1307	—	714.2	3.5	350
	present coupled compact IRBF-Parallel	4 × 4	4	2942	21.9(14)	151.7	16.3	408

present coupled compact IRBF-Parallel	6×6	9	2831	16.7(8)	215.2	11.5	128

4.9   Concluding remarks

In this chapter, we carry out a convergence analysis for different types of domain decomposition (DD) preconditioners implemented with the coupled compact IRBF. The performance of the present coupled compact IRBF based algorithms are analysed in terms of the iteration count with different grid sizes, numbers of sub-domains and overlap sizes. The numerical results show that

i. the present coupled compact IRBF two-level multiplicative algorithm is the best one compared with the other present coupled compact IRBF based algorithms.

ii. the present coupled compact IRBF two-level multiplicative algorithm is better than the HOC two-level multiplicative algorithm for the case of 1% and 25% overlaps. For other overlap cases, the present coupled compact IRBF two-level multiplicative algorithm is comparable with the HOC two-level multiplicative algorithm.

In the implementation of the present coupled compact IRBF in the DD preconditioners, we found that the incorporation of a coarse mesh problem into the multiplicative preconditioner is necessary to obtain a significant reduction in the computational iteration count. The present coupled compact IBRF two-level multiplicative method yields small iteration counts over a wide range of numbers of sub-domains, grid sizes and overlap sizes in our examples.

The present work introduces highly accurate serial and parallel algorithms using the coupled compact IRBF for heat and fluid flow problems. The advantage of the proposed serial and parallel schemes is that they are able to produce almost the same level of accuracy as that of the single domain scheme. In computational examples, the results produced by serial and parallel algorithms are very compatible with other methods such as the finite element method (FEM) and the finite difference method (FDM). The capability of producing the stable and highly accurate results of the proposed algorithms is due to the utilisation of the coarse mesh of the two-level DD and the coupled compact IRBF approximation. The serial and parallel algorithms offer a divide-and-conquer solution for large-scale

partial differential equation (PDE) problems. Therefore, the proposed algorithms may be used as alternatives to the single domain scheme to solve large-scale problems which the single domain scheme is generally struggling to solve due to its ill-conditioned or fully populated companion matrix.

Next chapter will propose a combined compact IRBF which is an advanced version of the coupled compact IRBF ; and, will also introduce preconditioning technique to provide stable calculations of IRBF approximations at large values of the shape parameter, where the ill-condition problem becomes severe.

Chapter 5

Combined compact flat integrated RBF scheme for fluid flows

In this chapter, we propose a simple but effective preconditioning technique to improve the numerical stability of integrated radial basis function (IRBF) methods. The proposed preconditioner is simply the inverse of a well-conditioned matrix that is constructed using non-flat IRBFs. Much larger values of the free shape parameter of IRBFs can thus be employed and better accuracy for smooth solution problems can be achieved. Furthermore, to improve the accuracy of local IRBF methods, we propose a new stencil, namely combined compact IRBF, in which (i) the starting points are fourth-order derivatives; and, (ii) nodal values of first- and second-order derivatives at side nodes of the stencil are included in the computation of first- and second-order derivatives at the middle node. The proposed stencil can be employed in uniform/nonuniform Cartesian grids. The preconditioning technique in combination with the combined compact IRBF scheme employed with large values of the shape parameter are tested with elliptic equations and then applied to simulate several fluid flow problems governed by Poisson, Burgers, convection-diffusion, and Navier-Stokes equations. Highly accurate and stable solutions are obtained. In some cases, the preconditioned schemes are shown to be several orders of magnitude more accurate than those without preconditioning.

5.1 Introduction

During the last decades, radial basis function (RBFs) have found increasingly widespread use for numerical solution of the partial differential equation (PDE) systems. Hardy (1971, 1990) devised multiquadric (MQ) schemes for scattered data fitting and general multi-dimensional data interpolation problems in geophysical engineering. Buhmann (1990) and Madych and Nelson (1990) showed that RBF approximation methods converge fast as the density of RBFs and their shape parameters increase. Kansa (1990a,b) first implemented RBFs (here referred to as direct/differential RBF or DRBF methods) for solving PDEs. Since then, DRBF methods have been increasingly used for the solution of elliptic, parabolic and hyperbolic PDEs which govern many engineering problems. In (Fedoseyev et al., 2002; Driscoll and Fornberg, 2002; Li et al., 2003b; Cheng et al., 2003; Fornberg and Wright, 2004), practitioners demonstrated that the elliptic PDE solutions using DRBFs converge much faster than those based on polynomial approximations. Mai-Duy and Tran-Cong (2001b, 2003) proposed the idea of using indirect/integrated RBFs (IRBFs) for the solution of PDEs. Numerical results in (Mai-Duy and Tran-Cong, 2001a,b, 2003, 2005; Sarra, 2006; Ngo-Cong et al., 2012; Tien et al., 2015b,c) showed that the integral approach is more accurate than the differential approach. In these works, the authors claimed that because the integration is a smoothing operation and the integrated basis functions are of higher orders, the integral approach has the ability to yield a faster converging solution.

However, despite the success of RBF methods in many scientific and engineering applications, their accuracy is dependent on a user defined shape parameter β and the optimal value of β depends on the function to be interpolated, the configuration of nodal points, the RBF type, and the machine precision (Buhmann, 1990; Madych and Nelson, 1990; Carlson and Foley, 1991; Rippa, 1999; Power and Barraco, 2002; Li et al., 2003b; Shu et al., 2003). The matrix condition of the RBF method grows exponentially with the RBF width. For many problems, e.g. those having smooth solutions, the optimal value of the RBF width is known to be normally large however the corresponding coefficient matrix becomes ill-

conditioned. An on-going problem involving the use of RBFs is how to choose the optimal value or even a consistently "good" value of β, which has received a great deal of attention of many researchers. Rippa (1999) presented an algorithm for selecting a good value of the shape parameter by minimising a cost function that imitates the error between the radial interpolant and the unknown function. For smooth functions, it was shown that without round-off error the highest accuracy for a given number of nodal points is regularly achieved when the RBFs become increasingly flat (Driscoll and Fornberg, 2002). Wang and Liu (2002a) studied the effect of shape parameters on the numerical accuracy of radial point interpolation meshless (radial PIM). Theoretical and computational aspects of increasingly flat RBF interpolations were discussed in (Larsson and Fornberg, 2005). Fornberg and Wright (2004) proposed the Contour-Padé algorithm which can stably compute the whole region of the shape parameter on a complex plane. Many different approaches to enhance the stability of DRBF methods have been proposed, for example (Kansa and Hon, 2000; Shu et al., 2003; Libre et al., 2008; Emdadi et al., 2008; Fornberg et al., 2011; Fasshauer and Mccourt, 2012; Stefano and Gabriele, 2013; Larsson et al., 2013; Fornberg et al., 2013) and the references therein. For IRBF approaches, Sarra (2006) studied the case of global flat IRBFs. It was observed that the even-order IRBFs are generally most accurate and most poorly conditioned for large values of the shape parameter β. Additionally, numerical results in (Mai-Duy and Tran-Cong, 2005; Sarra, 2006) showed that the use of higher-order IRBFs can lead to better accuracy.

Motivated by the aforementioned works, this chapter proposes (i) an easy-to-implement but effective preconditioning technique for compact IRBF schemes to alleviate ill-condition problems arising from using large values of β; and, (ii) a combined compact IRBF approximation scheme using high-order IRBFs to enhance the solution accuracy, especially in the large value range of β (Mai-Duy and Tran-Cong, 2005; Sarra, 2006). Unlike compact IRBF schemes previously proposed in (Thai-Quang et al., 2012b; Mai-Duy and Tran-Cong, 2013; Tien et al., 2015c; Chu and Fan, 2000), a preconditioning technique is employed here. The present preconditioned combined compact IRBF scheme is able to stably compute second-order PDE problems with much larger values of β. We derive expressions

for evaluation of first- and second-order derivative operators for solving PDE problems and demonstrate the stability and accuracy of the new scheme through various numerical experiments. It should be emphasised that a mesh-free property of RBFs allows lengths between nodes in the stencil to be different. It will be shown that a high level of accuracy is still achieved when combined compact IRBF stencils are applied to problems with curved boundaries. Unlike RBF-DQ methods, our proposed approximations are compact, which helps achieve a high level of accuracy (e.g. avoid the loss of information in the approximation near the curved boundary).

The structure of this chapter is organised as follows. Section 5.2 numerically discusses the condition number of IRBFs over a wide range of β. To enhance the accuracy, a new approximation scheme (combined compact IRBF) is proposed in Section 5.3. Following this, a simple preconditioning technique is proposed in Section 5.4 to retain the accuracy of the combined compact IRBF when working in the large value range of β. Numerical examples in which the combined compact IRBF results are compared with some other solutions, where appropriate, are presented in Section 5.5. Finally, some concluding remarks are given in Section 5.6.

5.2 Numerical observations on condition numbers of IRBFs

Several IRBF approximation schemes were reported in (Mai-Duy and Tran-Cong, 2001b; Thai-Quang et al., 2012b; Mai-Duy and Tran-Cong, 2013; Tien et al., 2015c) and they are summarised here for convenience. In IRBF approaches, the MQ function is usually chosen as the basis function, i.e. (1.6).

For second-order PDEs, the integral approach normally starts with the decomposition of the second-order derivatives of a variable, u, into RBFs

$$\frac{d^2u(\eta)}{d\eta^2} = \sum_{i=1}^{m} w_i G_i(\eta), \tag{5.1}$$

where $\{G_i(\eta)\}_{i=1}^{m}$ is the set of RBFs; and, $\{w_i\}_{i=1}^{m}$ is the set of weights/coefficients

to be found. Approximate representations for the first-order derivatives and the functions itself are then obtained through the integration processes

$$\frac{du(\eta)}{d\eta} = \sum_{i=1}^{m} w_i I_{1i}(\eta) + c_1, \tag{5.2}$$

$$u(\eta) = \sum_{i=1}^{m} w_i I_{2i}(\eta) + c_1 \eta + c_2, \tag{5.3}$$

where $I_{1i}(\eta) = \int G_i(\eta)d\eta$; $I_{2i}(\eta) = \int I_{1i}(\eta)d\eta$; and, c_1 and c_2 are the constants of integration. If basis functions are further integrated, the similar notation will be used, e.g. $I_{3i}(\eta) = \int I_{2i}(\eta)d\eta$ and $I_{4i}(\eta) = \int I_{3i}(\eta)d\eta$. The analytic form of the IRBFs up to eighth-order can be found in (Mai-Duy, 2005).

For IRBF approaches, the starting point in the integration process can be different. The IRBF scheme is said to be of order k if the starting point is the kth-order derivative. In the literature, numerical examples of Sarra (2006); Wathen and Zhu (2015) show that the higher the order of the IRBF, the higher the matrix condition number will be. To illustrate this trend, Figure 5.1 shows a comparison of the condition numbers among the IRBFs against the shape parameter β with a fixed number of grid points of 31 on a domain of [0, 1]. However, when the number of RBFs is reduced to 3 and larger values of β are used, as shown in Figure 5.2, the observation just mentioned is reversed. It can be seen that the conditions of $\mathbf{G}$ are the highest while those of $\mathbf{I}_4$ are the lowest. The higher the order of the IRBF, the smaller the matrix condition number will be. This is a very interesting behavior for which, unfortunately, a theoretical explanation cannot be offered at this stage. This can be seen as another advantage of using integrated RBFs over differentiated ones when local RBF methods are employed with large values of β. It is noted that global IRBFs, where all RBFs are employed (i.e. the observation in Figure 5.1), are fully populated and tend to be ill-conditioned as β increases while local IRBFs, using 3 RBFs (i.e. the observation in Figure 5.2), have more relaxed condition numbers and can be well-behaved up to a certain large value of β. It is shown shortly that three-point stencils have the advantage that the approximation at the interior nodes near the boundary does not involve the nodal values outside the domain.
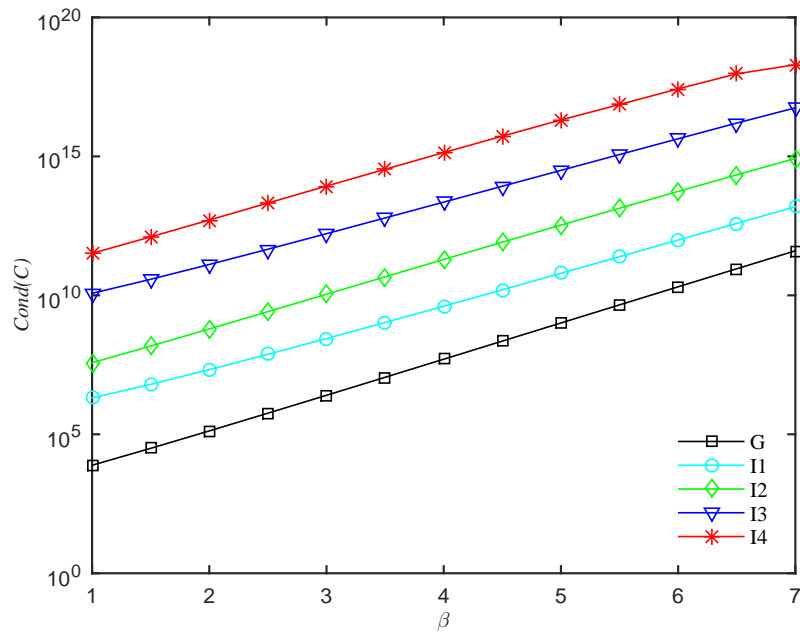
Figure 5.1 The effect of β on the condition numbers of the IRBFs: the number of RBFs used is 31.
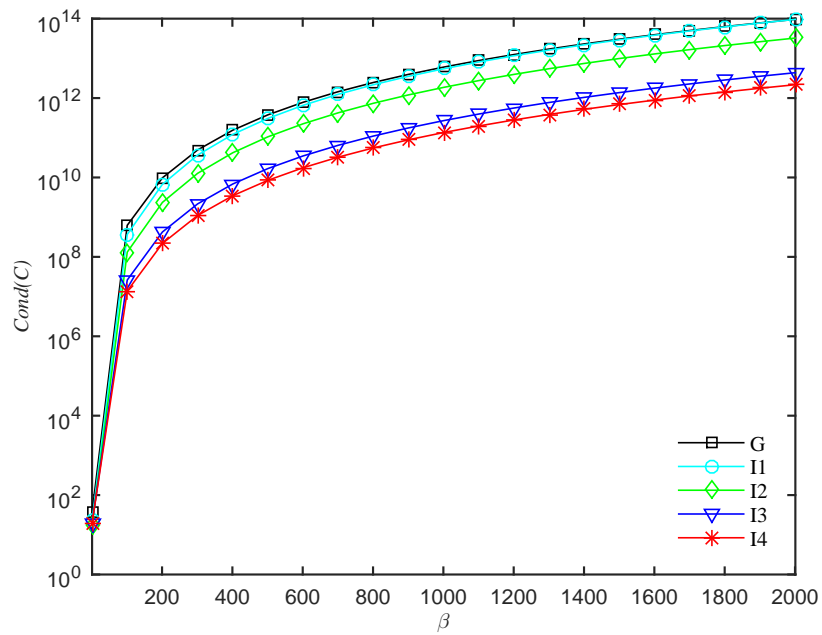
Figure 5.2 The effect of β on the condition numbers of the IRBFs: the number of RBFs used is 3.

5.3 Combined compact integrated RBF scheme

From the above mentioned observations, we propose a new approximation method using fourth-order derivatives as the starting points in the process of integration in order to achieve better accuracy.

Consider a two-dimensional domain Ω, which is represented by a uniform Cartesian grid. The nodes are indexed in the x-direction by the subscript i ($i \in \{1, 2, ..., n_x\}$) and in the y-direction by j ($j \in \{1, 2, ..., n_y\}$). For rectangular domains, let N be the total number of nodes ($N = n_x \times n_y$) and N_{ip} be the number of interior nodes ($N_{ip} = (n_x - 2) \times (n_y - 2)$). At an interior grid point $\mathbf{x}_{i,j} = (x_{(i,j)}, y_{(i,j)})^T$ where $i \in \{2, 3, ..., n_x - 1\}$ and $j \in \{2, 3, ..., n_y - 1\}$, the associated stencils to be considered here are two local stencils: $\{x_{(i-1,j)}, x_{(i,j)}, x_{(i+1,j)}\}$ in the x-direction and $\{y_{(i,j-1)}, y_{(i,j)}, y_{(i,j+1)}\}$ in the y-direction. Hereafter, for brevity, η denotes either x or y in a generic local stencil $\{\eta_1, \eta_2, \eta_3\}$, where $\eta_1 < \eta_2 < \eta_3$ and $\eta_2 \equiv \eta_{(i,j)}$, are illustrated in Figure 5.3.

Figure 5.3 Compact three-point 1D-IRBF stencil for interior nodes.

The integral process of the present combined compact IRBF starts with the decomposition of fourth-order derivatives of a variable, u, into RBFs

$$\frac{d^4 u(\eta)}{d\eta^4} = \sum_{i=1}^{m} w_i G_i(\eta). \tag{5.4}$$

Approximate representations for the third- to first-order derivatives and the functions itself are then obtained through the integration processes

$$\frac{d^3 u(\eta)}{d\eta^3} = \sum_{i=1}^{m} w_i I_{1i}(\eta) + c_1, \tag{5.5}$$

$$\frac{d^2 u(\eta)}{d\eta^2} = \sum_{i=1}^{m} w_i I_{2i}(\eta) + c_1 \eta + c_2, \tag{5.6}$$

$$\frac{du(\eta)}{d\eta} = \sum_{i=1}^{m} w_i I_{3i}(\eta) + \frac{1}{2}c_1\eta^2 + c_2\eta + c_3, \tag{5.7}$$

$$u(\eta) = \sum_{i=1}^{m} w_i I_{4i}(\eta) + \frac{1}{6}c_1\eta^3 + \frac{1}{2}c_2\eta^2 + c_3\eta + c_4, \tag{5.8}$$

where $I_{1i}(\eta) = \int G_i(\eta)d\eta$; $I_{2i}(\eta) = \int I_{1i}(\eta)d\eta$; $I_{3i}(\eta) = \int I_{2i}(\eta)d\eta$; $I_{4i}(\eta) = \int I_{3i}(\eta)d\eta$; and, c_1, c_2, c_3, and c_4 are the constants of integration. However, for the solution of second-order PDEs, only (5.6)-(5.8) are needed. It is noted that it is possible to implement integrated RBFs in higher dimensions to construct compact IRBF. However, with the proposed compact approximation approach, the use of IRBFs in one dimension leads to conversion matrices of much smaller size and a relatively sparse system matrix.

5.3.1 First-order derivative approximations

For the combined compact approximation of the first-order derivatives at interior nodes, extra information is chosen as not only $\left\{ \frac{du_1}{d\eta}; \frac{du_3}{d\eta} \right\}$ but also $\left\{ \frac{d^2u_1}{d\eta^2}; \frac{d^2u_3}{d\eta^2} \right\}$. We construct the conversion system over a 3-point stencil as follows.

$$\begin{bmatrix} u_1 \\ u_2 \\ u_3 \\ \frac{du_1}{d\eta} \\ \frac{du_3}{d\eta} \\ \frac{d^2u_1}{d\eta^2} \\ \frac{d^2u_3}{d\eta^2} \end{bmatrix} = \underbrace{\begin{bmatrix} \mathbf{I}_4 \\ \mathbf{I}_3 \\ \mathbf{I}_2 \end{bmatrix}}_{\mathbf{C}} \begin{bmatrix} w_1 \\ w_2 \\ w_3 \\ c_1 \\ c_2 \\ c_3 \\ c_4 \end{bmatrix}, \tag{5.9}$$

where $\frac{du_i}{d\eta} = \frac{du}{d\eta}(\eta_i)$ with $i \in \{1, 2, 3\}$; $\mathbf{C}$ is the conversion matrix; and, $\mathbf{I}_2$, $\mathbf{I}_3$, and $\mathbf{I}_4$ are defined as

$$\mathbf{I}_2 = \begin{bmatrix} I_{21}(\eta_1) & I_{22}(\eta_1) & I_{23}(\eta_1) & \eta_1 & 1 & 0 & 0 \\ I_{21}(\eta_3) & I_{22}(\eta_3) & I_{23}(\eta_3) & \eta_3 & 1 & 0 & 0 \end{bmatrix}. \tag{5.10}$$

$$\mathbf{I}_3 = \begin{bmatrix} I_{31}(\eta_1) & I_{32}(\eta_1) & I_{33}(\eta_1) & \frac{1}{2}\eta_1^2 & \eta_1 & 1 & 0 \\ I_{31}(\eta_3) & I_{32}(\eta_3) & I_{33}(\eta_3) & \frac{1}{2}\eta_3^2 & \eta_3 & 1 & 0 \end{bmatrix}. \tag{5.11}$$

$$\mathbf{I}_4 = \begin{bmatrix} I_{41}(\eta_1) & I_{42}(\eta_1) & I_{43}(\eta_1) & \frac{1}{6}\eta_1^3 & \frac{1}{2}\eta_1^2 & \eta_1 & 1 \\ I_{41}(\eta_2) & I_{42}(\eta_2) & I_{43}(\eta_2) & \frac{1}{6}\eta_2^3 & \frac{1}{2}\eta_2^2 & \eta_2 & 1 \\ I_{41}(\eta_3) & I_{42}(\eta_3) & I_{43}(\eta_3) & \frac{1}{6}\eta_3^3 & \frac{1}{2}\eta_3^2 & \eta_3 & 1 \end{bmatrix}. \tag{5.12}$$

Solving (5.9) yields

$$\begin{bmatrix} w_1 \\ w_2 \\ w_3 \\ c_1 \\ c_2 \\ c_3 \\ c_4 \end{bmatrix} = \mathbf{C}^{-1} \begin{bmatrix} u_1 \\ u_2 \\ u_3 \\ \frac{du_1}{d\eta} \\ \frac{du_3}{d\eta} \\ \frac{d^2 u_1}{d\eta^2} \\ \frac{d^2 u_3}{d\eta^2} \end{bmatrix}, \tag{5.13}$$

which maps the vector of nodal values of the function and its first- and second-order derivatives to the vector of RBF coefficients including the four integration constants. The first-order derivative at the middle point is computed by substituting (5.13) into (5.7) and taking $\eta = \eta_2$

$$\frac{du_2}{d\eta} = \underbrace{\mathbf{I}_{3m}\mathbf{C}^{-1}}_{\mathbf{D}_1} \begin{bmatrix} \mathbf{u} \\ \frac{du_1}{d\eta} \\ \frac{du_3}{d\eta} \\ \frac{d^2 u_1}{d\eta^2} \\ \frac{d^2 u_3}{d\eta^2} \end{bmatrix}, \tag{5.14}$$

or

$$\frac{du_2}{d\eta} = \mathbf{D}_1(1:3)\mathbf{u} + \mathbf{D}_1(4:5)\begin{bmatrix} \frac{du_1}{d\eta} \\ \frac{du_3}{d\eta} \end{bmatrix} + \mathbf{D}_1(6:7)\begin{bmatrix} \frac{d^2 u_1}{d\eta^2} \\ \frac{d^2 u_3}{d\eta^2} \end{bmatrix}, \tag{5.15}$$

where $\mathbf{D}_1$ is a row vector of length 7, the associated notation "$a : b$" is used to indicate the vector entries from the the column a to b; $\mathbf{u} = [u_1, u_2, u_3]^T$; and,

$$\mathbf{I}_{3m} = \begin{bmatrix} I_{31}(\eta_2) & I_{32}(\eta_2) & I_{33}(\eta_2) & \frac{1}{2}\eta_2^2 & \eta_2 & 1 & 0 \end{bmatrix}. \tag{5.16}$$

By taking derivative terms to the left side and nodal variable values to the right side, (5.15) reduces to

$$\begin{bmatrix} -\mathbf{D}_1(4) & 1 & -\mathbf{D}_1(5) \end{bmatrix} \mathbf{u}' + \begin{bmatrix} -\mathbf{D}_1(6) & 0 & -\mathbf{D}_1(7) \end{bmatrix} \mathbf{u}'' = \mathbf{D}_1(1:3)\mathbf{u}, \quad (5.17)$$

where $\mathbf{u}' = \left[\frac{du_1}{d\eta}, \frac{du_2}{d\eta}, \frac{du_3}{d\eta} \right]^T$ and $\mathbf{u}'' = \left[\frac{d^2 u_1}{d\eta^2}, \frac{d^2 u_2}{d\eta^2}, \frac{d^2 u_3}{d\eta^2} \right]^T$.

At the boundary nodes, the first-order derivatives are approximated in special compact stencils. Consider the boundary node η_1. Its associated stencil is $\{\eta_1, \eta_2, \eta_3, \eta_4\}$ as shown in Figure 5.4 and extra information is chosen as $\frac{du_2}{d\eta}$ and $\frac{d^2 u_2}{d\eta^2}$. The conversion system over this special stencil is presented as the following matrix-vector multiplication

Figure 5.4 Special compact four-point 1D-IRBF stencil for boundary nodes.

$$\begin{bmatrix} u_1 \\ u_2 \\ u_3 \\ u_4 \\ \frac{du_2}{d\eta} \\ \frac{d^2 u_2}{d\eta^2} \end{bmatrix} = \underbrace{\begin{bmatrix} \mathbf{I}_{4sp} \\ \mathbf{I}_{3sp} \\ \mathbf{I}_{2sp} \end{bmatrix}}_{\mathbf{C}_{sp}} \begin{bmatrix} w_1 \\ w_2 \\ w_3 \\ w_4 \\ c_1 \\ c_2 \\ c_3 \\ c_4 \end{bmatrix}, \quad (5.18)$$

where $\mathbf{C}_{sp}$ is the conversion matrix; and, $\mathbf{I}_{2sp}$, $\mathbf{I}_{3sp}$, and $\mathbf{I}_{4sp}$ are defined as

$$\mathbf{I}_{2sp} = \begin{bmatrix} I_{21}(\eta_2) & I_{22}(\eta_2) & I_{23}(\eta_2) & I_{24}(\eta_2) & \eta_2 & 1 & 0 & 0 \end{bmatrix}. \quad (5.19)$$

$$\mathbf{I}_{3sp} = \begin{bmatrix} I_{31}(\eta_2) & I_{32}(\eta_2) & I_{33}(\eta_2) & I_{34}(\eta_2) & \frac{1}{2}\eta_2^2 & \eta_2 & 1 & 0 \end{bmatrix}. \quad (5.20)$$

$$
\mathbf{I}_{4sp} =
\begin{bmatrix}
I_{41}(\eta_1) & I_{42}(\eta_1) & I_{43}(\eta_1) & I_{44}(\eta_1) & \frac{1}{6}\eta_1^3 & \frac{1}{2}\eta_1^2 & \eta_1 & 1 \\
I_{41}(\eta_2) & I_{42}(\eta_2) & I_{43}(\eta_2) & I_{44}(\eta_2) & \frac{1}{6}\eta_2^3 & \frac{1}{2}\eta_2^2 & \eta_2 & 1 \\
I_{41}(\eta_3) & I_{42}(\eta_3) & I_{43}(\eta_3) & I_{44}(\eta_3) & \frac{1}{6}\eta_3^3 & \frac{1}{2}\eta_3^2 & \eta_3 & 1 \\
I_{41}(\eta_4) & I_{42}(\eta_4) & I_{43}(\eta_4) & I_{44}(\eta_4) & \frac{1}{6}\eta_4^3 & \frac{1}{2}\eta_4^2 & \eta_4 & 1
\end{bmatrix}.
\tag{5.21}
$$

Solving (5.18) yields

$$
\begin{bmatrix}
w_1 \\
w_2 \\
w_3 \\
w_4 \\
c_1 \\
c_2 \\
c_3 \\
c_4
\end{bmatrix}
= \mathbf{C}_{sp}^{-1}
\begin{bmatrix}
u_1 \\
u_2 \\
u_3 \\
u_4 \\
\frac{du_2}{d\eta} \\
\frac{d^2 u_2}{d\eta^2}
\end{bmatrix}.
\tag{5.22}
$$

The boundary value of the first-order derivative of u is thus obtained by substituting (5.22) into (5.7) and taking $\eta = \eta_1$

$$
\frac{du_1}{d\eta} = \underbrace{\mathbf{I}_{3b}\mathbf{C}_{sp}^{-1}}_{\mathbf{D}_{1sp}}
\begin{bmatrix}
\mathbf{u} \\
\frac{du_2}{d\eta} \\
\frac{d^2 u_2}{d\eta^2}
\end{bmatrix},
\tag{5.23}
$$

or

$$
\frac{du_1}{d\eta} = \mathbf{D}_{1sp}(1:4)\mathbf{u} + \mathbf{D}_{1sp}(5)\frac{du_2}{d\eta} + \mathbf{D}_{1sp}(6)\frac{d^2 u_2}{d\eta^2},
\tag{5.24}
$$

where $\mathbf{u} = [u_1, u_2, u_3, u_4]^T$ and

$$
\mathbf{I}_{3b} =
\begin{bmatrix}
I_{31}(\eta_1) & I_{32}(\eta_1) & I_{33}(\eta_1) & I_{34}(\eta_1) & \frac{1}{2}\eta_1^2 & \eta_1 & 1 & 0
\end{bmatrix}.
\tag{5.25}
$$

By taking derivative terms to the left side and nodal variable values to the right side, (5.24) reduces to

$$
\begin{bmatrix} 1 & -\mathbf{D}_{1sp}(5) & 0 & 0 \end{bmatrix} \mathbf{u}' +
\begin{bmatrix} 0 & -\mathbf{D}_{1sp}(6) & 0 & 0 \end{bmatrix} \mathbf{u}'' = \mathbf{D}_{1sp}(1:4)\mathbf{u},
\tag{5.26}
$$

where $\mathbf{u}' = \left[\frac{du_1}{d\eta}, \frac{du_2}{d\eta}, \frac{du_3}{d\eta}, \frac{du_4}{d\eta}\right]^T$ and $\mathbf{u}'' = \left[\frac{d^2 u_1}{d\eta^2}, \frac{d^2 u_2}{d\eta^2}, \frac{d^2 u_3}{d\eta^2}, \frac{d^2 u_4}{d\eta^2}\right]^T$.

5.3.2 Second-order derivative approximations

For the combined compact approximation of the second-order derivatives at interior nodes, we employ the same extra information used in the approximation of the first-order derivative, involving $\left\{\frac{du_1}{d\eta}; \frac{du_3}{d\eta}\right\}$ and $\left\{\frac{d^2u_1}{d\eta^2}; \frac{d^2u_3}{d\eta^2}\right\}$. Therefore, the second-order derivative at the middle point is computed by simply substituting (5.13) into (5.6) and taking $\eta = \eta_2$

$$\frac{d^2u_2}{d\eta^2} = \underbrace{\mathbf{I}_{2m}\mathbf{C}^{-1}}_{\mathbf{D}_2} \begin{bmatrix} \mathbf{u} \\ \frac{du_1}{d\eta} \\ \frac{du_3}{d\eta} \\ \frac{d^2u_1}{d\eta^2} \\ \frac{d^2u_3}{d\eta^2} \end{bmatrix}, \tag{5.27}$$

or

$$\frac{d^2u_2}{d\eta^2} = \mathbf{D}_2(1:3)\mathbf{u} + \mathbf{D}_2(4:5)\begin{bmatrix} \frac{du_1}{d\eta} \\ \frac{du_3}{d\eta} \end{bmatrix} + \mathbf{D}_2(6:7)\begin{bmatrix} \frac{d^2u_1}{d\eta^2} \\ \frac{d^2u_3}{d\eta^2} \end{bmatrix}, \tag{5.28}$$

where $\mathbf{u} = [u_1, u_2, u_3]^T$ and

$$\mathbf{I}_{2m} = \begin{bmatrix} I_{21}(\eta_2) & I_{22}(\eta_2) & I_{23}(\eta_2) & \eta_2 & 1 & 0 & 0 \end{bmatrix}. \tag{5.29}$$

By taking derivative terms to the left side and nodal variable values to the right side, (5.28) reduces to

$$\begin{bmatrix} -\mathbf{D}_2(4) & 0 & -\mathbf{D}_2(5) \end{bmatrix}\mathbf{u}' + \begin{bmatrix} -\mathbf{D}_2(6) & 1 & -\mathbf{D}_2(7) \end{bmatrix}\mathbf{u}'' = \mathbf{D}_2(1:3)\mathbf{u}, \tag{5.30}$$

where $\mathbf{u}' = \left[\frac{du_1}{d\eta}, \frac{du_2}{d\eta}, \frac{du_3}{d\eta}\right]^T$ and $\mathbf{u}'' = \left[\frac{d^2u_1}{d\eta^2}, \frac{d^2u_2}{d\eta^2}, \frac{d^2u_3}{d\eta^2}\right]^T$.

At the boundary nodes, e.g. $\eta = \eta_1$, we employ the same special stencil, e.g. $\{\eta_1, \eta_2, \eta_3, \eta_4\}$, and extra information, e.g. $\frac{du_2}{d\eta}$ and $\frac{d^2u_2}{d\eta^2}$, used in the approximation of the first-order derivatives. Therefore, approximate expression for the second-order derivative at η_1 in the physical space is obtained by simply substituting

(5.22) into (5.6) and taking $\eta = \eta_1$

$$\frac{d^2 u_1}{d\eta^2} = \underbrace{\mathbf{I}_{2b} \mathbf{C}_{sp}^{-1}}_{\mathbf{D}_{2sp}} \begin{bmatrix} \mathbf{u} \\ \frac{du_2}{d\eta} \\ \frac{d^2 u_2}{d\eta^2} \end{bmatrix}, \tag{5.31}$$

or

$$\frac{d^2 u_1}{d\eta^2} = \mathbf{D}_{2sp}(1:4)\mathbf{u} + \mathbf{D}_{2sp}(5)\frac{du_2}{d\eta} + \mathbf{D}_{2sp}(6)\frac{d^2 u_2}{d\eta^2}, \tag{5.32}$$

where $\mathbf{u} = [u_1, u_2, u_3, u_4]^T$ and

$$\mathbf{I}_{2b} = \begin{bmatrix} I_{21}(\eta_1) & I_{22}(\eta_1) & I_{23}(\eta_1) & I_{24}(\eta_1) & \eta_1 & 1 & 0 & 0 \end{bmatrix}. \tag{5.33}$$

By taking derivative terms to the left side and nodal variable values to the right side, (5.32) reduces to

$$\begin{bmatrix} 0 & -\mathbf{D}_{2sp}(5) & 0 & 0 \end{bmatrix} \mathbf{u}' + \begin{bmatrix} 1 & -\mathbf{D}_{2sp}(6) & 0 & 0 \end{bmatrix} \mathbf{u}'' = \mathbf{D}_{2sp}(1:4)\mathbf{u}, \tag{5.34}$$

where $\mathbf{u}' = \left[\frac{du_1}{d\eta}, \frac{du_2}{d\eta}, \frac{du_3}{d\eta}, \frac{du_4}{d\eta} \right]^T$ and $\mathbf{u}'' = \left[\frac{d^2 u_1}{d\eta^2}, \frac{d^2 u_2}{d\eta^2}, \frac{d^2 u_3}{d\eta^2}, \frac{d^2 u_4}{d\eta^2} \right]^T$.

5.3.3   Matrix assembly for first- and second-order derivative approximations

The IRBF system on a grid line for the first-order derivative is obtained by letting the interior node take values from 2 to $(n_\eta - 1)$ in (5.17); and, making use of (5.26) for the boundary nodes 1 and n_η. In a similar manner, the IRBF system on a grid line for the second-order derivative is obtained by letting the interior node take values from 2 to $(n_\eta - 1)$ in (5.30); and, making use of (5.34) for the boundary nodes 1 and n_η. The resultant matrix assembly is expressed as

$$\underbrace{\begin{bmatrix} \mathbf{A}_1 & \mathbf{B}_1 \\ \mathbf{A}_2 & \mathbf{B}_2 \end{bmatrix}}_{\text{Coefficient matrix}} \begin{bmatrix} \mathbf{u}'^n \\ \mathbf{u}''^n \end{bmatrix} = \begin{bmatrix} \mathbf{R}_1 \\ \mathbf{R}_2 \end{bmatrix} \mathbf{u}^n, \tag{5.35}$$

where $\mathbf{A}_1$, $\mathbf{A}_2$, $\mathbf{B}_1$, $\mathbf{B}_2$, $\mathbf{R}_1$, and $\mathbf{R}_2$ are $n_\eta \times n_\eta$ matrices; $\mathbf{u}'^n = \left[u_1'^n, u_2'^n, ..., u_{n_\eta}'^n \right]^T$; $\mathbf{u}''^n = \left[u_1''^n, u_2''^n, ..., u_{n_\eta}''^n \right]^T$; and, $\mathbf{u}^n = \left[u_1^n, u_2^n, ..., u_{n_\eta}^n \right]^T$. The coefficient ma-

trix is sparse with diagonal sub-matrices. Solving (5.35) yields

$$\mathbf{u}'^n = \mathbf{D}_\eta \mathbf{u}^n, \tag{5.36}$$

$$\mathbf{u}''^n = \mathbf{D}_{\eta\eta} \mathbf{u}^n, \tag{5.37}$$

where $\mathbf{D}_\eta$ and $\mathbf{D}_{\eta\eta}$ are $n_\eta \times n_\eta$ matrices. It can be seen that values of the first-and second-order derivatives at a grid node are expressed as linear combinations of nodal variable values on a grid line. In the case of the Dirichlet boundary conditions, by collocating the PDE at the interior grid nodes and making use of (5.36) and (5.37), a determined system of algebraic equations is obtained, which can be solved for the field variable at the interior grid nodes. With derivatives depending on nodal variable values on a grid line, the sparseness level of the global system matrix is reduced in comparison with that of the coefficient matrix in equation (5.35).

It is noted that the use of fourth-order IRBFs here (i.e. combined compact IRBF) is more straight-forward to include first- and second-order derivative values than the use of second-order IRBFs (Tien et al., 2015c; Thai-Quang et al., 2012b). The former involves only one conversion matrix while there are two conversion matrices required for the latter: one taking extra first-order derivative values and the other taking second-order derivative values.

5.4 Preconditioning technique for the combined compact IRBF

To improve the stability of the combined compact IRBF in the large value range of β, we construct a new equivalent conversion system by multiplying a preconditioning matrix $\mathbf{C^*}^{-1}$ to both sides of the original conversion system (5.9) as

follows.

$$
\mathbf{C}^{*-1}
\begin{bmatrix}
u_1 \\
u_2 \\
u_3 \\
\frac{du_1}{d\eta} \\
\frac{du_3}{d\eta} \\
\frac{d^2 u_1}{d\eta^2} \\
\frac{d^2 u_3}{d\eta^2}
\end{bmatrix}
= \underbrace{\mathbf{C}^{*-1}\mathbf{C}}_{\mathbf{C}_p}
\begin{bmatrix}
w_1 \\
w_2 \\
w_3 \\
c_1 \\
c_2 \\
c_3 \\
c_4
\end{bmatrix},
\tag{5.38}
$$

where $\mathbf{C}$ is the original conversion matrix in (5.9); $\mathbf{C}^{*-1}$ is the preconditioning matrix which has exactly the same form as the original conversion matrix $\mathbf{C}$ but uses a different value of β. Usually, β used in $\mathbf{C}^{*-1}$ is taken to be relatively small, for example $\beta = 10$, so that its corresponding condition number is in a well-behaved range; and, $\mathbf{C}_p$ is a new conversion matrix. This numerical treatment is expected to bypass the ill-condition problems when β in the original conversion matrix $\mathbf{C}$ becomes large (but not go to infinity as the information in $\mathbf{C}$ is lost in this limit due to the current use of finite (double) precision).

Solving (5.38) yields

$$
\begin{bmatrix}
w_1 \\
w_2 \\
w_3 \\
c_1 \\
c_2 \\
c_3 \\
c_4
\end{bmatrix}
= \mathbf{C}_p^{-1}\mathbf{C}^{*-1}
\begin{bmatrix}
u_1 \\
u_2 \\
u_3 \\
\frac{du_1}{d\eta} \\
\frac{du_3}{d\eta} \\
\frac{d^2 u_1}{d\eta^2} \\
\frac{d^2 u_3}{d\eta^2}
\end{bmatrix}.
\tag{5.39}
$$

In a similar manner detailed in Section 5.3, one is able to derive the first- and second-order derivative approximations with the new conversion system. It is noted that the proposed preconditioning technique is only needed when one implements the combined compact IRBF in the large range of β where the ill-condition problems occur. In the small range of β, for example $\beta = \{1, 2, ..., 100\}$, the "pure" combined compact IRBF normally works fine.

5.5 Numerical examples

We evaluate the performance of the present scheme through the following measures.

i. The root mean square error (RMS) is defined as

$$RMS = \sqrt{\frac{\sum_{i=1}^{N} \left(f_i - \overline{f}_i\right)^2}{N}}, \tag{5.40}$$

where f_i and $\overline{f}_i$ are the computed and exact values of the solution f at the i-th node, respectively; and, N is the number of nodes over the whole domain.

ii. The global convergence rate, α, with respect to the grid refinement is defined through

$$Error(h) \approx \gamma h^\alpha = O(h^\alpha). \tag{5.41}$$

where h is the grid size; and, γ and α are exponential model's parameters.

For comparison purposes, in Sections 5.5.1 and 5.5.2, we also implement the global DRBF scheme of Kansa (1990a,b), the compact IRBF scheme of Thai-Quang et al. (2012b), and the standard central FDM for numerical solutions. It is noted that the proposed preconditioning technique described in Section 5.4 is also applied for the compact IRBF-Precond version.

For fluid flow examples in Sections 5.5.3 to 5.5.5 and 5.5.8, we choose a large shape parameter, $\beta = 1000$, for the original conversion matrix $\mathbf{C}$ and a small shape parameter, $\beta = 10$, for the preconditioning matrix $\mathbf{C*}^{-1}$; and, in the examples of Taylor-Green vortex flows, i.e. Sections 5.5.6 and 5.5.7, we choose a large shape parameter, $\beta = 500$, for the original conversion matrix $\mathbf{C}$ and a small shape parameter, $\beta = 10$, for the preconditioning matrix $\mathbf{C*}^{-1}$. We employ the fully coupled procedure which was detailed in (Tien et al., 2015b) to calculate Navier-Stokes equations in Sections 5.5.6 to 5.5.8.

In this work, calculations are done with a Dell computer Optiplex 9010 version 2013. Its specifications are intel(R) core(TM) i7-3770 CPU 3.40 GHz 3.40 GHz,

memory(RAM) of 8GB(7.89 usable) and 64-bit operating system. The Matlab(R) version 2014 is utilised.

5.5.1 Second-order ODE

In order to study the 1D spatial accuracy of the present combined compact IRBF approximation schemes, we consider the following equations

$$\frac{d^2u}{dx^2} = -\pi^2 sin(\pi x), \tag{5.42}$$

$$\frac{du}{dx} = \pi cos(\pi x), \tag{5.43}$$

on a domain $[0, 1]$, subjected to the Dirichlet boundary condition derived from the following exact solution

$$\overline{u} = sin(\pi x). \tag{5.44}$$

Nodal values of both first- and second-order derivatives of u are computed. The calculations are carried out on uniform grids of $\{11, 51, 101\}$. We employ a wide range of β, $\{1, 101, 201, ..., 2001\}$. Figures 5.5, 5.8, and 5.11 illustrate the effect of β on the condition number of the conversion matrix, where we can see that the present combined compact IRBF-Precond has much lower condition numbers than the "pure" combined compact IRBF. Figures 5.6, 5.7, 5.9, 5.10, 5.12, and 5.13 show that the present combined compact IRBF-Precond scheme is more accurate than the DRBF, compact IRBF and compact IRBF-Precond schemes for computing $\frac{du}{dx}$ and $\frac{d^2u}{dx^2}$ in the large value range of β. These Figures also show that the present preconditioning technique leads to a significant improvement in the matrix condition number of the combined compact IRBF and the compact IRBF over the large value range of β.

To study the computational efficiency of the combined compact IRBF and the compact IRBF, we employ different sets of grid points with an increment of 10 (i.e. $\{11, 21, ...\}$) and carry out the simulation until the solution accuracy achieves a target RMS level of 5×10^{-6}. Results obtained are shown in Figure 5.14, indicating that the present combined compact IRBF scheme uses a smaller
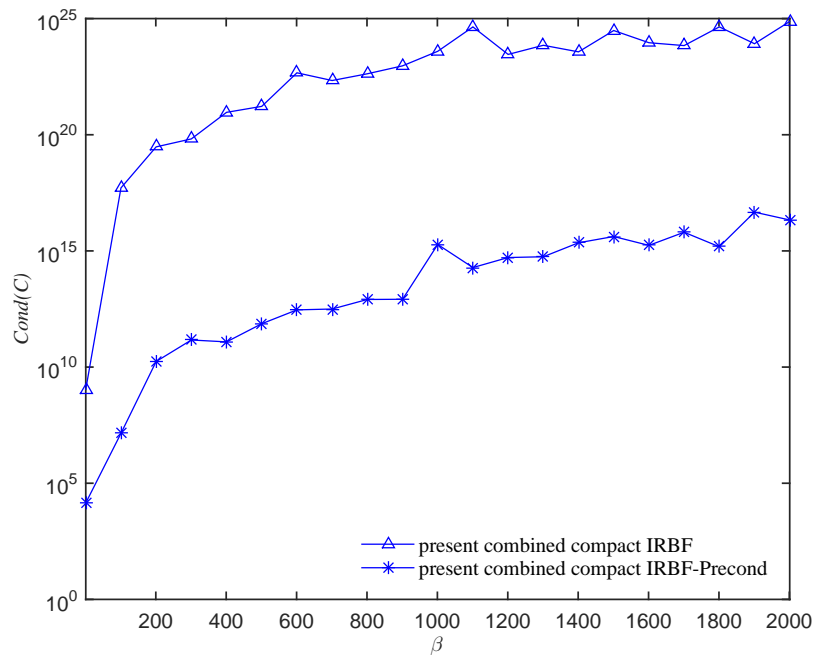
Figure 5.5 Second-order ODE, $nx = 11$: The effect of β on the condition number of the conversion matrix.
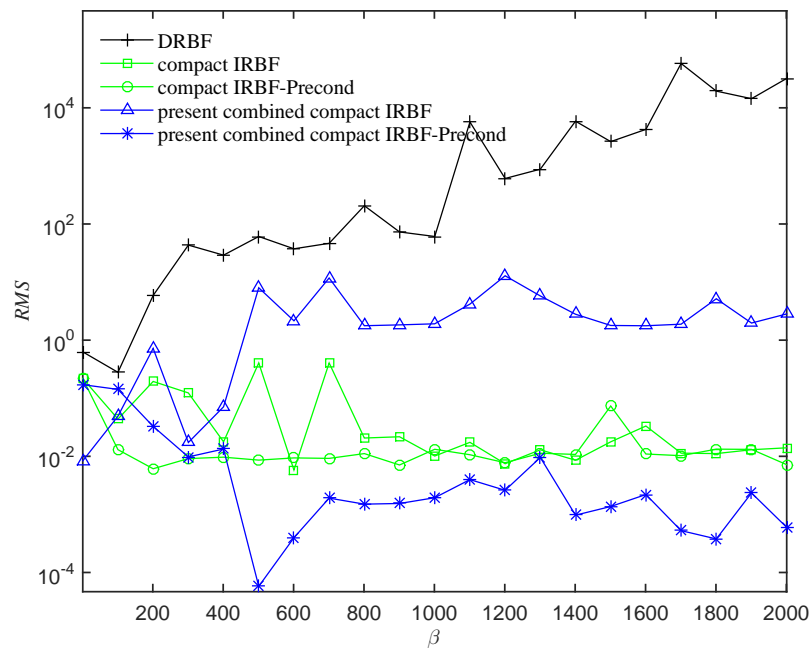
Figure 5.6 Second-order ODE, $nx = 11$: The effect of β on the solution accuracy RMS of first-order derivative approximations.
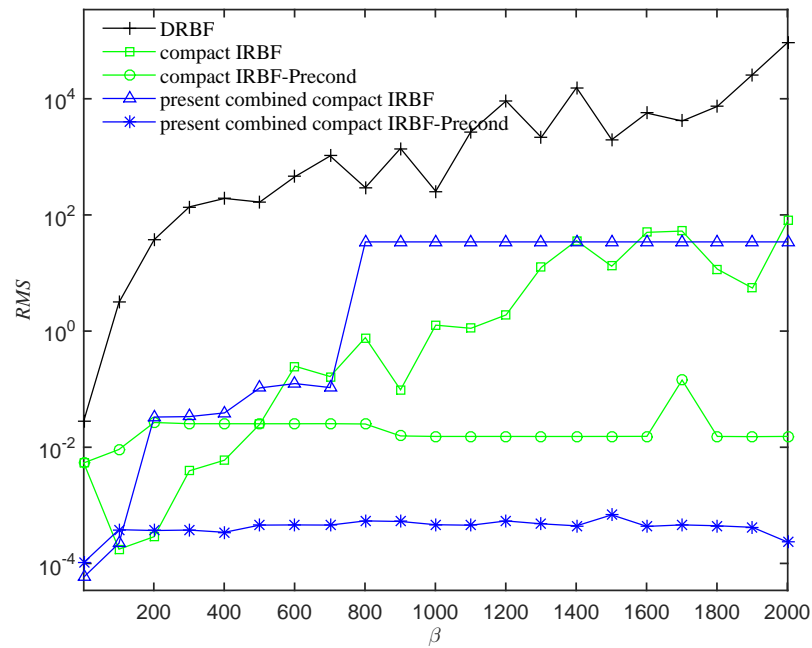
Figure 5.7 Second-order ODE, $nx = 11$: The effect of β on the solution accuracy RMS of second-order derivative approximations.
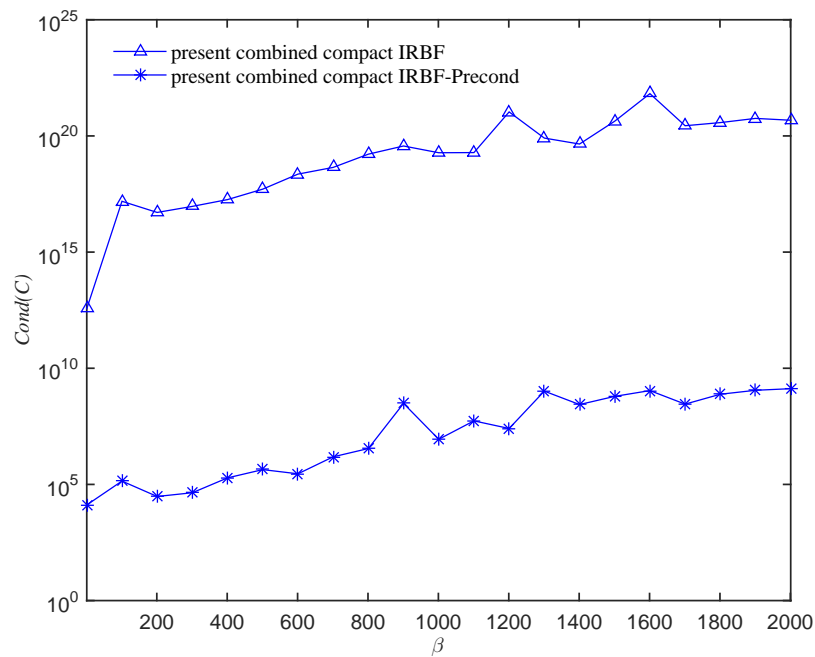
Figure 5.8 Second-order ODE, $nx = 51$: The effect of β on the condition number of the conversion matrix.
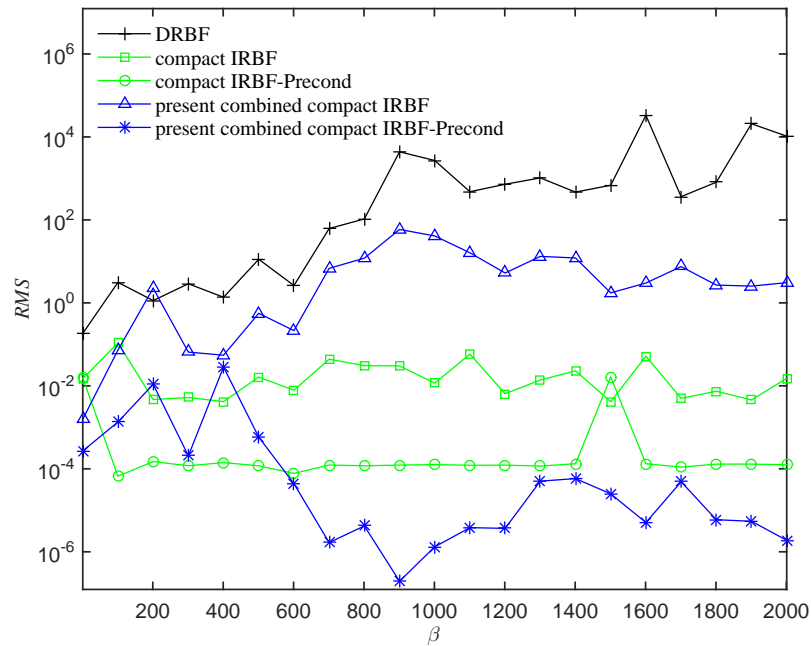
Figure 5.9 Second-order ODE, $nx = 51$: The effect of β on the solution accuracy RMS of first-order derivative approximations.
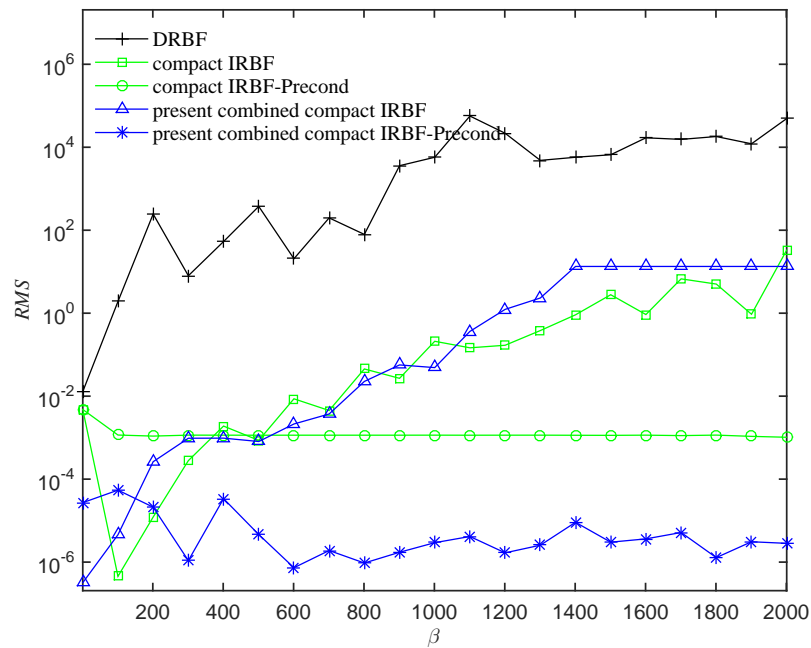
Figure 5.10 Second-order ODE, $nx = 51$: The effect of β on the solution accuracy RMS of second-order derivative approximations.
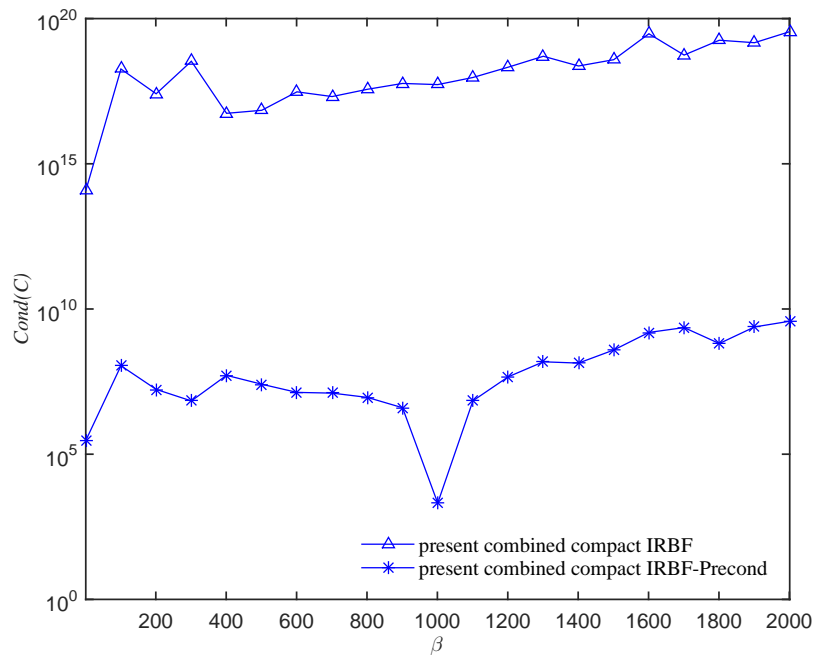
Figure 5.11 Second-order ODE, $nx = 101$: The effect of β on the condition number of the conversion matrix.
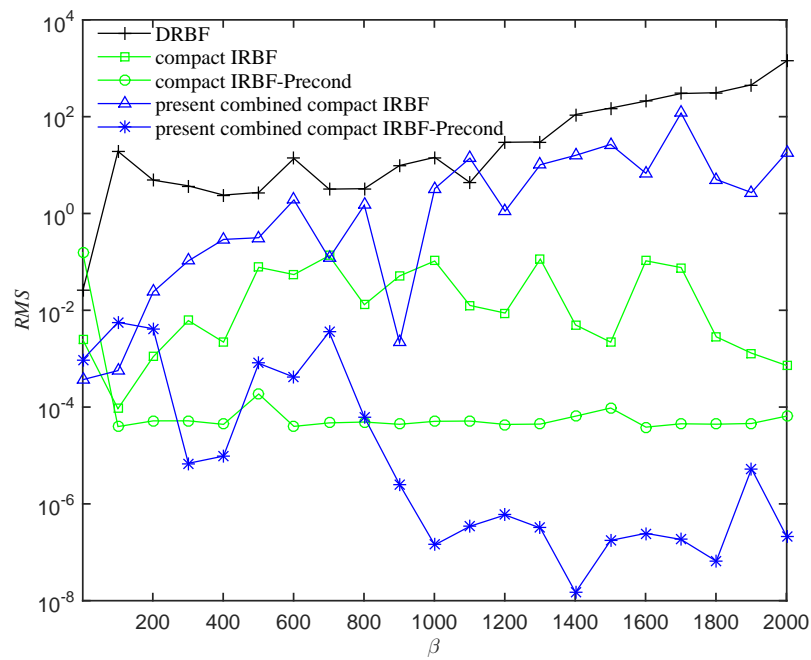
Figure 5.12 Second-order ODE, $nx = 101$: The effect of β on the solution accuracy RMS of first-order derivative approximations.
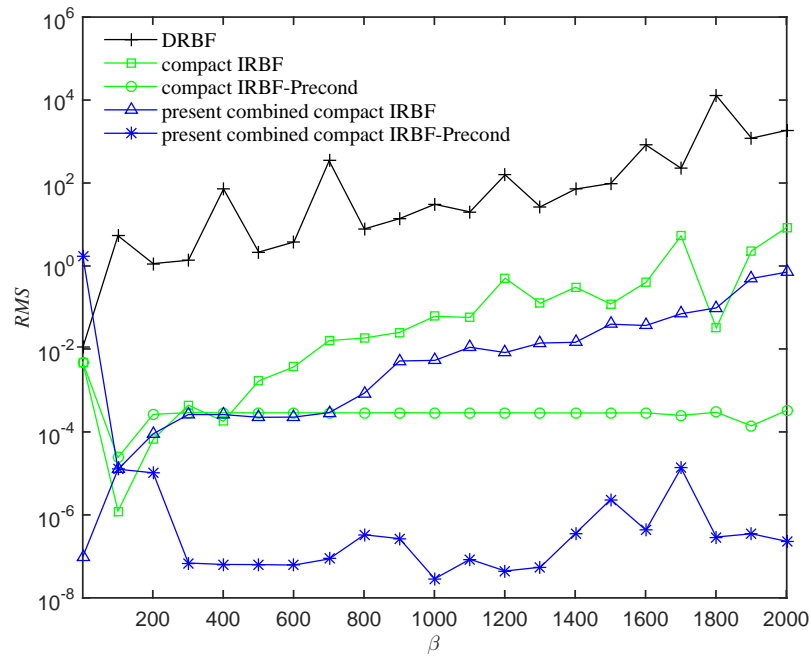
Figure 5.13 Second-order ODE, $nx = 101$: The effect of β on the solution accuracy RMS of second-order derivative approximations.

number of grids and takes much less time to reach the target accuracy than the compact IRBF.
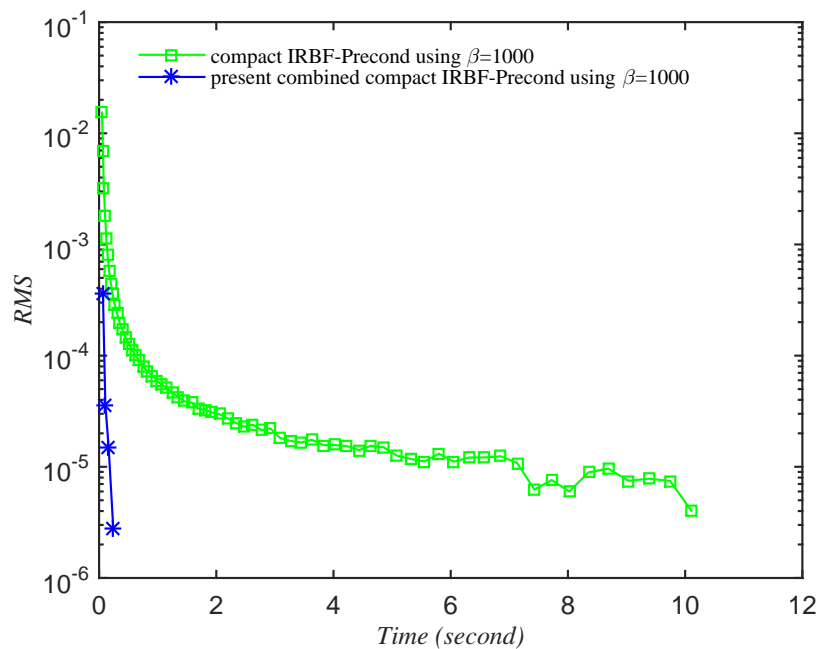
Figure 5.14 Second-order ODE, $\{11, 21, ...\}$: The computational cost to achieve the target accuracy of 5×10^{-6}. The final grid is 661 for the compact IRBF and 41 for the combined compact IRBF.

5.5.2 Poisson equation

In order to study the 2D spatial accuracy of the present combined compact IRBF approximation schemes, we consider the following Poisson equation

$$\frac{d^2u}{dx_1^2} + \frac{d^2u}{dx_2^2} = -2\pi^2 \cos(\pi x_1)\cos(\pi x_2), \qquad (5.45)$$

on a square domain $[0,1]^2$, subjected to the Dirichlet boundary condition derived from the following exact solution

$$\overline{u} = \cos(\pi x_1)\cos(\pi x_2). \qquad (5.46)$$

The calculations are carried out on uniform grids of $\{11 \times 11, 51 \times 51, 101 \times 101\}$. A set of β of $\{1, 101, 201, ..., 2001\}$ is chosen. As in the case of the second-order ODE (i.e. Section 5.5.1), the present combined compact IRBF-Precond scheme outperforms the DRBF, compact IRBF and compact IRBF-Precond schemes in terms of the solution accuracy and stability (Figures 5.15 to 5.17). These Figures also indicate that the stability of the combined compact IRBF and the compact IRBF is much improved with the present preconditioning technique.
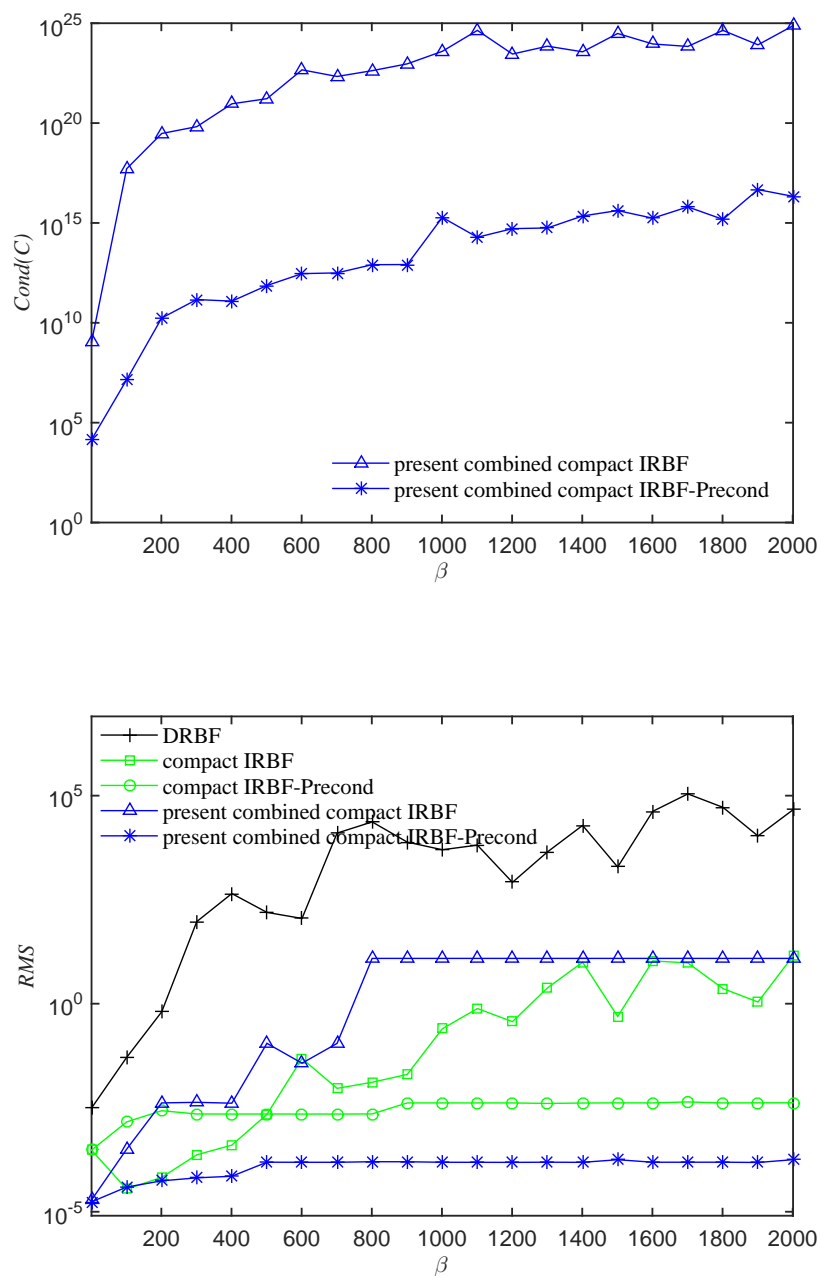
Figure 5.15 Poisson equation, 11×11: The effect of β on the condition number of the conversion matrix (top) and on the solution accuracy RMS (bottom).
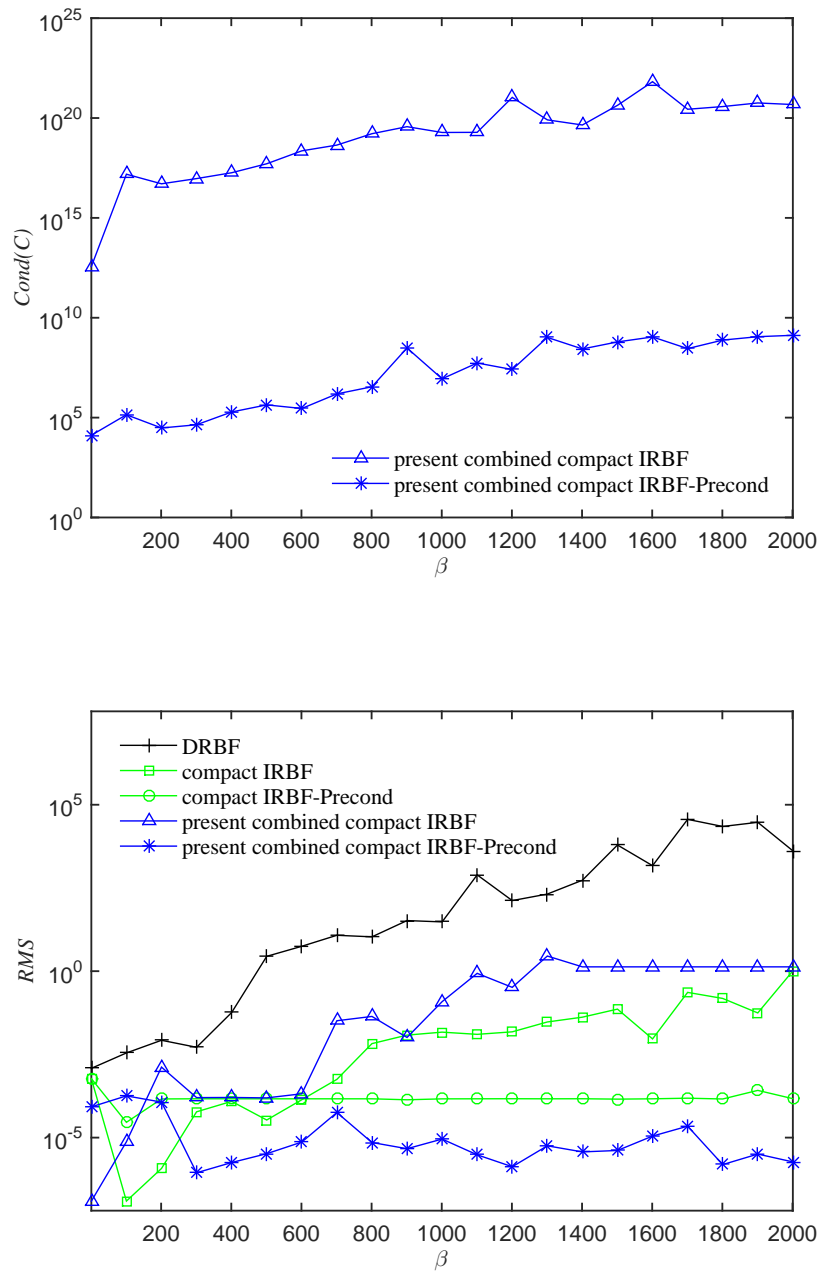
Figure 5.16 Poisson equation, 51×51: The effect of β on the condition number of the conversion matrix (top) and on the solution accuracy RMS (bottom).

To study the computational efficiency of the combined compact IRBF and the compact IRBF, we increase the density of grids as $\{11 \times 11, 21 \times 21, ...\}$ until the solution accuracy achieves a target RMS level of 5×10^{-5}. Figure 5.18 shows that the present scheme combined compact IRBF uses a much smaller number
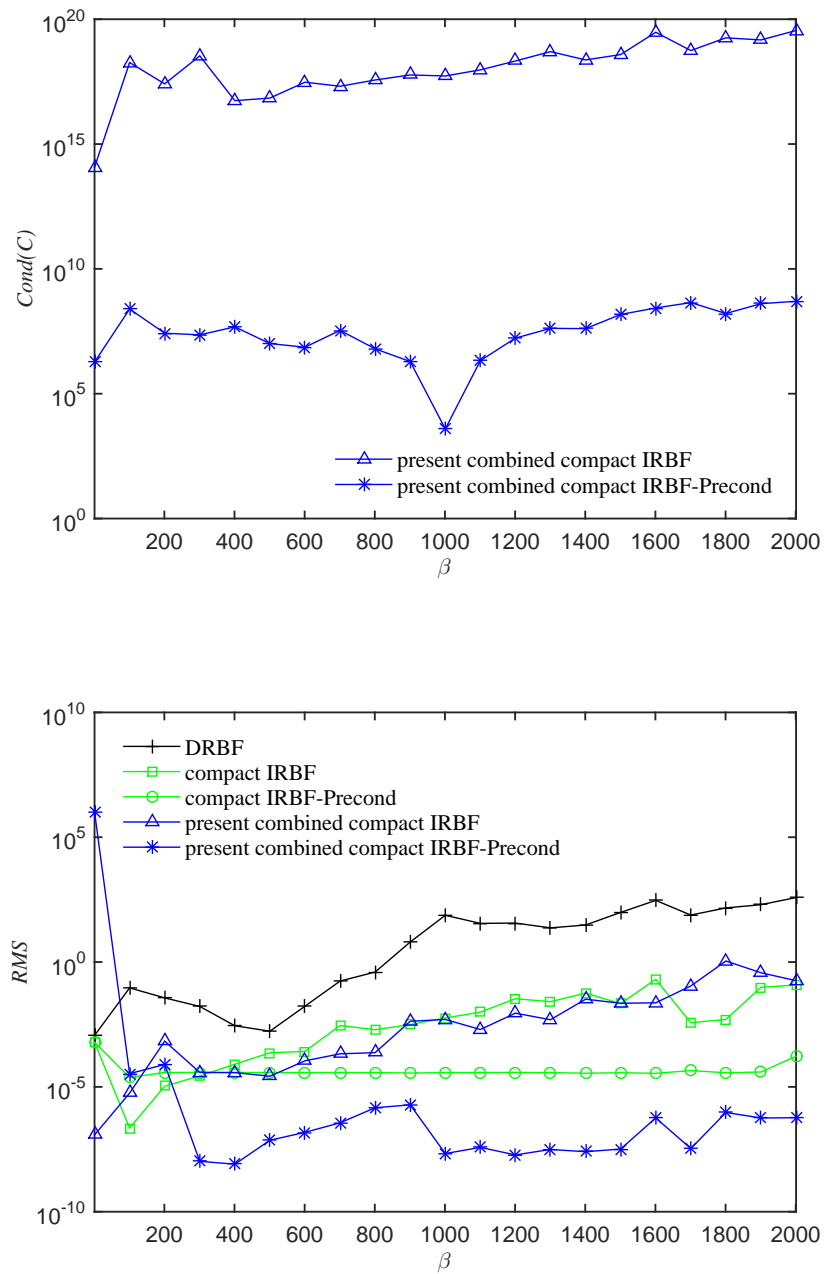
Figure 5.17 Poisson equation, 101×101: The effect of β on the condition number of the conversion matrix (top) and on the solution accuracy RMS (bottom).

of grids and takes much less time to reach the target accuracy than the compact IRBF.
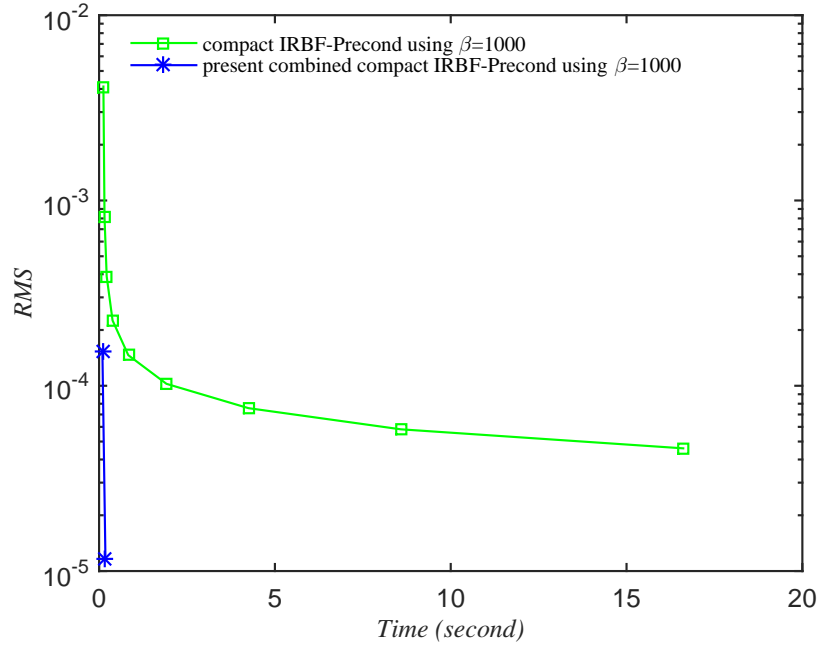
Figure 5.18 Poisson equation, $\{11 \times 11, 21 \times 21, ...\}$: The computational cost to achieve the target accuracy of 5×10^{-5}. The final grid is 91×91 for the compact IRBF and 21×21 for the combined compact IRBF.

5.5.3 Heat equation

By selecting the following heat equation, the performance of the present combined compact IRBF scheme can be studied for the diffusive term only

$$\frac{\partial u}{\partial t} = \frac{\partial^2 u}{\partial x^2}, \quad a \le x \le b, \quad t \ge 0, \tag{5.47}$$

$$u(x, 0) = u_0(x), \quad a \le x \le b, \tag{5.48}$$

$$u(a, t) = u_{\Gamma_1}(t) \quad \text{and} \quad u(b, t) = u_{\Gamma_2}(t), \quad t \ge 0, \tag{5.49}$$

where u and t are the temperature and time, respectively; and, $u_0(x)$, $u_{\Gamma_1}(t)$, and $u_{\Gamma_2}(t)$ are prescribed functions. The temporal discretisation of (5.47) with the Crank-Nicolson scheme gives

$$\frac{u^n - u^{n-1}}{\Delta t} = \frac{1}{2}\left\{\frac{\partial^2 u^n}{\partial x^2} + \frac{\partial^2 u^{n-1}}{\partial x^2}\right\}, \tag{5.50}$$

where the superscript n denotes the current time level. (5.50) can be rewritten as

$$\left\{1 - \frac{\Delta t}{2}\frac{\partial^2}{\partial x^2}\right\}u^n = \left\{1 + \frac{\Delta t}{2}\frac{\partial^2}{\partial x^2}\right\}u^{n-1}. \tag{5.51}$$

Consider (5.47) on a segment $[0, \pi]$ with the initial and boundary conditions

$$u(x, 0) = \sin(2x), \quad 0 < x < \pi. \tag{5.52}$$

$$u(0, t) = u(\pi, t) = 0, \quad t \geq 0. \tag{5.53}$$

The exact solution of this problem is

$$\overline{u}(x, t) = \sin(2x)e^{-4t}. \tag{5.54}$$

The spatial accuracy of the proposed scheme is tested on various uniform grids $\{11, 21, ..., 101\}$. We employ here a small time step, $\Delta t = 10^{-6}$, to minimise the effect of the approximation error in time. The solution is computed at $t = 0.0125$. Figure 5.19 shows that the combined compact IRBF-Precond using $\beta = 1000$ outperforms the FDM in terms of both the solution accuracy and the convergence rate.

5.5.4 Burgers equation

With Burgers equation, the performance of the present combined compact IRBF scheme can be investigated for both the convective and diffusive terms

$$\frac{\partial u}{\partial t} + u\frac{\partial u}{\partial x} = \frac{1}{Re}\frac{\partial^2 u}{\partial x^2}, \quad a \leq x \leq b, \quad t \geq 0, \tag{5.55}$$

$$u(x, 0) = u_0(x), \quad a \leq x \leq b, \tag{5.56}$$

$$u(a, t) = u_{\Gamma_1}(t) \quad \text{and} \quad u(b, t) = u_{\Gamma_2}(t), \quad t \geq 0, \tag{5.57}$$

where $Re > 0$ is the Reynolds number; and, $u_0(x)$, $u_{\Gamma_1}(t)$, and $u_{\Gamma_2}(t)$ are prescribed functions. The temporal discretisations of (5.55) using the Adams-Bashforth scheme for the convective term and Crank-Nicolson scheme for the diffusive term,
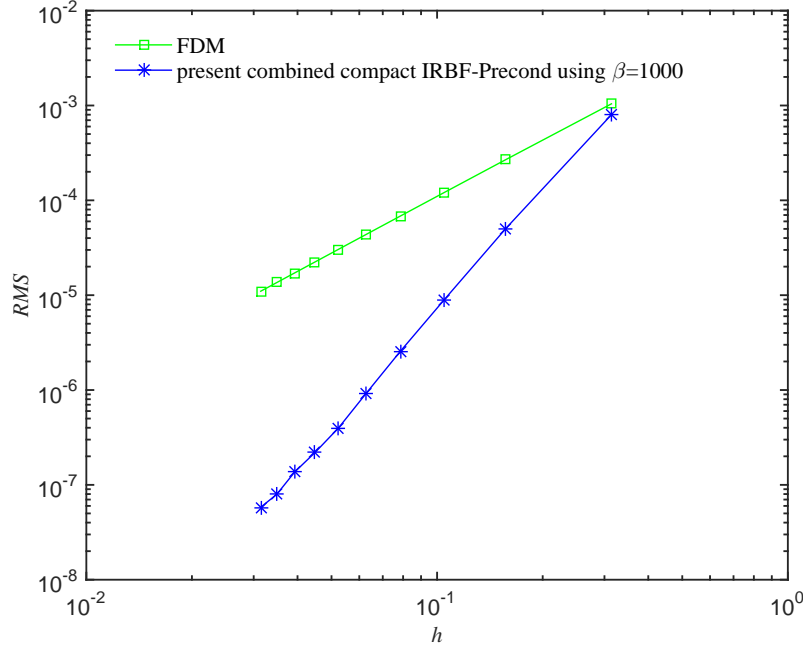
Figure 5.19 Heat equation, $\{11, 21, ..., 101\}$, $Re = 100$, $\Delta t = 10^{-6}$, $t = 0.0125$: The effect of the grid size h on the solution accuracy RMS. The solution converges as $O(h^{1.98})$ for the FDM and $O(h^{4.21})$ for the combined compact IRBF-Precond scheme.

result in

$$\frac{u^n - u^{n-1}}{\Delta t} + \left\{\frac{3}{2}\left(u\frac{\partial u}{\partial x}\right)^{n-1} - \frac{1}{2}\left(u\frac{\partial u}{\partial x}\right)^{n-2}\right\} = \frac{1}{2Re}\left\{\frac{\partial^2 u^n}{\partial x^2} + \frac{\partial^2 u^{n-1}}{\partial x^2}\right\}, \tag{5.58}$$

or

$$\left\{1 - \frac{\Delta t}{2Re}\frac{\partial^2}{\partial x^2}\right\}u^n = \left\{1 + \frac{\Delta t}{2Re}\frac{\partial^2}{\partial x^2}\right\}u^{n-1} - \Delta t\left\{\frac{3}{2}\left(u\frac{\partial u}{\partial x}\right)^{n-1} - \frac{1}{2}\left(u\frac{\partial u}{\partial x}\right)^{n-2}\right\}. \tag{5.59}$$

The problem is considered on a segment $0 \le x \le 1$, $t \ge 0$ in the form (Hassanien et al., 2005)

$$\bar{u}(x, t) = \frac{\alpha_0 + \mu_0 + (\mu_0 - \alpha_0)\exp(\lambda)}{1 + \exp(\lambda)}, \tag{5.60}$$

where $\lambda = \alpha_0 Re(x - \mu_0 t - \beta_0)$, $\alpha_0 = 0.4$, $\beta_0 = 0.125$, $\mu_0 = 0.6$, and $Re = 100$. The initial and boundary conditions can be derived from the analytic solution (5.60). The calculations are carried out on a set of uniform grids $\{11, 21, ..., 101\}$. The time step $\Delta t = 10^{-6}$ is chosen. The errors of the solution are calculated at the time $t = 0.0125$. Figure 5.20 displays that the present combined compact IRBF-Precond using $\beta = 1000$ has much lower errors than the FDM. Also, its

convergence rate is much better than that of the FDM.
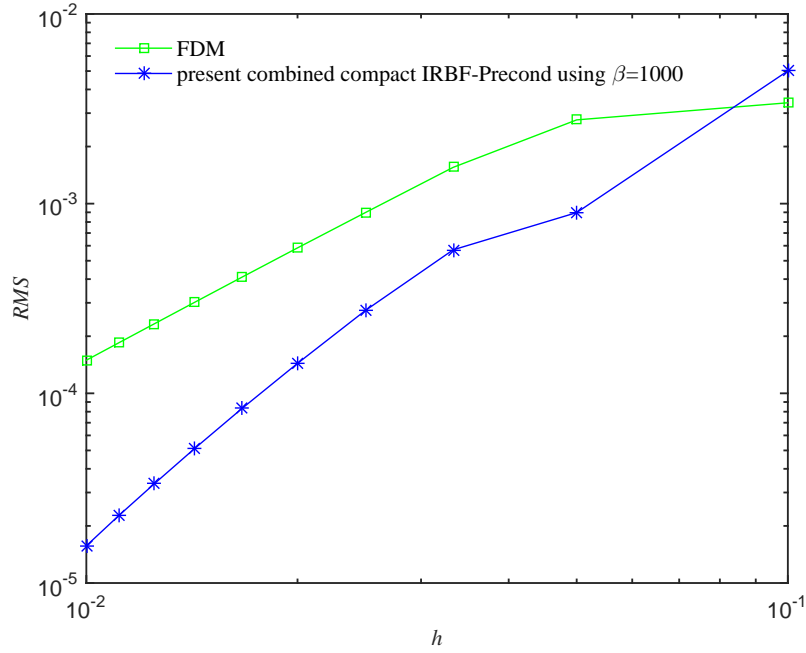
Figure 5.20 Burgers equation, $\{11, 21, ..., 101\}$, $Re = 100$, $\Delta t = 10^{-6}$, $t = 0.0125$: The effect of the grid size h on the solution accuracy RMS. The solution converges as $O(h^{1.48})$ for the FDM and $O(h^{2.47})$ for the combined compact IRBF-Precond scheme.

5.5.5 Convection-diffusion equations

To study the performance of the present combined compact IRBF approximation in simulating convection diffusion problems, we employ the alternating direction implicit (ADI) procedure which was detailed in (Tien et al., 2015c). A two-dimensional unsteady convection-diffusion equation for a variable u is expressed as follows.

$$\frac{\partial u}{\partial t} + c_x \frac{\partial u}{\partial x} + c_y \frac{\partial u}{\partial y} = d_x \frac{\partial^2 u}{\partial x^2} + d_y \frac{\partial^2 u}{\partial y^2} + f_b, \quad (x, y, t) \in \Omega \times [0, T], \qquad (5.61)$$

subject to the initial condition

$$u(x, y, 0) = u_0(x, y), \quad (x, y) \in \Omega, \qquad (5.62)$$

and the Dirichlet boundary condition

$$u(x, y, t) = u_\Gamma(x, y, t), \quad (x, y) \in \Gamma, \tag{5.63}$$

where Ω is a two-dimensional rectangular domain; Γ is the boundary of Ω; $[0, T]$ is the time interval; f_b is the driving function; u_0 and u_Γ are some given functions; c_x and c_y are the convective velocities; and, d_x and d_y are the diffusive coefficients.

In this work, we consider $f_b = 0$, in a square $\Omega = [0, 2]^2$ with the following analytic solution (Noye and Tan, 1989)

$$\overline{u}(x, y, t) = \frac{1}{4t + 1} exp \left[-\frac{(x - c_x t - 0.5)^2}{d_x(4t + 1)} - \frac{(y - c_y t - 0.5)^2}{d_y(4t + 1)} \right]. \tag{5.64}$$

From (5.64), one can derive the initial and boundary conditions. We consider two sets of parameters (Ma et al., 2012)

Case I: $c_x = c_y = 0.8$, $d_x = d_y = 0.01$, $t = 1.25$, $\Delta t = 2.5E - 4$.

Case II: $c_x = c_y = 80$, $d_x = d_y = 0.01$, $t = 0.0125$, $\Delta t = 2.5E - 6$.

The corresponding Peclet number is thus $Pe = 2$ for case I and $Pe = 200$ for case II. To study the accuracy of the solution with the grid refinement, we employ sets of uniform grids as shown in Figures 5.21 and 5.22. The results in these Figures show that the accuracy and the convergence rate of the proposed combined compact IRBF-Precond using $\beta = 1000$ are much better than those of the FDM. For case I, the convergence rates are $O(h^{3.38})$ and $O(h^{1.55})$ for the combined compact IRBF and the FDM, respectively. For case II, the convergence rates are $O(h^{2.71})$ and $O(h^{0.85})$ for the combined compact IRBF and the FDM, respectively.

5.5.6 Taylor-Green vortex in rectangular domain

To study the performance of the present combined compact IRBF approximation in simulating viscous flows in a rectangular domain, we consider a transient viscous flow problem, namely Taylor-Green vortex which is governed by Navier-Stokes equations. The problem has the analytical solutions as follows (Tian et al.,
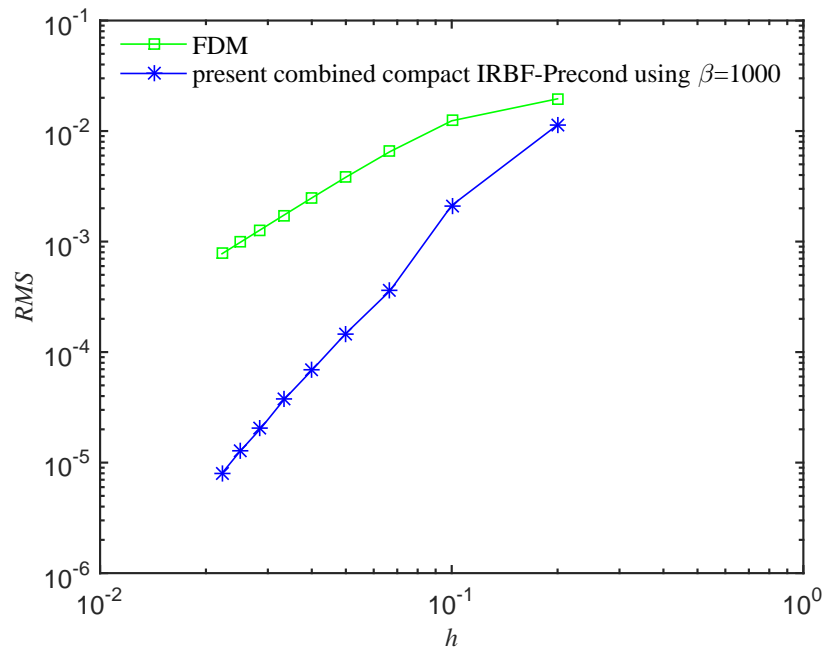
Figure 5.21 Unsteady convection-diffusion equation, $\{11 \times 11, 21 \times 21, ..., 91 \times 91\}$, case I: The effect of the grid size h on the solution accuracy RMS. The solution converges as $O(h^{1.55})$ for the FDM and $O(h^{3.38})$ for the combined compact IRBF-Precond scheme.
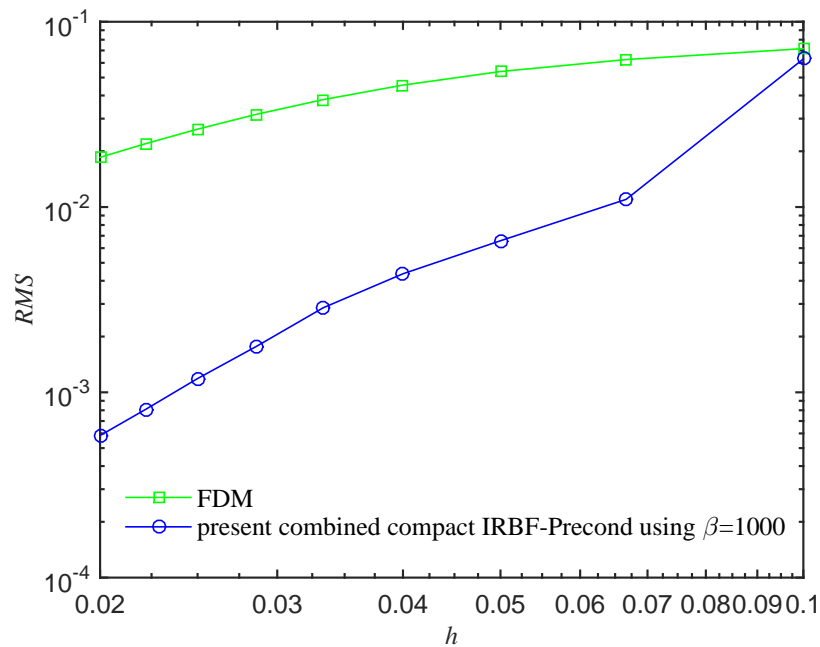
Figure 5.22 Unsteady convection-diffusion equation, $\{21 \times 21, 31 \times 31, ..., 101 \times 101\}$, case II: The effect of the grid size h on the solution accuracy RMS. The solution converges as $O(h^{0.85})$ for the FDM and $O(h^{2.71})$ for the combined compact IRBF-Precond scheme.

2011).

$$\overline{u}(x_1, x_2, t) = -\cos(kx_1)\sin(kx_2)\exp(-2k^2t/Re), \qquad (5.65)$$

$$\overline{v}(x_1, x_2, t) = \sin(kx_1)\cos(kx_2)\exp(-2k^2t/Re), \qquad (5.66)$$

$$\overline{p}(x_1, x_2, t) = -1/4\left\{\cos(2kx_1) + \cos(2kx_2)\right\}\exp(-4k^2t/Re), \qquad (5.67)$$

where $0 \le x_1, x_2 \le 2\pi$. Calculations are carried out for $k = 2$ on a set of uniform grid, $\{11 \times 11, 21 \times 21, ..., 51 \times 51\}$. A fixed time step $\Delta t = 0.002$ and $Re = 100$ are employed. Numerical solutions are computed at $t = 2$. The exact solution, i.e. equations (5.65)-(5.67), provides the initial field at $t = 0$ and the time-dependent boundary conditions. Table 5.1 shows the accuracy comparison between the present scheme and the high-order compact (HOC) finite difference scheme of Tian et al. (2011) (fourth-order). It is seen that the present scheme is superior to the HOC in terms of both the level of accuracy and the convergence rate. The solutions for the u- and v-velocities and for pressure converge, respectively, as $O(h^{3.91})$ and $O(h^{3.81})$ for the present method, and only $O(h^{2.92})$ and $O(h^{3.28})$ for the HOC.

5.5.7 Taylor-Green vortex in non-rectangular domain

In order to analyse the performance of the present combined compact IRBF approximation scheme in solving the transient viscous flow in a non-rectangular domain, we consider the case of an array of decaying vortices with the analytical solutions (Tien et al., 2015b) described by

$$\overline{u}(x_1, x_2, t) = \sin(\pi x_1)\cos(\pi x_2)\exp(-2\pi^2 t/Re), \qquad (5.68)$$

$$\overline{v}(x_1, x_2, t) = -\sin(\pi x_2)\cos(\pi x_1)\exp(-2\pi^2 t/Re), \qquad (5.69)$$

$$\overline{p}(x_1, x_2, t) = 1/2\left\{\cos^2(\pi x_2) - \sin^2(\pi x_1)\right\}\exp(-4\pi^2 t/Re). \qquad (5.70)$$

The flow is computed in a circular domain with radius of unity and centred at the origin of the coordinate system. The problem domain is embedded in a uniform Cartesian grid on $\Omega = [-1.5, 1.5]^2$ and the grid nodes exterior to the domain are removed. The interior nodes falling within a small distance $\delta = h/8$, where

Table 5.1 Taylor-Green vortex, rectangular domain: *RMS* errors and convergence rates.

Grid	present combined compact IRBF using $\beta = 500$			HOC (Tian et al., 2011)		
	u-error	v-error	p-error	u-error	v-error	p-error
11×11	9.0757315E-02	9.0757322E-02	2.3542625E-01	7.0070489E-02	7.0070489E-02	1.0764149E-01
21×21	3.8338024E-03	3.8338114E-03	1.3288235E-02	9.0692193E-03	9.0692193E-03	1.0567607E-02
31×31	1.0201809E-03	1.0201870E-03	3.3851835E-03	2.8851487E-03	2.8851487E-03	2.9103288E-03
41×41	3.6194151E-04	3.6194102E-04	1.4603595E-03	1.2238736E-03	1.2238736E-03	1.1356134E-03
51×51	1.5492043E-04	1.5482812E-04	4.1378984E-04	6.3063026E-04	6.3063026E-04	5.3933641E-04
Rate	$O(h^{3.91})$	$O(h^{3.91})$	$O(h^{3.81})$	$O(h^{2.92})$	$O(h^{2.92})$	$O(h^{3.28})$

h is the grid size, to the boundary will also be discarded (Mai-Duy and Tran-Cong, 2010). The boundary nodes are generated through the intersection of the grid lines and the boundary as demonstrated in Figure 5.23. The calculations are carried out using several uniform grids, $\{10 \times 10, 20 \times 20, ..., 50 \times 50\}$. The Reynolds number is set to be $Re = 5$ and numerical solutions are computed at $t = 0.3$ using a fixed time step $\Delta t = 0.001$. The initial field at $t = 0$ and time-dependent boundary conditions are given by (5.68)-(5.70). Table 5.2 illustrates the accuracy comparison between the present scheme and the compact IRBF approach of Tien et al. (2015b). It is observed that errors produced by the present scheme are much lower than those generated by the compact IRBF.
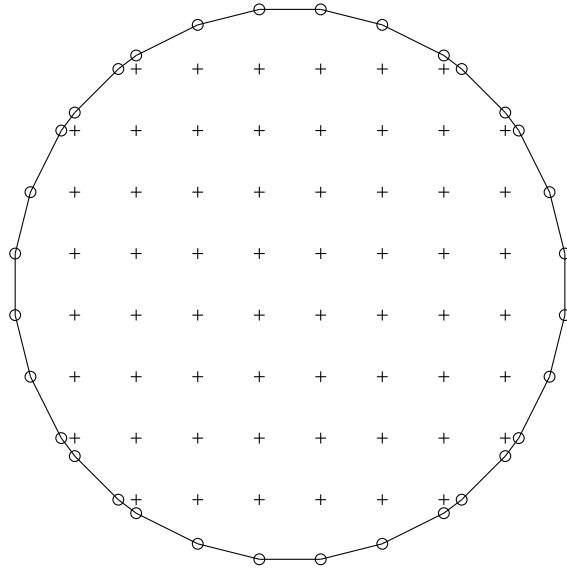
Figure 5.23 Taylor-Green vortex, non-rectangular domain, spatial discretisation: $+$ represents interior nodes; and, $\circ$ represents boundary nodes.

5.5.8 Irregular bottom lid driven cavity

The lid driven cavity with a deformed base presented in (Udaykumar et al., 1996; Shyy et al., 1996; Mariani and Prata, 2008; Tien et al., 2015b) is chosen to validate the performance of the present approximation scheme in simulating fluid flow problems in an irregular domain. The base is deformed sinusoidally with an amplitude of 10 percent of the base. The computational do-

Table 5.2 Taylor Green vortex, non-rectangular domain: *RMS* errors and convergence rates.

Grid	present combined compact IRBF using $\beta = 500$			compact IRBF using $\beta = 40$ (Tien et al., 2015b)		
	u-error	v-error	p-error	u-error	v-error	p-error
10×10	6.7854399E-03	7.3789723E-03	1.5666056E-02	5.0940713E-02	3.9890094E-02	9.5986185E-02
20×20	7.3935223E-04	5.3269646E-04	7.4691913E-03	1.1003665E-03	7.9266552E-04	2.2013746E-03
30×30	1.3671917E-04	1.1479088E-04	2.5417428E-04	9.7670238E-05	8.1362620E-05	5.1711179E-04
40×40	4.5332629E-05	3.4903187E-05	3.1245155E-04	5.8426984E-05	2.8665169E-05	2.1616129E-04
50×50	1.7119756E-05	1.6100433E-05	8.5671434E-05	3.3759336E-05	2.3569385E-05	1.4680716E-04
Rate	$O(h^{3.53})$	$O(h^{3.63})$	$O(h^{3.20})$	$O(h^{4.44})$	$O(h^{4.59})$	$O(h^{3.88})$

main and boundary conditions are illustrated in Figure 5.24. The interior and boundary nodes are generated in a similar manner described in Section 5.5.7. The spatial discretisation is shown in Figure 5.25. A range of uniform grids, $\{53 \times 53, 63 \times 63, 83 \times 83, 93 \times 93\}$ is employed in the simulation. A fixed time step and Reynolds number are chosen to be $\Delta t = 0.001$ and $Re = 1000$, respectively. The results obtained by the present method are compared with those reported in (Shyy et al., 1996; Mariani and Prata, 2008; Tien et al., 2015b), where appropriate. From the literature, the finite volume method (FVM) results using the well-tested body-fitted coordinate formulation and the dense grid of 121×121 presented in Shyy et al. (1996) have been considered as "Benchmark" results for comparison purposes.
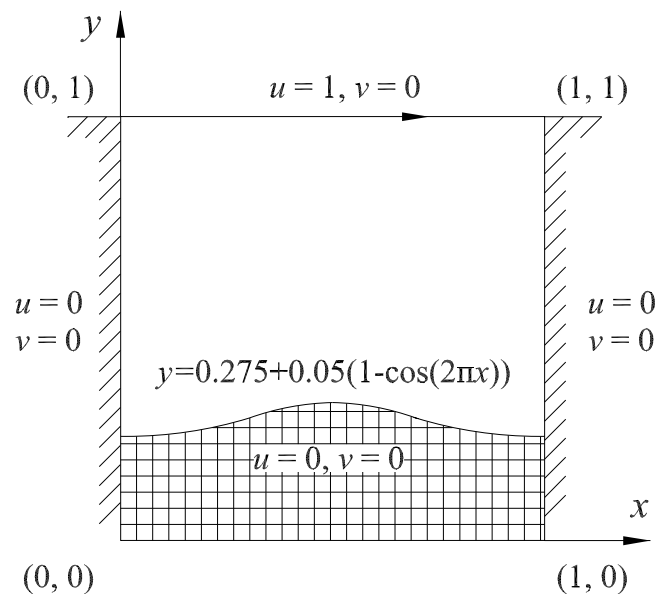
Figure 5.24 Irregular bottom lid driven cavity: problem configuration and boundary conditions.

Table 5.25 shows the present results for the extrema of the vertical and horizontal velocity profiles along the vertical centreline of the cavity. With relatively coarse grids, the results obtained by the present scheme are very comparable with other schemes using much denser grids. Although good numerical results are acquired, the effects of irregular boundaries on the solution accuracy and stability are still not theoretically explained, and further studies are needed.

Figure 5.26 displays horizontal and vertical velocity profiles along the vertical centreline for different grid sizes, where a grid convergence of the present scheme

Table 5.3 Irregular bottom lid driven cavity, $\beta = 1000$, $Re = 1000$: Extrema of the vertical and horizontal velocity profiles along the vertical centreline of the cavity.

Method	Grid	u_{min}	y_{min}	v_{max}	y_{max}
Present combined compact IRBF	53×53	-0.3781442	0.4975	0.2180640	0.5601
Present combined compact IRBF	63×63	-0.3924106	0.4959	0.2214069	0.5563
Present combined compact IRBF	83×83	-0.3958749	0.4951	0.2274348	0.5547
Present combined compact IRBF	93×93	-0.3979039	0.4949	0.2292693	0.5549
compact IRBF (u, v, p) (Tien et al., 2015b)	53×53	-0.3695975	0.4989	0.2165344	0.5638
compact IRBF (u, v, p) (Tien et al., 2015b)	63×63	-0.3847773	0.4967	0.2239138	0.5589
compact IRBF (u, v, p) (Tien et al., 2015b)	83×83	-0.3950552	0.4953	0.2282167	0.5555
compact IRBF (u, v, p) (Tien et al., 2015b)	93×93	-0.3972010	0.4950	0.2286893	0.5548
FVM[a] (u, v, p) (Mariani and Prata, 2008)	100×100	≈ -0.3524	≈ 0.4929	—	—
Benchmark FVM[a] (u, v, p) (Shyy et al., 1996)	121×121	≈ -0.3808	≈ 0.5017	≈ 0.2362	≈ 0.5610

[a] FVM results extracted from Figures in (Shyy et al., 1996; Mariani and Prata, 2008)
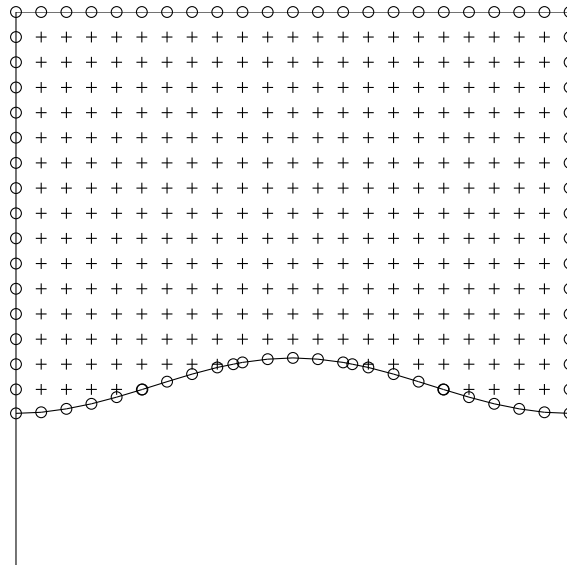
Figure 5.25 Irregular bottom lid driven cavity, spatial discretisation: $+$ represents interior nodes; $\circ$ represents boundary nodes.

is obviously observed (i.e. the present solution approaches the benchmark solution with a fast rate as the grid density is increased). The present scheme effectively achieves the benchmark results with a grid of only 83×83 in comparison with the grid of 121×121 used to obtain the benchmark results in (Shyy et al., 1996). In addition, the present results with a grid of only 53×53 outperform those of Mariani and Prata (2008) using the grid of 100×100.

To exhibit contour plots of the flow, we employ the grid of 83×83. Figures 5.27 and 5.28 show streamlines (which are derived from the velocity) and pressure deviation contours, respectively. These plots are in close agreement with those reported in the literature. Additionally, Figure 5.29 shows the iso-vorticity lines of the present simulation.
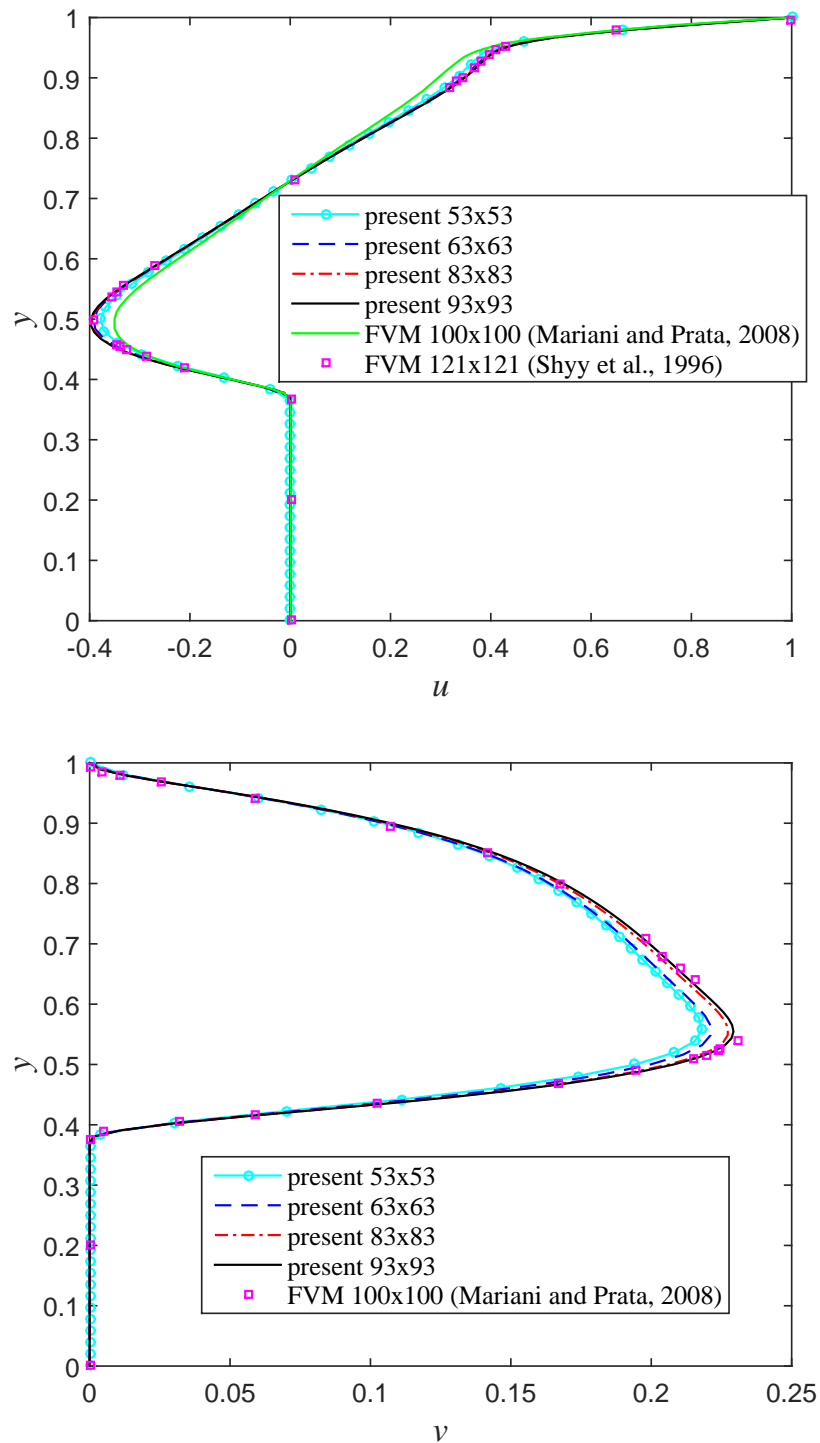
Figure 5.26 Irregular bottom lid driven cavity, $\beta = 1000$, $Re = 1000$: Profiles of the u-velocity (top) and v-velocity (bottom) along the vertical centreline as the grid density increases. It is noted that the curves for the last two grids are indistinguishable and in good agreement with the benchmark results of Shyy et al. (1996).
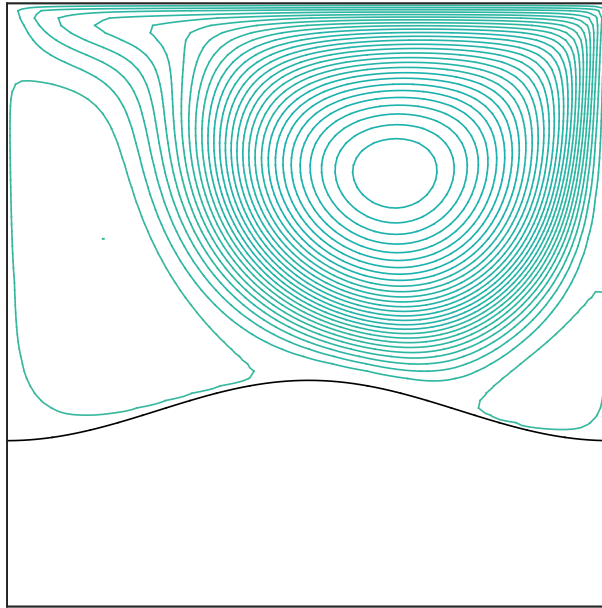
Figure 5.27 Irregular bottom lid driven cavity, $\beta = 1000$, $Re = 1000$: Streamlines of the flow with the grid of 83×83. The plot contains 30 contour lines whose levels vary linearly from the minimum to maximum values; and, it is in good agreement with that of Shyy et al. (1996).
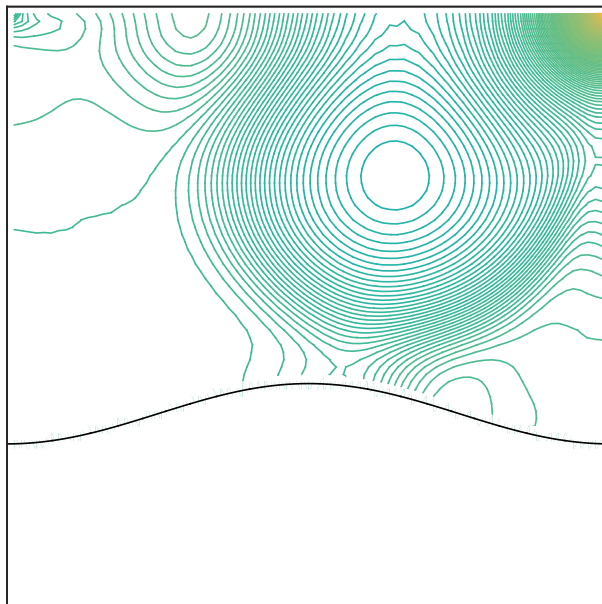
Figure 5.28 Irregular bottom lid driven cavity, $\beta = 1000$, $Re = 1000$: Static pressure contours of the flow with the grid of 83×83. The plot contains 160 contour lines whose levels vary linearly from the minimum to maximum values.
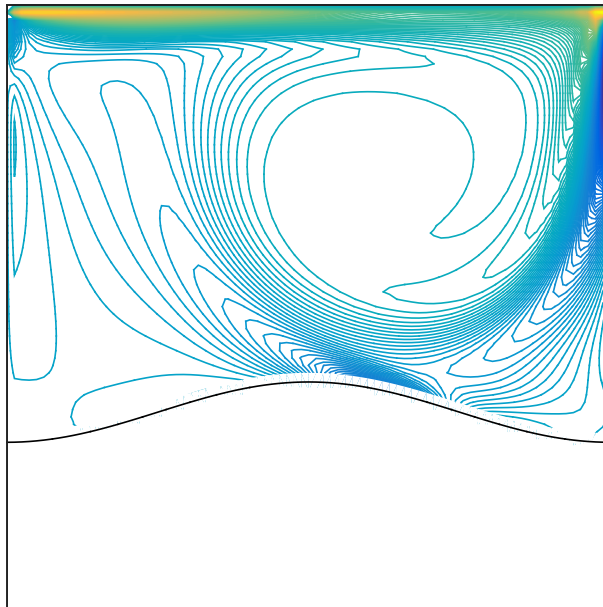
Figure 5.29 Irregular bottom lid driven cavity, $\beta = 1000$, $Re = 1000$: Iso-vorticity lines of the flow with the grid of 83×83. The plot contains 160 contour lines whose levels vary linearly from the minimum to maximum values.

5.6 Concluding remarks

The main purpose of this work is to provide a scheme that allows for stable calculation of IRBF approximations at large values of the shape parameter, where the ill-condition problem becomes severe. The increasing flat region of RBF is of particular interest since it often corresponds to the most accurate RBF approximations as shown in recent works (Larsson et al., 2013; Fornberg et al., 2013). In the chapter, we have proposed an idea of using high-order IRBFs to construct combined compact approximations, which allows a more straightforward incorporation of nodal values of first- and second-order derivatives, and yields better solution accuracy over compact approximations. Then, we have proposed a preconditioning technique to circumvent the ill-condition problems of compact IRBF approaches associated with large values of the shape parameter β and the stability is shown to be significantly improved. In elliptic equation tests, we have found that in the large value range of β the proposed combined compact IRBF-Precond solutions are many orders of magnitude better than those of the DRBF, compact IRBF, and compact IRBF-Precond schemes. In the simulation of several fluid flow problems, the new method performs significantly better than the standard central FDM, the HOC and the compact IRBF. This study provides an effective tool for the numerical exploration of IRBFs in the large value range of the shape parameter. The present robust and highly accurate approximation method based on MQ RBFs is promising for many scientific and engineering problems governed by PDEs.

In the next chapter, the combined compact scheme will be employed for solving various fluid flow problems culminating in the solution of fluid structure interaction problems.

Chapter 6

Fluid structure interaction applications

In this study, we present a high-order numerical method based on a combined compact integrated RBF (IRBF) approximation for viscous flow and fluid structure interaction (FSI) problems. In the method, the fluid variables are locally approximated by using the combined compact IRBF, and the incompressible Navier-Stokes equations are solved by using the velocity-pressure formulation in a direct fully coupled approach. The fluid solver is verified through various problems including heat, Burgers, convection-diffusion equations, Taylor-Green vortex and lid driven cavity flows. It is then applied to simulate some FSI problems in which an elastic structure is immersed in a viscous incompressible fluid. For FSI simulations, we employ the immersed boundary framework using a regular Eulerian computational grid for the fluid mechanics together with a Lagrangian representation of the immersed boundary. The numerical results obtained by the present scheme are highly accurate or in good agreement with those reported in earlier studies of the same problems.

6.1 Introduction

Although many scientific and engineering problems involve fluid structure interaction (FSI), thorough study of such problems remains a challenge due to their strong nonlinearity and multidisciplinary requirements (Chakrabarti, 2005; Dowell and Hall, 2001; Morand and Ohayon, 1995). For most FSI problems, closed

form analytic methods to the model equations are often not available, while laboratory experiments are not practical due to limited resources. Therefore, to investigate the fundamental physics involved in the complicated interaction between fluids and solids, one has to rely on numerical methods (Hou et al., 2012b).

In this study, we are interested in the interaction of a viscous incompressible fluid with an immersed elastic membrane. The immersed boundary method (IBM), originally developed by Peskin (1977), is designed to solve this kind of problem. The IBM is a mixed Eulerian-Lagrangian scheme in which the fluid dynamics based on the Navier-Stokes (N-S) equations are described in Eulerian form, and the elasticity of the structure is described in Lagrangian form. The IBM considers the structure as an immersed boundary which can be represented by a singular force in the N-S equations rather than a real body. It avoids grid-conforming difficulties associated with the moving boundary faced by conventional body-fitted methods. The fluid computation is done on a fixed, uniform computational lattice and the representation of the immersed boundary is independent of this lattice. The immersed boundary exerts a singular force on the nearby lattice points of the fluid with the help of a computational model of the Dirac δ-function. At the same time, the representative material points of the immersed boundary move at the local fluid velocity, which is obtained by interpolation from the nearby lattice points of the fluid. The same δ-function weights are used in the interpolation step as in the application of the boundary forces on the fluid. Computer simulations using the IBM such as blood flow in the heart (Peskin, 1977; McQueen et al., 1982), insect flight (Miller and Peskin, 2004), aquatic animal locomotion (Fauci and Peskin, 1988), bio-film processing (Dillon et al., 1996), and flow past a pick-up truck (Iaccarino et al., 2004) have exhibited the great potential of the IBM in FSI applications. Reviews on immersed methods can be found in (Mittal and Iaccarino, 2005; Sotiropoulos and Yang, 2014).

High-order approximation schemes have the ability to produce highly accurate solutions to incompressible viscous flow problems. With these schemes, a high level of accuracy can be achieved using a relatively coarse discretisation. Many types of high-order approximation methods have been reported in the literature. Botella and Peyret (1998) developed a Chebyshev collocation method for the lid-

driven cavity flow. Various types of high-order compact (HOC) finite difference algorithms were proposed (Lele, 1992; Tian et al., 2011; Fadel et al., 2011). On the other hand, radial basis function networks (RBFs) have gained a lot of attention from researchers (Kansa, 1990a,b; Fasshauer, 2007). Different schemes of integrated RBF approximation (here referred to as IRBF) were developed in the literature (Ngo-Cong et al., 2012; Thai-Quang et al., 2012b; Mai-Duy and Tran-Cong, 2013; Tien et al., 2015c). In (Tien et al., 2015b), the authors developed a high-order fully coupled scheme based on compact IRBF approximations for viscous flow problems, where nodal first- and second-derivative values are included in the stencil approximation and the starting points in the integration process are second-order derivatives. In their work, the N-S governing equations are taken in the primitive form where the velocity and pressure fields are solved in a direct fully coupled approach. With relatively coarse meshes, the compact IRBF produces very accurate solutions to many fluid flow problems in comparison with some other methods such as the standard central finite different method (FDM) and the HOC. Recently, Tien et al. (2015a) proposed a combined compact IRBF approximation scheme, where nodal first- and second-derivative values are also included in the stencil approximation, but the starting points are fourth-order derivatives. The fourth-order IRBF approach allows a more straight-forward incorporation of nodal values of first- and second-order derivatives, and yields better accuracy over previous IRBF approximation schemes.

In this chapter, we will incorporate the high-order combined compact IRBF approximation introduced in (Tien et al., 2015a) into the fully coupled N-S approach reported in (Tien et al., 2015b). The new high-order fluid solver is verified through various problems such as heat, Burgers, convection-diffusion equations, Taylor-Green vortex and lid driven cavity flows. It will show that highly accurate results are obtained with the present approach. Then, we embed the fluid solver in the IBM procedure outlined in (Lai and Peskin, 2000; Brittany and Jeffrey) to simulate FSI problems in which a stretched elastic fibre/membrane relaxes in a viscous fluid. Comparisons between the present scheme and some others, where appropriate, are presented; and, numerical studies of the grid convergence and order of accuracy are also included.

The remainder of this chapter is organised as follows: Sections 6.2 first reviews the spatial disretisation using the combined compact IRBF. Following this, Section 6.3 briefly describes the fully coupled approach for N-S equations. Section 6.4 summarises the mathematical formulation of the IBM. In Section 6.5, various numerical examples are presented and the present results are compared with some benchmark solutions, where appropriate. Finally, concluding remarks are given in Section 6.6.

6.2 Review of combined compact IRBF scheme

Consider a two-dimensional domain Ω, which is represented by a uniform Cartesian grid. The nodes are indexed in the x-direction by the subscript i ($i \in \{1, 2, ..., n_x\}$) and in the y-direction by j ($j \in \{1, 2, ..., n_y\}$). For rectangular domains, let N be the total number of nodes ($N = n_x \times n_y$) and N_{ip} be the number of interior nodes ($N_{ip} = (n_x - 2) \times (n_y - 2)$). At an interior grid point $\mathbf{x}_{i,j} = (x_{(i,j)}, y_{(i,j)})^T$ where $i \in \{2, 3, ..., n_x - 1\}$ and $j \in \{2, 3, ..., n_y - 1\}$, the associated stencils to be considered here are two local stencils: $\{x_{(i-1,j)}, x_{(i,j)}, x_{(i+1,j)}\}$ in the x-direction and $\{y_{(i,j-1)}, y_{(i,j)}, y_{(i,j+1)}\}$ in the y-direction. Hereafter, for brevity, η denotes either x or y in a generic local stencil $\{\eta_1, \eta_2, \eta_3\}$, where $\eta_1 < \eta_2 < \eta_3$, as illustrated in Figure 6.1.
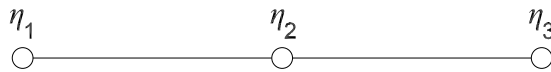
Figure 6.1 Compact 3-point 1D-IRBF stencil for interior nodes.

The integral process of the present combined compact IRBF starts with the decomposition of fourth-order derivatives of a variable, u, into RBFs

$$\frac{d^4 u(\eta)}{d\eta^4} = \sum_{i=1}^{m} w_i G_i(\eta). \tag{6.1}$$

Approximate representations for the third- to first-order derivatives and the func-

tions itself are then obtained through the integration processes

$$\frac{d^3 u(\eta)}{d\eta^3} = \sum_{i=1}^{m} w_i I_{1i}(\eta) + c_1, \tag{6.2}$$

$$\frac{d^2 u(\eta)}{d\eta^2} = \sum_{i=1}^{m} w_i I_{2i}(\eta) + c_1\eta + c_2, \tag{6.3}$$

$$\frac{du(\eta)}{d\eta} = \sum_{i=1}^{m} w_i I_{3i}(\eta) + \frac{1}{2}c_1\eta^2 + c_2\eta + c_3, \tag{6.4}$$

$$u(\eta) = \sum_{i=1}^{m} w_i I_{4i}(\eta) + \frac{1}{6}c_1\eta^3 + \frac{1}{2}c_2\eta^2 + c_3\eta + c_4, \tag{6.5}$$

where $I_{1i}(\eta) = \int G_i(\eta)d\eta$; $I_{2i}(\eta) = \int I_{1i}(\eta)d\eta$; $I_{3i}(\eta) = \int I_{2i}(\eta)d\eta$; $I_{4i}(\eta) = \int I_{3i}(\eta)d\eta$; and, c_1, c_2, c_3, and c_4 are the constants of integration. The analytic form of the IRBFs up to eighth-order can be found in (Mai-Duy, 2005). It is noted that, for the solution of second-order PDEs, only (6.3)-(6.5) are needed.

6.2.1 First-order derivative approximations

For the combined compact approximation of the first-order derivatives at interior nodes, extra information is chosen as not only $\left\{ \frac{du_1}{d\eta}; \frac{du_3}{d\eta} \right\}$ but also $\left\{ \frac{d^2 u_1}{d\eta^2}; \frac{d^2 u_3}{d\eta^2} \right\}$. We construct the conversion system over a 3-point stencil as follows.

$$\begin{bmatrix} u_1 \\ u_2 \\ u_3 \\ \frac{du_1}{d\eta} \\ \frac{du_3}{d\eta} \\ \frac{d^2 u_1}{d\eta^2} \\ \frac{d^2 u_3}{d\eta^2} \end{bmatrix} = \underbrace{\begin{bmatrix} \mathbf{I_4} \\ \mathbf{I_3} \\ \mathbf{I_2} \end{bmatrix}}_{\mathbf{C}} \begin{bmatrix} w_1 \\ w_2 \\ w_3 \\ c_1 \\ c_2 \\ c_3 \\ c_4 \end{bmatrix}, \tag{6.6}$$

where $\frac{du_i}{d\eta} = \frac{du}{d\eta}(\eta_i)$ with $i \in \{1, 2, 3\}$; $\mathbf{C}$ is the conversion matrix; and, $\mathbf{I}_2$, $\mathbf{I}_3$, and $\mathbf{I}_4$ are defined as

$$\mathbf{I}_2 = \begin{bmatrix} I_{21}(\eta_1) & I_{22}(\eta_1) & I_{23}(\eta_1) & \eta_1 & 1 & 0 & 0 \\ I_{21}(\eta_3) & I_{22}(\eta_3) & I_{23}(\eta_3) & \eta_3 & 1 & 0 & 0 \end{bmatrix}. \tag{6.7}$$

$$\mathbf{I}_3 = \begin{bmatrix} I_{31}(\eta_1) & I_{32}(\eta_1) & I_{33}(\eta_1) & \frac{1}{2}\eta_1^2 & \eta_1 & 1 & 0 \\ I_{31}(\eta_3) & I_{32}(\eta_3) & I_{33}(\eta_3) & \frac{1}{2}\eta_3^2 & \eta_3 & 1 & 0 \end{bmatrix}. \tag{6.8}$$

$$\mathbf{I}_4 = \begin{bmatrix} I_{41}(\eta_1) & I_{42}(\eta_1) & I_{43}(\eta_1) & \frac{1}{6}\eta_1^3 & \frac{1}{2}\eta_1^2 & \eta_1 & 1 \\ I_{41}(\eta_2) & I_{42}(\eta_2) & I_{43}(\eta_2) & \frac{1}{6}\eta_2^3 & \frac{1}{2}\eta_2^2 & \eta_2 & 1 \\ I_{41}(\eta_3) & I_{42}(\eta_3) & I_{43}(\eta_3) & \frac{1}{6}\eta_3^3 & \frac{1}{2}\eta_3^2 & \eta_3 & 1 \end{bmatrix}. \tag{6.9}$$

Solving (6.6) yields

$$\begin{bmatrix} w_1 \\ w_2 \\ w_3 \\ c_1 \\ c_2 \\ c_3 \\ c_4 \end{bmatrix} = \mathbf{C}^{-1} \begin{bmatrix} u_1 \\ u_2 \\ u_3 \\ \frac{du_1}{d\eta} \\ \frac{du_3}{d\eta} \\ \frac{d^2u_1}{d\eta^2} \\ \frac{d^2u_3}{d\eta^2} \end{bmatrix}, \tag{6.10}$$

which maps the vector of nodal values of the function and its first- and second-order derivatives to the vector of RBF coefficients including the four integration constants. The first-order derivative at the middle point is computed by substituting (6.10) into (6.4) and taking $\eta = \eta_2$

$$\frac{du_2}{d\eta} = \underbrace{\mathbf{I}_{3m}\mathbf{C}^{-1}}_{\mathbf{D}_1} \begin{bmatrix} \mathbf{u} \\ \frac{du_1}{d\eta} \\ \frac{du_3}{d\eta} \\ \frac{d^2u_1}{d\eta^2} \\ \frac{d^2u_3}{d\eta^2} \end{bmatrix}, \tag{6.11}$$

or

$$\frac{du_2}{d\eta} = \mathbf{D}_1(1:3)\mathbf{u} + \mathbf{D}_1(4:5) \begin{bmatrix} \frac{du_1}{d\eta} \\ \frac{du_3}{d\eta} \end{bmatrix} + \mathbf{D}_1(6:7) \begin{bmatrix} \frac{d^2u_1}{d\eta^2} \\ \frac{d^2u_3}{d\eta^2} \end{bmatrix}, \tag{6.12}$$

where $\mathbf{D}_1$ is a row vector of length 7, the associated notation "$a : b$" is used to indicate the vector entries from the the column a to b; $\mathbf{u} = [u_1, u_2, u_3]^T$; and,

$$\mathbf{I}_{3m} = \begin{bmatrix} I_{31}(\eta_2) & I_{32}(\eta_2) & I_{33}(\eta_2) & \frac{1}{2}\eta_2^2 & \eta_2 & 1 & 0 \end{bmatrix}. \tag{6.13}$$

By taking derivative terms to the left side and nodal variable values to the right side, (6.12) reduces to

$$\begin{bmatrix} -\mathbf{D}_1(4) & 1 & -\mathbf{D}_1(5) \end{bmatrix} \mathbf{u}' + \begin{bmatrix} -\mathbf{D}_1(6) & 0 & -\mathbf{D}_1(7) \end{bmatrix} \mathbf{u}'' = \mathbf{D}_1(1:3)\mathbf{u}, \tag{6.14}$$

where $\mathbf{u}' = \begin{bmatrix} \frac{du_1}{d\eta}, \frac{du_2}{d\eta}, \frac{du_3}{d\eta} \end{bmatrix}^T$ and $\mathbf{u}'' = \begin{bmatrix} \frac{d^2u_1}{d\eta^2}, \frac{d^2u_2}{d\eta^2}, \frac{d^2u_3}{d\eta^2} \end{bmatrix}^T$.

At the boundary nodes, the first-order derivatives are approximated in special compact stencils. Consider the boundary node, e.g. η_1. Its associated stencil is $\{\eta_1, \eta_2, \eta_3, \eta_4\}$ as shown in Figure 6.2 and extra information is chosen as $\frac{du_2}{d\eta}$ and

Figure 6.2 Special compact 4-point 1D-IRBF stencil for boundary nodes.

$\frac{d^2u_2}{d\eta^2}$. The conversion system over this special stencil is presented as the following matrix-vector multiplication

$$\begin{bmatrix} u_1 \\ u_2 \\ u_3 \\ u_4 \\ \frac{du_2}{d\eta} \\ \frac{d^2u_2}{d\eta^2} \end{bmatrix} = \underbrace{\begin{bmatrix} \mathbf{I}_{4sp} \\ \mathbf{I}_{3sp} \\ \mathbf{I}_{2sp} \end{bmatrix}}_{\mathbf{C}_{sp}} \begin{bmatrix} w_1 \\ w_2 \\ w_3 \\ w_4 \\ c_1 \\ c_2 \\ c_3 \\ c_4 \end{bmatrix}, \tag{6.15}$$

where $\mathbf{C}_{sp}$ is the conversion matrix; and, $\mathbf{I}_{2sp}$, $\mathbf{I}_{3sp}$, and $\mathbf{I}_{4sp}$ are defined as

$$\mathbf{I}_{2sp} = \begin{bmatrix} I_{21}(\eta_2) & I_{22}(\eta_2) & I_{23}(\eta_2) & I_{24}(\eta_2) & \eta_2 & 1 & 0 & 0 \end{bmatrix}. \tag{6.16}$$

$$\mathbf{I}_{3sp} = \begin{bmatrix} I_{31}(\eta_2) & I_{32}(\eta_2) & I_{33}(\eta_2) & I_{34}(\eta_2) & \frac{1}{2}\eta_2^2 & \eta_2 & 1 & 0 \end{bmatrix}. \tag{6.17}$$

$$\mathbf{I}_{4sp} = \begin{bmatrix} I_{41}(\eta_1) & I_{42}(\eta_1) & I_{43}(\eta_1) & I_{44}(\eta_1) & \frac{1}{6}\eta_1^3 & \frac{1}{2}\eta_1^2 & \eta_1 & 1 \\ I_{41}(\eta_2) & I_{42}(\eta_2) & I_{43}(\eta_2) & I_{44}(\eta_2) & \frac{1}{6}\eta_2^3 & \frac{1}{2}\eta_2^2 & \eta_2 & 1 \\ I_{41}(\eta_3) & I_{42}(\eta_3) & I_{43}(\eta_3) & I_{44}(\eta_3) & \frac{1}{6}\eta_3^3 & \frac{1}{2}\eta_3^2 & \eta_3 & 1 \\ I_{41}(\eta_4) & I_{42}(\eta_4) & I_{43}(\eta_4) & I_{44}(\eta_4) & \frac{1}{6}\eta_4^3 & \frac{1}{2}\eta_4^2 & \eta_4 & 1 \end{bmatrix}. \tag{6.18}$$

Solving (6.15) yields

$$\begin{bmatrix} w_1 \\ w_2 \\ w_3 \\ w_4 \\ c_1 \\ c_2 \\ c_3 \\ c_4 \end{bmatrix} = \mathbf{C}_{sp}^{-1} \begin{bmatrix} u_1 \\ u_2 \\ u_3 \\ u_4 \\ \frac{du_2}{d\eta} \\ \frac{d^2 u_2}{d\eta^2} \end{bmatrix}. \tag{6.19}$$

The boundary value of the first-order derivative of u is thus obtained by substituting (6.19) into (6.4) and taking $\eta = \eta_1$

$$\frac{du_1}{d\eta} = \underbrace{\mathbf{I}_{3b}\mathbf{C}_{sp}^{-1}}_{\mathbf{D}_{1sp}} \begin{bmatrix} \mathbf{u} \\ \frac{du_2}{d\eta} \\ \frac{d^2 u_2}{d\eta^2} \end{bmatrix}, \tag{6.20}$$

or

$$\frac{du_1}{d\eta} = \mathbf{D}_{1sp}(1:4)\mathbf{u} + \mathbf{D}_{1sp}(5)\frac{du_2}{d\eta} + \mathbf{D}_{1sp}(6)\frac{d^2 u_2}{d\eta^2}, \tag{6.21}$$

where $\mathbf{u} = [u_1, u_2, u_3, u_4]^T$ and

$$\mathbf{I}_{3b} = \begin{bmatrix} I_{31}(\eta_1) & I_{32}(\eta_1) & I_{33}(\eta_1) & I_{34}(\eta_1) & \frac{1}{2}\eta_1^2 & \eta_1 & 1 & 0 \end{bmatrix}. \tag{6.22}$$

By taking derivative terms to the left side and nodal variable values to the right

side, (6.21) reduces to

$$\begin{bmatrix} 1 & -\mathbf{D}_{1sp}(5) & 0 & 0 \end{bmatrix} \mathbf{u}' + \begin{bmatrix} 0 & -\mathbf{D}_{1sp}(6) & 0 & 0 \end{bmatrix} \mathbf{u}'' = \mathbf{D}_{1sp}(1:4)\mathbf{u}, \quad (6.23)$$

where $\mathbf{u}' = \begin{bmatrix} \frac{du_1}{d\eta}, \frac{du_2}{d\eta}, \frac{du_3}{d\eta}, \frac{du_4}{d\eta} \end{bmatrix}^T$ and $\mathbf{u}'' = \begin{bmatrix} \frac{d^2u_1}{d\eta^2}, \frac{d^2u_2}{d\eta^2}, \frac{d^2u_3}{d\eta^2}, \frac{d^2u_4}{d\eta^2} \end{bmatrix}^T$.

6.2.2 Second-order derivative approximations

For the combined compact approximation of the second-order derivatives at interior nodes, we employ the same extra information used in the approximation of the first-order derivative, involving $\left\{ \frac{du_1}{d\eta}; \frac{du_3}{d\eta} \right\}$ and $\left\{ \frac{d^2u_1}{d\eta^2}; \frac{d^2u_3}{d\eta^2} \right\}$. Therefore, the second-order derivative at the middle point is computed by simply substituting (6.10) into (6.3) and taking $\eta = \eta_2$

$$\frac{d^2u_2}{d\eta^2} = \underbrace{\mathbf{I}_{2m}\mathbf{C}^{-1}}_{\mathbf{D}_2} \begin{bmatrix} \mathbf{u} \\ \frac{du_1}{d\eta} \\ \frac{du_3}{d\eta} \\ \frac{d^2u_1}{d\eta^2} \\ \frac{d^2u_3}{d\eta^2} \end{bmatrix}, \quad (6.24)$$

or

$$\frac{d^2u_2}{d\eta^2} = \mathbf{D}_2(1:3)\mathbf{u} + \mathbf{D}_2(4:5) \begin{bmatrix} \frac{du_1}{d\eta} \\ \frac{du_3}{d\eta} \end{bmatrix} + \mathbf{D}_2(6:7) \begin{bmatrix} \frac{d^2u_1}{d\eta^2} \\ \frac{d^2u_3}{d\eta^2} \end{bmatrix}, \quad (6.25)$$

where $\mathbf{u} = [u_1, u_2, u_3]^T$ and

$$\mathbf{I}_{2m} = \begin{bmatrix} I_{21}(\eta_2) & I_{22}(\eta_2) & I_{23}(\eta_2) & \eta_2 & 1 & 0 & 0 \end{bmatrix}. \quad (6.26)$$

By taking derivative terms to the left side and nodal variable values to the right side, (6.25) reduces to

$$\begin{bmatrix} -\mathbf{D}_2(4) & 0 & -\mathbf{D}_2(5) \end{bmatrix} \mathbf{u}' + \begin{bmatrix} -\mathbf{D}_2(6) & 1 & -\mathbf{D}_2(7) \end{bmatrix} \mathbf{u}'' = \mathbf{D}_2(1:3)\mathbf{u}, \quad (6.27)$$

where $\mathbf{u}' = \begin{bmatrix} \frac{du_1}{d\eta}, \frac{du_2}{d\eta}, \frac{du_3}{d\eta} \end{bmatrix}^T$ and $\mathbf{u}'' = \begin{bmatrix} \frac{d^2u_1}{d\eta^2}, \frac{d^2u_2}{d\eta^2}, \frac{d^2u_3}{d\eta^2} \end{bmatrix}^T$.

At the boundary nodes, i.e. $\eta = \eta_1$, we employ the same special stencil, i.e.

$\{\eta_1, \eta_2, \eta_3, \eta_4\}$, and extra information, i.e. $\frac{du_2}{d\eta}$ and $\frac{d^2 u_2}{d\eta^2}$, used in the approximation of the first-order derivatives. Therefore, approximate expression for the second-order derivative at η_1 in the physical space is obtained by simply substituting (6.19) into (6.3) and taking $\eta = \eta_1$

$$\frac{d^2 u_1}{d\eta^2} = \underbrace{\mathbf{I}_{2b}\mathbf{C}_{sp}^{-1}}_{\mathbf{D}_{2sp}} \begin{bmatrix} \mathbf{u} \\ \frac{du_2}{d\eta} \\ \frac{d^2 u_2}{d\eta^2} \end{bmatrix}, \qquad (6.28)$$

or

$$\frac{d^2 u_1}{d\eta^2} = \mathbf{D}_{2sp}(1:4)\mathbf{u} + \mathbf{D}_{2sp}(5)\frac{du_2}{d\eta} + \mathbf{D}_{2sp}(6)\frac{d^2 u_2}{d\eta^2}, \qquad (6.29)$$

where $\mathbf{u} = [u_1, u_2, u_3, u_4]^T$ and

$$\mathbf{I}_{2b} = \begin{bmatrix} I_{21}(\eta_1) & I_{22}(\eta_1) & I_{23}(\eta_1) & I_{24}(\eta_1) & \eta_1 & 1 & 0 & 0 \end{bmatrix}. \qquad (6.30)$$

By taking derivative terms to the left side and nodal variable values to the right side, (6.29) reduces to

$$\begin{bmatrix} 0 & -\mathbf{D}_{2sp}(5) & 0 & 0 \end{bmatrix}\mathbf{u}' + \begin{bmatrix} 1 & -\mathbf{D}_{2sp}(6) & 0 & 0 \end{bmatrix}\mathbf{u}'' = \mathbf{D}_{2sp}(1:4)\mathbf{u}, \quad (6.31)$$

where $\mathbf{u}' = \left[\frac{du_1}{d\eta}, \frac{du_2}{d\eta}, \frac{du_3}{d\eta}, \frac{du_4}{d\eta}\right]^T$ and $\mathbf{u}'' = \left[\frac{d^2 u_1}{d\eta^2}, \frac{d^2 u_2}{d\eta^2}, \frac{d^2 u_3}{d\eta^2}, \frac{d^2 u_4}{d\eta^2}\right]^T$.

6.2.3 Matrix assembly for first- and second-order derivative approximations

The IRBF system on a grid line for the first-order derivative is obtained by letting the interior node take values from 2 to $(n_\eta - 1)$ in (6.14); and, making use of (6.23) for the boundary nodes 1 and n_η. In a similar manner, the IRBF system on a grid line for the second-order derivative is obtained by letting the interior node take values from 2 to $(n_\eta - 1)$ in (6.27); and, making use of (6.31) for the boundary nodes 1 and n_η. The resultant matrix assembly is expressed as

$$\underbrace{\begin{bmatrix} \mathbf{A}_1 & \mathbf{B}_1 \\ \mathbf{A}_2 & \mathbf{B}_2 \end{bmatrix}}_{\text{Coefficient matrix}} \begin{bmatrix} \mathbf{u}'^n \\ \mathbf{u}''^n \end{bmatrix} = \begin{bmatrix} \mathbf{R}_1 \\ \mathbf{R}_2 \end{bmatrix} \mathbf{u}^n, \qquad (6.32)$$

where $\mathbf{A}_1$, $\mathbf{A}_2$, $\mathbf{B}_1$, $\mathbf{B}_2$, $\mathbf{R}_1$, and $\mathbf{R}_2$ are $n_\eta \times n_\eta$ matrices; $\mathbf{u}'^n = \left[u_1'^{\,n}, u_2'^{\,n}, ..., u_{n_\eta}'^{\,n} \right]^T$; $\mathbf{u}''^n = \left[u_1''^{\,n}, u_2''^{\,n}, ..., u_{n_\eta}''^{\,n} \right]^T$; and, $\mathbf{u}^n = \left[u_1^{\,n}, u_2^{\,n}, ..., u_{n_\eta}^{\,n} \right]^T$. The coefficient matrix is sparse with diagonal sub-matrices. Solving (6.32) yields

$$\mathbf{u}'^n = \mathbf{D}_\eta \mathbf{u}^n, \tag{6.33}$$

$$\mathbf{u}''^n = \mathbf{D}_{\eta\eta} \mathbf{u}^n, \tag{6.34}$$

where $\mathbf{D}_\eta$ and $\mathbf{D}_{\eta\eta}$ are $n_\eta \times n_\eta$ matrices.

6.2.4 Numerical implementation

For convenience in terms of numerical implementation, the formulation developed in Section 6.2.1 to 6.2.3 can be written in an intrinsic coordinate system as shown in Figure 6.3 (top).
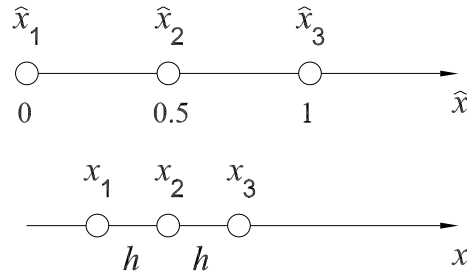
Figure 6.3 Intrinsic coordinate system (top), $\hat{x}$, and actual coordinate system (bottom), x, in which h is actual grid size.

The relationship between the derivatives in the intrinsic coordinate system and the corresponding ones in the actual coordinate system with a particular grid size, h, Figure 6.3 (bottom), is as follows.

$$\frac{du}{dx} = \frac{du}{d\hat{x}}\frac{d\hat{x}}{dx} = \frac{1}{2h}\frac{du}{d\hat{x}}. \tag{6.35}$$

$$\frac{d^2u}{dx^2} = \frac{1}{(2h)^2}\frac{d^2u}{d\hat{x}^2}. \tag{6.36}$$

Thus, the conversion matrix, $\mathbf{C}$, needs be computed and inverted once. Subsequently, as the grid size h changes, these matrices can be obtained by a simple

factor.

The present compact IRBF stencils can be extended to the three-dimensional case since their approximations in each direction are constructed independently. As shown above, the IRBF approximation expressions are first derived in 1D and they are utilised to form the approximations in 2D. This procedure is also applicable to the 3D case.

6.3 Review of fully coupled procedure for Navier-Stokes

The transient N-S equations for an incompressible viscous fluid in the primitive variables are expressed in the dimensionless non-conservative forms as follows.

$$
\frac{\partial u}{\partial t} + \underbrace{\left\{ u\frac{\partial u}{\partial x} + v\frac{\partial u}{\partial y} \right\}}_{N(u)} = -\frac{\partial p}{\partial x} + \frac{1}{Re} \underbrace{\left\{ \frac{\partial^2 u}{\partial x^2} + \frac{\partial^2 u}{\partial y^2} \right\}}_{L(u)}, \tag{6.37}
$$

$$
\frac{\partial v}{\partial t} + \underbrace{\left\{ u\frac{\partial v}{\partial x} + v\frac{\partial v}{\partial y} \right\}}_{N(v)} = -\frac{\partial p}{\partial y} + \frac{1}{Re} \underbrace{\left\{ \frac{\partial^2 v}{\partial x^2} + \frac{\partial^2 v}{\partial y^2} \right\}}_{L(v)}, \tag{6.38}
$$

$$
\frac{\partial u}{\partial x} + \frac{\partial v}{\partial y} = 0, \tag{6.39}
$$

where u, v and p are the velocity components in the x-, y-directions and static pressure, respectively; $Re = Ul/\nu$ is the Reynolds number, in which ν, l and U are the kinematic viscosity, characteristic length and characteristic speed of the flow, respectively. For simplicity, we employ notations $N(u)$ and $N(v)$ to represent the convective terms in the x- and y-directions, respectively; and, $L(u)$ and $L(v)$ to denote the diffusive terms in the x- and y-directions, respectively.

The temporal discretisations of (6.37)-(6.39), using the Adams-Bashforth scheme for the convective terms and Crank-Nicolson scheme for the diffusive terms, result in

$$
\frac{u^n - u^{n-1}}{\Delta t} + \left\{ \frac{3}{2}N(u^{n-1}) - \frac{1}{2}N(u^{n-2}) \right\} = -G_x(p^{n-\frac{1}{2}}) + \frac{1}{2Re}\left\{ L(u^n) + L(u^{n-1}) \right\}, \tag{6.40}
$$

$$\frac{v^n - v^{n-1}}{\Delta t} + \left\{\frac{3}{2}N(v^{n-1}) - \frac{1}{2}N(v^{n-2})\right\} = -G_y(p^{n-\frac{1}{2}}) + \frac{1}{2Re}\left\{L(v^n) + L(v^{n-1})\right\},$$
(6.41)

$$D_x(u^n) + D_y(v^n) = 0,$$
(6.42)

where n denotes the current time level; G_x and G_y are gradients in the x- and y-directions, respectively; and, D_x and D_y are gradients in the x- and y-directions, respectively.

Taking the unknown quantities in (6.40)-(6.42) to the left hand side and the known quantities to the right hand side, and then collocating them at the interior nodal points result in the matrix-vector form

$$\begin{bmatrix} \mathbf{K} & \mathbf{0} & \mathbf{G}_x \\ \mathbf{0} & \mathbf{K} & \mathbf{G}_y \\ \mathbf{D}_x & \mathbf{D}_y & \mathbf{0} \end{bmatrix} \begin{bmatrix} \mathbf{u}^n \\ \mathbf{v}^n \\ \mathbf{p}^{n-\frac{1}{2}} \end{bmatrix} = \begin{bmatrix} \mathbf{r}_x^n \\ \mathbf{r}_y^n \\ \mathbf{0} \end{bmatrix},$$
(6.43)

where

$$\mathbf{K} = \frac{1}{\Delta t}\left\{\mathbf{I} - \frac{\Delta t}{2Re}\mathbf{L}\right\},$$
(6.44)

$$\mathbf{r}_x^n = \frac{1}{\Delta t}\left\{\mathbf{I} + \frac{\Delta t}{2Re}\mathbf{L}\right\}\mathbf{u}^{n-1} - \left\{\frac{3}{2}\mathbf{N}(\mathbf{u}^{n-1}) - \frac{1}{2}\mathbf{N}(\mathbf{u}^{n-2})\right\},$$
(6.45)

$$\mathbf{r}_y^n = \frac{1}{\Delta t}\left\{\mathbf{I} + \frac{\Delta t}{2Re}\mathbf{L}\right\}\mathbf{v}^{n-1} - \left\{\frac{3}{2}\mathbf{N}(\mathbf{v}^{n-1}) - \frac{1}{2}\mathbf{N}(\mathbf{v}^{n-2})\right\},$$
(6.46)

$\mathbf{u}^n$ and $\mathbf{v}^n$ are vectors containing the nodal values of u^n and v^n at the boundary and interior nodes, respectively, while $\mathbf{p}^{n-\frac{1}{2}}$ is a vector containing the values of $p^{n-\frac{1}{2}}$ at the interior nodes only; $\mathbf{I}$ is the identity matrix; and, $\mathbf{N}$ and $\mathbf{L}$ are the matrix operators for the approximation of the convective and diffusive terms, respectively.

6.4   Summary of immersed boundary method

In this chapter, we provide a brief overview of the IBM and the reader is referred to (Lai and Peskin, 2000; Brittany and Jeffrey) for further details. For simplicity, we consider a model problem of a two-dimensional Newtonian, incompressible fluid and a one-dimensional, closed, elastic membrane. The fluid is defined on

a periodic box $\Omega = [0,1]^2$ using the Eulerian coordinates $\mathbf{x} = (x,y)$. The fluid contains an immersed neutrally-buoyant membrane $\Gamma \subset \Omega$, using the Lagrangian coordinates $s \in [0,1]$. It is noted that the lattice points are fixed but the boundary points are moving, and those two sets of points usually do not coincide with each other. We discretise Ω using a uniform $n_x \times n_y$ grid. Then, we set the mesh size of the immersed boundary to be $n_b = 3 \times n_x$, so that there are approximately 3 immersed boundary points per mesh width.

The IBM is mathematically defined by a set of differential equations involving a mixture of Eulerian and Lagrangian variables. The motion of the fluid-membrane is governed by the incompressible N-S equations

$$\rho \left(\frac{\partial \mathbf{u}}{\partial t} + \mathbf{u} \cdot \nabla \mathbf{u} \right) = -\nabla p + \mu \nabla^2 \mathbf{u} + \mathbf{f}, \tag{6.47}$$

$$\nabla \cdot \mathbf{u} = 0, \tag{6.48}$$

where $\mathbf{u} = \mathbf{u}(\mathbf{x},t) = (u(\mathbf{x},t), v(\mathbf{x},t))$ and $p = p(\mathbf{x},t)$ are the fluid velocity and pressure at location $\mathbf{x}$ and time t, respectively; ρ and μ are the constant fluid density and dynamic viscosity, respectively; and, $\mathbf{f} = \mathbf{f}(\mathbf{x},t) = (f_x(\mathbf{x},t), f_y(\mathbf{x},t))$ is the external body force through which the immersed boundary is coupled to the fluid

$$\mathbf{f}(\mathbf{x},t) = \int_\Gamma \mathbf{F}(s,t)\delta(\mathbf{x} - \mathbf{X}(s,t))ds, \tag{6.49}$$

where $\mathbf{X}(s,t) = (X(s,t), Y(s,t))$ is a parametric curve representing the immersed boundary configuration; the delta function $\delta(\mathbf{x}) = d_h(x)d_h(y)$ is a Cartesian product of one-dimensional Dirac delta functions, which is used to transmit the Lagrangian immersed boundary force from Γ onto adjacent Eulerian fluid nodes. The one-dimensional Dirac delta function is chosen as

$$d_h(r) = \begin{cases} \frac{1}{8h}\left(3 - 2|r|/h + \sqrt{1 + 4|r|/h - 4\left(|r|/h\right)^2}\right), & |r| \leq h, \\ \frac{1}{8h}\left(5 - 2|r|/h - \sqrt{-7 + 12|r|/h - 4\left(|r|/h\right)^2}\right), & h \leq |r| \leq 2h, \\ 0, & \text{otherwise}, \end{cases} \tag{6.50}$$

in which h is the grid size; and, $\mathbf{F}(s,t)$ is the elastic force density which is a

function of the current immersed boundary configuration

$$\mathbf{F}(s,t) = \boldsymbol{\mathcal{F}}\left(\mathbf{X}(s,t)\right) = \sigma \frac{\partial}{\partial s}\left(\frac{\partial \mathbf{X}(s,t)}{\partial s}\left(1 - \frac{\varepsilon}{|\frac{\partial \mathbf{X}(s,t)}{\partial s}|}\right)\right), \tag{6.51}$$

which corresponds to membrane points linked together by linear springs with spring constant σ. If we assume the equilibrium strain $\varepsilon = 0$, then (6.51) reduces to

$$\mathbf{F}(s,t) = \boldsymbol{\mathcal{F}}\left(\mathbf{X}(s,t)\right) = \sigma \frac{\partial^2 \mathbf{X}(s,t)}{\partial s^2}. \tag{6.52}$$

The final equation needed to close the system is an evolution equation for the immersed boundary, which comes from the simple requirement that Γ must travel at the local fluid velocity (the non-slip condition)

$$\frac{\partial \mathbf{X}(s,t)}{\partial t} = \mathbf{U}(\mathbf{X}(s,t),t) = \int_{\Omega} \mathbf{u}(\mathbf{x},t)\delta(\mathbf{x} - \mathbf{X}(s,t))d\mathbf{x}, \tag{6.53}$$

where $\mathbf{U}$ is the boundary speed. The delta function δ here imposes the Eulerian flow velocity on the adjacent Lagrangian boundary nodes.

IBM algorithm   Next, we describe the algorithm used in this work, which is a discrete version of Equations (6.47), (6.48), (6.49), (6.51), and (6.53). Assuming that the velocity field and the membrane position are already known at time t^{n-2}, $t^{n-3/2}$, and t^{n-1}. The procedure for updating these values to time t^n is as follows.

At half time step:

Step 1.   Update position of membrane

$$\frac{\mathbf{X}^{n-1/2}(s) - \mathbf{X}^{n-1}(s)}{\Delta t/2} = \sum_{\Omega} \mathbf{u}^{n-1}\delta(\mathbf{x} - \mathbf{X}^{n-1}(s))h^2. \tag{6.54}$$

Step 2.   Compute membrane force density

$$\mathbf{F}^{n-1/2}(s) = \boldsymbol{\mathcal{F}}\left(\mathbf{X}^{n-1/2}(s)\right). \tag{6.55}$$

Step 3.   Calculate force coming from membrane

$$\mathbf{f}^{n-1/2}(\mathbf{x}) = \sum_{\Gamma} \mathbf{F}^{n-1/2}(s)\delta(\mathbf{x} - \mathbf{X}^{n-1/2}(s))\Delta s. \tag{6.56}$$

Step 4.   Solve for fluid motion

$$\rho \left[\frac{\mathbf{u}^{n-1/2} - \mathbf{u}^{n-1}}{\Delta t/2} + \left\{ \frac{3}{2}\mathbf{N}\left(\mathbf{u}^{n-1}\right) - \frac{1}{2}\mathbf{N}\left(\mathbf{u}^{n-2}\right) \right\} \right]$$
$$= \mathbf{G}\tilde{p}^{n-1/2} + \frac{\mu}{2}\left\{ \mathbf{L}\left(\mathbf{u}^{n-1/2}\right) + \mathbf{L}\left(\mathbf{u}^{n-1}\right) \right\} + \mathbf{f}^{n-1/2}. \tag{6.57}$$

$$\mathbf{D} \cdot \mathbf{u}^{n-1/2} = 0. \tag{6.58}$$

Once $\mathbf{u}^{n-1/2}$ are known, we use them to take a full step from time t^{n-1} to t^n, as follows.

At full time step:

Step 5. Solve for fluid motion

$$\rho \left[\frac{\mathbf{u}^{n} - \mathbf{u}^{n-1}}{\Delta t} + \left\{ \frac{3}{2}\mathbf{N}\left(\mathbf{u}^{n-1/2}\right) - \frac{1}{2}\mathbf{N}\left(\mathbf{u}^{n-3/2}\right) \right\} \right]$$
$$= \mathbf{G}p^{n-1/2} + \frac{\mu}{2}\left\{ \mathbf{L}\left(\mathbf{u}^{n}\right) + \mathbf{L}\left(\mathbf{u}^{n-1}\right) \right\} + \mathbf{f}^{n-1/2}. \tag{6.59}$$

$$\mathbf{D} \cdot \mathbf{u}^{n} = 0. \tag{6.60}$$

Step 6. Update position of membrane

$$\frac{\mathbf{X}^{n}(s) - \mathbf{X}^{n-1}(s)}{\Delta t} = \sum_{\Omega} \mathbf{u}^{n-1/2}\delta(\mathbf{x} - \mathbf{X}^{n-1/2}(s))h^2. \tag{6.61}$$

6.5   Numerical examples

We chose the multiquadric (MQ) function as the basis function, i.e. (1.6), in the present calculations. The value of $\beta = 10$ is chosen for calculations in the present work. We evaluate the performance of the present scheme through the following measures

i. The root mean square error (RMS) is defined as

$$RMS = \sqrt{\frac{\sum_{i=1}^{N} \left(f_i - \overline{f}_i\right)^2}{N}}, \tag{6.62}$$

where f_i and $\overline{f}_i$ are the computed and exact values of the solution f at the i-th node, respectively; and, N is the number of nodes over the whole domain.

ii. The maximum absolute error (L_∞) is defined as

$$L_\infty = \max_{i=1,\dots,N} |f_i - \overline{f}_i|. \tag{6.63}$$

iii. The global convergence rate, α, with respect to the grid refinement is defined through

$$RMS(h) \approx \gamma h^\alpha = O(h^\alpha), \tag{6.64}$$

where h is the grid size; and, γ and α are exponential model's parameters.

iv. A flow is considered as reaching its steady state when

$$\sqrt{\frac{\sum_{i=1}^{N} \left(f_i^n - f_i^{n-1}\right)^2}{N}} < 10^{-9}. \tag{6.65}$$

v. Difference (%) between computed and analytical values is defined to be

$$\frac{f - \overline{f}}{\overline{f}} \times 100. \tag{6.66}$$

For comparison purposes, we also implement the standard FDM, the HOC scheme of Tian et al. (2011) and the coupled compact IRBF scheme of Tien et al. (2015c) for numerical calculations.

6.5.1   Heat equation

By selecting the following heat equation, the performance of the present combined compact IRBF scheme can be studied for the diffusive term only as

$$\frac{\partial u}{\partial t} = \frac{\partial^2 u}{\partial x^2}, \quad a \le x \le b, \quad t \ge 0, \tag{6.67}$$

$$u(x,0) = u_0(x), \quad a \le x \le b, \tag{6.68}$$

$$u(a,t) = u_{\Gamma_1}(t) \quad \text{and} \quad u(b,t) = u_{\Gamma_2}(t), \quad t \ge 0, \tag{6.69}$$

where u and t are the field variable and time, respectively; and, $u_0(x)$, $u_{\Gamma_1}(t)$, and $u_{\Gamma_2}(t)$ are prescribed functions. The temporal discretisation of (6.67) with the Crank-Nicolson scheme gives

$$\frac{u^n - u^{n-1}}{\Delta t} = \frac{1}{2}\left\{\frac{\partial^2 u^n}{\partial x^2} + \frac{\partial^2 u^{n-1}}{\partial x^2}\right\}, \tag{6.70}$$

where the superscript n denotes the current time step. (6.70) can be rewritten as

$$\left\{1 - \frac{\Delta t}{2}\frac{\partial^2}{\partial x^2}\right\}u^n = \left\{1 + \frac{\Delta t}{2}\frac{\partial^2}{\partial x^2}\right\}u^{n-1}. \tag{6.71}$$

Consider (6.67) on a segment $[0,\pi]$ with the initial and boundary conditions

$$u(x,0) = \sin(2x), \quad 0 < x < \pi. \tag{6.72}$$

$$u(0,t) = u(\pi,t) = 0, \quad t \ge 0. \tag{6.73}$$

The exact solution of this problem can be verified to be

$$\bar{u}(x,t) = \sin(2x)e^{-4t}. \tag{6.74}$$

The spatial accuracy of the present scheme is investigated using various uniform grids $\{11, 13, ..., 25\}$. We employ here a small time step, $\Delta t = 10^{-6}$, to minimise the effect of the approximation error in time. The solution is computed at $t = 0.0125$. Figure 6.4 shows that the present combined compact IRBF outperforms the standard central FDM, the HOC, and the coupled compact IRBF in terms

of both the solution accuracy and the convergence rate.
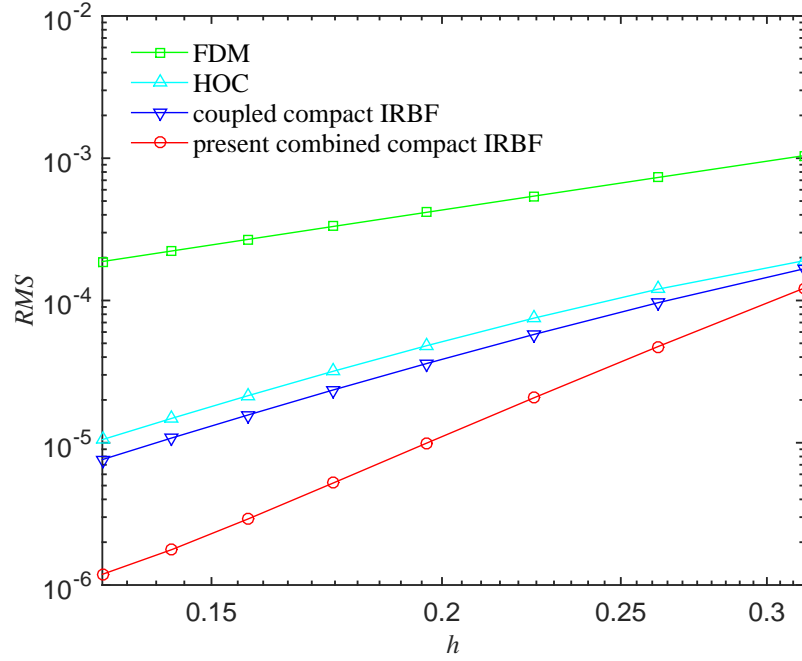
Figure 6.4 Heat equation, $\{11, 13, ..., 25\}$, $\Delta t = 10^{-6}$, $t = 0.0125$: The effect of the grid size h on the solution accuracy RMS. The solution converges as $O(h^{1.96})$ for the central FDM, $O(h^{3.34})$ for the HOC, $O(h^{3.54})$ for the coupled compact IRBF, and $O(h^{5.35})$ for the present combined compact IRBF.

6.5.2 Burgers equation

With Burgers equation, the performance of the present combined compact IRBF scheme can be investigated for both the convective and diffusive terms as

$$\frac{\partial u}{\partial t} + u\frac{\partial u}{\partial x} = \frac{1}{Re}\frac{\partial^2 u}{\partial x^2}, \quad a \leq x \leq b, \quad t \geq 0, \tag{6.75}$$

$$u(x, 0) = u_0(x), \quad a \leq x \leq b, \tag{6.76}$$

$$u(a, t) = u_{\Gamma_1}(t) \quad \text{and} \quad u(b, t) = u_{\Gamma_2}(t), \quad t \geq 0, \tag{6.77}$$

where $Re > 0$ is the Reynolds number; and, $u_0(x)$, $u_{\Gamma_1}(t)$, and $u_{\Gamma_2}(t)$ are prescribed functions. The temporal discretisations of (6.75) using the Adams-Bashforth scheme for the convective term and Crank-Nicolson scheme for the diffusive term,

result in

$$\frac{u^n - u^{n-1}}{\Delta t} + \left\{ \frac{3}{2} \left(u\frac{\partial u}{\partial x} \right)^{n-1} - \frac{1}{2} \left(u\frac{\partial u}{\partial x} \right)^{n-2} \right\} = \frac{1}{2Re} \left\{ \frac{\partial^2 u^n}{\partial x^2} + \frac{\partial^2 u^{n-1}}{\partial x^2} \right\},$$
(6.78)

or

$$\left\{ 1 - \frac{\Delta t}{2Re} \frac{\partial^2}{\partial x^2} \right\} u^n = \left\{ 1 + \frac{\Delta t}{2Re} \frac{\partial^2}{\partial x^2} \right\} u^{n-1} - \Delta t \left\{ \frac{3}{2} \left(u\frac{\partial u}{\partial x} \right)^{n-1} - \frac{1}{2} \left(u\frac{\partial u}{\partial x} \right)^{n-2} \right\}.$$
(6.79)

The problem is considered on a segment $0 \leq x \leq 1$ in the form (Hassanien et al., 2005)

$$\overline{u}(x,t) = \frac{\alpha_0 + \mu_0 + (\mu_0 - \alpha_0)\exp(\lambda)}{1 + \exp(\lambda)},$$
(6.80)

where $\lambda = \alpha_0 Re(x - \mu_0 t - \beta_0)$, $\alpha_0 = 0.4$, $\beta_0 = 0.125$, $\mu_0 = 0.6$, and $Re = 200$. The initial and boundary conditions can be derived from the analytic solution (6.80). The calculations are carried out on a set of uniform grids $\{61, 71, ..., 121\}$. The time step $\Delta t = 10^{-6}$ is chosen. The errors of the solution are calculated at the time $t = 0.0125$. Figure 6.5 shows that the present combined compact IRBF overwhelms the standard central FDM, HOC, coupled compact IRBF schemes in terms of both the solution accuracy and the convergence rate.

6.5.3 Convection-diffusion equations

To study the performance of the present combined compact IRBF approximation in simulating convection-diffusion problems, we employ the alternating direction implicit (ADI) procedure which was detailed in (Tien et al., 2015c). A two-dimensional unsteady convection-diffusion equation for a variable u is expressed as follows.

$$\frac{\partial u}{\partial t} + c_x \frac{\partial u}{\partial x} + c_y \frac{\partial u}{\partial y} = d_x \frac{\partial^2 u}{\partial x^2} + d_y \frac{\partial^2 u}{\partial y^2} + f_b, \quad (x, y, t) \in \Omega \times [0, T],$$
(6.81)

subject to the initial condition

$$u(x, y, 0) = u_0(x, y), \quad (x, y) \in \Omega,$$
(6.82)
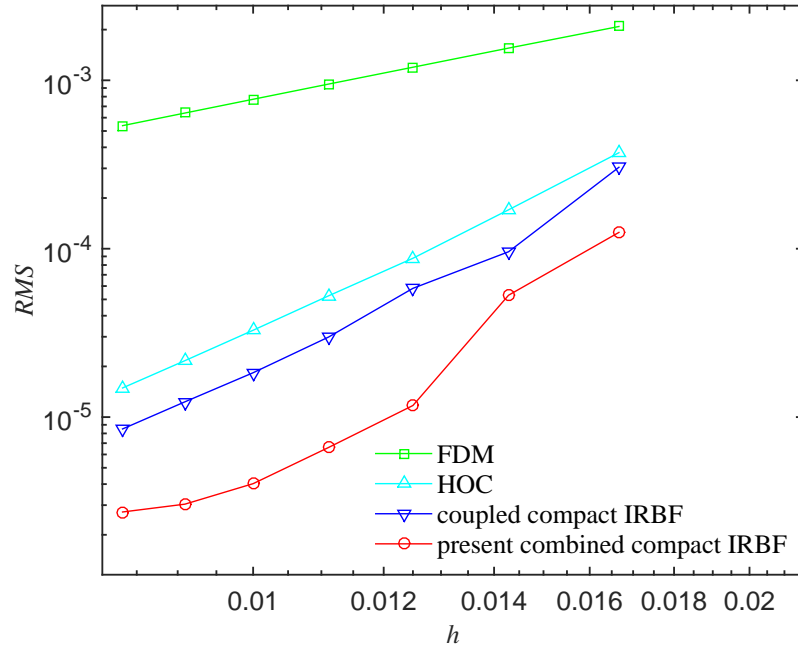
Figure 6.5 Burgers equation, $\{61, 71, ..., 121\}$, $Re = 200$, $\Delta t = 10^{-6}$, $t = 0.0125$: The effect of the grid size h on the solution accuracy RMS. The solution converges as $O(h^{1.96})$ for the central FDM, $O(h^{4.62})$ for the HOC, $O(h^{5.03})$ for the coupled compact IRBF, and $O(h^{5.81})$ for the present combined compact IRBF.

and the Dirichlet boundary condition

$$u(x, y, t) = u_\Gamma(x, y, t), \quad (x, y) \in \Gamma, \tag{6.83}$$

where Ω is a two-dimensional rectangular domain; Γ is the boundary of Ω; $[0, T]$ is the time interval; f_b is the driving function; u_0 and u_Γ are some given functions; c_x and c_y are the convective velocities; and, d_x and d_y are the diffusive coefficients.

In this work, we consider $f_b = 0$, in a square $\Omega = [0, 2]^2$ with the following analytic solution (Noye and Tan, 1989)

$$\overline{u}(x, y, t) = \frac{1}{4t + 1} exp\left[-\frac{(x - c_x t - 0.5)^2}{d_x(4t + 1)} - \frac{(y - c_y t - 0.5)^2}{d_y(4t + 1)}\right]. \tag{6.84}$$

From (6.84), one can derive the initial and boundary conditions. We consider two sets of parameters

Case I: $c_x = c_y = 0.8$, $d_x = d_y = 0.01$, $t = 0.0125$, $\Delta t = 1E - 6$.

Case II: $c_x = c_y = 80$, $d_x = d_y = 0.01$, $t = 0.0125$, $\Delta t = 1E - 6$.

The corresponding Peclet number is thus $Pe = 2$ for case I and $Pe = 200$ for case II. Figures 6.6 and 6.7 show analyses of the solution accuracy when the grid size is refined. It can be seen that the accuracy and convergence rate of the present combined compact IRBF scheme are much better than those of the central FDM, the HOC, and the coupled compact IRBF.
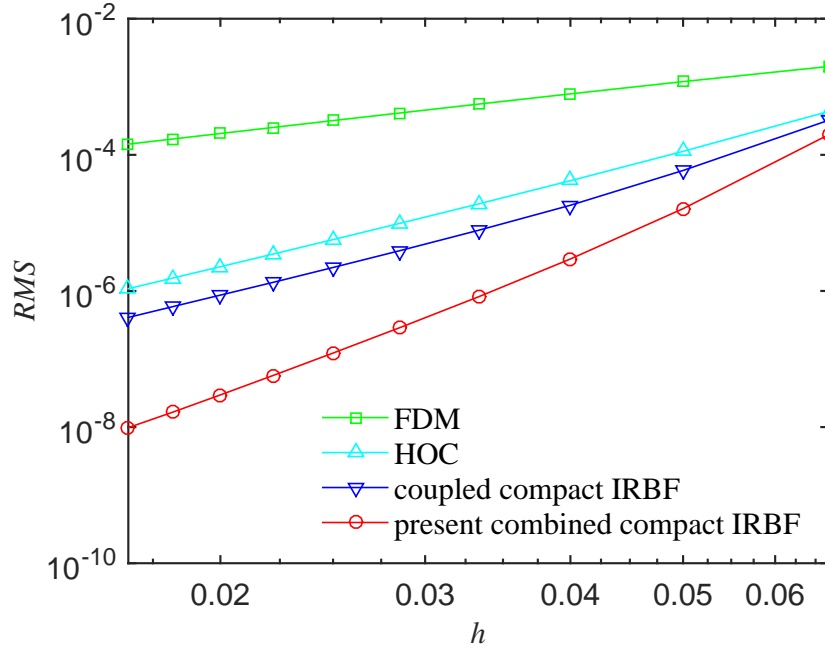
Figure 6.6 Unsteady convection-diffusion equation, $\{31 \times 31, 41 \times 41, ..., 121 \times 121\}$, case I: The effect of the grid size h on the solution accuracy RMS. The solution converges as $O(h^{1.90})$ for the central FDM, $O(h^{4.29})$ for the HOC, $O(h^{4.71})$ for the coupled compact IRBF, and $O(h^{7.02})$ for the present combined compact IRBF.

6.5.4 Taylor-Green vortex

To study the performance of the combination of the combined compact IRBF and the fully coupled approaches in simulating viscous flow, we consider a transient flow problem, namely Taylor-Green vortex Tian et al. (2011). This problem is governed by the N-S equations (6.40)-(6.42) and has the analytical solutions

$$\overline{u}(x_1, x_2, t) = -\cos(kx_1)\sin(kx_2)\exp(-2k^2t/Re), \qquad (6.85)$$

$$\overline{v}(x_1, x_2, t) = \sin(kx_1)\cos(kx_2)\exp(-2k^2t/Re), \qquad (6.86)$$

$$\overline{p}(x_1, x_2, t) = -1/4\{\cos(2kx_1) + \cos(2kx_2)\}\exp(-4k^2t/Re), \qquad (6.87)$$
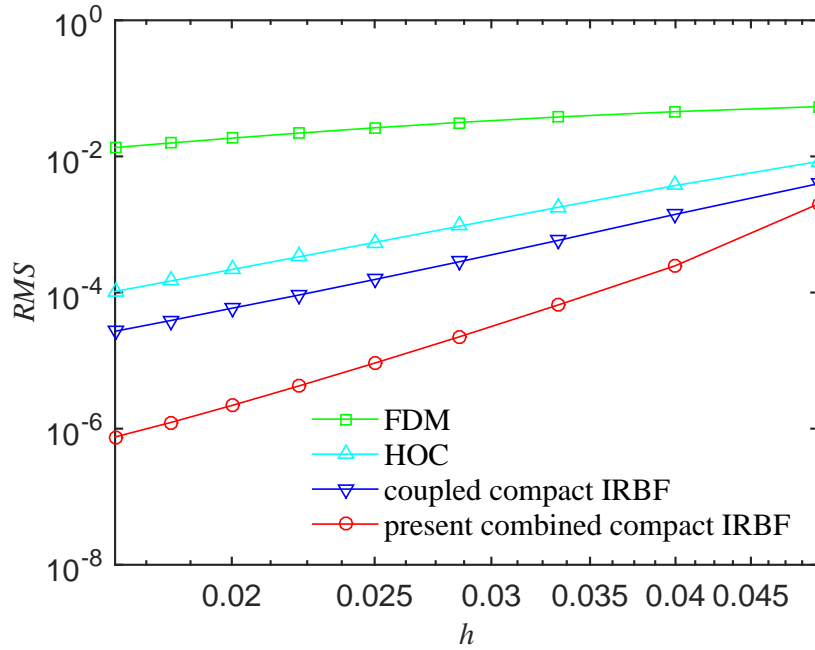
Figure 6.7 Unsteady convection-diffusion equation, $\{41 \times 41, 51 \times 51, ..., 121 \times 121\}$, case II: The effect of the grid size h on the solution accuracy RMS. The solution converges as $O(h^{1.28})$ for the central FDM, $O(h^{4.04})$ for the HOC, $O(h^{4.56})$ for the coupled compact IRBF, and $O(h^{7.04})$ for the present combined compact IRBF.

where $0 \leq x_1, x_2 \leq 2\pi$. Calculations are carried out for $k = 2$ on a set of uniform grids, $\{11 \times 11, 21 \times 21, ..., 51 \times 51\}$. A fixed time step $\Delta t = 0.002$ and $Re = 100$ are employed. Numerical solutions are computed at $t = 2$. The exact solutions, i.e. equations (6.85)-(6.87), provide the initial field at $t = 0$ and the time-dependent boundary conditions. Table 6.1 shows the accuracy comparison of the present scheme with the HOC scheme of Tian et al. (2011) and the compact IRBF scheme of Tien et al. (2015b). It is seen that the present scheme produces much better accuracy than the two other schemes; and, its convergence rates are much higher than those of the HOC and the compact IRBF, i.e. $O(h^{7.02})$ compared to $O(h^{5.35})$ of the compact IRBF and $O(h^{2.92})$ of the HOC for the u-velocity; and, $O(h^{8.51})$ compared to $O(h^{4.48})$ of the compact IRBF and $O(h^{3.28})$ of the HOC for the pressure.

6.5.5 Lid driven cavity

The classical lid driven cavity flow has been considered as a test problem for the evaluation of numerical methods and the validation of fluid flow solvers for the

Table 6.1 Taylor-Green vortex: RMS errors and convergence rates.

Grid	*u*-error	*v*-error	*p*-error
	present combined compact IRBF		
11×11	1.0652655E+00	1.0584558E+00	6.6053162E+00
21×21	6.4466038E-04	6.3416436E-04	5.5476571E-03
31×31	1.1927530E-04	1.1745523E-04	1.6486893E-04
41×41	1.8243332E-05	1.7849839E-05	1.8919708E-05
51×51	1.4261494E-05	1.2104415E-05	1.1300027E-05
Rate	$O(h^{7.02})$	$O(h^{7.10})$	$O(h^{8.51})$
	compact IRBF (Tien et al., 2015b)		
11×11	1.7797233E-01	1.7797723E-01	3.0668704E-01
21×21	4.6366355E-03	4.6366340E-03	8.5913505E-03
31×31	5.3168859E-04	5.3168061E-04	2.6550518E-03
41×41	1.0970214E-04	1.0968156E-04	3.4713723E-04
51×51	3.2428099E-05	3.2378594E-05	2.6244035E-04
Rate	$O(h^{5.35})$	$O(h^{5.35})$	$O(h^{4.48})$
	HOC (Tian et al., 2011)		
11×11	7.0070489E-02	7.0070489E-02	1.0764149E-01
21×21	9.0692193E-03	9.0692193E-03	1.0567607E-02
31×31	2.8851487E-03	2.8851487E-03	2.9103288E-03
41×41	1.2238736E-03	1.2238736E-03	1.1356134E-03
51×51	6.3063026E-04	6.3063026E-04	5.3933641E-04
Rate	$O(h^{2.92})$	$O(h^{2.92})$	$O(h^{3.28})$

past decades. Figure 6.8 shows the problem definition and boundary conditions. Uniform grids of $\{31 \times 31, 51 \times 51, 71 \times 71, 91 \times 91, 111 \times 111\}$ and $Re = 1000$
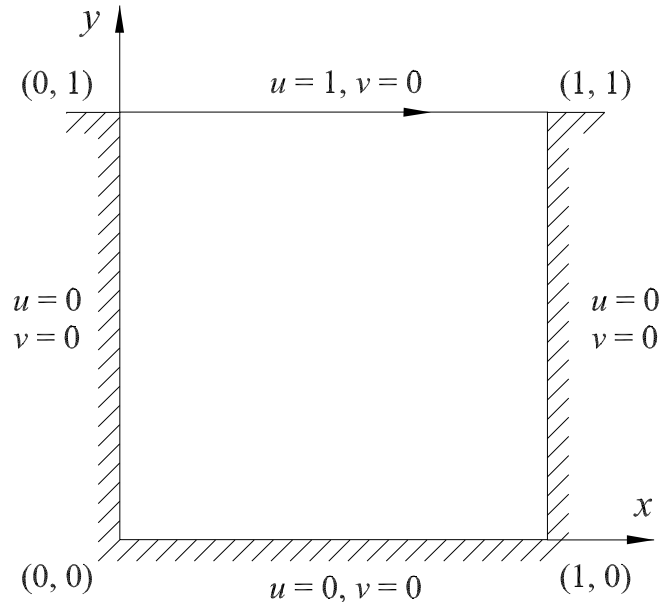
Figure 6.8 Lid driven cavity: problem configurations and boundary conditions.

are employed in the simulation. A fixed time step is chosen to be $\Delta t = 0.001$. Numerical results of the present scheme are compared with those of some others

(Botella and Peyret, 1998; Tien et al., 2015b; Ghia et al., 1982; Gresho et al., 1984; Bruneau and Jouron, 1990; Deng et al., 1994b; Sahin and Owens, 2003; Thai-Quang et al., 2012a). From the literature, FDM results using very dense grids presented by Ghia et al. (1982) and pseudo-spectral results presented by Botella and Peyret (1998) have been referred to as "Benchmark" results for comparison purposes.

Table 6.2 shows the present results for the extrema of the vertical and horizontal velocity profiles along the horizontal and vertical centrelines of the cavity. The "Errors" evaluated are relative to the "Benchmark" results of Botella and Peyret (1998). With relatively coarser grids, the results obtained by the present scheme are very comparable with others using denser grids.

Figure 6.9 displays velocity profiles along the vertical and horizontal centrelines for different grid sizes, where the grid convergence of the present scheme is clearly observed (i.e. the present solution approaches the benchmark solution with a fast rate as the grid density is increased). The present scheme effectively achieves the benchmark results with a grid of only 71×71 in comparison with the grid of 129×129 used to obtain the benchmark results in (Ghia et al., 1982). In addition, those velocity profiles, with the grid of 71×71, are displayed in Figure 6.10, where the present solutions match the benchmark ones very well.

To exhibit contour plots of the flow, Figures 6.11 and 6.12 show streamlines and iso-vorticity lines, respectively, which are derived from the velocity field. Figure 6.13 shows the pressure deviation contours of the present simulation. These plots are also in good agreement with those reported in the literature.

6.5.6 Elastic flat fibre (surface)

To investigate the accuracy of the combined compact IRBF in solving FSI problems, we consider a flat fibre problem which was studied in (Stockie, 1997; Gong et al., 2008). For comparison purposes, we set up the problem parameters and configurations to be the same as those used in (Stockie, 1997). Figure 6.14 depicts the problem configurations. The fluid domain is a unit square with periodic

Table 6.2 Lid driven cavity, $Re = 1000$: Extrema of the vertical and horizontal velocity profiles along the horizontal and vertical centrelines of the cavity, respectively. "Errors" are relative to the "Benchmark" data.

Method	Grid	u_{min}	Error (%)	y_{min}	v_{max}	Error (%)	x_{max}	v_{min}	Error (%)	x_{min}
present combined compact IRBF	31×31	-0.3666974	5.63	0.1979	0.3550856	5.80	0.1601	-0.4851327	7.96	0.8932
present combined compact IRBF	51×51	-0.3756440	3.33	0.1760	0.3640018	3.43	0.1603	-0.5110586	3.04	0.9035
present combined compact IRBF	71×71	-0.3837160	1.25	0.1725	0.3717639	1.37	0.1590	-0.5210042	1.15	0.9078
present combined compact IRBF	91×91	-0.3866230	0.50	0.1718	0.3747332	0.59	0.1584	-0.5248188	0.43	0.9088
present combined compact IRBF	111×111	-0.3877643	0.21	0.1716	0.3759610	0.26	0.1581	-0.5262950	0.15	0.9091
compact IRBF (u, v, p), Tien et al. (2015b)	51×51	-0.3611357	7.06	0.1819	0.3481667	7.63	0.1621	-0.4853383	7.92	0.9025
compact IRBF (u, v, p), Tien et al. (2015b)	71×71	-0.3807425	2.01	0.1741	0.3685353	2.23	0.1593	-0.5156774	2.16	0.9079
compact IRBF (u, v, p), Tien et al. (2015b)	91×91	-0.3857664	0.72	0.1725	0.3738367	0.82	0.1585	-0.5231499	0.75	0.9089
compact IRBF (u, v, p), Tien et al. (2015b)	111×111	-0.3873278	0.32	0.1720	0.3755235	0.38	0.1582	-0.5254043	0.32	0.9091
compact IRBF (u, v, p), Thai-Quang et al. (2012a)	71×71	-0.3755225	3.36	0.1753	0.3637009	3.51	0.1608	-0.5086961	3.49	0.9078
compact IRBF (u, v, p), Thai-Quang et al. (2012a)	91×91	-0.3815923	1.80	0.1735	0.3698053	1.89	0.1594	-0.5174658	1.82	0.9085
compact IRBF (u, v, p), Thai-Quang et al. (2012a)	111×111	-0.3840354	1.17	0.1728	0.3722634	1.24	0.1588	-0.5209683	1.16	0.9088
compact IRBF (u, v, p), Thai-Quang et al. (2012a)	129×129	-0.3848064	0.97	0.1724	0.3729119	1.07	0.1586	-0.5223350	0.90	0.9089
FVM (u, v, p), Deng et al. (1994b)	128×128	-0.38511	0.89	—	0.37369	0.86	—	-0.5228	0.81	—
FDM $(\psi - \omega)$, Ghia et al. (1982)	129×129	-0.38289	1.46	0.1719	0.37095	1.59	0.1563	-0.5155	2.20	0.9063
FEM (u, v, p), Gresho et al. (1984)	129×129	-0.375	3.49	0.160	0.362	3.96	0.160	-0.516	2.10	0.906
FDM (u, v, p), Bruneau and Jouron (1990)	256×256	-0.3764	3.13	0.1602	0.3665	2.77	0.1523	-0.5208	1.19	0.9102
FVM (u, v, p), Sahin and Owens (2003)	257×257	-0.388103	0.12	0.1727	0.376910	0.01	0.1573	-0.528447	0.26	0.9087
Benchmark, Botella and Peyret (1998)		-0.3885698		0.1717	0.3769447		0.1578	-0.5270771		0.9092

Figure 6.9 Lid driven cavity, $Re = 1000$: Profiles of the u-velocity along the vertical centreline (top) and the v-velocity along the horizontal centreline (bottom) as the grid density increases.
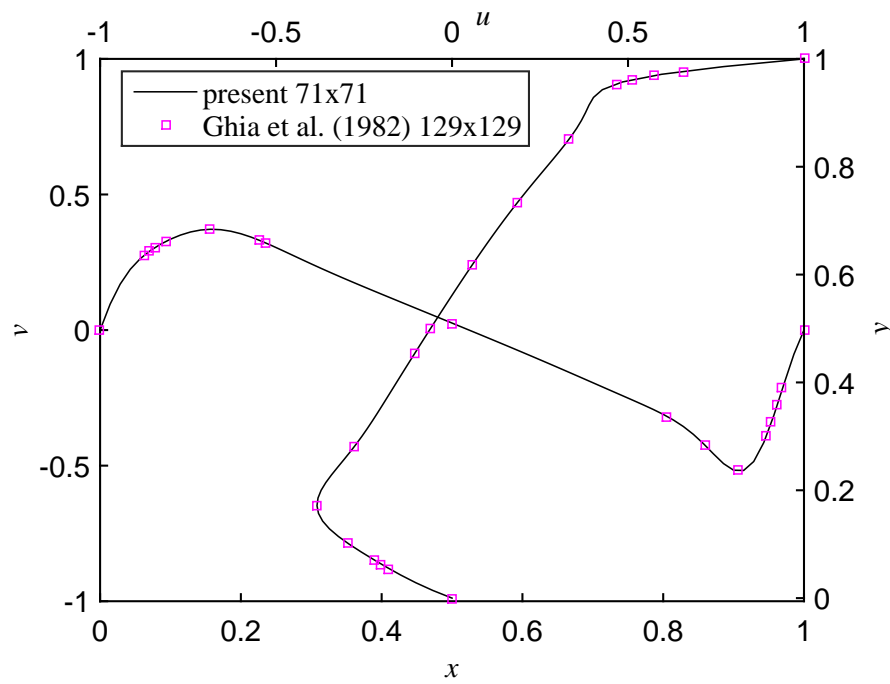
Figure 6.10 Lid driven cavity, $Re = 1000$: Profiles of the u-velocity along the vertical centreline and the v-velocity along the horizontal centreline.
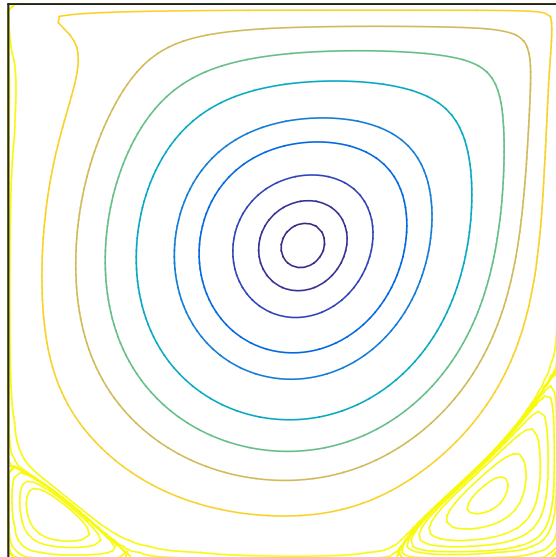
Figure 6.11 Lid driven cavity, $Re = 1000$, 91×91: Streamlines of the flow. The contour values used here are taken to be the same as those in (Ghia et al., 1982).
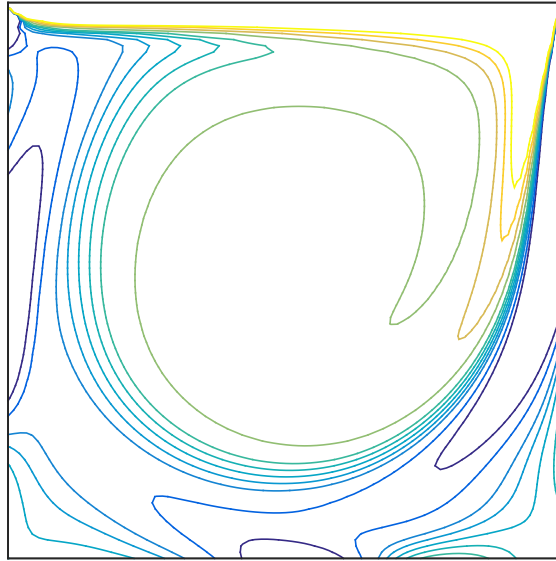
Figure 6.12 Lid driven cavity, $Re = 1000$, 91×91: Iso-vorticity lines of the flow. The contour values used here are taken to be the same as those in (Ghia et al., 1982).
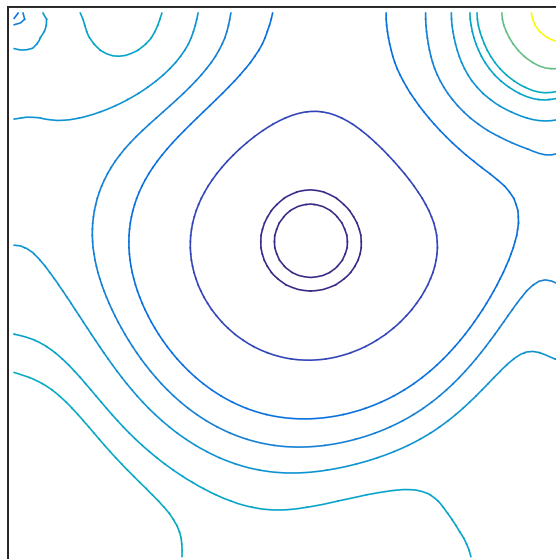
Figure 6.13 Lid driven cavity, $Re = 1000$, 91×91: Static pressure contours of the flow. The contour values used here are taken to be the same as those in (Botella and Peyret, 1998).
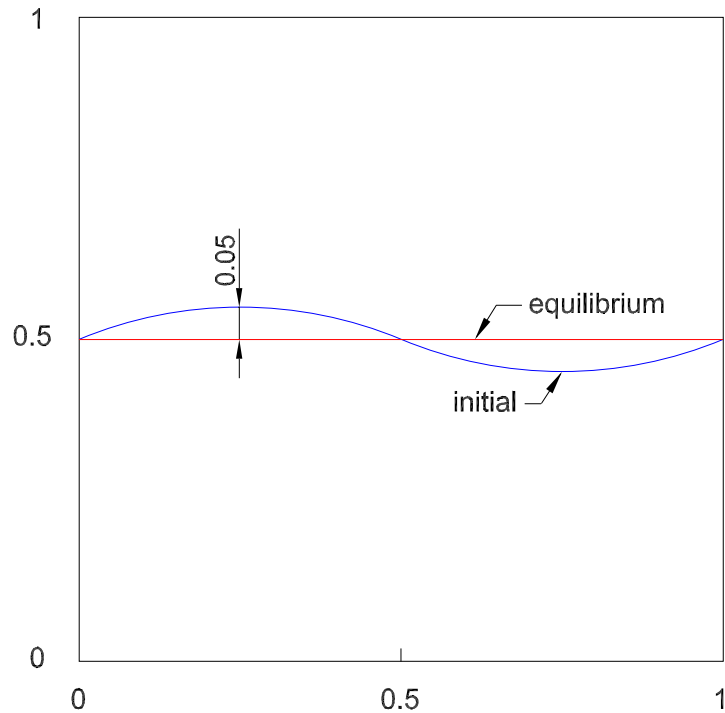
Figure 6.14 Fibre: The initial fibre position is a sinusoidal curve. The equilibrium state is a flat surface.

boundary conditions in the x- and y-directions. The viscosity and density constants are chosen as $\mu = 1$ and $\rho = 1$, respectively. The initial position is a sinusoidal curve described by

$$\mathbf{X}(s,0) = \left(s, \frac{1}{2} + A \, \sin(2\pi s) \right),$$ \hfill (6.88)

where the constant A is set to 0.05. The fluid is initially at rest

$$\mathbf{u}(\mathbf{x}, 0) = 0.$$ \hfill (6.89)

The purpose of this simulation is to test the decay rate of the maximum height of the fibre. Figure 6.15 plots a sample of the computed maximum height of the immersed fibre as a function of time, which oscillates with a decaying amplitude. There are two quantities that can easily be obtained from this information in order to make comparisons with the analytic results (Stockie, 1997):

   i. The decay rate, $Dr(\lambda)$, for the smallest wave number 2π mode which can be determined by measuring the rate at which the maximum fibre height
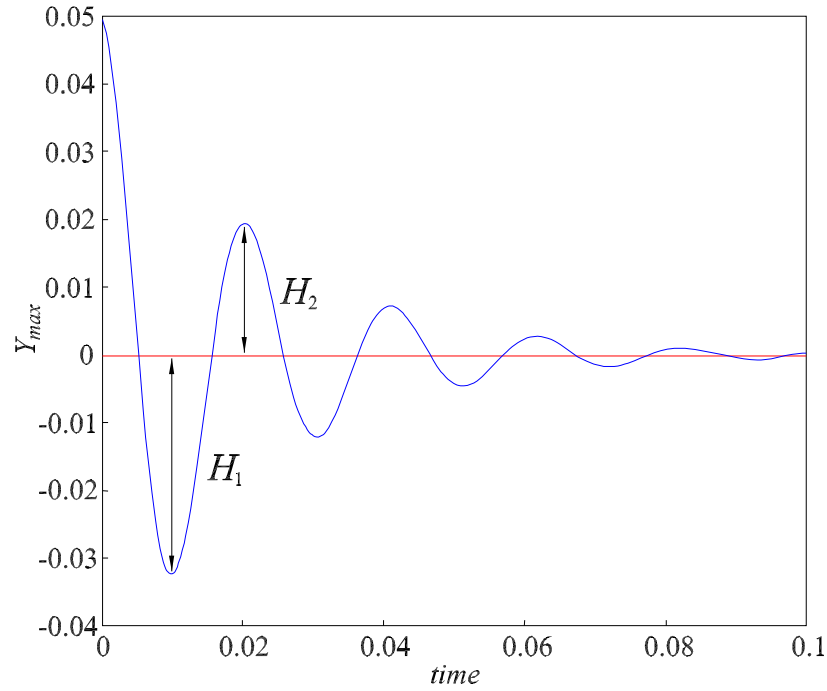
Figure 6.15 Fibre: A sample of computed maximum fibre height versus time.

decays to zero

$$Dr(\lambda) = \frac{1}{t_2 - t_1} ln \left(\frac{H_2}{H_1} \right). \tag{6.90}$$

ii. The frequency, $Fr(\lambda)$, which can be calculated from the period of the fibre oscillations

$$Fr(\lambda) = \frac{\pi}{t_2 - t_1}. \tag{6.91}$$

The results are summarised in Table 6.4 for various values of the fibre spring constant $\sigma = \{1, 20, 100, 1000, 10000, 100000\}$. With relatively coarse grids, the present decay rate shows very good agreement with the analytical results, and so does the frequency. The relative difference is within 6.3% for all values of σ. The decay rates produced by the present scheme are generally more accurate than those of the FDM reported in (Stockie, 1997).

To measure the effect of the spatial discretisation on the solution accuracy, we compute the problem on successively finer grids $\{20 \times 20, 40 \times 40, ..., 140 \times 140\}$. Table 6.4 lists a series of computations for $\sigma = 100000$ at which the largest discrepancy between the computed and analytical decay rates occurs. The differ-

Table 6.3 Fibre: Analytical and computed values of the decay rate $Dr(\lambda)$ and frequency $Fr(\lambda)$ for the solution mode with the smallest wave number 2π. The difference is computed relative to the analytical value.

				present combined compact IRBF					
Parameters				Smallest decay rate $Dr(\lambda)$			Frequency $Fr(\lambda)$		
σ	$n_x \times n_y$	n_b	Δt	Computed	Analytical	Difference (%)	Computed	Analytical	Difference (%)
1	40×40	120	1×10^{-2}	-1.6	-1.6	0.0	1	0	—
20	40×40	120	1×10^{-3}	-25	-26	3.8	28	28	0.0
100	40×40	120	5×10^{-4}	-33	-33	0.0	84	86	2.3
1000	40×40	120	2×10^{-4}	-49	-51	3.9	302	310	2.6
10000	60×60	180	2×10^{-5}	-80	-84	4.8	1033	1039	0.6
100000	100×100	300	2×10^{-6}	-133	-142	6.3	3364	3390	0.8

				FDM (Stockie, 1997)					
Parameters				Smallest decay rate $Dr(\lambda)$			Frequency $Fr(\lambda)$		
σ	$n_x \times n_y$	n_b	Δt	Computed	Analytical	Difference (%)	Computed	Analytical	Difference (%)
1	64×64	192	—	-1.5	-1.6	6.3	0	0	—
20	64×64	192	—	-24	-26	7.7	30	28	7.1
100	64×64	192	—	-32	-33	3.0	85	86	1.2
1000	64×64	192	—	-46	-51	9.8	310	310	0.0
10000	64×64	192	—	-75	-84	10.7	1030	1039	0.9
100000	64×64	192	—	-131	-142	7.7	3360	3390	0.9

Table 6.4 Fibre, $\sigma = 100000$, and $\Delta t = 2 \times 10^{-6}$: Grid convergence of λ to the analytical value $\lambda \approx -142 + 3390\, i$. The maximum norm errors are based on comparisons between the computed decay rate $Dr(\lambda)$ and the analytical decay rate of -142.

$n_x \times n_y$	$Dr(\lambda)$	$Fr(\lambda)$	Error	Local rate[(*)]
present combined compact IRBF				
20×20	-69	3027	73	—
40×40	-96	3279	46	0.7
60×60	-117	3342	25	1.5
80×80	-127	3349	15	1.7
100×100	-133	3364	9	2.3
120×120	-137	3378	5	3.6
140×140	-140	3378	2	4.6
FDM (Stockie, 1997)				
$n_x \times n_y$	$Dr(\lambda)$	$Fr(\lambda)$	Error	Local rate[(*)]
16×16	-73	2960	69	—
32×32	-100	3260	42	0.7
64×64	-131	3360	11	1.9
128×128	-147	3370	5	1.1
256×256	-140	3370	2	1.3

[(*)]Local rate=$-\log[error_{new}/error_{old}]/\log[n_{x\,new}/n_{x\,old}]$.

ence between the computed and analytical results decreases as the number of grid points increases; while, the local convergence rate does not settle down to any value, it does appear to be in between first- and fourth-order spatial accuracy. It can be seen that the present combined compact IRBF, with the much coarser grid of only 140×140, reaches the same level of accuracy of the FDM using the very dense grid of 256×256 as presented in (Stockie, 1997).

Using the parameters described in Table 6.4, we plot the evolution of Y_{max} towards the equilibrium condition as shown in Figure 6.16, which shows that the computed solutions converge to the correct steady state. In Figure 6.17, the profiles of the fibre and the velocity and pressure fields at various times are plotted. These plots are in good agreement with those reported in (Gong et al., 2008). In Figure 6.18, we plot the u- and v-velocity profiles along the horizontal and vertical centrelines, respectively, with the grid refinement for $\sigma = 100000$ at $t = 0.005$. It can be seen that the solution converges at the grid of 120×120.

6.5.7 Enclosed elastic tubular membrane

We now consider another FSI problem, a stretched pressurised tubular membrane immersed in a viscous fluid, which is a typical test for FSI solvers seen in the lit-
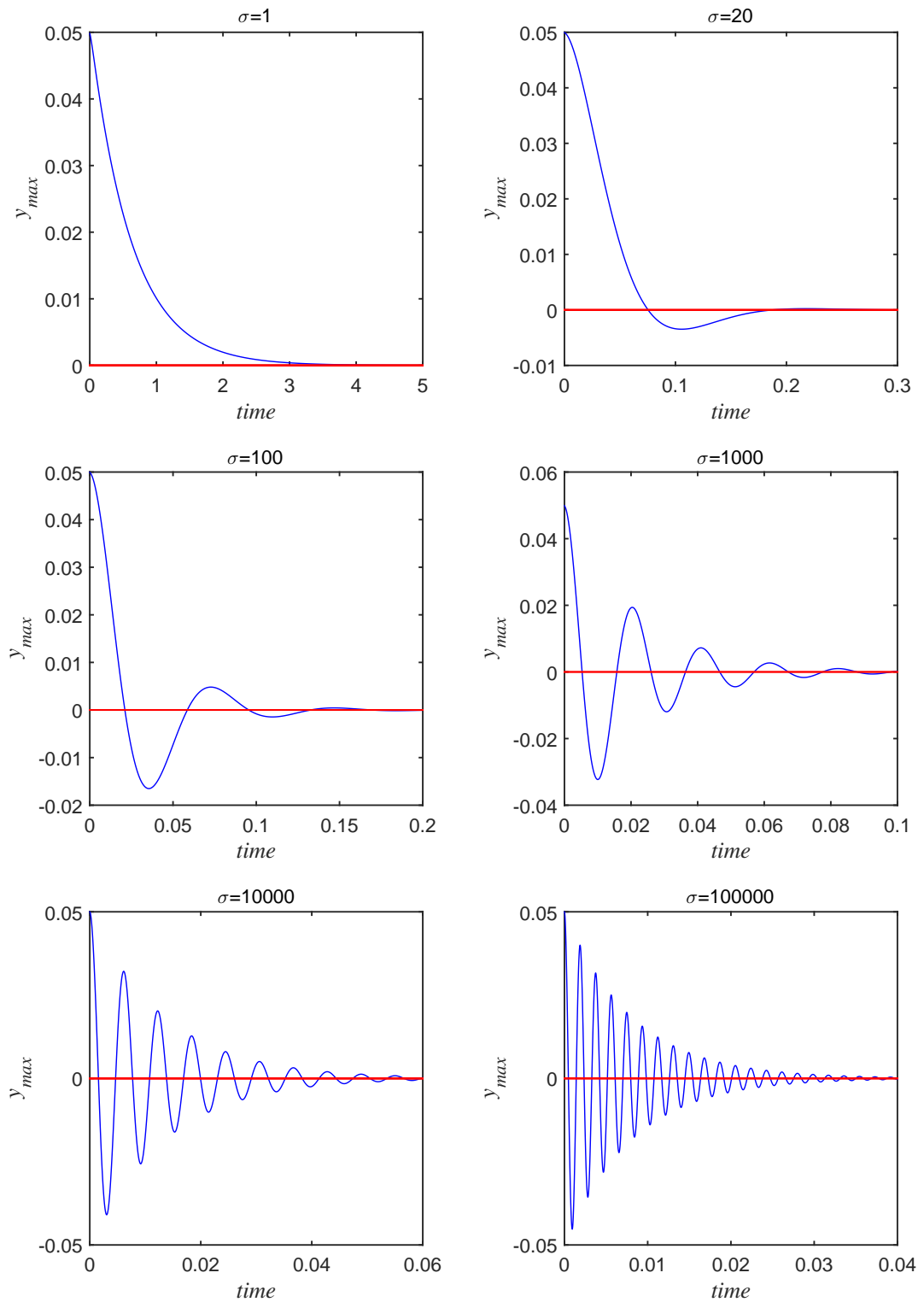
Figure 6.16 Fibre: Evolution of Y_{max} for different spring constants. The fibre oscillates as it converges to the equilibrium state.
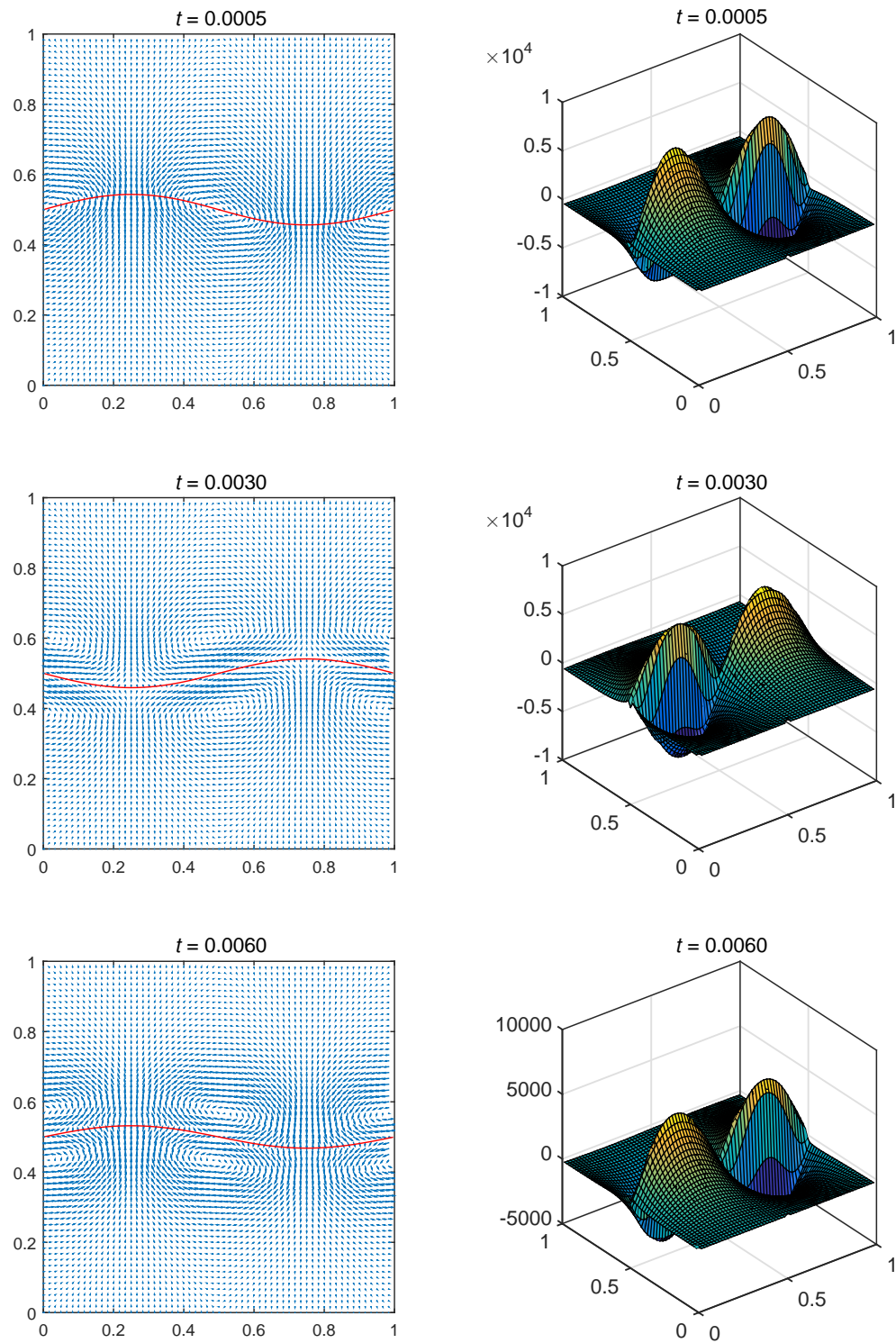
Figure 6.17 Fibre, $\sigma = 10000, n_x = n_y = 60, n_b = 180$, and $\Delta t = 2 \times 10^{-5}$: Velocity field and profiles of the fibre (left hand column); and, pressure field (right hand column) at three different times.
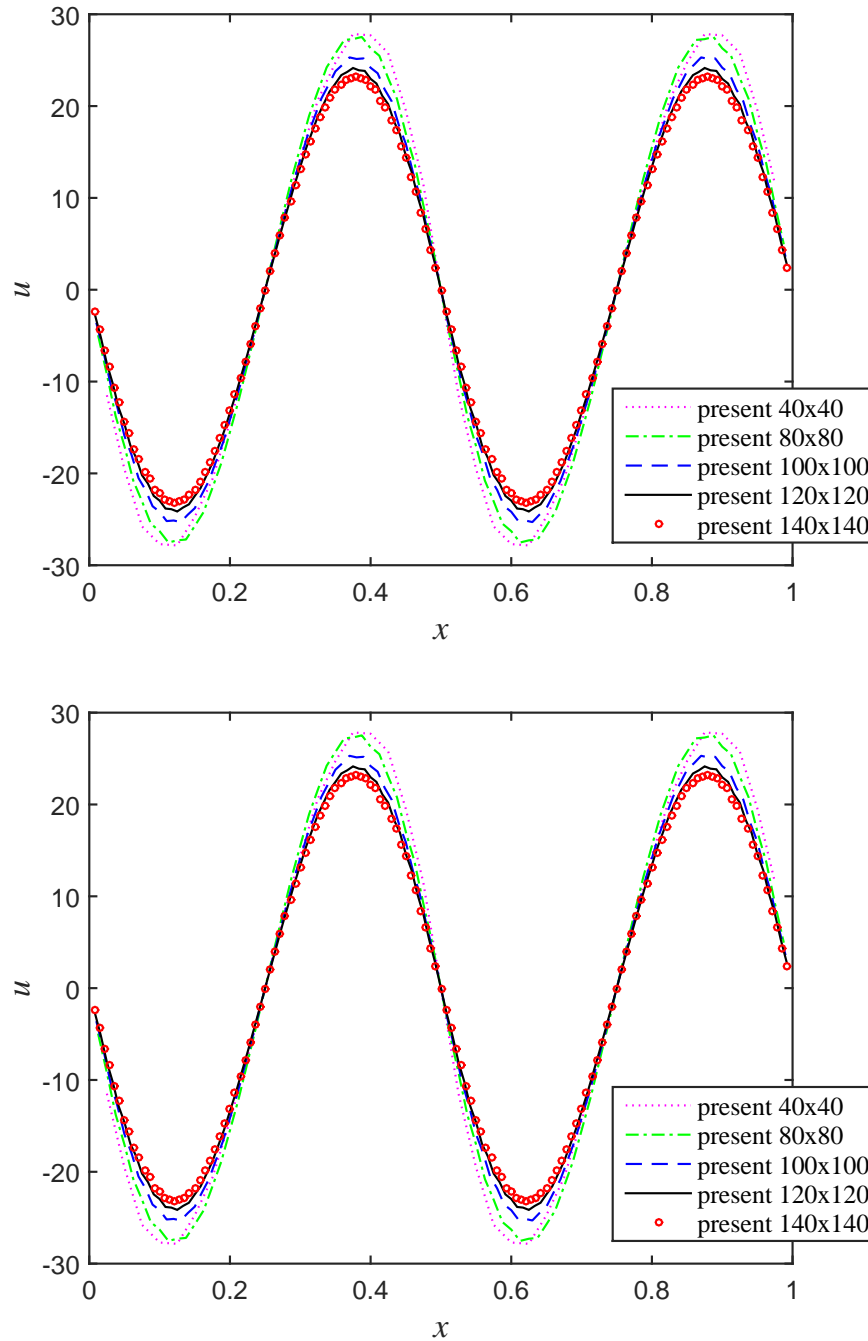
Figure 6.18 Fibre, $\sigma = 100000$, $\Delta t = 2 \times 10^{-6}$, and $t = 0.005$: Profiles of the u-velocity along the horizontal centreline (top) and the v-velocity along the vertical centreline (bottom). It is noted that the curves for the last two grids are almost indistinguishable, which shows that the solution converges at the grid of 120×120.

erature to date (Stockie, 1997; Leveque and Li, 1997; Stockie and Wetton, 1999; Lee and Leveque, 2003; Le, 2005; Newren, 2007; Cheng and Zhang, 2010; Jeffrey; Griffith, 2012). For comparison, we deliberately set parameters and conditions of the problem to be the same as those used in (Stockie, 1997; Stockie and Wetton, 1999; Jeffrey). We assume that the inflated and stretched shape of the membrane is defined as an ellipse with major and minor radii $a = 0.4$ and $b = 0.2$, respectively. Due to the restoring force of the elastic boundary and the incompressibility of the fluid inside the membrane, when the membrane is relaxed its shape should converge to an equilibrium circular steady state with radius $r = \sqrt{ab} \approx 0.2828$. The initial and equilibrium positions of the elastic membrane are depicted in Figure 6.19. We supplement the system of equations described in Section 6.4 with
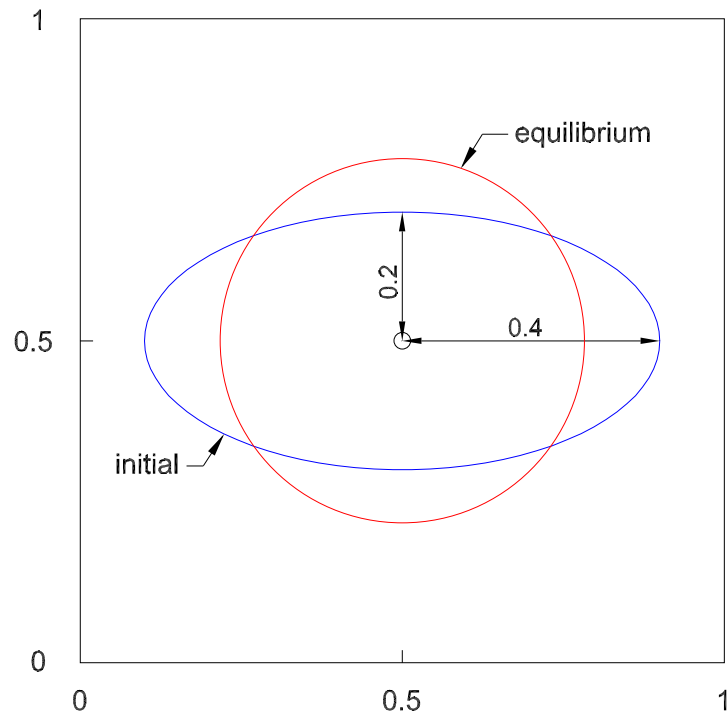
Figure 6.19 Tubular membrane: The initial membrane configuration is a tube with elliptical cross section with semi-axes 0.4 and 0.2. The equilibrium state is a circular tube with a radius approximately 0.2828.

the initial conditions

$$\mathbf{X}(s, 0) = \left(\frac{1}{2} + a\, \cos(2\pi s), \frac{1}{2} + b\, \sin(2\pi s) \right), \tag{6.92}$$

and

$$\mathbf{u}(\mathbf{x}, 0) = 0. \tag{6.93}$$

corresponding to a tubular membrane with elliptical cross section in a stationary fluid. For completeness, we set the following parameters

$$\mu = 1, \ \rho = 1, \ \text{and} \ \sigma = 10000. \tag{6.94}$$

Because the chosen spring constant σ is stiff, the dynamics occur over a small time scale ($t \le 0.04$) and require a small time step to resolve.

Figure 6.20 presents the velocity field and evolution of the system at the first time step and $t = 0.0010, 0.0015, 0.0020, 0.0035, 0.0045$ when the boundary speed and flow are relatively large. It is shown that the restoring movement of the membrane boundary induces an oscillating flow with vortices at the diagonal corners. The results are consistent with those of (Cheng and Zhang, 2010; Jeffrey; Griffith, 2012).

Because the membrane is closed and the fluid is incompressible, the volume inside the oscillating membrane remains constant. By plotting the maximum and minimum radii of the membrane in time, shown in Figure 6.21, we verify that the approximate solution converges to the correct steady state. The results are in good agreement with those presented in (Jeffrey).

The area (or "volume") of fluid inside the membrane can be effectively used as a measure of the numerical error. It is well known that immersed boundary computations can suffer from poor area conservation, which becomes significant during extreme flow condition such as that we are considering here with large σ. Where appropriate, the combined compact IRBF results are compared with those of the central FDM reported in (Stockie, 1997; Stockie and Wetton, 1999) in which the authors implemented the FDM with various time-stepping discretisation schemes, Runge-Kutta (RK), forward Euler/backward Euler (FE/BE), Crank-Nicholson (CN), and midpoint (MP). Table 6.5 presents an analysis to study the conservation of the enclosed area. It could be seen that the present numerical errors are very small, less than $1.1929E - 01\%$, and they are much smaller than those obtained by the FDM.

In Figure 6.22, we plot the u- and v-velocity profiles along the horizontal and ver-
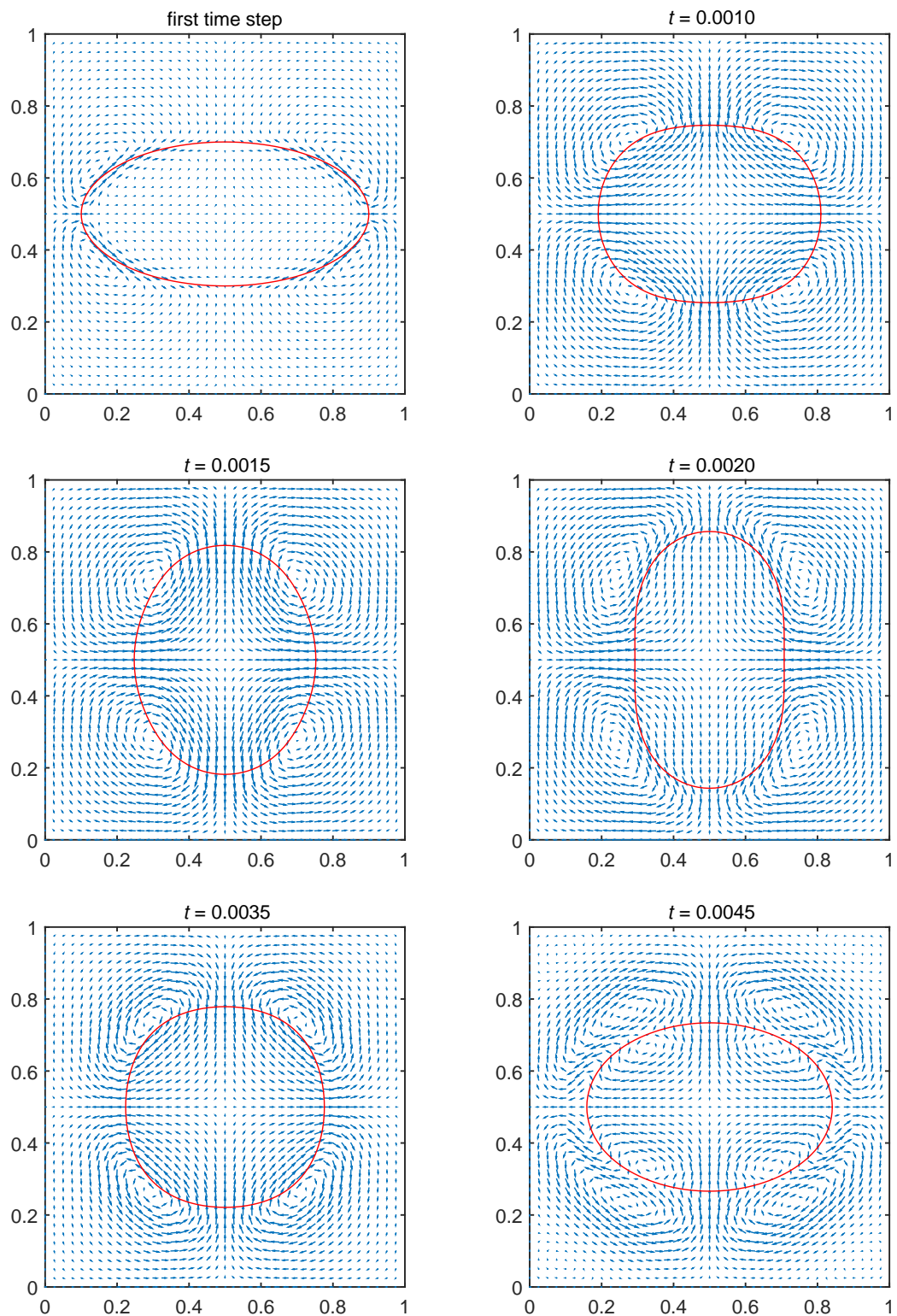
**Figure 6.20** Tubular membrane, $\sigma = 10000$, $n_x = n_y = 40$, $n_b = 120$, and $\Delta t = 5 \times 10^{-5}$: Velocity field and profiles of the membrane at different times.

Table 6.5 Tubular membrane, $\sigma = 10000$, and $t = 0.020$: The conservation of the area enclosed by the membrane. The "area loss" is computed relative to the exact area. The area A is numerically computed using the instantaneous membrane profile.

Method	Parameters			Computed area	Exact area	Area loss
	$n_x \times n_y$	n_b	Δt	A	A_e	%
present combined compact IRBF	20×20	60	1×10^{-4}	0.2506400	0.2513274	2.7350E-01
present combined compact IRBF	40×40	120	5×10^{-5}	0.2510325	0.2513274	1.1733E-01
present combined compact IRBF	60×60	180	2×10^{-5}	0.2511366	0.2513274	7.5940E-02
present combined compact IRBF	80×80	240	1×10^{-5}	0.2511915	0.2513274	5.4095E-02
present combined compact IRBF	100×100	300	1×10^{-5}	0.2512219	0.2513274	4.1998E-02
present combined compact IRBF	120×120	360	5×10^{-6}	0.2512397	0.2513274	3.4913E-02
present combined compact IRBF	140×140	420	2×10^{-6}	0.2512522	0.2513274	2.9923E-02
FDM-RK1 (Stockie and Wetton, 1999)	64×64	192	1.3×10^{-5} (max)	—	0.2513274	2.8
FDM-RK4 (Stockie and Wetton, 1999)	64×64	192	8.0×10^{-5} (max)	—	0.2513274	2.4
FDM-FE/BE (Stockie and Wetton, 1999)	64×64	192	7.0×10^{-5} (max)	—	0.2513274	4.4
FDM-CN (Stockie, 1997)	64×64	192	6.0×10^{-5} (max)	—	0.2513274	7.6
FDM-MP (Stockie and Wetton, 1999)	64×64	192	8.0×10^{-5} (max)	—	0.2513274	8.4
FDM-MP (Stockie and Wetton, 1999)	64×64	192	1.6×10^{-4} (max)	—	0.2513274	13.1
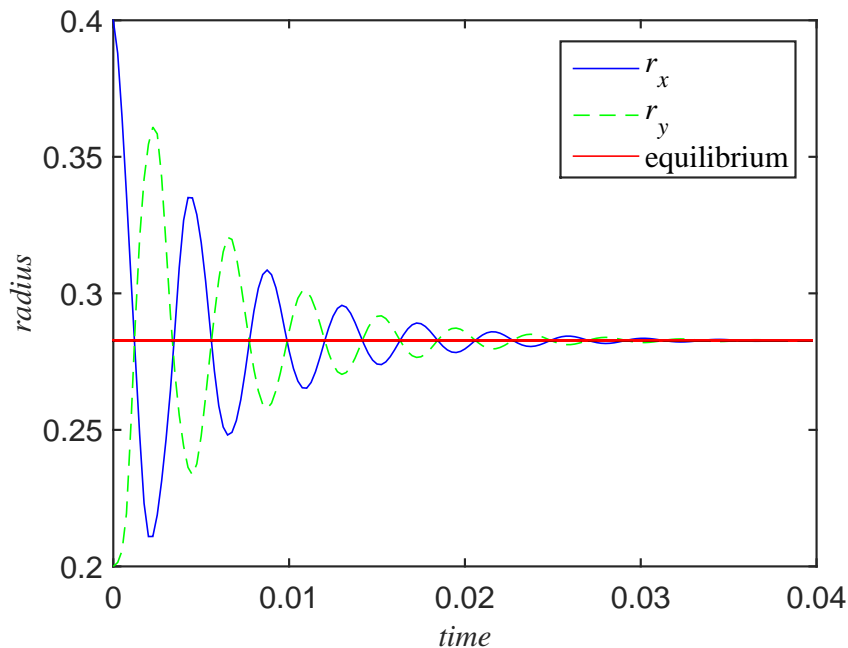
Figure 6.21 Tubular membrane, $\sigma = 10000$, $n_x = n_y = 80$, $n_b = 240$, and $\Delta t = 1 \times 10^{-5}$: Evolution of r_x and r_y. The cross section oscillates as it converges to the equilibrium state.

tical centrelines, respectively, at $t = 0.02$ for different grid sizes. The parameters used are described in Table 6.5. It is seen that the present solution approaches its convergent state with a fast rate as the grid size and the time step are decreased. The velocity profiles are consistent with those results reported in the literature.

Figure 6.23 presents the pressure distribution at different times. It can be seen that the contractive boundary force generates an abrupt pressure jump inside and outside the membrane. These plots are in good agreement with those reported in the literature.

In order to make further comparison with FDM results obtained in (Stockie, 1997; Stockie and Wetton, 1999), we particularly increase the spring constant to $\sigma = 100000$. Table 6.6 shows that present combined compact IRBF produces much smaller area losses than those obtained by the FDM.

To evaluate the effects of the regularised delta function, which is first/second-order accurate, on the overall accuracy, a grid convergence study for this problem is carried out. Results concerning velocities on three different grids, $[40 \times 40, 80 \times 80, 160 \times 160]$, are compared with those on a fine grid of $[320 \times 320]$. Parameters
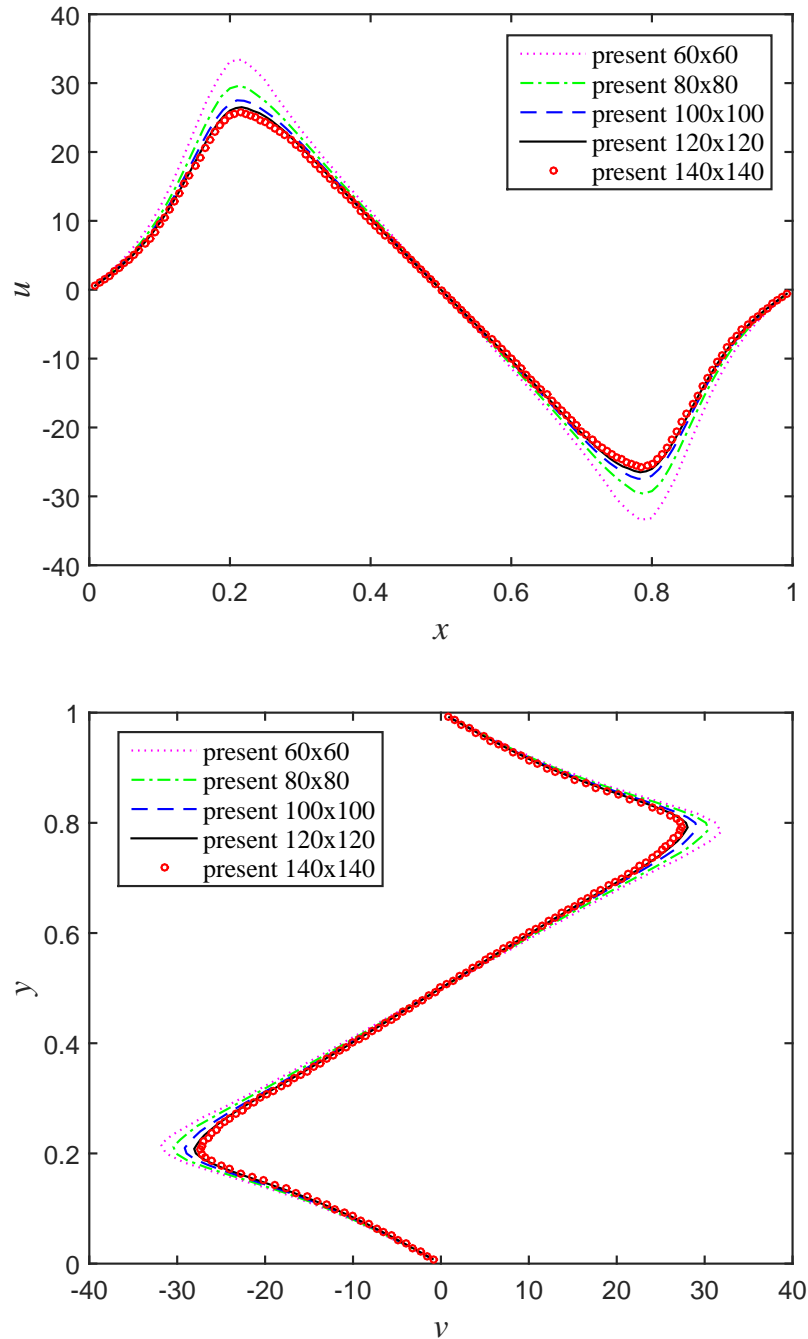
Figure 6.22 Tubular membrane, $\sigma = 10000$, and $t = 0.01$: Profiles of the u-velocity along the horizontal centreline (top) and the v-velocity along the vertical centreline (bottom). It is noted that the curves for the last two grids are almost indistinguishable, which shows that the solution converges at the grid of 120×120.
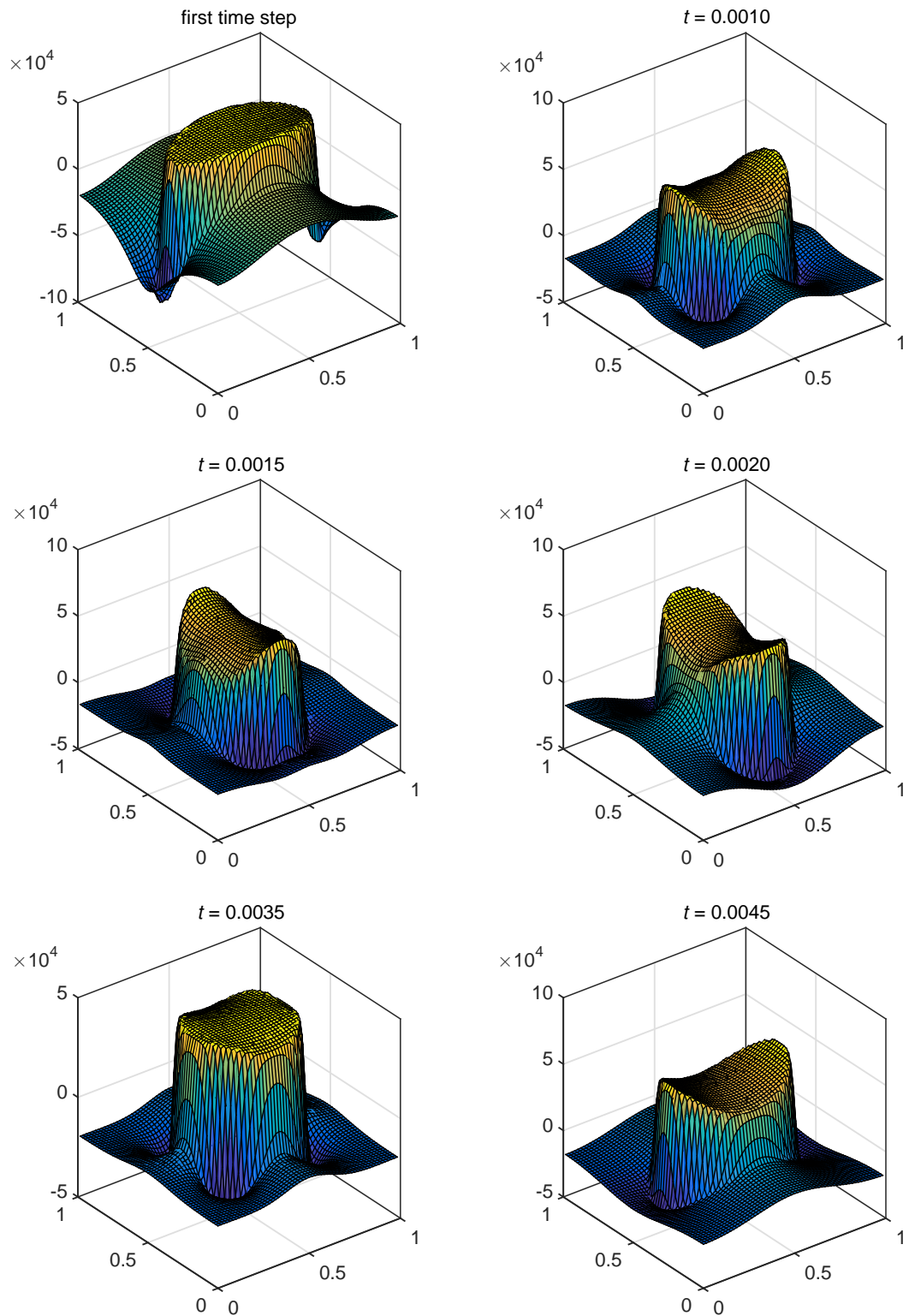
Figure 6.23 Tubular membrane, $\sigma = 10000$, $n_x = n_y = 60$, $n_b = 180$, $\Delta t = 2 \times 10^{-5}$: Pressure distribution at different times.

Table 6.6 Tubular membrane, $\sigma = 100000$, and $t = 0.005$: The conservation of the area enclosed by the membrane. The "area loss" is computed relative to the exact area. The area A is numerically computed using the instantaneous membrane profile.

Method	Parameters			Computed area A	Exact area A_e	Area loss %
	$n_x \times n_y$	n_b	Δt			
present combined compact IRBF	20×20	60	5×10^{-5}	0.2506783	0.2513274	2.5829E-01
present combined compact IRBF	40×40	120	2×10^{-5}	0.2510409	0.2513274	1.1399E-01
present combined compact IRBF	60×60	180	1×10^{-5}	0.2510734	0.2513274	1.0108E-01
present combined compact IRBF	80×80	240	5×10^{-6}	0.2511273	0.2513274	7.9614E-02
present combined compact IRBF	120×120	360	2×10^{-6}	0.2511778	0.2513274	5.9510E-02
present combined compact IRBF	140×140	420	1×10^{-6}	0.2511921	0.2513274	5.3846E-02
FDM-RK1 (Stockie and Wetton, 1999)	64×64	192	1.0×10^{-6} (max)	—	0.2513274	4.4
FDM-RK4 (Stockie and Wetton, 1999)	64×64	192	3.0×10^{-5} (max)	—	0.2513274	4.4
FDM-FE/BE (Stockie and Wetton, 1999)	64×64	192	1.0×10^{-5} (max)	—	0.2513274	5.2
FDM-CN (Stockie, 1997)	64×64	192	1.0×10^{-5} (max)	—	0.2513274	6.8
FDM-MP (Stockie and Wetton, 1999)	64×64	192	2.5×10^{-5} (max)	—	0.2513274	6.8
FDM-MP (Stockie and Wetton, 1999)	64×64	192	5.0×10^{-5} (max)	—	0.2513274	11.9

used are $\sigma = 10000$, $\Delta t = 2 \times 10^{-6}$, an ellipse with major axis of 0.75 and minor axis of 0.5 and a flow domain of $[0, 2] \times [0, 2]$. The present results and those obtained by the second-order accurate FDM (Leveque and Li, 1997) are shown in Table 6.7. It can be seen that similar rates are obtained; however, for all grids employed, the present solution is about one and two orders of magnitude better than the FDM one. It is expected that improved rates of the proposed method can be acquired if a fixed smooth function (Lai and Peskin, 2000) is employed to replace the delta function.

Table 6.7 Tubular membrane, $t = 0$: Velocity errors versus the grid refinement.

$n_x \times n_y$	$L_\infty(u)$	Local rate[*]	$L_\infty(v)$	Local rate[*]
	present combined compact IRBF			
40×40	5.7921E-04	—	1.0641E-04	—
80×80	1.9506E-04	1.57	4.2909E-05	1.31
160×160	6.0462E-05	1.69	1.3957E-05	1.62
	FDM (Leveque and Li, 1997)			
$n_x \times n_y$	$L_\infty(u)$	Local rate[*]	$L_\infty(v)$	Local rate[*]
40×40	1.0170E-02	—	5.0540E-03	—
80×80	4.4694E-03	1.19	2.0512E-03	1.30
160×160	1.5012E-03	1.57	7.4032E-04	1.47

[*]Local rate=-log$[error_{new}/error_{old}]$/log$[n_{xnew}/n_{xold}]$.

6.6 Concluding Remarks

In this chapter, we have successfully implemented the combined compact IRBF scheme along with the fully coupled velocity-pressure approach for simulating fluid flow problems and with the IBM for FSI simulations in the Cartesian-grid point-collocation structure. Computational results of fluid flow problems indicate that the present scheme is superior to the standard FDM, HOC, compact IRBF, and coupled compact IRBF schemes in terms of the solution accuracy and the convergence rate with the grid refinement. It is shown that the present scheme achieves up to eight-order accuracy when simulating the fluid flow problems. Numerical results of immersed fibre/membrane FSI problems show that the present scheme generally produces more accurate solutions and better convergence rates in comparison with the FDM approaches reported in the literature. Very good results are obtained using relatively coarse grids. In this work, the essence of the combined compact IRBF, fully coupled velocity-pressure and IBM methods are outlined; and, the high-order solution accuracy, better decay rate, and better volume conservation features are demonstrated. It is believed that the combined compact IRBF approximation primarily contributes to achieving significant improvements in the solution accuracy.

Chapter 7

Conclusions

This chapter concludes the thesis by a summary of research contributions and some suggestions for future development.

Research contributions:

The strongest contribution of this thesis is in line with developing the high-order combined compact integrated RBF (IRBF) method for solving fluid flow and fluid structure interaction problems, which is presented in Chapters 5 and 6. The new scheme significantly improves the stability, efficiency, and solution accuracy on the previous compact and coupled compact IRBF schemes. The better performance of the combined compact IRBF algorithm is achieved owing to

- using fourth-order derivatives as the starting points in the process of integration.

- simultaneously combining extra information, which are nodal values of first- and second-order derivatives through the four integration constants, into the approximation of the derivatives.

Additionally, contributions of each chapter are summarised as follows.

Chapter 2 implements the high-order compact IRBF scheme, where first- and second-order derivative values of the field variables are included in the approximation of the first- and second-order derivatives respectively, in combination

with the direct fully coupled velocity-pressure approach in the Cartesian-grid point-collocation structure. Like finite difference methods (FDMs), the present approximation technique involves 3 nodes in each direction, which results in a sparse system matrix. Numerical examples of several fluid flow problems indicate that the results of the present scheme are superior to those of the standard finite difference method (FDM) scheme and some high-order compact (HOC) finite difference schemes in terms of the solution accuracy and the convergence rate with the grid refinement.

Chapter 3 proposes the coupled compact IRBF scheme. The proposed scheme is constructed over a three-point stencil, where nodal first- and second-order derivative values of the field variable are both incorporated into the approximation by means of their identity equations. This leads to a significant improvement in accuracy and stability in comparison with the normal compact IRBF. Numerical examples of problems governed by partial differential equation (PDE) indicate that the results obtained by the present scheme are superior to those of the compact IRBF, HOC and some other high-order schemes.

Chapter 4 introduces highly accurate serial and parallel algorithms using the coupled compact IRBF for heat and fluid flow problems. The advantage of the proposed serial and parallel schemes is that they are able to produce almost the same level of accuracy as that of the single domain scheme. In computational examples, the results produced by serial and parallel algorithms are very compatible with other methods such as the finite element method (FEM) and the FDM. The serial and parallel algorithms offer a divide-and-conquer solution for large-scale PDE problems. Therefore, the proposed algorithms may be used as alternatives to the single domain scheme to solve large-scale problems which the single domain scheme is generally struggling to solve due to its ill-conditioned or fully populated companion matrix.

Chapter 5 proposes an idea of using high-order IRBFs to construct combined compact approximations, which allows a more straight-forward incorporation of nodal values of first- and second-order derivatives, and yields better solution accuracy over compact approximations. Then, a preconditioning technique to

circumvent the ill-condition problems of compact IRBF approaches associated with large values of the shape parameter β is proposed. The stability of the new algorithm is shown to be significantly improved. In elliptic equation tests, we have found that in the large value range of β the proposed combined compact IRBF-Precond solutions are many orders of magnitude better than those of the differential RBF, compact IRBF, and compact IRBF-Precond schemes. In the simulation of several fluid flow problems, the new method performs significantly better than the standard central FDM, the HOC and the compact IRBF.

Chapter 6 successfully implements the combined compact IRBF scheme along with the fully coupled velocity-pressure approach for simulating fluid flow problems and with the IBM for FSI simulations in the Cartesian-grid point-collocation structure. Computational results of fluid flow problems indicate that the present scheme is superior to the standard FDM, HOC, compact IRBF, and coupled compact IRBF schemes in terms of the solution accuracy and the convergence rate with the grid refinement. It is shown that the present scheme achieves up to eight-order accuracy when simulating the fluid flow problems. Numerical results of immersed fibre/membrane FSI problems show that the present scheme generally produces more accurate solutions and better convergence rates in comparison with the FDM approaches reported in the literature.

Although the focus of the thesis is on fluid dynamics, the proposed algorithms can also be applied to solve other engineering and scientific problems, which are governed by the PDEs, in various fields such as health and environment, construction and transportation, and etc. These algorithms are expected to produce very high solution accuracy at an improved computational efficiency. As a result, physical problems can be more accurately handled with less computational time.

Suggested works:

While several high-order approximation schemes are proposed with certain successes, culminating in the introduction of the combined compact scheme and its application into FSI problems, these schemes are still in their natural formulation and only primary problems and applications are considered. For example, Cartesian grids (rectangular and non-rectangular) are considered in the thesis

due to their great effectiveness. However, it is expected that there may be some difficulties in handling complex geometries and large deformation when using the Cartesian grid, for example obtaining sufficient fluid grids between very thin boundary gaps. The arbitrary node distribution may be helpful in such extreme cases and the research of IRBF methods based on scattered nodes is therefore worth investigating. To improve the work, the following ideas are suggested for possible further developments:

- Further improve the stability and efficiency of the proposed schemes through splitting techniques.

- Extend the proposed schemes to more complicated and practical fluid flow and FSI problems in two and three dimensions. We believe that the two dimensional IRBF methods can be extended to three dimensional problems in a straight-forward manner.

- Numerical results show that the shape parameter largely influences the solution accuracy. Therefore, developing strategies to optimise the RBF-width is very necessary.

- Develop element-free solvers based on the high-order approximation schemes for a wider range of problems, where large fluid/structure deformation is required, such as flow analysis in rotary vane vacuum pumps, turbulent and multi-phase flows, crack propagation, fatigue development, and etc.

- Develop more efficient parallel solvers based on the high-level accurate schemes for large-scale problems, requiring much more degrees of freedom, for example flooding, ocean pollution, global warming, and etc.

- Investigate the performance of the high-order IRBF schemes on scattered/arbitrary nodes and apply them to solve problems where extremely thin layers of fluid occur, for example the case in which two structures contact each other and they compress the fluid between them.

Appendix A

Analytic forms of RBFs and IRBFs

The following are analytic forms of RBFs and IRBFs, which are reproduced from (Mai-Duy, 2005).

A.1   Direct approach

$$D_{1i} = \frac{x - c_i}{[(x - c_i)^2 + a_i^2]^{1/2}} \tag{A.1}$$

$$D_{2i} = \frac{a_i^2}{[(x - c_i)^2 + a_i^2]^{3/2}} \tag{A.2}$$

$$D_{3i} = \frac{-3a_i^2(x - c_i)}{[(x - c_i)^2 + a_i^2]^{5/2}} \tag{A.3}$$

$$D_{4i} = \frac{3a_i^2 \left[4(x - c_i)^2 - a_i^2\right]}{[(x - c_i)^2 + a_i^2]^{7/2}} \tag{A.4}$$

A.2   Indirect approach

$$I_{1i} = \frac{(x - c_i)}{2}A + \frac{a_i{}^2}{2}B \tag{A.5}$$

$$I_{2i} = \left(\frac{-a_i{}^2}{3} + \frac{(x - c_i)^2}{6}\right)A + \frac{a_i{}^2(x - c_i)}{2}B \tag{A.6}$$

$$I_{3i} = \left(\frac{-13a_i{}^2(x - c_i)}{48} + \frac{(x - c_i)^3}{24}\right)A + \left(\frac{-a_i{}^4}{16} + \frac{a_i{}^2(x - c_i)^2}{4}\right)B \tag{A.7}$$

$$I_{4i} = \left(\frac{a_i{}^4}{45} - \frac{83a_i{}^2(x-c_i)^2}{720} + \frac{(x-c_i)^4}{120} \right) A + \left(\frac{-3a_i{}^4(x-c_i)}{48} + \frac{4a_i{}^2(x-c_i)^3}{48} \right) B$$

(A.8)

where $A = \sqrt{(x-c_i)^2 + a_i{}^2}$ and $B = ln\left((x-c_i) + \sqrt{(x-c_i)^2 + a_i{}^2} \right)$.

References

Abdallah, S. (1987). Numerical solutions for the incompressible Navier-Stokes equations in primitive variables using a non-staggered grid, Part II. *Journal of Computational Physics*, 70(1):193–202.

Acharya, S., Baliga, B. R., Karki, K., Murthy, J. Y., Prakash, C., and Vanka, S. P. (2007). Pressure-based finite-volume methods in computational fluid dynamics. *Journal of Heat Transfer*, 129(4):407–424.

Adam, Y. (1977). Highly accurate compact implicit methods and boundary conditions. *Journal of Computational Physics*, 24(1):10–22.

Ammara, I. and Masson, C. (2004). Development of a fully coupled control-volume finite element method for the incompressible Navier-Stokes equations. *International Journal for Numerical Methods in Fluids*, 44(6):621–644.

An-Vo, D. A., Mai-Duy, N., and Tran-Cong, T. (2010). Simulation of Newtonian-fluid flows with C 2-continuous two-node integrated-RBF elements. *Structural Longevity*, 4(1):39–45.

Atluri, S. N. and Zhu, T. (1998). A new meshless local Petrov-Galerkin (MLPG) approach in computational mechanics. *Computational Mechanics*, 22(2):117–127.

Avi, R. M., Craig, S., and Ronald, F. (2011). A symmetric positive definite formulation for monolithic fluid structure interaction. *Journal of Computational Physics*, 230(4):1547–1566.

Babuska, I. and Melenk, J. M. (1997). The partition of unity method. *International Journal for Numerical Methods in Engineering*, 40(4):727–758.

Badia, S., Nobile, F., and Vergara, C. (2008). Fluid-structure partitioned procedures based on Robin transmission conditions. *Journal of Computational Physics*, 227(14):7027–7051.

Belytschko, T., Krongauz, Y., Orga, D., Fleming, M., and Krysl, P. (1996). Meshless methods: an overview and recent developments. *Computer Methods in Applied Mechanics & Engineering*, 139(1):3–47.

Belytschko, T., Lu, Y. Y., and Gu, L. (1994). Element-free Galerkin methods. *International Journal for Numerical Methods in Engineering*, 37(2):229–256.

Biringen, S. and Chow, C. Y. (2011). *An introduction to computational fluid mechanics by example.* John Wiley & Sons, Hoboken, New Jersey, US.

Bonet, J. and Kulasegaram, S. (2000). Correction and stabilization of smooth particle hydrodynamics methods with applications in metal forming simulations. *International Journal for Numerical Methods in Engineering*, 47(6):1189–1214.

Botella, O. and Peyret, R. (1998). Benchmark spectral results on the lid-driven cavity flow. *Computers & Fluids*, 27(4):421–433.

Braaten, M. E. and Patankar, S. V. (1990). Fully coupled solution of the equations for incompressible recirculating flows using a penalty-function finite-difference formulation. *Computational Mechanics*, 6(2):143–155.

Braaten, M. E. and Shyy, W. (1986). Comparison of iterative and direct solution methods for viscous flow calculations in body-fitted coordinates. *International Journal for Numerical Methods in Fluids*, 6(6):325–349.

Brittany, D. F. and Jeffrey, W. MatIB user guide. *Massachusetts Institute of Technology - Cambridge*, (accessed the URL on 3rd November 2015).

Bruneau, C. H. and Jouron, C. (1990). An efficient scheme for solving steady incompressible Navier-Stokes equations. *Journal of Computational Physics*, 89(2):389–413.

Bruneau, C. H. and Saad, M. (2006). The 2D lid-driven cavity problem revisited. *Computers & Fluids*, 35(3):326–348.

Buhmann, M. D. (1990). Multivariate interpolation in odd-dimensional euclidean spaces using multiquadrics. *Constructive Approximation*, 6(1):21–34.

Cai, X. (2003). *Advanced Topics in Computational Partial Differential Equations*, volume 33 of *Lecture Notes in Computational Science & Engineering*. Springer, Berlin, Germany.

Caretto, L. S., Curr, R. M., and Spalding, D. B. (1972). Two numerical methods for three-dimensional boundary layers. *Computer Methods in Applied Mechanics & Engineering*, 1(1):39–57.

Carlson, R. E. and Foley, T. A. (1991). The parameter R2 in multiquadric interpolation. *Computers & Mathematics with Applications*, 21(9):29–42.

Chakrabarti, S. (2005). *Numerical Models in Fluid-Structure Interaction, Advances in Fluid Mechanics*, volume 42. WIT Press, Ashurst Lodge, Ashurst, Southampton, SO40 7AA.

Chen, Y., Lee, J., and Eskandarian, A. (2006). *Meshless Methods in Solid Mechanics*. Springer, NY 10013, USA.

Cheng, A. H. D., Golberg, M. A., Kansa, E. J., and Zammito, G. (2003). Exponential convergence and $H − c$ multiquadric collocation method for partial differential equations. *Numerical Methods for Partial Differential Equations*, 19(5):571–594.

Cheng, Y. G. and Zhang, H. (2010). Immersed boundary method and lattice Boltzmann method coupled FSI simulation of mitral leaflet flow. *Computers & Fluids*, 39(5):871–881.

Chu, P. C. and Fan, C. (2000). A three-point sixth-order staggered combined compact difference scheme. *Mathematical & computer modelling*, 32(3–4):323–340.

Colonius, T. (2004). Modeling artificial boundary conditions for compressible flow. *Annual Review of Fluid Mechanics*, 36:315–345.

Danaila, I. (2007). *An introduction to scientific computing: twelve computational projects solved with MATLAB*. Springer, NY 10013, USA.

Darwish, M., Sraj, I., and Moukalled, F. (2009). A coupled finite volume solver for the solution of incompressible flows on unstructured grids. *Journal of Computational Physics*, 228(1):180–201.

Dehghan, M. and Mohebbi, A. (2008). High-order compact boundary value method for the solution of unsteady convection-diffusion problems. *Mathematics & Computers in Simulation*, 79(3):683–699.

Deng, G., Piquet, J., Queutey, P., and Visonneau, M. (1994a). A new fully coupled solution of the Navier-Stokes equations. *International Journal for Numerical Methods in Fluids*, 19(7):605–639.

Deng, G. B., Piquet, J., Queutey, P., and Visonneau, M. (1994b). Incompressible-flow calculations with a consistent physical interpolation finite-volume approach. *Computers & Fluids*, 23(8):1029–1047.

Dillon, R., Fauci, L., Fogelson, A., and III, D. G. (1996). Modeling biofilm processes using the immersed boundary method. *Journal of Computational Physics*, 129(1):57–73.

Dilts, G. A. (1999). Moving-least-squares-particle hydrodynamics-I. consistency and stability. *International Journal for Numerical Methods in Engineering*, 44(8):1115–1155.

Dowell, E. H. and Hall, K. C. (2001). Modeling of fluid-structure interaction. *Annual Review of Fluid Mechanics*, 33(1):445–490.

Driscoll, T. A. and Fornberg, B. (2002). Interpolation in the limit of increasingly flat radial basis functions. *Computers & Mathematics with Applications*, 43(3–5):413–422.

Duarte, C. A. and Oden, J. T. (1996). Hp clouds-an hp meshless method. *Numerical Methods for Partial Differential Equations*, 12(6):673–706.

Elgohary, T. A., Dong, L., Junkins, J. L., and Atluri, S. N. (2014a). A simple, fast, and accurate time-integrator for strongly nonlinear dynamical systems. *Computer Modeling in Engineering & Sciences*, 100(3):249–275.

Elgohary, T. A., Dong, L., Junkins, J. L., and Atluri, S. N. (2014b). Time

domain inverse problems in nonlinear systems using collocation & radial basis functions. *Computer Modeling in Engineering & Sciences*, 100(1):59–84.

Elman, H. C., Howle, V. E., Shadid, J. N., and Tuminario, R. S. (2003). A parallel block multi-level preconditioner for the 3D incompressible Navier-Stokes equations. *Journal of Computational Physics*, 187(2):504–523.

Emdadi, A., Kansa, E., Libre, N., Rahimian, M., and Shekarchi, M. (2008). Stable PDE solution methods for large multiquadric shape parameters. *Computer Modeling in Engineering & Sciences*, 25(1):23–41.

Fadel, H., Agouzoul, M., and Jimack, P. K. (2011). High-order finite difference schemes for incompressible flows. *International Journal for Numerical Methods in Fluids*, 65(9):1050–1070.

Fasshauer, G. (2007). *Meshfree approximation methods with Matlab*. World Scientific Publishing, 5 Toh Tuck Link, Singapore 596224.

Fasshauer, G. E. and Mccourt, M. J. (2012). Stable evaluation of Gaussian radial basis function interpolants. *SIAM Journal on Scientific Computing*, 34(2):A737–A762.

Fauci, L. J. and Peskin, C. S. (1988). A computational model of aquatic animal locomotion. *Journal of Computational Physics*, 77(1):85–108.

Fedoseyev, A. I., Friedman, M. J., and Kansa, E. J. (2002). Improved multiquadric method for elliptic partial differential equations via PDE collocation on the boundary. *Computers & Mathematics with Applications*, 43(3–5):439–455.

Fornberg, B., Larsson, E., and Flyer, N. (2011). Stable computations with Gaussian radial basis functions. *SIAM Journal on Scientific Computing*, 33(2):869–892.

Fornberg, B., Lehto, E., and Powell, C. (2013). Stable calculation of Gaussian-based RBF-FD stencils. *Computers & Mathematics with Applications*, 65(4):627–637.

Fornberg, B. and Wright, G. (2004). Stable computation of multiquadric inter-

polants for all values of the shape parameter. *Computers & Mathematics with Applications*, 48(5–6):853–867.

Furuichi, M., May, D., and Tackley, P. (2011). Development of a Stokes flow solver robust to large viscosity jumps using a Schur complement approach with mixed precision arithmetic. *Journal of Computational Physics*, 230(24):8835–8851.

Galpin, P. F., Doormaal, J. P. V., and Raithby, G. D. (1985). Solution of the incompressible mass and momentum equations by application of a coupled equation line solver. *International Journal for Numerical Methods in Fluids*, 5(7):615–625.

Gamet, L., Ducros, F., Nicoud, F., and Poinsot, T. (1999). Compact finite difference schemes on non-uniform meshes. Application to direct numerical simulations of compressible flows. *International Journal for Numerical Methods in Fluids*, 29(2):159–191.

Ghia, U., Ghia, K. N., and Shin, C. T. (1982). High-resolutions for incompressible flows using Navier-Stokes equations and a multigrid method. *Journal of Computational Physics*, 48:387–411.

Gingold, R. A. and Monaghan, J. J. (1977). Smoothed particle hydrodynamics: theory and application to non-spherical stars. *Monthly Notices of the Royal Astronomical Society*, 181(3):375–389.

Girault, V. (1974). Theory of a finite difference method on irregular networks. *SIAM Journal on Numerical Analysis*, 11(2):260–282.

Gong, Z. X., Huang, H. X., and Lu, C. J. (2008). Stability analysis of the immersed boundary method for a two-dimensional membrane with bending rigidity. *Communications in Computational Physics*, 3(3):704–723.

Gresho, P. M., Chan, S. T., Lee, R. L., and Upson, C. D. (1984). A modified finite element method for solving the time-dependent, incompressible Navier-Stokes equations. Part 2: Applications. *International Journal for Numerical Methods in Fluids*, 4:619–640.

Griffith, B. E. (2012). On the volume conservation of the immersed boundary method. *Communications in Computational Physics*, 12(2):401–432.

Hanby, R. F., Silvester, D. J., and Chew, J. W. (1996). A comparison of coupled and segregated iterative solution techniques for incompressible swirling flow. *International Journal for Numerical Methods in Fluids*, 22:353–373.

Hardy, R. L. (1971). Multiquadric equations of topography and other irregular surfaces. *Journal of Geophysical Research*, 76(8):1905–1915.

Hardy, R. L. (1990). Theory and applications of the multiquadric-biharmonic method 20 years of discovery 1968-1988. *Computers & Mathematics with Applications*, 19(8-9):163–208.

Hassanien, I. A., Salama, A. A., and Hosham, H. A. (2005). Fourth-order finite difference method for solving Burgers equation. *Applied Mathematics & Computation*, 170(2):781–800.

Henniger, R., Obrist, D., and Kleiser, L. (2010). High-order accurate solution of the incompressible Navier-Stokes equations on massively parallel computers. *Journal of Computational Physics*, 229(10):3543–3572.

Hirsh, R. S. (1975). Higher order accurate difference solutions of fluid mechanics problems by a compact differencing technique. *Journal of Computational Physics*, 19(1):90–109.

Hon, Y. C., Sarler, B., and Dong, D. F. (2015). Local radial basis function collocation method for solving thermo-driven fluid-flow problems with free surface. *Engineering Analysis with Boundary Elements*, 57:2–8.

Hou, G., Wang, J., and Layton, A. (2012a). Numerical methods for fluid-structure interaction - a review. *Community Computational Physics*, 12(2):337–377.

Hou, G., Wang, J., and Layton, A. (2012b). Numerical methods for fluid-structure interaction - a review. *Community Computational Physics*, 12(2):337–377.

Hubner, B., Walhorn, E., and Dinkler, D. (2004). A monolithic approach to fluid-structure interaction using space-time finite elements. *Computer Methods in Applied Mechanics & Engineering*, 193(23 - 26):2087–2104.

Iaccarino, G., Kalitzin, G., Moin, P., and Khalighi, B. (2004). Local grid refinement for an immersed boundary RANS solver. 42nd *AIAA Aerospace Sciences Meeting and Exhibit, Reno, Nevada.*

Jeffrey, K. W. Immersed boundary method for shared-memory architectures. (accessed the URL on 3rd November 2015).

Jenkins, E. W., Kees, C. E., Kelley, C. T., and Miller, C. T. (2001). An aggregation-based domain decomposition preconditioner for groundwater flow. *SIAM Journal on Scientific Computing*, 23(2):430–441.

Kalita, J. C., Dalal, D. C., and Dass, A. K. (2002). A class of higher order compact schemes for the unsteady two-dimensional convection-diffusion equation with variable convection coefficients. *International Journal for Numerical Methods in Fluids*, 38(12):1111–1131.

Kansa, E. J. (1990a). Multiquadrics-a scattered data approximation scheme with applications to computational fluid-dynamics-I. Surface approximations and partial derivative estimates. *Computers & Mathematics with Applications*, 19(8–9):127–145.

Kansa, E. J. (1990b). Multiquadrics-a scattered data approximation scheme with applications to computational fluid-dynamics-II. Solutions to parabolic, hyperbolic and elliptic partial differential equations. *Computers & Mathematics with Applications*, 19(8–9):147–161.

Kansa, E. J. and Hon, Y. C. (2000). Circumventing the ill-conditioning problem with multiquadric radial basis functions: Applications to elliptic partial differential equations. *Computers & Mathematics with Applications*, 39(7–8):123–137.

Karaa, S. and Zhang, J. (2004). High order ADI method for solving unsteady convection-diffusion problems. *Journal of Computational Physics*, 198(1):1–9.

Karki, K. C. and Mongia, H. C. (1990). Evaluation of a coupled solution approach for fluid flow calculations in body-fitted co-ordinates. *International Journal for Numerical Methods in Fluids*, 11(1):1–20.

Kosec, G., Zaloznik, M., Sarler, B., and Combeau, H. (2011). A meshless approach towards solution of macrosegregation phenomena. *Computers, Materials, & Continua*, 22(2):169–195.

Kun, Z., Mo, Y., and Yuwen, Z. (2012). A compact finite-difference scheme based on the projection method for natural-convection heat transfer. *Numerical Heat Transfer, Part B: Fundamentals*, 61(4):259–278.

Lai, M. C. and Peskin, C. S. (2000). An immersed boundary method with formal second-order accuracy and reduced numerical viscosity. *Journal of Computational Physics*, 160(2):705–719.

Lancaster, P. and Salkauskas, K. (1981). Surfaces generated by moving least squares methods. *Mathematics of Computation*, 37(155):141–158.

Larsson, E. and Fornberg, B. (2005). Theoretical and computational aspects of multivariate interpolation with increasingly flat radial basis functions. *Computers & Mathematics with Applications*, 49(1):103–130.

Larsson, E., Lehto, E., Heryudono, A., and Fornberg, B. (2013). Stable computation of differentiation matrices and scattered node stencils based on Gaussian radial basis functions. *SIAM Journal on Scientific Computing*, 35(4):A2096–A2119.

Le, D. V. (2005). *An immersed interface method for solving viscous incompressible flows involving rigid and flexible boundaries*. PhD thesis, Singapore-MIT Alliance.

Lee, L. and Leveque, R. J. (2003). An immersed interface method for incompressible Navier–Stokes equations. *SIAM Journal on Scientific Computing*, 25(3):832–856.

Lele, S. K. (1992). Compact finite difference schemes with spectral-like resolution. *Journal of Computational Physics*, 103(1):16–42.

Leveque, R. J. and Li, Z. (1997). Immersed interface methods for Stokes flow with elastic boundaries or surface tension. *SIAM Journal on Scientific Computing*, 18(3):709–735.

Li, H. and Mulay, S. S. (2013). *Meshless methods and their numerical properties.* CRC Press.

Li, H., Ng, T. Y., Cheng, J. Q., and Lam, K. Y. (2003a). Hermite–cloud: a novel true meshless method. *Computational Mechanics*, 33(1):30–41.

Li, H., Wang, Q. X., and Lam, K. Y. (2004). Development of a novel meshless local kriging (lokriging) method for structural dynamic analysis. *Computer Methods in Applied Mechanics & Engineering*, 193(23):2599–2619.

Li, J., Cheng, A. H. D., and Chen, C. S. (2003b). A comparison of efficiency and error convergence of multiquadric collocation method and finite element method. *Engineering Analysis with Boundary Elements*, 27(3):251–257.

Li, M. and Tang, T. (2001). A compact fourth-order finite difference scheme for unsteady viscous incompressible flows. *Journal of Scientific Computing*, 16(1):29–45.

Libre, N. A., Emdadi, A., Kansa, E. J., Rahimian, M., and Shekarchi, M. (2008). A stabilized RBF collocation scheme for Neumann type boundary value problems. *Computer Modeling in Engineering & Sciences*, 24(1):61–80.

Liszka, T. and Orkisz, J. (1980). The finite difference method at arbitrary irregular grids and its application in applied mechanics. *Computers & Structures*, 11(1-2):83–95.

Liu, G. R. (2003). *Mesh free methods: moving beyond the finite element method.* CRC press.

Liu, W. K., Chen, Y., Chang, C. T., and Belytschko, T. (1996). Advances in multiple scale kernel particle methods. *Computational Mechanics*, 18(2):73–111.

Liu, W. K., Jun, S., and Zhang, Y. F. (1995). Reproducing kernel particle methods. *International journal for numerical methods in fluids*, 20(8-9):1081–1106.

Lucy, L. B. (1977). A numerical approach to the testing of the fission hypothesis. *The Astronomical Journal*, 82(12):1013–1024.

Ma, Y., Fu, D., Kobayashi, T., and Taniguchi, N. (1999). Numerical solution of

the incompressible Navier-Stokes equations with an upwind compact difference scheme. *International Journal for Numerical Methods in Fluids*, 30(5):509–521.

Ma, Y., Sun, C. P., Haake, D. A., Churchill, B. M., and Ho, C. M. (2012). A high-order alternating direction implicit method for the unsteady convection-dominated diffusion problem. *International Journal for Numerical Methods in Fluids*, 70(6):703–712.

Madych, W. R. and Nelson, S. A. (1990). Multivariate interpolation and conditionally positive definite functions. II. *Mathematics of Computation*, 54(189):211–230.

Mahesh, K. (1998). A family of high order finite difference schemes with good spectral resolution. *Journal of Computational Physics*, 145(1):332–358.

Mai-Duy, N. (2005). Solving high order ordinary differential equations with radial basis function networks. *International Journal for Numerical Methods in Engineering*, 62(6):824–852.

Mai-Duy, N. and Tanner, R. I. (2007). A collocation method based on one-dimensional RBF interpolation scheme for solving PDEs. *International Journal of Numerical Methods for Heat & Fluid Flow*, 17(2):165–186.

Mai-Duy, N. and Tran-Cong, T. (2001a). Numerical solution of differential equations using multiquadric radial basis function networks. *Neural Networks*, 14(2):185–199.

Mai-Duy, N. and Tran-Cong, T. (2001b). Numerical solution of Navier-Stokes equations using multiquadric radial basis function networks. *International Journal for Numerical Methods in Fluids*, 37(1):65–86.

Mai-Duy, N. and Tran-Cong, T. (2003). Approximation of function and its derivatives using radial basis function networks. *Applied Mathematical Modelling*, 27(3):197–220.

Mai-Duy, N. and Tran-Cong, T. (2005). An efficient indirect RBFN-based method for numerical solution of PDEs. *Numerical Methods for Partial Differential Equations*, 21(4):770–790.

Mai-Duy, N. and Tran-Cong, T. (2007). A cartesian-grid collocation method based on radial basis-function networks for solving PDEs in irregular domains. *Numerical Methods for Partial Differential Equations*, 23(5):1192–1210.

Mai-Duy, N. and Tran-Cong, T. (2010). A numerical study of 2D integrated RBFNs incorporating Cartesian grids for solving 2D elliptic differential problems. *Numerical Methods for Partial Differential Equations*, 26(6):1443–1462.

Mai-Duy, N. and Tran-Cong, T. (2011). Compact local integrated-RBF approximations for second-order elliptic differential problems. *Journal of Computational Physics*, 230(12):4772–4794.

Mai-Duy, N. and Tran-Cong, T. (2013). A compact five-point stencil based on integrated RBFs for 2D second-order differential problems. *Journal of Computational Physics*, 235:302–321.

Mariani, V. C. and Prata, A. T. (2008). A Eulerian-Lagrangian method applied to fluid flow in lid-driven cavities with irregular bottom walls. *Numerical Heat Transfer Part B-Fundamentals*, 53(3):206–233.

May, D. A. and Moresi, L. (2008). Preconditioned iterative methods for stokes flow problems arising in computational geodynamics. *Physics of the Earth & Planetary Interiors*, 171(1):33–47.

Mazhar, Z. (2001). A procedure for the treatment of the velocity-pressure coupling problem in incompressible fluid flow. *Numerical Heat Transfer Part B-Fundamentals*, 39(1):91–100.

McQueen, D. M., Peskin, C. S., and Yellin, E. L. (1982). Fluid dynamics of the mitral valve: physiological aspects of a mathematical model. *American Journal of Physiology-Heart & Circulatory Physiology*, 242(6):H1095–H1110.

Miller, L. A. and Peskin, C. S. (2004). When vortices stick: an aerodynamic transition in tiny insect flight. *Journal of Experimental Biology*, 207(17):3073–3088.

Mittal, R. and Iaccarino, G. (2005). Immersed boundary methods. *Annual Review of Fluid Mechanics*, 37:239–261.

Moin, P. and Kim, J. (1980). On the numerical solution of time-dependent viscous incompressible fluid flows involving solid boundaries. *Journal of Computational Physics*, 35(3):381–392.

Morand, H. J. P. and Ohayon, R. (1995). *Fluid-Structure Interaction: Applied Numerical Methods.* John Wiley.

Mramor, K., Vertnik, R., and Sarler, B. (2013). Low and intermediate *Re* solution of lid driven cavity problem by local radial basis function collocation method. *Computers, Materials & Continua*, 1(1):1–21.

Nayroles, B., Touzot, G., and Villon, P. (1992). Generalizing the finite element method: Diffuse approximation and diffuse elements. *Computational Mechanics*, 10(5):307–318.

Newren, E. P. (2007). *Enhancing the immersed boundary method: stability, volume conservation, and implicit solvers.* PhD thesis, The University of Utah.

Ngo-Cong, D., Mai-Duy, N., Karunasena, W., and Tran-Cong, T. (2012). A numerical procedure based on 1D-IRBFN and local MLS-1D-IRBFN methods for fluid-structure interaction analysis. *Computer Modeling in Engineering & Sciences*, 83(5):459–498.

Nguyen, V. P., Rabczuk, T., Bordas, S., and Duflot, M. (2008). Meshless methods: a review and computer implementation aspects. *Mathematics & Computers in Simulation*, 79(3):763–813.

Niyogi, P., Chakrabartty, S. K., and Laha, M. K. (2009). *Introduction to computational fluid dynamics.* Dorling Kindersley, 482, F. I. E., Patparganj, Delhi 110 092, India.

Noye, B. J. and Tan, H. H. (1989). Finite difference methods for solving the two-dimensional advection-diffusion equation. *International Journal for Numerical Methods in Fluids*, 9(1):75–98.

Onate, E., Idelsohn, S., Zienkiewicz, O. C., and Taylor, R. L. (1996). A finite point method in computational mechanics. applications to convective transport

and fluid flow. *International Journal for Numerical Methods in Engineering*, 39(22):3839–3866.

Palma, J. M. L. M., Amesto, P. R., Michel, D., Marta, M., and Lopes, J. C. (2008). *High Performance Computing for Computational Science-VECPAR 2008: 8th International Conference, Toulouse, France, June 24-27, 2008. Revised Selected Papers*, volume 5336. Springer.

Pascau, A. and Perez, C. (1996). A comparison of segregated and coupled methods for the solution of the incompressible Navier-Stokes equations. *Communications in Numerical Methods in Engineering*, 12(10):617–630.

Patankar, S. V. and Spalding, D. B. (1972). A calculation procedure for heat, mass and momentum transfer in three-dimensional parabolic flows. *International Journal of Heat & Mass Transfer*, 15(10):1767–1806.

Perot, J. B. (1993). An analysis of the fractional step method. *Journal of Computational Physics*, 108(1):51–58.

Peskin, C. S. (1977). Numerical analysis of blood flow in the heart. *Journal of Computational Physics*, 25(3):220–252.

Power, H. and Barraco, V. (2002). A comparison analysis between unsymmetric and symmetric radial basis function collocation methods for the numerical solution of partial differential equations. *Computers & Mathematics with Applications*, 43(3-5):551–583.

Quarteroni, A. and Valli, A. (1999). *Domain decomposition methods for partial differential equations*. Clarendon Press, Oxford.

Rabczuk, T., Belytschko, T., and Xiao, X. P. (2004). Stable particle methods based on lagrangian kernels. *Computer Methods in Applied Mechanics & Engineering*, 193(12):1035–1063.

Richards, C. W. and Crane, C. M. (1979). The accuracy of finite difference schemes for the numerical solution of the Navier-Stokes equations. *Applied Mathematical Modelling*, 3(3):205–211.

Rippa, S. (1999). An algorithm for selecting a good value for the parameter c in

radial basis function interpolation. *Advances in Computational Mathematics*, 11(2-3):193–210.

Rubin, S. G. and Khosla, P. K. (1977). Polynomial interpolation methods for viscous flow calculations. *Journal of Computational Physics*, 24(3):217–244.

Ryzhakov, P. B., Rossi, R., Idelsohn, S. R., and Onate, E. (2010). A monolithic lagrangian approach for fluid-structure interaction problems. *Computational Mechanics*, 46(6):883–899.

Saad, Y. and Schultz, M. H. (1986). GMRES: A generalized minimal residual algorithm for solving nonsymmetric linear systems. *SIAM Journal on Scientific & Statistical Computing*, 7(3):856–869.

Sahin, M. and Owens, R. (2003). A novel fully implicit finite volume method applied to the lid-driven cavity problem - Part I: High Reynolds number flow calculations. *International Journal for Numerical Methods in Fluids*, 42(1):57–77.

Sarra, S. A. (2006). Integrated multiquadric radial basis function approximation methods. *Computers & Mathematics with Applications*, 51(8):1283–1296.

Sellountos, E. J., Polyzos, D., and Atluri, S. N. (2012). A new and simple meshless LBIE-RBF numerical scheme in linear elasticity. *Computer Modeling in Engineering & Sciences*, 89(6):511–549.

Sheu, T. W. H., Kao, N. S. C., Chiu, P. H., and Lin, C. S. (2011). Development of an upwinding scheme through the minimization of modified wavenumber error for the incompressible Navier-Stokes equations. *Numerical Heat Transfer, Part B: Fundamentals*, 60(3):179–202.

Shu, C., Ding, H., and Yeo, K. (2003). Local radial basis function-based differential quadrature method and its application to solve two-dimensional incompressible NavierStokes equations. *Computer Methods in Applied Mechanics & Engineering*, 192(7-8):941–954.

Shu, C. and Wu, Y. L. (2007). Integrated radial basis functions-based differential

quadrature method and its performance. *International Journal for Numerical Methods in Fluids*, 53(6):969–984.

Shyy, W., Udaykumar, H. S., Rao, M. M., and Smith, R. W. (1996). *Computational fluid dynamics with Moving boundaries*. Taylor&Francis, 1900 Frost Road, Suite 101, Bristol, PA 19007-1598.

Silvester, D., Elman, H., Kay, D., and Wathen, A. (2001). Efficient preconditioning of the linearized Navier-Stokes equations for incompressible flow. *Journal of Computational & Applied Mathematics*, 128(1):261–279.

Smith, B. F., Bjorstad, P. E., and Gropp, W. D. (1996). *Domain Decomposition Parallel Multilevel Methods for Elliptic Partial Differential Equations*. Cambridge University Press, NY 10011-4211, USA.

Sotiropoulos, F. and Yang, X. (2014). Immersed boundary methods for simulating fluid–structure interaction. *Progress in Aerospace Sciences*, 65:1–21.

Spotz, W. F. and Carey, G. F. (1995). High-order compact scheme for the steady stream-function vorticity equations. *International Journal for Numerical Methods in Engineering*, 38(20):3497–3512.

Stefano, D. M. and Gabriele, S. (2013). A new stable basis for radial basis function interpolation. *Journal of Computational & Applied Mathematics*, 253:1–13.

Stockie, J. M. (1997). *Analysis and computation of immersed boundaries, with application to pulp fibres*. PhD thesis, The University of British Columbia.

Stockie, J. M. and Wetton, B. R. (1999). Analysis of stiffness in the immersed boundary method and implications for time-stepping schemes. *Journal of Computational Physics*, 154(1):41–64.

Strang, G. (2007). *Computational science and engineering*. Wellesley-Cambridge Press, MA 02482, USA.

Thai-Quang, N., Le-Cao, K., Mai-Duy, N., and Tran-Cong, T. (2012a). A high-order compact local integrated-RBF scheme for steady-state incompressible viscous flows in the primitive variables. *Computer Modeling in Engineering & Sciences*, 84(6):528–557.

Thai-Quang, N., Mai-Duy, N., D.Tran, C., and Tran-Cong, T. (2013). A direct forcing immersed boundary method employed with compact integrated RBF approximations for heat transfer and fluid flow problems. *Computer Modeling in Engineering & Sciences*, 96(1):49–90.

Thai-Quang, N., Mai-Duy, N., Tran, C. D., and Tran-Cong, T. (2012b). High-order alternating direction implicit method based on compact integrated-RBF approximations for unsteady/steady convection-diffusion equations. *Computer Modeling in Engineering & Sciences*, 89(3):189–220.

Tian, Z., Liang, X., and Yu, P. (2011). A higher order compact finite difference algorithm for solving the incompressible Navier-Stokes equations. *International Journal for Numerical Methods in Engineering*, 88(6):511–532.

Tian, Z. F. and Ge, Y. B. (2007). A fourth-order compact ADI method for solving two-dimensional unsteady convection-diffusion problems. *Journal of Computational & Applied Mathematics*, 198(1):268–286.

Tien, C. M. T., Mai-Duy, N., Tran, C. D., and Tran-Cong, T. (2015a). A numerical study of compact approximations based on flat integrated radial basis functions for second-order differential equations. *Computers & Mathematics with Applications (under review)*.

Tien, C. M. T., Thai-Quang, N., Mai-Duy, N., Tran, C. D., and Tran-Cong, T. (2015b). High-order fully coupled scheme based on compact integrated RBF approximation for viscous flows in regular and irregular domains. *Computer Modeling in Engineering & Sciences*, 105(4):301–340.

Tien, C. M. T., Thai-Quang, N., Mai-Duy, N., Tran, C. D., and Tran-Cong, T. (2015c). A three-point coupled compact integrated RBF scheme for second-order differential problems. *Computer Modeling in Engineering & Sciences*, 104(6):425–469.

Toselli, A. and Widlund, O. (2005). *Domain Decomposition Methods - Algorithms and Theory*. Springer, Berlin, Germany.

Udaykumar, H. S., Shyy, W., and Rao, M. M. (1996). ELAFINT: A mixed

Eulerian-Lagrangian method for fluid flows with complex and moving boundaries. *International Journal for Numerical Methods in Fluids*, 22(8):691–712.

Uhlmann, M. (2005). An immersed boundary method with direct forcing for the simulation of particular flows. *Journal of Computational Physics*, 209(2):448–476.

Vanka, S. P. (1986a). Block-implicit multigrid solution of Navier-Stokes equations in primitive variables. *Journal of Computational Physics*, 65(1):138–158.

Vanka, S. P. (1986b). A calculation procedure for three-dimensional steady recirculating flows using multigrid methods. *Computer Methods in Applied Mechanics & Engineering*, 55(3):321–338.

Vierendeels, J., Dumont, K., and Verdonck, P. R. (2008). A partitioned strongly coupled fluid-structure interaction method to model heart valve dynamics. *Journal of Computational & Applied Mathematics*, 215(2):602–609.

Wang, J. G. and Liu, G. R. (2002a). On the optimal shape parameters of radial basis functions used for 2-D meshless methods. *Computer methods in applied mechanics and engineering*, 191(23):2611–2630.

Wang, J. G. and Liu, G. R. (2002b). A point interpolation meshless method based on radial basis functions. *International Journal for Numerical Methods in Engineering*, 54(11):1623–1648.

Wathen, A. J. and Zhu, S. (2015). On spectral distribution of kernel matrices related to radial basis functions. *Numerical Algorithms*, 70(4):709–726.

Wood, C., Gil, A. J., Hassan, O., and Bonet, J. (2010). Partitioned block-Gauss-Seidel coupling for dynamic fluid-structure interaction. *Computers & Structures*, 88(23–24):1367–1382.

You, D. (2006). A high-order Pade ADI method for unsteady convection-diffusion equations. *Journal of Computational Physics*, 214(1):1–11.

Zedan, M. and Schneider, G. E. (1985). A coupled strongly implicit procedure for velocity and pressure computation in fluid flow problems. *Numerical Heat Transfer*, 8(5):537–557.

Zerroukat, M., Power, H., and Chen, C. S. (1998). A numerical method for heat transfer problems using collocation and radial basis functions. *International Journal for Numerical Methods in Engineering*, 42(7):1263–1278.